SYNTHESIS, STRUCTURE AND PROPERTIES OF CARBOXYLATE COORDINATION POLYMERS

Rebecca Clulow

A Thesis Submitted for the Degree of PhD
at the
University of St Andrews

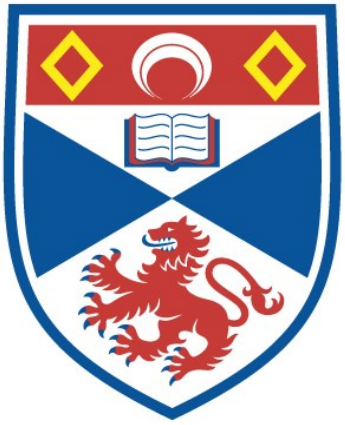

2019

Identifiers to use to cite or link to this thesis:
DOI: https://doi.org/10.17630/sta/10023-18591
http://hdl.handle.net/10023/18591

Synthesis, Structure and Properties of Carboxylate Coordination Polymers

Rebecca Clulow

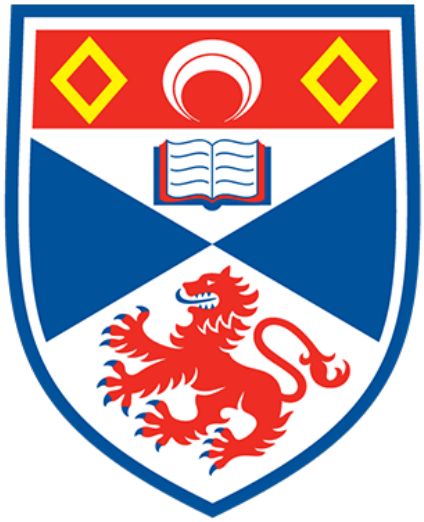

University of St Andrews

This thesis is submitted in partial fulfilment for the degree of

Doctor of Philosophy (PhD)

at the University of St Andrews

March 2019

Candidate's declaration

I, Rebecca Clulow, do hereby certify that this thesis, submitted for the degree of PhD, which is approximately 36,000 words in length, has been written by me, and that it is the record of work carried out by me, or principally by myself in collaboration with others as acknowledged, and that it has not been submitted in any previous application for any degree.

I was admitted as a research student at the University of St Andrews in September 2015.

I received funding from an organisation or institution and have acknowledged the funder(s) in the full text of my thesis.

Date Signature of candidate

Supervisor's declaration

I hereby certify that the candidate has fulfilled the conditions of the Resolution and Regulations appropriate for the degree of PhD in the University of St Andrews and that the candidate is qualified to submit this thesis in application for that degree.

Date Signature of supervisor

Permission for publication

In submitting this thesis to the University of St Andrews we understand that we are giving permission for it to be made available for use in accordance with the regulations of the University Library for the time being in force, subject to any copyright vested in the work not being affected thereby. We also understand, unless exempt by an award of an embargo as requested below, that the title and the abstract will be published, and that a copy of the work may be made and supplied to any bona fide library or research worker, that this thesis will be electronically accessible for personal or research use and that the library has the right to migrate this thesis into new electronic forms as required to ensure continued access to the thesis.

I, Rebecca Clulow, have obtained, or am in the process of obtaining, third-party copyright permissions that are required or have requested the appropriate embargo below.

The following is an agreed request by candidate and supervisor regarding the publication of this thesis:

Printed copy

Embargo on all of print copy for a period of 1 year on the following ground(s):

- Publication would preclude future publication

Supporting statement for printed embargo request

The thesis contains research which has not yet been published and therefore, publication of this thesis would preclude further publications

Electronic copy

Embargo on all of electronic copy for a period of 1 year on the following ground(s):

- Publication would preclude future publication

Supporting statement for electronic embargo request

The thesis contains research which has not yet been published and therefore, publication of this thesis would preclude further publications

Title and Abstract

- I require an embargo on the abstract only.

Date Signature of candidate

Date Signature of supervisor

Underpinning Research Data or Digital Outputs

Candidate's declaration

I, Rebecca Clulow, understand that by declaring that I have original research data or digital outputs, I should make every effort in meeting the University's and research funders' requirements on the deposit and sharing of research data or research digital outputs.

Date Signature of candidate

Permission for publication of underpinning research data or digital outputs

We understand that for any original research data or digital outputs which are deposited, we are giving permission for them to be made available for use in accordance with the requirements of the University and research funders, for the time being in force.

We also understand that the title and the description will be published, and that the underpinning research data or digital outputs will be electronically accessible for use in accordance with the license specified at the point of deposit, unless exempt by award of an embargo as requested below.

The following is an agreed request by candidate and supervisor regarding the publication of underpinning research data or digital outputs:

Embargo on all of electronic files for a period of 1 year on the following ground(s):

- Publication would preclude future publication

Supporting statement for embargo request

Much of the data contains research which has not yet been published and would therefore preclude further publications

Date Signature of candidate

Date Signature of supervisor

Abstract

The work in this thesis focuses on several coordination polymers, their crystal structures and their potential applications as functional materials, in particular, their ferroelectric and magnetic properties.

The mechanism of the known ferroelectric phase transition of $(C_3NO_2H_7)_3CaCl_2$ (TSCC) was studied in detail using both X-ray and neutron diffraction data. The key structural changes occurring in the vicinity of T_C were identified in the Ca-O-C bond angles, which change by up to 12˚. The structure of the compound was determined between 300 and 20 K to investigate potential phase transitions as suggested in the literature. The diffraction data did not suggest an additional phase transition within this temperature range. However, the detailed crystallographic studies did uncover new evidence of ferrielectricity, which is consistent with electrical hysteresis data.

The origins of the ferroelectricity of TSCC were also probed through the synthesis and characterisation of a range TSCC-related compounds which incorporated a range of alternative halides and metal 2+ cations. Each compound formed coordination polymers which were linked by sarcosine molecules, although the connectivity and structures formed were dependent upon the composition. Whilst none of the TSCC derivatives had ferroelectric properties, diffraction experiments were limited to a low temperature of 90 K and there could be additional phase transitions below this point.

A family of oxalate-based coordination polymers $ALi_3M(C_2O_4)_3$ with a perovskite-like structures were also synthesised. The structural flexibility of these systems was investigated through the incorporation of different A site cations and their magnetic properties were investigated. Polyhedral distortions increase significantly upon the inclusion of rubidium or caesium. Both $KLi_3Co(C_2O_4)_3$ and $KLi_3Ni(C_2O_4)_3$ have weak antiferromagnetic exchange and μ_{eff} of 4.82 μ_B and 3.62 μ_B, respectively. The syntheses and structures of four new oxalate containing compounds, namely $Rb_2Co(C_2O_4)_2.4H_2O$, $Rb_2CoCl_2(C_2O_4)$, $K_2Li_2Cu(C_2O_4)_3$ and $Li_4Co(C_2O_4)_3$, which could have interesting magnetic and electrochemical properties, are also reported.

Acknowledgements

First and foremost, I would like to thank my supervisor Prof Philip Lightfoot for the opportunity to continue my studies as a PhD student and join his research group. Especially, for taking a personal interest in my work and for always finding the time to offer advice and guidance despite any other commitments. I would also like to thank Prof James Scott and Dr Finlay Morrison, without whom the work on TSCC would not have been possible.

During the course of my PhD I've had the opportunity to undertake experiments at the ISIS neutron and muon source and I'm very grateful to Dr Silvia Capelli, the instrument scientist at SXD for her expertise in single crystal neutron diffraction and her patient guidance during my time at ISIS. Additionally, I would like to thank Dr Mike Probert at Newcastle University for collecting single X-ray diffraction data at extremely low temperatures.

Over the course of the project, multiple analytical techniques have been used which would not have been possible without the guidance of Mrs Sylvia Williamson, Dr Gavin Peters and Dr Yuri Andreev at the University of St Andrews. Specifically, I would like to thank Prof Alex Slawin and Dr David Cordes for their invaluable guidance during the analysis of single crystal diffraction data and for giving up their weekends to carry out multiple variable temperature diffraction experiments on my behalf. I must also thank Prof Stephen Lee from the School of Physics for the use of the SQUID instrument, his help in the data analysis and for making time to answer all of my questions.

I would also like to thank all of my friends, in particular, Jason, Kerry, Lauren and Catherine who have made the last four years so enjoyable. Additionally, I would like to thank all members of the Lightfoot group past and present for welcoming me to the group and for making the lab a pleasant and enjoyable place to work. A huge thank you

must also go to my family, Gary, Jeed, Thomas and Natalie for their continued support, guidance and encouragement over the last four years.

Funding

This work was supported by the Engineering and Physical Sciences Research Council grant number EP/K503162-1 and the School of Chemistry at the University of St Andrews

Primary data underpinning the thesis are available at:
https://doi.org/10.17630/000ddea9-f1d9-4ef7-b7e4-b57342d69fe4

Table of Contents

List of Publications

Ferrielectricity in the metal-organic ferroelectric tris-sarcosine calcium chloride

J. F. Scott, F. D. Morrison, A. M. Z. Slawin, P. Lightfoot, R. Clulow, A. S. A. Gherson, A. M. Bumstead, J. Gardner, S. C. Capelli, M. R. Probert, S. Sahoo, J. S. Young, R. S. Katiyar and E. K. H. Salje, *Phys. Rev. B*, 2017, **95**, 094119.

New sarcosine–metal halide complexes related to ferroelectric TSCC

R. Clulow and P. Lightfoot, *CrystEngComm*, 2018, **20**, 4012–4019.

A hybrid fluoride layered perovskite, $(enH_2)MnF_4$

T. Li, R. Clulow, A. J. Bradford, S. L. Lee, A. M. Z. Slawin and P. Lightfoot, *Dalt. Trans.*, 2019, **48**, 4784-4787

List of Abbreviations

ADP	Atomic Displacement Parameter
BSCl	Bis-Sarcosine Calcium Chloride Dihydrate
BSMgC	Bis-Sarcosine Magnesium Chloride Dihydrate
BSMnC	Bis-Sarcosine Manganese Chloride Dihydrate
BVS	Bond Valence Sum
DSC	Differential Scanning Calorimetry
DTA	Differential Thermal Analysis
EDX	Energy Dispersive X-ray Spectroscopy
EPR	Electron Paramagnetic Resonance
GSAS	General Structure Analysis System
PIEFACE	Polyhedra Inscribing Ellipsoids For Analysis of Coordination Environments
R1	R Factor
SEM	Scanning Electron Microscopy
SQUID	Superconducting Quantum Interference Device
T_C	Curie Temperature
TGA	Thermal Gravimetric Analysis
TSCB	Tris-Sarcosine Calcium Bromide
TSCI	Tetra-Sarcosine Calcium Iodide Dihydrate
TSMgB	Tris-Sarcosine Magnesium Bromide Dihydrate
TSMnI	Tris-Sarcosine Manganese Iodide Dihydrate
TSSB	Tris-Sarcosine Strontium Bromide
TSSC	Tris-Sarcosine Strontium Chloride
wR2	Weighted R Factor

Chapter 1 Background and Introduction

1.1 Coordination Complexes and Polymers

Coordination compounds span a huge range of fields including functional materials, catalysis, and biological systems. Within functional materials, coordination compounds have potential applications in many areas, for example magnetism, porous materials and ferroelectrics.[1,2]

Coordination compounds are composed of a central atom or ion which is surrounded by coordinating molecules or ions. The central atom is often a metal and acts as an electron pair acceptor, whilst the surrounding molecules, known as ligands, act as electron pair donators. The number of electron pairs donated is equivalent to the coordination number of the complex. The most common values are two, four and six, but intermediate coordination numbers are also known to exist.[3]

Potential ligands include both neutral and anionic species, and these include H_2O, NH_3, phosphines, carboxylates ($RCOO^-$), OH^- and oxalate ($[C_2O_4]^{2-}$). In addition to a vast range of possible ligands, many can form multiple coordinate bonds and act as bridging or chelating ligands. The number of bonds formed by a ligand are indicated by the prefixes mono-, bi-, tri- or tetradentate.[4] If the ligands act as bridging ligands connecting multiple metal atoms, coordination polymers can be formed. The structures formed by coordination polymers include chain, layered and three-dimensional structures. The connectivity of metal centres has applications for the synthesis of porous materials and also introduces the possibility of magnetic exchange, which could have implications for the material's magnetic properties.[1,2]

1.2 Carboxylate Ligands

1.2.1 Monocarboxylates

Carboxylate ligands are among the most versatile ligands for coordination complexes. They introduce high structural diversity since they can adopt several different binding modes as depicted in Figure 1.1.[1] The ligands can act as polydentate, bridging or

chelating ligands thus allowing the formation of chains, layers and three-dimensional coordination polymers.[5,6,7] Additionally, the variety of binding modes allows both ferromagnetic and antiferromagnetic exchange. The *syn-anti* mode can allow ferromagnetic interactions, whilst both the *syn-syn* and *anti-anti* can form antiferromagnetic interactions.[2,8]

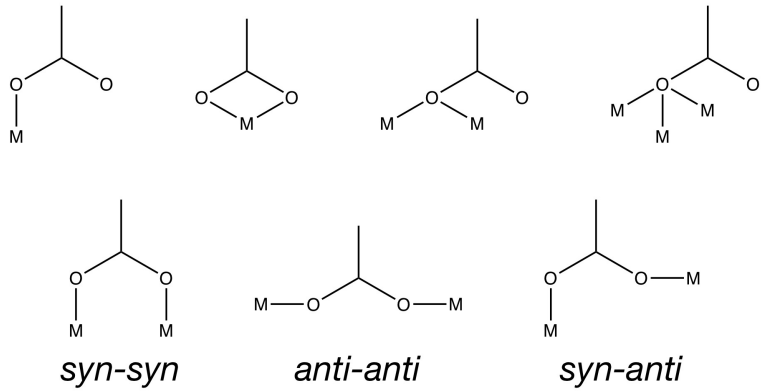

Figure 1.1: The seven basic binding modes of any carboxylate ligand[1]

The simplest mono carboxylate ligand is formate (HCO_2^-) and is known to form coordination complexes with interesting properties including ferroelectricity, antiferroelectricity and ferromagnetism.[9,10.6] One example is copper (II) formate tetrahydrate $Cu(COOH)_2(H_2O)_2.2H_2O$ which is antiferroelectric below 235.5 K.[6] The structure consists of copper formate layers which are separated by disordered water molecules, as shown by its crystal structure in Figure 1.2.[11] The ordering of the water molecules is thought to be responsible for the antiferroelectric phase transition. In addition, the material possesses antiferromagnetic properties below 17 K.[12]

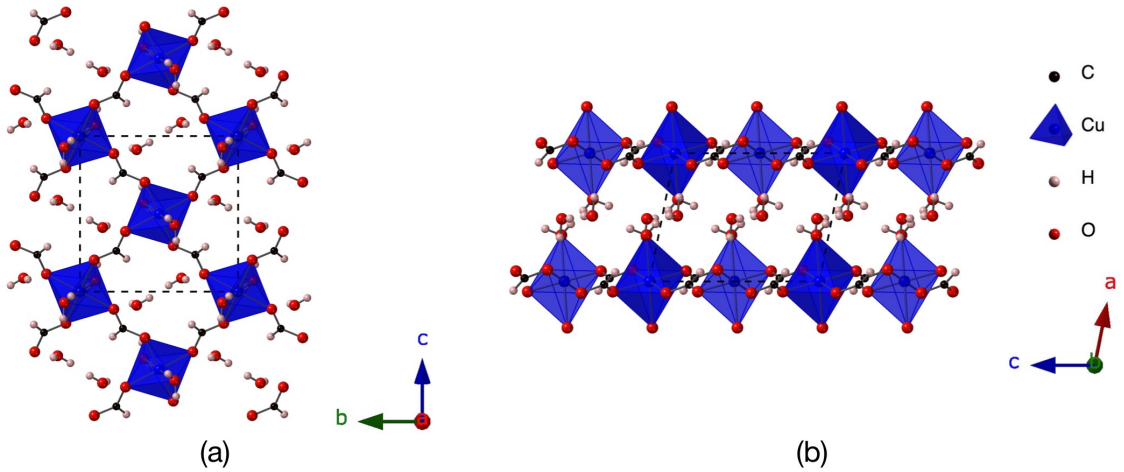

Figure 1.2: Crystal structure of copper (II) formate tetrahydrate $Cu(COOH)_2(H_2O)_2.2H_2O$ recreated derived from diffraction data collected at 200 K as reported by Zhang *et al.*[13]

The coordination polymer $Mn_3(COOH)_6.C_2H_5OH$ also utilises the formate bridging ligand. The structure forms a three-dimensional network of $MnMn_4$ tetrahedra which are linked by formate ligands; the resulting structure contains porous channels which can incorporate a variety of solvents (Figure 1.3).[7] The ethanol variant undergoes a ferroelectric phase transition at 165 K and is ferrimagnetic below 8.5 K.[14]

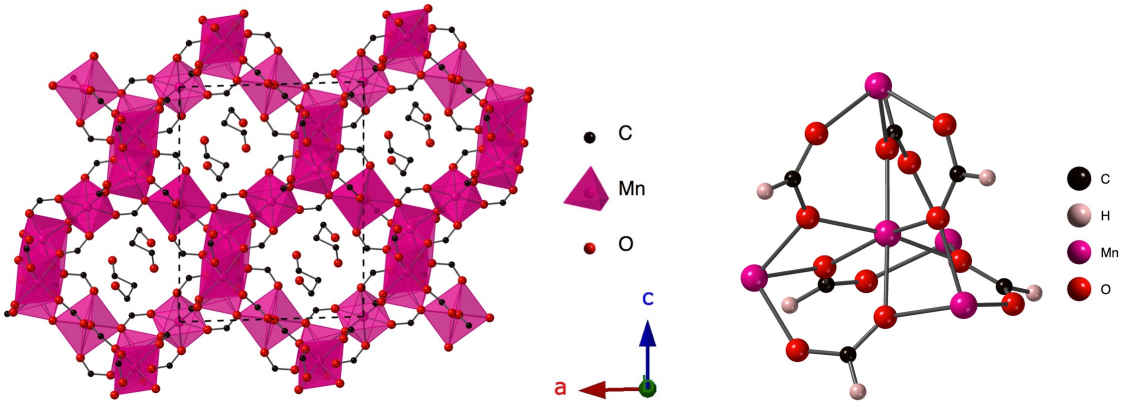

Figure 1.3: Crystal structure and tetrahedral $MnMn_4$ nodes of $Mn_3(COOH)_6.C_2H_5OH$ derived from diffraction data as reported by Cui *et al.*[15]

Another carboxylate ligand which forms a ferroelectric coordination polymer is propionic acid (CH_3CH_2COOH). One example is calcium strontium propionate ($Ca_2Sr(CH_3CH_2COO)_6$ which is ferroelectric below 282.6 K.[16] The high temperature phase adopts the $P4_12_12_1$ space group and the ferroelectric phase the $P4_1$ space group.[17,18] Two other compounds with the same stoichiometry, $Ca_2Ba(CH_3CH_2COO)_6$ and

$Ca_2Pb(CH_3CH_2COO)_6$, also possess interesting electrical properties. The barium derivative is ferroelectric at high pressure and the lead variant is a room temperature ferroelectric at ambient pressure.[19,10,20]

1.2.2. Dicarboxylates

An interesting variation on typical carboxylate ligands are the dicarboxylates, where the incorporation of two carboxylates increases the number of potential coordination sites. As a result, in addition to acting as bridging and chelating ligands, dicarboxylates can act as mono-, bi-, tri- and tetradentate ligands. A significant advantage of the dicarboxylates is the tunability of the R group in terms of size, flexibility and bite angles.[1]

The simplest dicarboxylate is the oxalate ligand which often acts as a rigid bidentate ligand, however there are 17 possible binding modes.[2] As a result, the oxalate ligand can form a wide range of structure types including chains, layers and 3D networks. Oxalate coordination compounds are already known to exist in nature and have been extensively studied in relation to molecular magnets.[21,22] The ligand can provide both antiferromagnetic and ferromagnetic exchange due to the multiple binding modes. [21,23] In addition, oxalate compounds have potential applications for battery materials. One example is the sodium iron oxalate reported by Yao *et al.* ($Na_2Fe(C_2O_4)F_2$). The compound contains infinite chains of Fe^{2+} atoms which are linked by oxalate bridging ligands (Figure 1.4), and has demonstrated interesting properties as a potential battery cathode.[24]

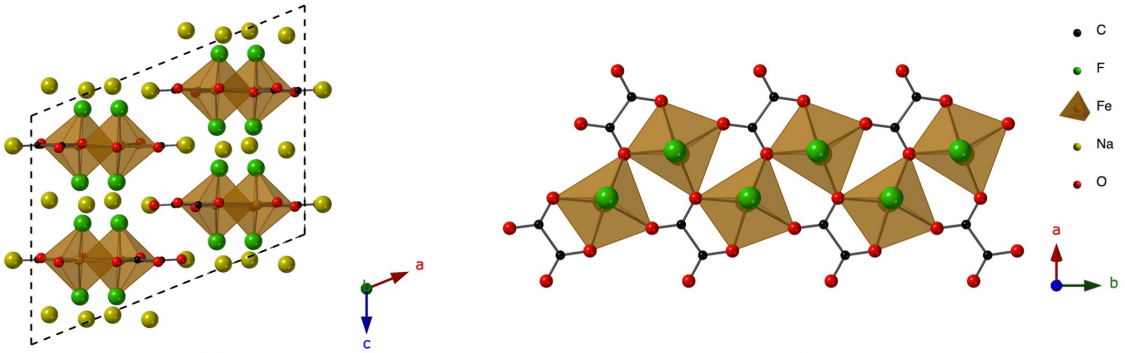

Figure 1.4: Crystal structure of $Na_2Fe(C_2O_4)F_2$ derived from single crystal diffraction data as reported by Yao *et al*.[24]

One of the most well-known examples of a dicarboxylate is Rochelle salt, potassium sodium tartrate ($KNa(C_4H_4O_6)$), which was the first ferroelectric crystal and was discovered by Valasek in 1921.[25] The material has two phase transitions, one at 255 K and the other at 297 K. Between the two temperatures, the compound adopts the polar $P2_1$ space group and displays ferroelectric properties. Outwith this temperature range, the material adopts the orthorhombic $P2_12_12_1$ space group and both phase transitions are second order. The structure of Rochelle salt in the paraelectric phase is shown in Figure 1.5.

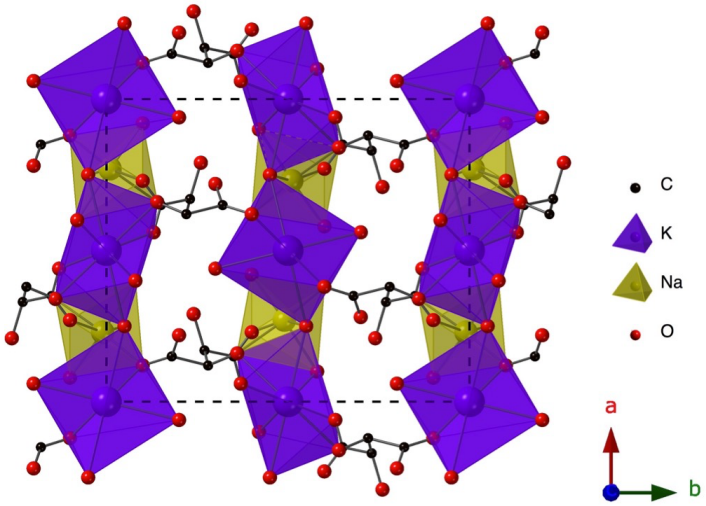

Figure 1.5: The crystal structure of Rochelle salt derived from diffraction data as reported by Beevers *et al.*[26]

1.2.3. Amino Acids

Amino acid ligands are also good candidates for coordination polymers since they are nontoxic and can introduce further structural diversity. The presence of the nitrogen atom increases the number of potential binding modes since they can be coordinated through either oxygen or nitrogen, or both atoms. Some of the potential binding modes of amino acids are depicted in Figure 1.6. Amino acids are most commonly utilised in their zwitterionic form, however the ligands can be used as both anionic and cationic species to produce charged and neutral complexes.

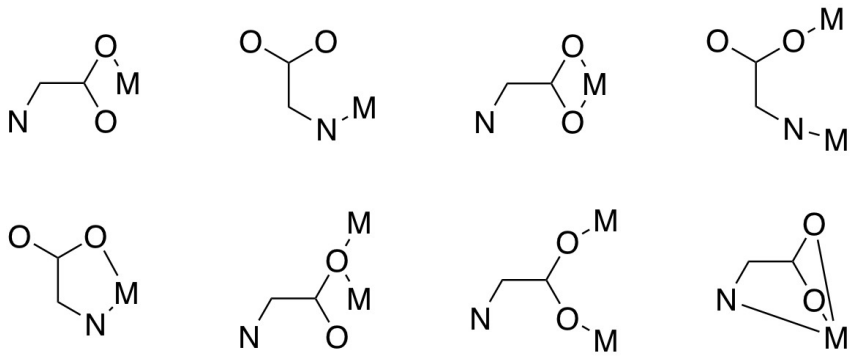

Figure 1.6: Eight possible binding modes of a generic amino acid[27]

In addition to the twenty standard amino acids, there are several examples of other amino acids which can be utilised in coordination compounds and polymers.[28] Whilst the most commonly used one is the simplest amino acid glycine, there have been several other reported compounds, including betaine, ornithine and sarcosine.[29]

A room temperature ferroelectric incorporating glycine has been previously reported by Pepinsky *et al.* with the composition $(NH_3CH_2COO)_2MnCl_2.2H_2O$. The compound consists of isolated Mn^{2+} octahedra with glycine, chloride and water molecules coordinated to the Mn^{2+} centre (Figure 1.7). The compound exhibits ferroelectric properties between 77 K and 328 K where the sample becomes dehydrated.[30]

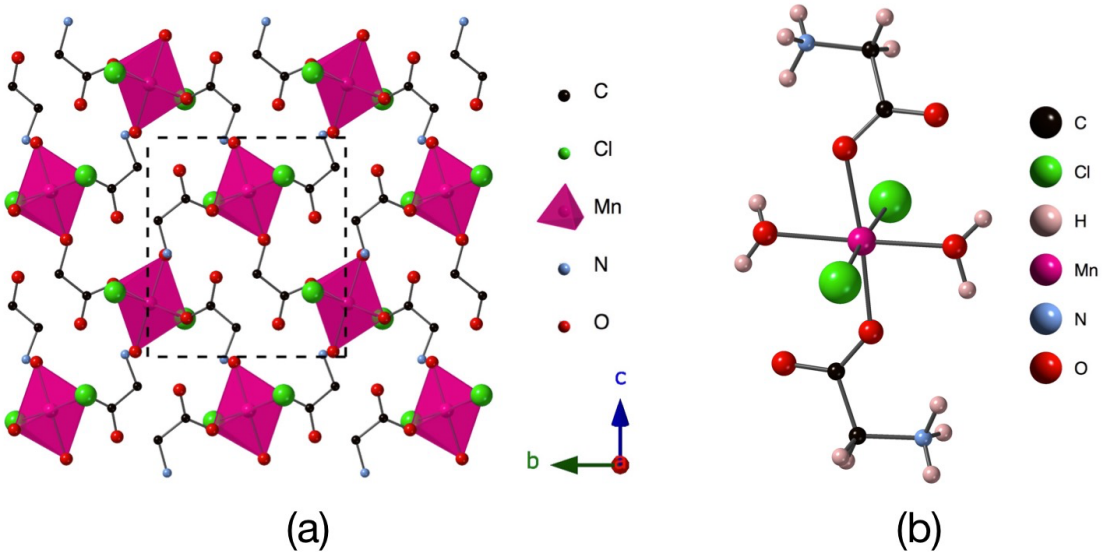

Figure 1.7: Crystal structure of $(NH_3CH_2COO)_2MnCl_2.2H_2O$ (a) viewed along the *a* axis and (b) Mn coordination environment

Another example of an amino acid-containing coordination polymer is *tris* sarcosine calcium chloride (TSCC) which is discussed extensively in chapter 4. The compound uses sarcosine (N-methylated glycine) as a bridging ligand to connect Ca^{2+} atoms in chains.[31] The compound is ferroelectric below ~130 K although the origins of this property are not completely understood.[32]

1.3 Hybrid Perovskites

Perovskites have the general formula ABX_3 where A is a large cation, normally an alkali metal, alkaline metal or a rare earth metal, B is a smaller cation, typically a transition metal and X is an anion which is often oxide. The structure consists of corner linked BX_6 octahedra with the A cations occupying the interstitial sites.[33] Perovskites are already known to possess a wide range of physical properties including ferroelectricity, magnetism and superconductivity, but many examples incorporate heavy metals in their structures which creates problems with regard to their toxicity, sustainability and cost.[33] The introduction of organic components could alleviate some of these issues and potentially introduce some new properties including lightness and tunability.

Hybrid perovskites incorporate organic components at either or both the A site and X site of the perovskite. Common organic A site cations include protonated amines whilst the X anions can include azides, iodides or the carboxylate formate.[34,35,36] Two examples are shown in Figure 1.8, in comparison to a conventional inorganic perovskite.

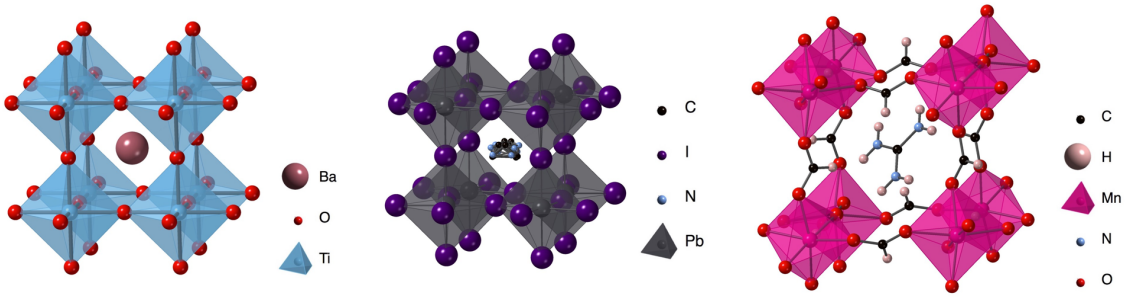

Figure 1.8: The as published crystal structures of (a) $BaTiO_3$,[37] (b) $CH_3NH_3PbI_3$[38]and (c) $(C(NH_2)_3Mn(COOH)_3$[39]

The relative size of each of the components plays a critical role in the types of structures formed. A simple relationship to define this is the tolerance factor which is defined by Equation 1.1, where R_A, R_B and R_X are the radii of the three ions.[40]

Equation 1.1

$$t = \frac{R_A + R_X}{\sqrt{2}(R_B + R_X)}$$

Cubic perovskites are typically formed for tolerance values between 0.9 - 1 and orthorhombic/rhombohedral perovskites are formed between 0.71 – 0.9. Values outside this range result in different types of structures.[33] The radii of organic ions can be difficult to quantify; recent work by Cheetham *et al.* has been able to estimate the effective radii of many commonly used organic A and X site ions.[41,42] To date, the only carboxylate ligand which has been utilised in a perovskite structure is the simplest monocarboxylate, formate, with several examples reported in the literature.[39,43]

Particularly interesting examples of carboxylate hybrid perovskites are the compounds $KLi_3Fe(C_2O_4)_3$ and $NH_4Li_3Fe(C_2O_4)_3$.[44,45] These compounds are isostructural and adopt a perovskite-like structure utilising the dicarboxylate oxalate as the X anion. Both

compounds are discussed in further detail in chapter 5. The structures of both have already been determined, but the properties of $KLi_3Fe(C_2O_4)_3$ are yet to be studied.

1.4 Electrical Properties

Many coordination polymers are already known to have electrical properties, such as copper formate tetrahydrate, dicalcium strontium propionate and potassium sodium tartrate which were introduced in the previous sections.[6,16,25] The relationship between these electrical properties is described by Figure 1.9. Ferroelectrics, as part of the family of dielectric materials, must also possess pyroelectric, piezoelectric and dielectric properties. Each class of materials has its own crystallographic requirements, properties and applications.[46] Aside from dielectrics, each of the electrical properties require non-centrosymmetric space groups, a subset of these, known as polar space groups give rise to both pyroelectric and ferroelectric properties.[47]

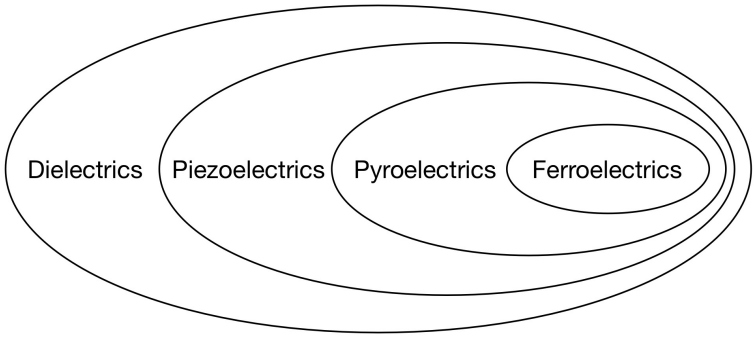

Figure 1.9: Venn diagram showing the relationship between various electric properties

1.4.1 Dielectric Materials

Dielectric materials can be defined as electrical insulators which can be polarised by an applied electric field. The induced polarisation has a linear relationship with the applied electric field. Typically, dielectrics are used as capacitor materials. [48]

1.4.2 Piezoelectric Materials

A sub group of dielectric materials exhibit piezoelectric properties where, under mechanical stress, an electric polarisation can be produced. In turn, an applied electrical field generates mechanical strain in the material. To exhibit these properties, the material must adopt a non-centrosymmetric space group.[46] The dependence of polarisation upon the applied mechanical stress is described by Equation 1.2 where *P* is the polarisation, σ is the applied stress and *d* the piezoelectric coefficient.[48]

Equation 1.2 $$P = d\sigma$$

Piezoelectric materials are commonly used as transducers and applications include audio pick-ups and loudspeakers. Materials used include PZT (lead zirconate titanate), which is a solid solution of $PbZrO_3$ and $PbTiO_3$, and Rochelle salt.[25,48,49]

1.4.3 Pyroelectric Materials

Pyroelectric materials exhibit a polarisation in response to changes in temperature. This relationship can be described by Equation 1.3, where π is the pyroelectric coefficient, P_s the saturation polarisation and *T* the temperature. The materials must adopt one of the ten polar point groups. Since pyroelectric materials will also have piezoelectric properties, the materials have potential applications for heat sensors and infrared detectors. One commonly used example is the compound triglycine sulfate (G_3S) which is used in infrared radiation detectors.[50,51]

Equation 1.3 $$\Delta P_s = \pi \Delta T$$

One significant limitation of pyroelectric materials lies in the dependence of the polarisation on temperature, and as a result the material cannot maintain their polarisation once the temperature is altered. Whilst the materials exhibit a spontaneous polarisation, its direction will not be switchable.[48]

1.4.4 Ferroelectricity

Ferroelectric properties are a special subgroup of dielectrics, as shown in Figure 1.9. Consequently, ferroelectric materials must also display piezoelectric and pyroelectric properties. In comparison to pyroelectric materials, ferroelectric materials must have a spontaneous polarisation which can be reversed by the application of an external electric field. In addition, the compounds can maintain their polarisation after the applied voltage is removed. The effect of electric field upon the induced polarisation of ferroelectric materials is shown in Figure 1.10. Instead of the linear relationship expected, a hysteresis loop is observed.

Under zero applied field, materials exhibit a remnant polarisation P_r. This can be increased to maximum known as the saturation polarisation P_s by an applied electric field. A key feature of ferroelectricity is the reversibility of the polarisation direction; the electric field required to switch the direction of the polarisation is known as the coercive field E_c.[46,52]

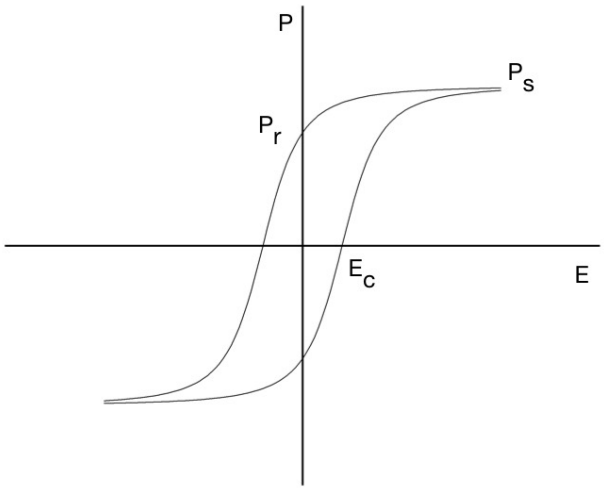

Figure 1.10: Schematic polarisation electric field hysteresis loop of a ferroelectric material

For ferroelectric properties to be present, the material must crystallise in one of the 10 polar point groups. Typically, the materials are only ferroelectric below a critical

temperature known as the Curie temperature or T_C. Above this point, the compound will adopt a high symmetry centrosymmetric space group, the high temperature structure is known as the paraelectric phase. Cooling through T_C results in a lower symmetry polar space group and ferroelectric properties. This drop in symmetry is known as 'symmetry breaking' and there are 88 possible paraelectric to ferroelectric phase transitions.[53,54]

There are two possible general mechanisms for ferroelectric phase transitions, referred to as order-disorder and displacive mechanisms; schematic representations of each are shown in Figure 1.11. The displacive mechanism relies on the relative displacements of ions. A classic example is $BaTiO_3$ where Ti cations exhibit off-centring in the ferroelectric phase, resulting in a net polarisation (Figure 1.11). The second type of mechanism involves the ordering of groups which are in random orientations at higher temperatures. A schematic of example of the ferroelectric $NaNO_2$ is shown in Figure 1.11. The NO_2 groups are disordered at elevated temperatures, but at low temperature are all orientated in the same direction. The characteristics of ferroelectric phase transitions can be further classified as 1st or 2nd order in relation to the spontaneous polarisation. First order transitions exhibit a discontinuous change in polarisation versus temperature, whereas 2nd order transitions are continuous.[46,55]

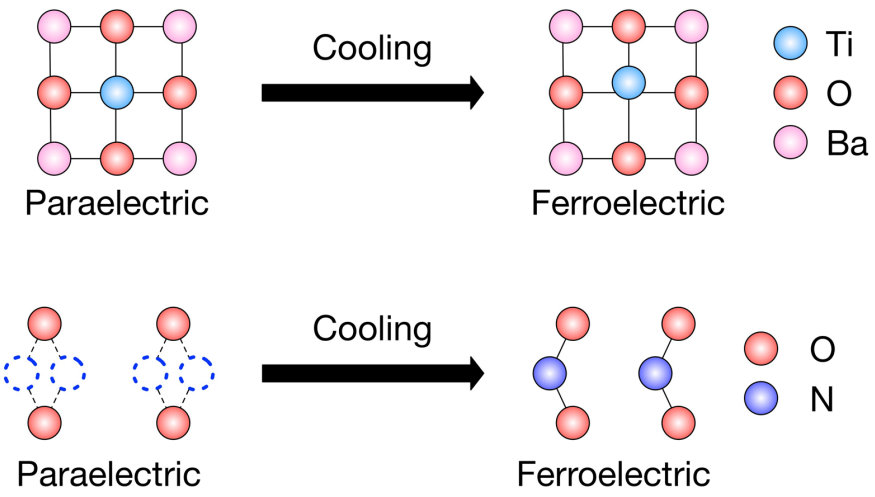

Figure 1.11: Mechanisms of ferroelectric phase transitions (top) displacive mechanism and (bottom) order-disorder mechanism

Ferroelectric materials have a wide range of applications including data storage, field effect transistors, IR detectors, piezoelectric sensors, non-linear optics and capacitors.[48,50,56] Whilst the first examples of ferroelectric materials were hybrid materials,[25,57] these were soon surpassed by inorganic oxides. Following the discovery of $BaTiO_3$, there have been relatively few examples of hybrid ferroelectric compounds.

1.5 Magnetic Properties

Magnetic ordering is already known to exist in several carboxylate coordination polymers, including copper (II) formate tetrahydrate and $Mn_3(COOH)_6.C_2H_5OH$, which were introduced in the earlier sections. Magnetic properties require unpaired electrons in the outer shell of atoms and, as a result, the properties are predominantly restricted to transition metals and lanthanoids. Consequently, metal-containing coordination polymers are prime candidates for magnetic properties. Magnetic materials have applications for information storage and transformer cores.[48]

The relative orientations of the spins of unpaired electrons give rise to several magnetic properties. A random orientation of neighbouring spins leads to simple paramagnetic behaviour. If the electrons can interact with each other, this can lead to unusual alignment of the relative spins. The three most common arrangements are shown schematically in Figure 1.12, the interaction of neighbouring spins can be described by the Hamiltonian of the Heisenberg equation as shown in Equation 1.4,[58] where J is the exchange constant and S is the total spin quantum number. For $J < 0$ anitferromagnetic exchange is favoured and for $J > 0$ ferromagnetic exchange**.** Ferromagnetic exchange results in every magnetic moment being orientated in the same direction whereas an antiparallel arrangement results in antiferromagnetic properties. The third type also has an antiparallel arrangement, but the magnitude of each is no longer equal leading to a net magnetisation in one direction.[48]

Equation 1.4 $$\mathcal{H} = -\sum_{ij} J_{ij}\, S_i \cdot S_j$$

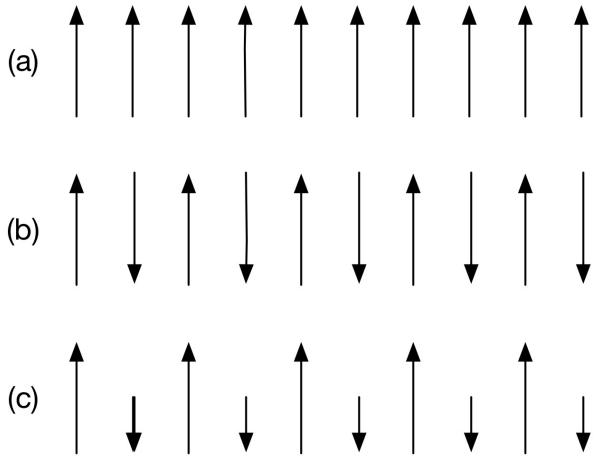

Figure 1.12: Schematic of neighbouring electron spins in (a) ferromagnetism, (b) antiferromagnetism and (c) ferrimagnetism

The behaviour of substances in a magnetic field can be described by Equation 1.5 where *B* is the magnetic flux density, *H* is the magnetic field, *M* is the magnetisation and μ_0 is the permeability of free space.

Equation 1.5 $$B = \mu_0(H + M)$$

The effect of an applied magnetic field on the magnetic properties of the materials is quantified by the magnetic susceptibility, χ, which is defined by Equation 1.6. Values of χ are typically normalised by dividing by number of moles, mass or volume. [59]

Equation 1.6 $$\chi = \frac{M}{H}$$

The magnitude of χ and its evolution with temperature are typically indicative of the types of magnetism. Paramagnetic materials typically have values in the range of 0.1-0.001, ferromagnetic materials in the range of 10^3 and antiferromagnetic materials 10^{-2}. The effect of temperature on the values of χ is depicted in Figure 1.13.

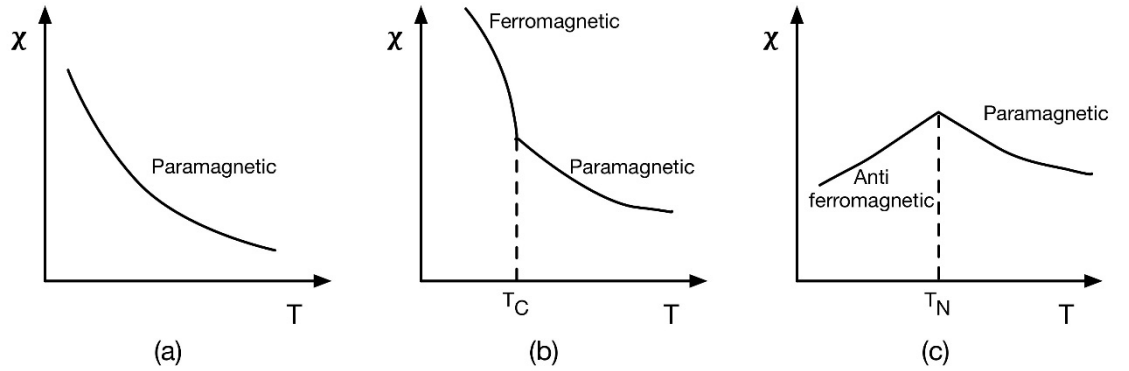

Figure 1.13: Evolution of χ with temperature for (a) paramagnetism, (b) ferromagnetism and (c) antiferromagnetism

Many materials undergo magnetic ordering at low temperatures. The critical temperatures at which ordering occurs are known as the Curie temperature, T_C, for paramagnetic to ferro/ferrimagnetism transitions and Néel point, T_N, for paramagnetic to antiferromagnetic transitions. [48]

The likelihood of magnetic ordering can be predicted by the temperature dependence of the magnetic susceptibility using the Curie-Weiss law (Equation 1.7) where χ is the magnetic susceptibility, C the Curie constant, θ the Weiss constant and T the temperature.[33]

Equation 1.7

$$\chi = \frac{C}{T - \theta}$$

The Weiss constant θ will have negative values for antiferromagnetism, positive for ferromagnetism and 0 for paramagnetic materials. These values can be determined from a plot of inverse magnetic susceptibility and temperature (Figure 1.14), where the *x* intercept is the Weiss constant and the gradient is equal to 1/*C*.

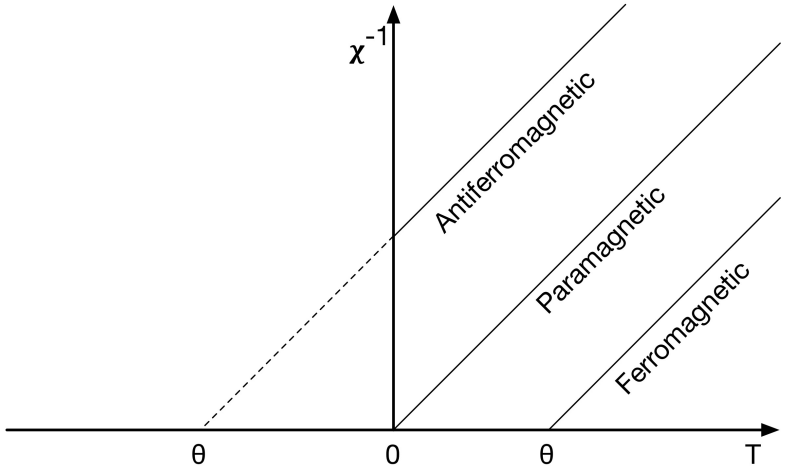

Figure 1.14: Inverse magnetic susceptibility versus temperature for paramagnetic, ferromagnetic and antiferromagnetic materials

The spin only magnetic moment can be determined using Equation 1.8 where *g* is the Landé *g* factor/gyromagnetic ratio ~2 and *S* is the spin quantum number. The values can be compared to $\mu_{eff,}$ the effective magnetic moment, which is calculated from experimental data using Equation 1.9, where *k* is the Boltzmann constant, *N* Avogadro's constant, μ_B the Bohr magneton, *C* the Curie constant, χ the magnetic susceptibility and *T* the temperature.

Equation 1.8

$$\mu_S = g\sqrt{S(S+1)}$$

Equation 1.9

$$\mu_{eff} = \sqrt{\frac{3k}{N\mu_B^2}}\sqrt{T\chi} \approx \sqrt{8C}$$

For magnetic ordering to occur, there must be overlap of the atomic orbitals of neighbouring metal atoms, either directly or by superexchange. One example in which superexchange gives rise to antiferromagnetic ordering is shown in Figure 1.15. The half-filled d_z^2 orbital of the Ni^{2+} atom overlaps with the filled p_z orbital of the oxygen atom. The two electrons occupying the p_z orbital have opposing spins which forces its two neighbouring Ni^{2+} atoms to have an antiparallel arrangement.

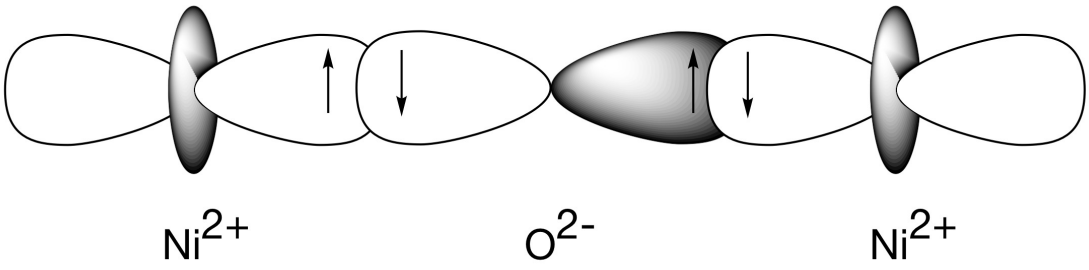

Figure 1.15: Antiferromagnetic superexchange of Ni^{2+} *d* electrons and O^{2-} *p* electrons

1.6 Aims and Objectives

The aims of this research were firstly to investigate the known ferroelectric phase transition of the metal-organic ferroelectric tris-sarcosine calcium chloride (TSCC) using detailed X-ray and neutron diffraction studies, and additionally, to identify any phase transitions at low temperatures. Several derivatives of TSCC were also synthesised to determine the role of each component on the ferroelectric properties and to investigate each as potential ferroelectric materials in their own right. The aims of the final section were to explore a family of oxalate-based coordination polymers with a perovskite-like structure, to probe the structural flexibility of the system and to investigate their magnetic properties.

1.7 Thesis Overview

The work presented in this thesis concerns the synthesis, characterisation and properties of a range of carboxylate coordination polymers with potential ferroelectric and magnetic properties.

The theory and basis for each of the experimental techniques used are summarised in chapter 2. The fundamentals of crystallography including unit cells, lattices, space groups and crystal systems are introduced. The origins of diffraction are presented and both single crystal and powder diffraction techniques are discussed. In addition, X-ray and neutron diffraction techniques are discussed and compared. Other techniques

utilised in this work including thermal analysis techniques, electron microscopy and magnetometry, are also discussed in detail.

Chapter 3 focuses on the ferroelectric compound *tris*-sarcosine calcium chloride, in particular, the mechanism of its ferroelectric phase transition which is studied using both X-ray and neutron diffraction. The most significant changes in structure surrounding the ferroelectric phase transition have been determined. The structure has also been investigated between 300 K and 20 K to identify other phase transitions.

The syntheses and structure of several tris sarcosine calcium chloride derivatives are reported in chapter 4. The effect of halogen substitution upon the structure and ferroelectric properties is investigated by the synthesis of iodide and bromide containing analogues. Additionally, the role of the alkaline earth metal is probed through the synthesis of magnesium, strontium and manganese derivatives. The synthesised compounds were analysed by single crystal X-ray diffraction, powder diffraction and electron microscopy. Differential scanning calorimetry data were used to investigate potential low temperature phase transitions.

In chapter 5, a series of perovskite-like oxalate compounds are reported. The structural flexibility of the series is investigated through the incorporation of different A site cations and its effect on the polyhedral distortion is studied in detail. The magnetic properties of three compounds, $KLi_3Fe(C_2O_4)_3$, $KLi_3Co(C_2O_4)_3$ and $KLi_3Ni(C_2O_4)_3$ are investigated using a SQUID (Superconducting Quantum Interference Device) instrument. Four additional oxalate coordination compounds and their syntheses are also reported.

The key results from the thesis are summarised in chapter 6 and potential future work is outlined.

1.8 References

1 Y. Z. Zheng, Z. Zheng and X. M. Chen, *Coord. Chem. Rev.*, 2014, **258**–**259**, 1–15.

2 C. N. R. Rao, S. Natarajan and R. Vaidhyanathan, *Angew. Chemie - Int. Ed.*, 2004, **43**, 1466–1496.

3 J. E. House, in *Inorganic Chemistry*, Academic Press, 2nd edn., 2013.

4 P. Atkins, T. Overton, J. Rourke, M. Weller and F. Armstrong, *Inorganic Chemistry*, Oxford University Press, Oxford, 5th edn., 2010.

5 V. M. Rao, D. N. Sathyanarayana and H. Manohar, *J. Chem. Soc. Dalt. Trans*, 1983, 2167–2173.

6 K. Okada, *Phys. Rev. Lett.*, 1965, **15**, 252–254.

7 Z. Wang, B. Zhang, H. Fujiwara, H. Kobayashi and M. Kurmoo, *Chem. Commun.*, 2004, **4**, 416–417.

8 S. Kitagawa, R. Kitaura and S. I. Noro, *Angew. Chemie - Int. Ed.*, 2004, **43**, 2334–2375.

9 M. Mączka, A. Ciupa, A. Gągor, A. Sieradzki, A. Pikul, B. Macalik and M. Drozd, *Inorg. Chem.*, 2014, **53**, 5260–5268.

10 M. Takashige, H. Iwamura, S. Hirotsu and S. Sawada, *J. Phys. Soc. Japan*, 1975, **38**, 1217.

11 R. Kiriyama, H. Ibamoto and K. Matsuo, *Acta Crystallogr.*, 1954, **7**, 482–483.

12 H. Kobayashi and T. Haseda, *J. Phys. Soc. Japan*, 1963, 18, 541–550.

13 B. Zhang, *CSD Commun.*, 2018.

14 Z. Wang, B. Zhang, M. Kurmoo, M. A. Green, H. Fujiwara, T. Otsuka and H. Kobayashi, *Inorg. Chem.*, 2005, **44**, 1230–1237.

15 H. B. Cui, Z. Wang, K. Takahashi, Y. Okano, H. Kobayashi and A. Kobayashi, *J. Am. Chem. Soc.*, 2006, **128**, 15074–15075.

16 B. T. Matthias and J. P. Remeika, *Phys. Rev.*, 1957, **107**, 1727.

17 H. Maruyama and Y. Tomiie, *J. Phys. Soc. Japan*, 1967, **23**, 899.

18 I. Mizutani, Y. Yamazaki, Y. Uesu, N. Yamada and J. Kobayashi, *J.Phys. Soc. Japan*, 1967, **23**, 900.

19 K. Gesi and K. Ozawa, *J. Phys. Soc. Japan*, 1975, **38**, 467–470.

20 K. Itoh, A. Niwata, W. Abe, H. Kasatani and E. Nakamura, *J. Phys. Soc. Japan*,

1992, **61**, 3593–3600.

21 E. J. Baran, *J. Coord. Chem.*, 2014, **67**, 3734–3768.

22 W. Yao, P. Lightfoot, T. Li, S. L. Lee, M. Xia and L. Clark, *Chem. Mater.*, 2017, **29**, 6616–6620.

23 J. S. Miller and M. Drillon, *Magnetism: Molecules to Materials IV*, Wiley-VCH, Weinheim, 2002, vol. 5.

24 W. Yao, M. Sougrati, K. Hoang, J. Hui, P. Lightfoot and A. R. Armstrong, *Chem. Mater.*, 2017, **29**, 2167–2172.

25 J. Valasek, *Phys. Rev.*, 1921, **17**, 475–481.

26 C. A. Beevers and W. Hughes, *Proc. R. Soc. London*, 1941, **177**, 251–259.

27 M. Fleck and A. M. Petrosyan, in *salts of Amino Acids: Crystallization, Structure and Properties*, Springer, 2014, pp. 83–137.

28 M. Fleck and A. M. Petrosyan, in *Salts of Amino Acids: Crystallization, Structure and Properties*, Springer, 2014, pp. 21–82.

29 M. Fleck and A. M. Petrosyan, in *Salts of Amino Acids: Crystallization, Structure and Properties*, Springer, 2014, pp. 139–206.

30 R. Pepinsky, K. Vedam and Y. Okaya, *Phys. Rev.*, 1958, **110**, 1309–1311.

31 T. Ashida, S. Bando and M. Kakudo, *Acta Crystallogr. Sect. B Struct. Crystallogr. Cryst. Chem.*, 1972, **28**, 1560–1565.

32 Y. Makita, *J. Phys. Soc. Japan*, 1965, **20**, 2074–2080.

33 R. D. J. Tilley, *Perovskites*, John Wiley & Sons Inc., Chichester, 1st edn., 2016.

34 X. H. Zhao, X. C. Huang, S. L. Zhang, D. Shao, H. Y. Wei and X. Y. Wang, *J. Am. Chem. Soc.*, 2013, **135**, 16006–16009.

35 D. B. Mitzi, C. A. Feild, W. T. A. Harrison and A. M. Guloy, *Nature*, 1994, **369**, 467–469.

36 P. Jain, V. Ramachandran, R. J. Clark, D. Z. Hai, B. H. Toby, N. S. Dalal, H. W. Kroto and A. K. Cheetham, *J. Am. Chem. Soc.*, 2009, **131**, 13625–13627.

37 R. H. Buttner and E. N. Maslen, *Acta Crystallogr. Sect. B*, 1992, **48**, 764–769.

38 Y. Yamada, T. Yamada, L. Q. Phuong, N. Maruyama, H. Nishimura, A. Wakamiya, Y. Murata and Y. Kanemitsu, *J. Am. Chem. Soc.*, 2015, **137**, 10456–10459.

39 K. L. Hu, M. Kurmoo, Z. Wang and S. Gao, *Chem. - A Eur. J.*, 2009, **15**, 12050–12064.

40 V. M. Goldschmidt, *Naturwissenschaften*, 1926, **14**, 477–485.

41 G. Kieslich, S. Sun and A. K. Cheetham, *Chem. Sci.*, 2014, **5**, 4712–4715.

42 G. Kieslich, S. Sun and A. K. Cheetham, *Chem. Sci.*, 2015, **6**, 3430–3433.

43 P. Jain, N. S. Dalal, B. H. Toby, H. W. Kroto and A. K. Cheetham, *J. Am. Chem. Soc.*, 2008, **130**, 10450–10451.

44 W. Yao, Y. Guo and P. Lightfoot, *Dalt. Trans.*, 2017, **46**, 13349–13351.

45 J. H. Li, H. Liu, L. Wei and G. M. Wang, *Solid State Sci.*, 2015, **48**, 225–229.

46 W. Zhang and R. Xiong, *Chem. Rev.*, 2012, **112**, 1163–1195.

47 P. S. Halasyamani and K. R. Poeppelmeier, *Chem. Mater.*, 1998, **10**, 2753–2769.

48 A. R. West, *Solid State Chemistry and its Applications*, John Wiley & Sons Ltd., Chichester, 2nd edn., 2014.

49 R. Guo, L. E. Cross, S.-E. Park, B. Noheda, D. E. Cox and G. Shirane, *Phys. Rev. Lett.*, 2000, **84**, 5423–5426.

50 M. E. Lines and A. M. Glass, in *Principles and Applications of Ferroelectrics and Related Materials*, Oxford Scholarship Online, Oxford, 2001, pp. 1–43.

51 M. I. Kay and R. Kleinberg, *Ferroelectrics*, 1973, **5**, 45–52.

52 M. E. Lines and A. M. Glass, in *Principles and Applications of Ferroelectrics and Related Materials*, Oxford Scholarship Online, Oxford, 2001, pp. 1–20.

53 P.-P. Shi, Y.-Y. Tang, P.-F. Li, W.-Q. Liao, Z.-X. Wang, Q. Ye and R.-G. Xiong, *Chem. Soc. Rev.*, 2016, **45**, 3811–3827.

54 K. Aizu, *Phys. Rev. B*, 1970, **2**, 754–772.

55 T. Hang, W. Zhang, H.-Y. Ye and R.-G. Xiong, *Chem. Soc. Rev.*, 2011, **40**, 3577–3598.

56 J. F. Scott, *Science (80-.).*, 2007, **315**, 954–959.

57 G. Busch and P. Scherrer, *Ferroelectrics*, 1987, **71**, 15–16.

58 S. Blundell, *Magnetism in Condensed Matter*, Oxford University Press, Oxford, 2001.

59 O. Kahn, *Molecular magnetism*, VCH, New York, 1993, vol. 103.

Chapter 2 Experimental Techniques

2.1 Introduction

The synthetic methods used in this work include simple slow evaporation and hydrothermal/solvothermal methods. Subsequently, a variety of techniques were used to characterise and analyse these products. The primary characterisation technique was diffraction, but the project also utilised thermal analysis, electron microscopy and magnetometry. The underlying theory behind each is described in detail in this chapter.

2.2 Synthesis Methods

2.2.1 Slow Evaporation

In the slow evaporation method, crystallisation occurs when a critical point is reached on the concentration versus temperature solubility curve as shown in Figure 2.1. However, the growth of high-quality single crystals can be much more problematic. In the under-saturated region, the concentration is not sufficient for either crystallisation or nucleation to occur. In the metastable region, whilst nucleation cannot occur, crystal growth is possible if there are potential nucleation sites, for example seed crystals or impurities. In the supersaturated zone, nucleation does occur readily but unfortunately this often leads to the production of many small and very poor-quality crystals. There are two ways to induce crystallisation, either by lowering the temperature or by increasing the concentration, and one simple way to increase the concentration is to remove solvent in a controlled manner.[1,2]

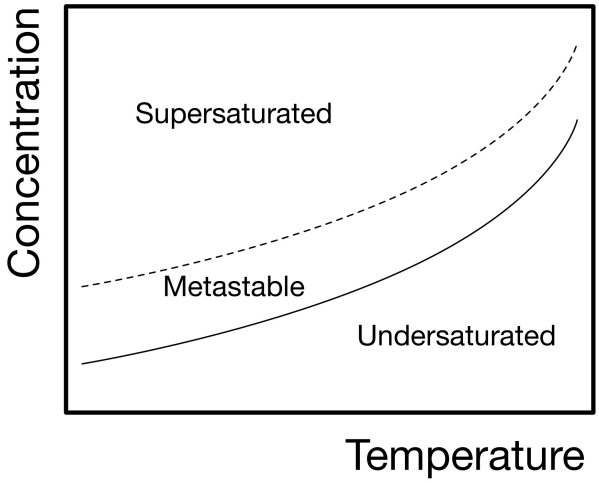

Figure 2.1: Typical solubility curve of concentration vs temperature

Perhaps the most basic method for this process is slow evaporation but while this has the benefit of simplicity, the results are often disappointing, with many poor/low quality crystals or fractured crystals if the solvent is removed completely. Ideally, the solvent should be allowed to evaporate until the metastable zone is reached, at which point the system should be sealed and the crystals should then be extracted once they have reached a sufficient size. Alternatively, seed crystals can be introduced during the metastable phase to produce large, high-quality, single crystals. Alternative concentration-based methods include vapour diffusion and gel crystallisation which offer greater controllability and flexibility, but are less straightforward in terms of set up.[1]

2.2.2 Solvothermal/Hydrothermal Synthesis

A temperature-based technique to induce crystallisation is solvothermal or hydrothermal synthesis, depending on the solvent used. Solvent and solid reagents are placed inside a Teflon lined autoclave and sealed as shown schematically in Figure 2.2. The autoclave is then heated to temperatures above the solvent's boiling point, typically in the region of 100 – 250 °C, before gradual cooling back to room temperature. The products, hopefully in the form of single crystals, are then analysed. The solvent acts as a pressure-transmitting medium and as a solvent for the other reactants. The induced

autogenous pressure can be controlled by both the volume of solvent and the temperature. The reaction conditions allow the synthesis of different phases which would not normally be accessible. In addition, heating times and acidity can have a significant effect on the products formed.[1,3] The technique is already extensively used in the synthesis of coordination polymers, Metal Organic Frameworks (MOFs) and zeolites. Due to the high pressures produced during reactions, the method can use significantly lower temperatures than conventional solid-state synthesis. [4,5]

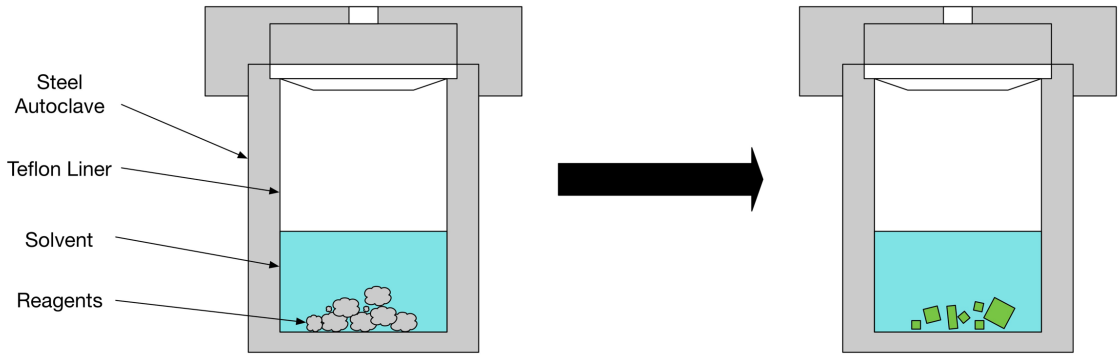

Figure 2.2: Schematic of autoclaves and solvothermal synthesis

2.3 Crystallography

Crystallography can be used to describe and classify the arrangement of atoms in any crystalline material, and hence, can be used to characterise the synthesised products. The technique can also provide insight in the properties of many materials.

The smallest repeating unit which contains the overall symmetry of the crystal is known as the primitive unit cell and this can be used to recreate the whole crystal. There are seven possible geometries of unit cell (crystal systems) as summarised in Table 2.1 and Figure 2.3 where *a*, *b* and *c* are the unit cell lengths and α, β, γ are the unit cell angles. The relationship between an array of identical points is known as the lattice. There are five lattice types, (P) primitive, (I) body centred, (F) face centred, side centred (A)/(B)/(C) and (R) rhombohedral which are shown in Figure 2.4. The combination of the lattice type with the essential symmetry of each crystal system results in 14 possible combinations, known as the Bravais lattices.[6]

Table 2.1: The unit cell shapes, symmetry and possible lattice types of the seven crystal systems

Crystal System	Unit Cell Shape	Essential Symmetry	Lattice Types
Cubic	$a = b = c$, $\alpha = \beta = \gamma = 90°$	Four threefold axes	*P*, *I*, *F*
Tetragonal	$a = b \neq c$, $\alpha = \beta = \gamma = 90°$	One fourfold axis	*P*, *I*
Hexagonal	$a = b \neq c$, $\alpha = \beta = 90°$, $\gamma = 120°$	One sixfold axis	*P*
Trigonal	$a = b \neq c$, $\alpha = \beta = 90°$, $\gamma = 120°$	One threefold axis	*P* (*R*)
Orthorhombic	$a \neq b \neq c$, $\alpha = \beta = \gamma = 90°$	Three twofold axes or mirror planes	*P*, *C*, *I*, *F*
Monoclinic	$a \neq b \neq c$, $\alpha = \gamma = 90°$ $\beta \neq 90°$	One twofold axis or mirror plane	*P*, *C*
Triclinic	$a \neq b \neq c$, $\alpha \neq \beta \neq \gamma \neq 90°$	None	*P*

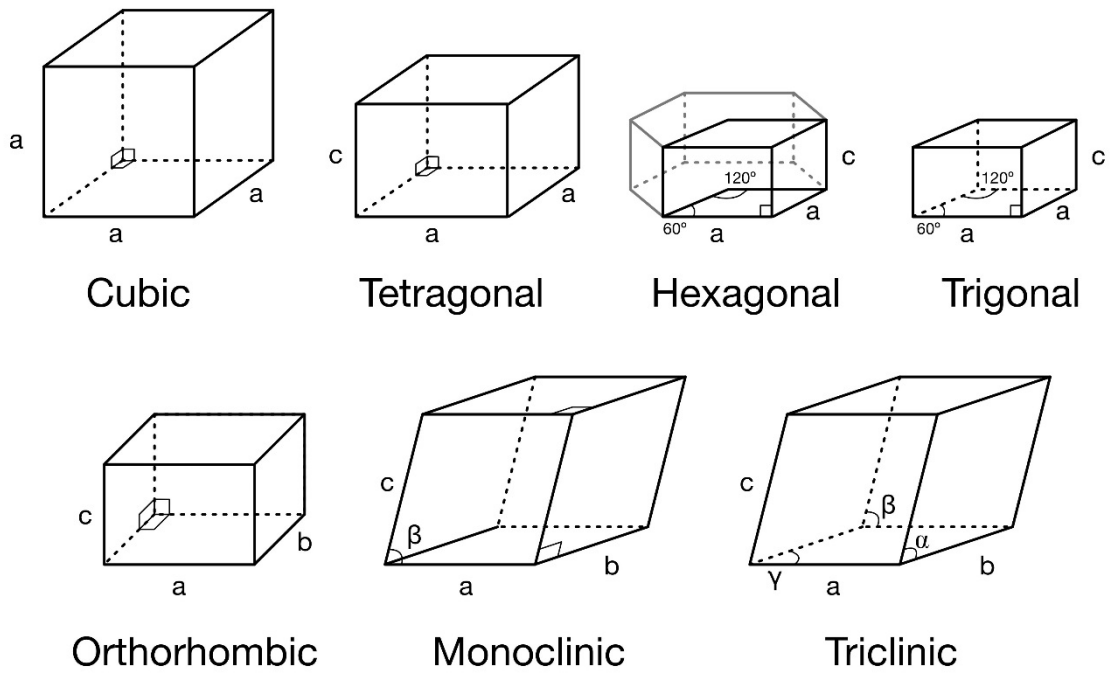

Figure 2.3: The unit cell geometries of the seven crystal systems

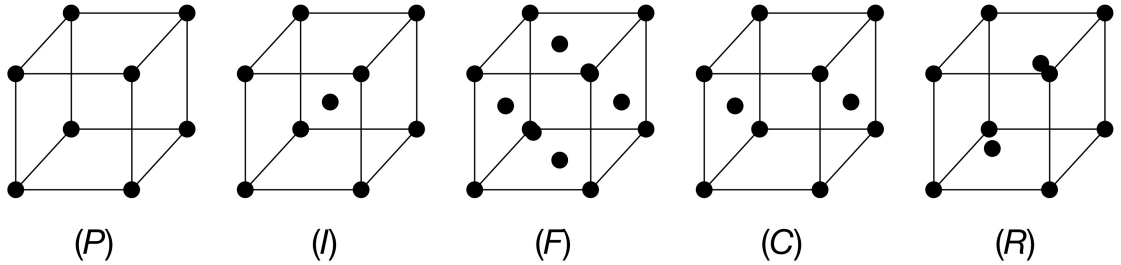

Figure 2.4: The five possible lattice types (*P*) primitive, (*I*) body centred, (*F*) face centred, *C* (side centred) and (*R*) rhombohedral

Whilst the crystal system and lattice provide information on the translational symmetry of the crystal, they do not include any details regarding the contents of the unit cell or their symmetry. The symmetry of a single molecule can be described by three possible types of symmetry element: inversion centres, rotation axes and mirror planes, which must all pass through a common point. The combination of these symmetry elements results in one of 32 distinct crystallographic point groups. The addition of translational symmetry, including glide planes, screw axes and lattice types, gives rise to 230 unique space groups which can describe the symmetry of any crystalline material. These 230 space groups can be categorised as centrosymmetric and non-centrosymmetric groups, which can dictate the material's properties. For example, ferroelectric properties require a polar space group which are a subset of the non-centrosymmetric space groups.[7] The details of each of the space groups are given in full in the International Tables for Crystallography.[8]

2.4 Diffraction

A useful tool for determining a material's crystal structure is diffraction. Diffraction is one of the most commonly used techniques for structural analysis in solid state chemistry and one of the most versatile. A combination of X-ray, neutron and electron diffraction can be used complimentarily to provide information on a crystal's bonding, chemistry and symmetry. The basis for the technique is described by Bragg's Law (Equation 2.1), where n is an integer, λ is the wavelength, d the spacing between the planes and θ the incident angle of the radiation. The incoming rays are diffracted by the

planes of atoms within the crystal structure and interfere either constructively or destructively to produce distinctive diffraction patterns. For constructive interference and maxima to occur, the path difference of the diffracted rays must be an integer value of the wavelength.

Equation 2.1 $$n\lambda = 2dsin\theta$$

The incoming rays are diffracted by adjacent planes as shown in Figure 2.5 where the path difference ($n\lambda$) between the two rays is the distance ABC. Using trigonometry, the distance AB can be written as

Equation 2.2 $$AB = dsin\theta$$

Equation 2.3 $$n\lambda = 2AB$$

Since the path difference equals 2 × AB, equation 2.2 can be substituted into equation 2.3 to give Bragg's law (Equation 2.1).

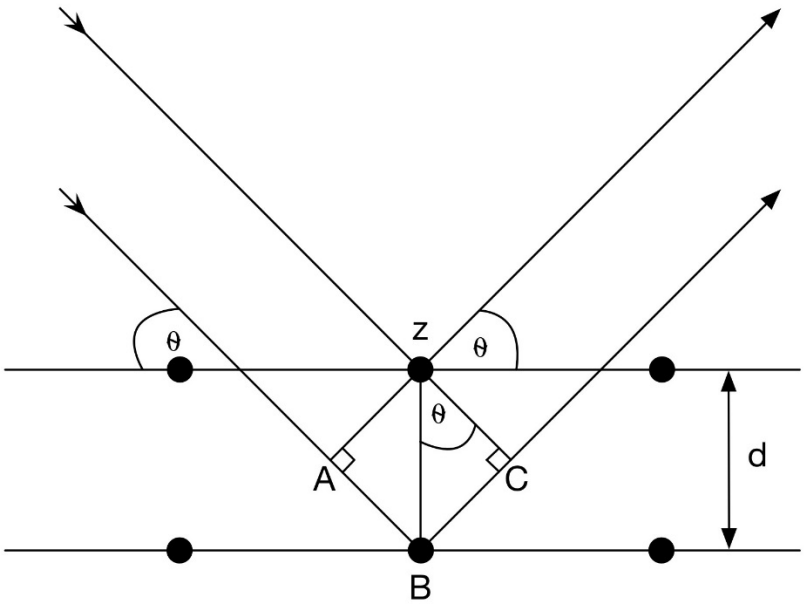

Figure 2.5: Schematic representation of diffraction by a plane of atoms and derivation of Bragg's law

2.5 Generation of X-rays

X-rays have long been used for structural analyses since their wavelengths are of similar dimensions to interatomic distances. X-rays are produced when a beam of electrons strikes a metal target, causing an electron from the 1*s* shell to be ionised. This vacancy in the inner electron shell is immediately filled by an electron from either the 2*p* or 3*p* orbital and releases energy in the form of X-ray radiation as depicted in Figure 2.6. The X-ray emission spectrum of copper is shown in Figure 2.6. The wavelengths of the Kα radiation which are characteristic of the metal target, are predicted by Moseley's Law and are inversely proportional to atomic number (Equation 2.4). Where *Z* is the atomic number, λ the wavelength, *C* and σ are constants.[4]

Equation 2.4 $$\lambda^{-\frac{1}{2}} = C(Z - \sigma)$$

Since the X-ray radiation can be produced by an electron from the 2*p* or 3*p* orbital, there are two possible wavelengths, K_α and K_β emitted. The K_α emission is further split into $K_{\alpha 1}$ and $K_{\alpha 2}$ depending on the relative spin of the 2*p* electron. The white radiation, or *Bremsstrahlung*, has a continuity of wavelengths and is the result of electrons decelerating as they interact with the metal target. For many experiments, monochromatic wavelengths are desirable, and consequently a metal filter is used to leave only the more intense K_α radiation.[4]

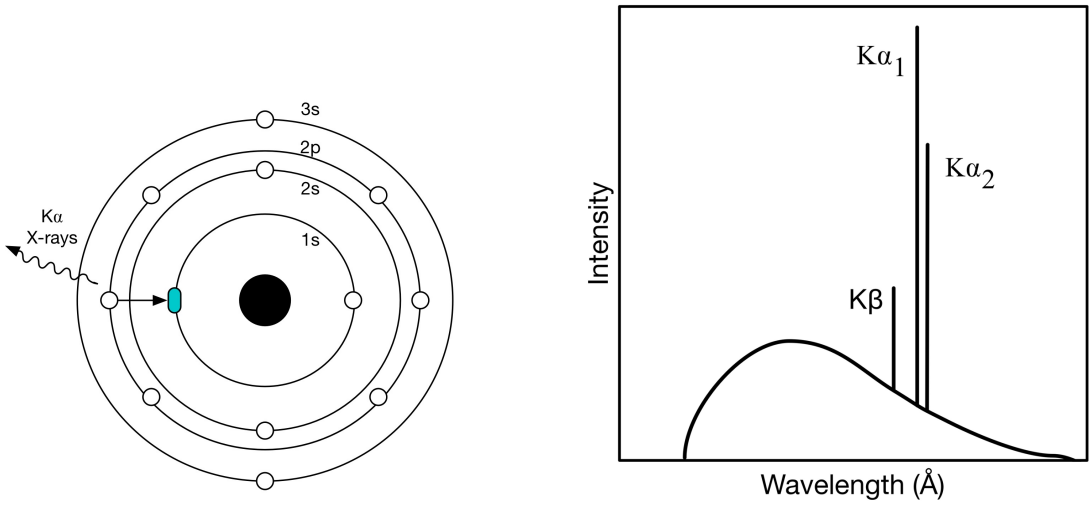

Figure 2.6: (left) Schematic representation of the generation of copper Kα radiation. (right) Typical X-ray emission spectrum[4]

2.6 X-ray Diffraction

X-ray diffraction is the most commonly used diffraction technique since it is inexpensive compared to both neutron and electron diffraction and readily available. Since X-rays are scattered by the electrons within atoms, the intensity of the diffracted X-rays is directly linked to the atomic numbers of each element. The scattering factors and their dependence on θ are shown in Figure 2.7.[9] This allows easy differentiation between different elements in most cases. Both powder and single crystals can be analysed by this technique. However, a significant limitation of the technique is its relative insensitivity to atoms of very low atomic number and difficulty in differentiating atoms of similar atomic number.

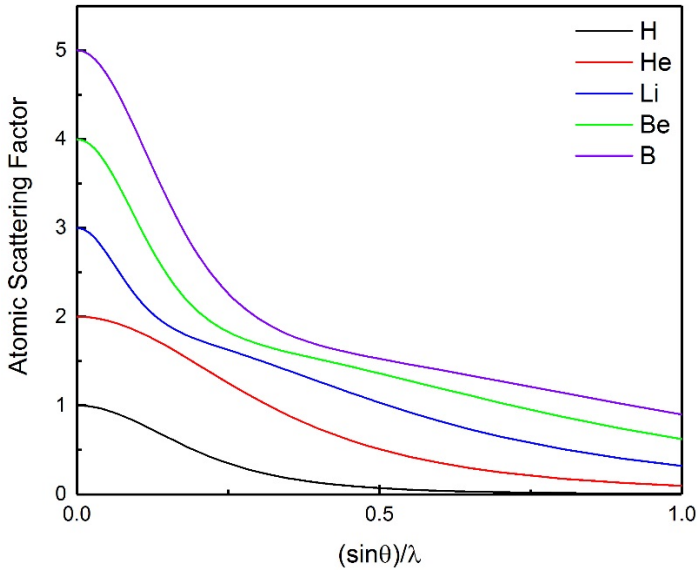

Figure 2.7: Atomic scattering factors of the first five elements and their dependence on (sin θ)/λ[8]

2.6.1 Single Crystal X-ray diffraction

Single crystals are selected using an optical microscope and mounted within the X-ray beam. The crystal is then rotated in small increments and the diffracted X-rays are detected at each crystal position.[10] There are typically two X-ray sources used for in-house diffractometers, namely sealed tube and rotating anode, which differ in X-ray flux and cost. As a result, the choice of X-ray source significantly effects the quality of diffraction data in terms of X-ray flux and the signal to noise ratio. During the production of X-rays, less than 1 % of the energy is converted to X-rays, while the rest is emitted as heat. As a result, water cooling systems are typically used to prevent the target metals from melting, and the X-ray flux is dictated by the efficiency of these systems. In the standard sealed tube source, electrons are generated from a tungsten filament and accelerated through a potential difference before striking the anode (metal target). The heat produced at the metal target limits the X-ray flux produced. In contrast, rotating anode sources are able to produce higher X-ray flux since the anode is continually rotating so that the area exposed to incoming electrons is always changing. This helps significantly with the cooling of the metal target.[11,12] Structural analysis is often carried out at low temperatures since atomic vibrations are reduced and higher Bragg angles

can be measured. Typically, gaseous nitrogen is used to achieve temperatures as low as 90 K, but helium gas can also be used if temperatures below this point are required.[11]

The primary diffractometer used during the project was a Rigaku SCXMini using a sealed tube X-ray source and Mo Kα radiation. Data were collected at room temperature and at 173 K using gaseous nitrogen. Structural analysis between 93 and 150 K also used liquid nitrogen and was carried out on a Rigaku FRX diffractometer with a rotating anode source and Mo Kα radiation. Liquid helium was used to access temperatures between 100 and 20 K using the XIPHOS 4 circle diffractometer at Newcastle University. This system was equipped with a rotating anode Mo Kα source and a three-stage closed-cycle Helium cryorefrigerator.[13]

The diffraction pattern of the compound is related to the crystal structure by a Fourier transform as shown in Equation 2.5 where *F* is the structure factor, *f* the atomic scattering factor of each atom, *x/y/z* the atomic coordinates and *h/k/l* the Miller indices for each reflection.[14]

Equation 2.5 $$F(hkl) = \sum_{j=1}^{N} f_j \exp\left[2\pi i\left(hx_j + ky_j + lz_j\right)\right]$$

The diffraction pattern can be converted to the electron density map of the crystal structure by a reverse Fourier transform (Equation 2.6) which can be used to determine the crystal structure. In this equation ρ is the electron density, *V* the unit cell volume and *F* the structure factor.[10,14]

Equation 2.6 $$\rho(xyz) = \frac{1}{V}\sum_{hkl}|F(hkl)| \cdot \exp\left[i\phi(hkl)\right] \cdot \exp\left[-2\pi i(hx + ky + lz)\right]$$

The magnitude of the structure factors, *F*, can be determined directly from the intensity of the diffraction peaks as shown by the relationship in Equation 2.7. To evaluate the structure factors, several corrections must be applied to the observed intensities in a process known as data reduction. These include the Lorentz polarisation and absorption corrections. The Lorentz and polarisation factors take into account the length of time

it takes for different lattice points to pass through the Ewald sphere and the polarisation of the X-rays. Whilst the magnitude can be easily calculated, the phase of each reflection, ϕ in Equation 2.6, is unknown.

Equation 2.7 $$F^{obs} \propto \sqrt{I^{obs}}$$

There are several possible solutions to the phase problem, including the Patterson synthesis, direct methods and dual space methods.[10] The Patterson Synthesis solves the phase problem by considering F^2 instead of F, as shown in Equation 2.8.[15] This produces a Patterson map which is similar to an electron density map but instead of atom positions, vectors between pairs of atoms are shown. This method is typically used for structures containing very heavy atoms. [10,15]

Equation 2.8 $$P(xyz) = \frac{1}{V}\sum_{h,k,l}|F_O(hkl)|^2 \cdot \exp\left[-2\pi i(hx + ky + lz)\right]$$

Direct methods are probably the most extensively used technique to resolve the phase problem and is the combination of several mathematical and probability relationships between the amplitudes and their phases. The method uses two basic assumptions to solve the phase problem; firstly that the electron density is always positive and secondly that the crystal structure is composed of distinct atoms. The third technique, dual space methods, alternates between direct and reciprocal space in an iterative process. [16]

After the basic structure has been completed the model is refined using least squares analysis. The hypothesised structure can be used to calculate structure factors using a Fourier transform (Equation 2.5) and these values can be compared to the observed structure factors to provide a measure of the quality of the model.[10] A common way to quantify this is the *R* factor or residual factor (*R*1) as shown in Equation 2.9. In this equation, F_O are the observed structure factors and F_C the calculated structure factors. The differences between F_O and F_C are summed and normalised by dividing by the sum of all the observed structure factors. Consequently, the *R* factor can be used to compare

different models for any completed crystal structure with typical values between 0.02 – 0.07.

Equation 2.9

$$R1 = \frac{\sum||F_0| - |F_c||}{\sum|F_0|}$$

The second commonly used parameter is the weighted *R* factor, *wR*2, which is defined by Equation 2.10. A key difference between the two *R* factors is that each reflection is multiplied by a weighting factor based upon their standard uncertainties (s.u.s.). Values of *wR*2 are typically substantially higher than *R*1.

Equation 2.10

$$wR2 = \sqrt{\frac{\sum w(F_0^2 - F_c^2)}{\sum w(wF_0^2)^2}}$$

2.6.2 Powder X-ray diffraction

X-ray diffraction can also be carried out on powdered samples, which can be considered as many small crystals with random orientations. Instead of producing discrete diffraction spots as seen in single crystal X-ray diffraction, the X-rays are diffracted in cones from the sample as seen in Figure 2.8. A typical powder X-ray diffraction pattern is shown in Figure 2.9 and may be visualised as a slice of the diffracted cones.[10] In this work, powder diffraction data were collected on PANalytical Empyrean diffractometers using monochromated Cu Kα_1 radiation, the reflection intensities were recorded in 0.017° 2θ intervals, and all data collection took place at room temperature.

Generally, single crystal diffraction allows much easier structural determination, however, the synthesis of high-quality single crystals can be challenging. Powder diffraction has the advantages of much shorter data collection times and can provide additional information regarding a sample's purity.[12]

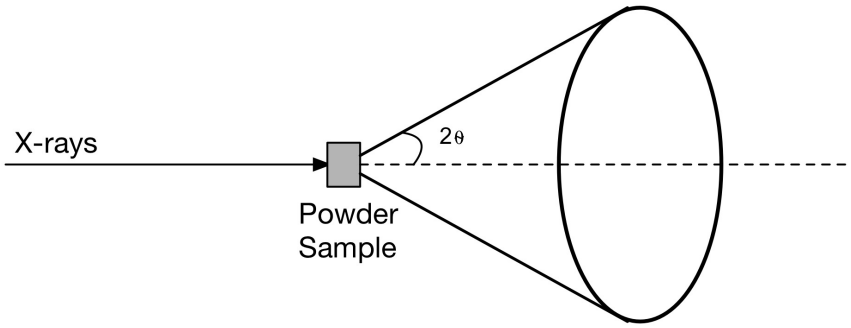

Figure 2.8: Schematic of a cone of diffracted X-rays produced by powder diffraction[17]

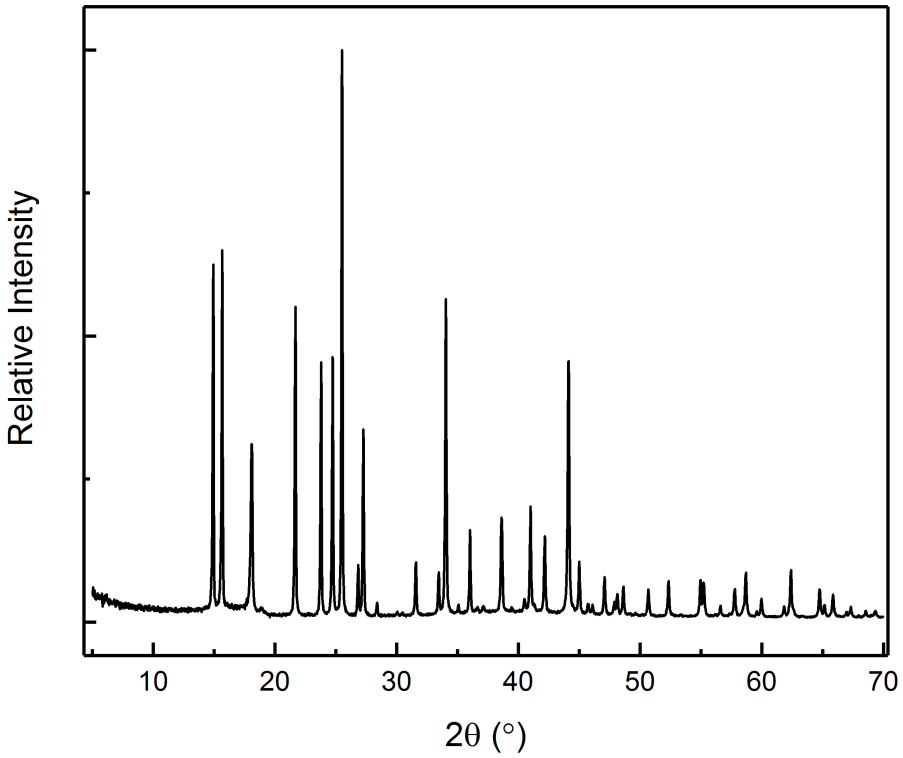

Figure 2.9: Typical powder X-ray diffraction pattern ($KLi_3Ni(C_2O_4)_3$)

Generally, powder diffraction analysis requires a calculated pattern based on an existing structural model, which is then compared to the experimental data. This is the basis for the Rietveld method[18] which uses a least squares minimisation (Equation 2.11) where *S* is a minimum or best fit, w_i a weighting factor, y_{oi} the observed intensity and y_{ci} the calculated intensity.[12,18]

Equation 2.11

$$S = \sum_i w_i \, (y_{oi} - y_{ci})^2$$

The refinement of the structural model is typically done using the General Structural Analysis System (GSAS) program[19] where parameters including background, zero-point, lattice parameters, profile and atomic positions can be refined. The strength of any structural model can be quantified using an *R* factor as seen previously for single crystal diffraction, but this is now based upon the intensities at any given 2θ point rather than structure factors as shown in Equation 2.12 where y_{oi} is the observed intensity and y_{ci} the calculated intensity. An equivalent weighted R factor can also be calculated using Equation 2.13 which prevents the most intense peaks from dominating. Another commonly used parameter is the goodness of fit or χ^2 which is defined by Equation 2.14 where *N* is the number of observations, *P* the number of refined parameters and *C* the number of constraints. For a perfect fit between the experimental and calculated data, the value of χ^2 would be one.[12]

Equation 2.12 $$R_p = \frac{\sum(y_{oi} - y_{ci})}{\sum y_{oi}}$$

Equation 2.13 $$R_{wp} = \sqrt{\left[\frac{\sum_i w_i(y_{oi} - y_{ci})^2}{\sum_i w_i(y_{oi})^2}\right]}$$

Equation 2.14 $$\chi^2 = \frac{\sum_i w_i(y_{oi} - y_{ci})^2}{N - P + C}$$

2.7 Neutron Diffraction

X-rays are useful for structural analysis since their wavelengths are approximately equal to interatomic distances. According to the de Broglie relationship (Equation 2.15) where λ is the wavelength, *h* is Planck's constant, *m* is mass and *v* is velocity; any moving particle will have an associated wavelength. As a result, neutrons can have wavelengths in the same region and therefore be useful for structural analysis.[10]

Equation 2.15 $$\lambda = \frac{h}{mv}$$

As mentioned in section 2.6, a major limitation of X-ray diffraction is the dependence of scattering factors on atomic number. Unlike X-ray diffraction, neutron scattering factors are not closely linked with atomic number. In fact there is no clear relationship between the two, as shown by the neutron coherent scattering lengths of the first 80 elements in Figure 2.10.[20] Additionally, the scattering factors of neutrons do not decrease at higher scattering angles as seen in X-ray diffraction, but remain constant.

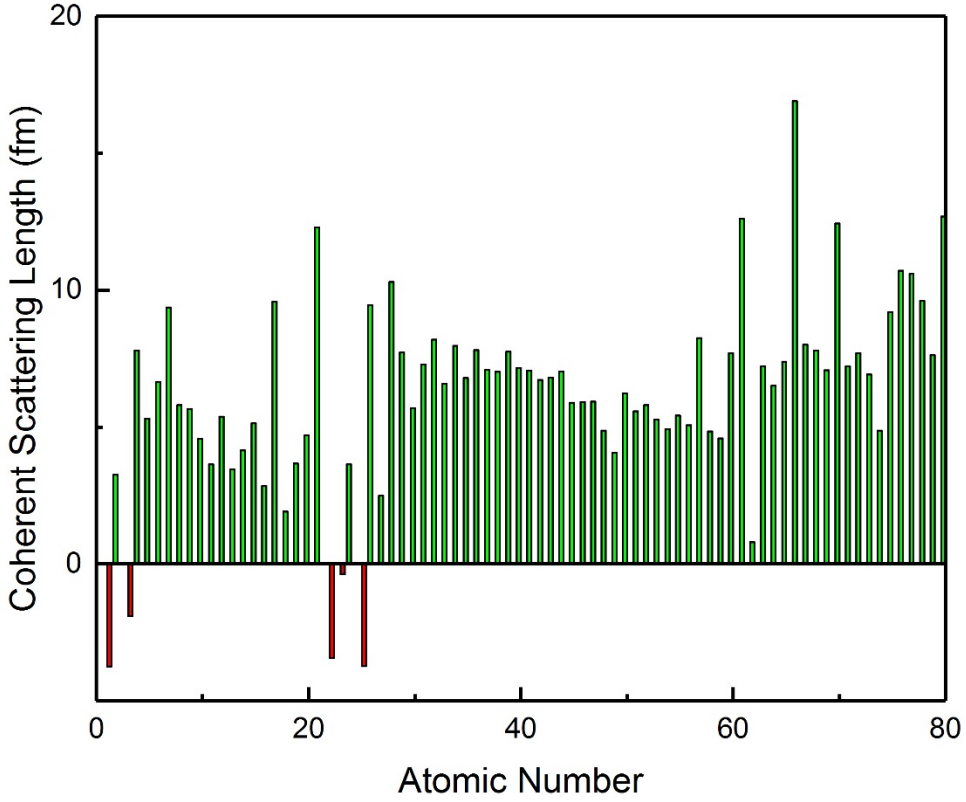

Figure 2.10: Neutron coherent scattering lengths of selected elements[20]

Whilst X-ray diffraction remains the most effective technique for structure determination, neutron diffraction can be used complimentarily to provide additional information concerning elements with low or very similar atomic weights. A major limitation of neutron diffraction lies in its cost and availability. Additionally, neutron sources are significantly less intense and therefore much larger samples and longer data collection times are required.[4] Because of these restrictive factors, the technique is only used where X-ray diffraction fails to provide sufficient structural information.

Neutrons can be generated using two typical methods, a reactor or a spallation source. The reactor source produces a continuous spectrum of wavelengths and as a consequence a crystal monochromator is necessary to remove the unwanted wavelengths. This results in a significantly lower intensity beam of neutrons. The spallation method used at the ISIS neutron and muon source, is able to produce significantly higher intensities of neutron flux.[4] The technique employs a polychromatic neutron beam which can be used in time-of-flight analysis.[21] In contrast to traditional diffraction techniques, θ is kept constant and the wavelength is a variable. This allows virtually all wavelengths to be used in diffraction experiments. The time of flight can be used to directly calculate *d* spacing using Bragg's law and the de Broglie relationship (Equation 2.16) where *m* is the mass of the neutron, *v* the velocity, *L* the distance travelled and *t* is the time of flight.[12]

Equation 2.16 $$d = \frac{\lambda}{2\,sin\,\theta} = \frac{h}{mv}\frac{1}{2\,sin\,\theta} = \frac{ht}{mL}\frac{1}{2\,sin\,\theta}$$

The spallation generation process begins with hydride ions which pass through a linear accelerator before alumina foil strips their electrons to produce a stream of protons. The protons are then accelerated in a synchrotron before colliding with a tungsten target. This collision produces neutrons which travel towards the various instruments for neutron diffraction.[22,23]

2.7.1 Single Crystal Diffractometer (SXD)

Single crystal neutron diffraction at ISIS is undertaken on the SXD instrument shown in Figure 2.11. The instrument consists of a hemisphere of 11 detectors which surround the sample allowing large areas of reciprocal space to be viewed. Both a cryostat and furnace can be used allowing temperatures between 300 mK and 300 K to be reached during diffraction experiments. The technique is particularly useful for investigating diffuse scattering, phase transitions, incommensurate structures and for determining hydrogen positions.[24]

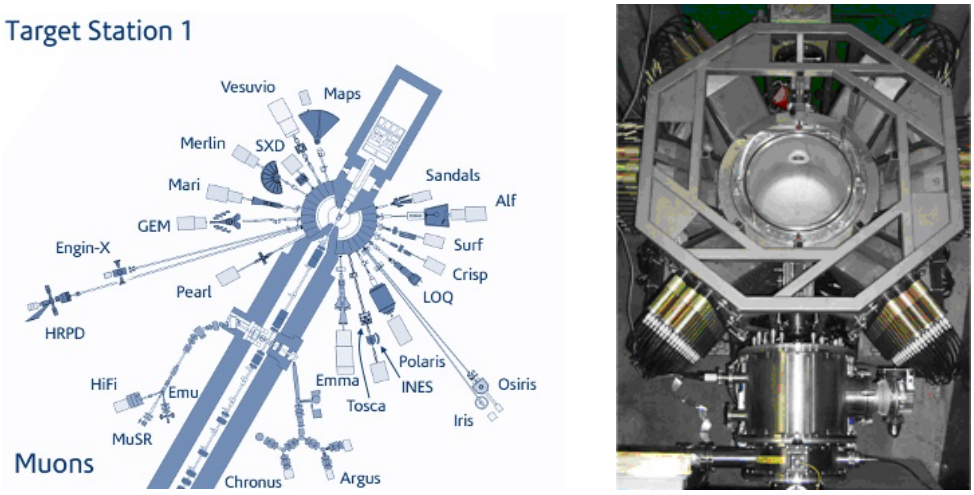

Figure 2.11: (left) Schematic image of target station one at ISIS including the SXD instrument at ISIS[25] (right) Image of the SXD diffractometer[24] reproduced from references 24 and 25

2.8 Bond Valence Method

The valence of any atom is ideally equal to the sum of the bond valences of the surrounding atoms, as defined in Equation 2.17. The bond valences of each can be calculated using Equation 2.18 and the experimentally determined bond lengths from diffraction data. In Equation 2.18, R_O is a tabulated parameter relating to the ideal bond length,[26] R_i is the observed bond lengths and b is an empirical constant, typically 0.37 Å.[27]

Equation 2.17 $$V = \sum(v_i)$$

Equation 2.18 $$V_i = exp\left(\frac{R_o - R_i}{b}\right)$$

The primary applications of the method are for predicting bond lengths, determining oxidation states, locating hydrogen atoms and for confirming the reliability of determined crystal structures. [4, 26]

2.9 Thermal Analysis

2.9.1 Thermal Gravimetric Analysis (TGA)

Thermal gravimetric analysis (TGA) monitors changes in mass as a function of temperature and can be used to investigate a compound's stability. Additionally, the technique can provide information regarding a compound's structure. Samples are heated in a furnace at a controlled rate under a controlled atmosphere whilst their mass is continuously recorded. A schematic TGA curve is shown in Figure 2.12, the decomposition temperature and change in mass can both be easily determined. The value of ΔM can be used to determine the compositional changes occurring during each decomposition step.[4] Any process involving a change in mass can be analysed and thus the technique has applications for studying decomposition, dehydration and oxidation reactions.[28] However, processes which are not accompanied by a change in mass such as phase transitions cannot be observed using this technique. Alternative thermal analysis techniques such as Differential Thermal Analysis (DTA) and Differential Scanning Calorimetry would be required in these cases.[29] TGA data were collected by Dr Gavin Peters at the University of St Andrews.

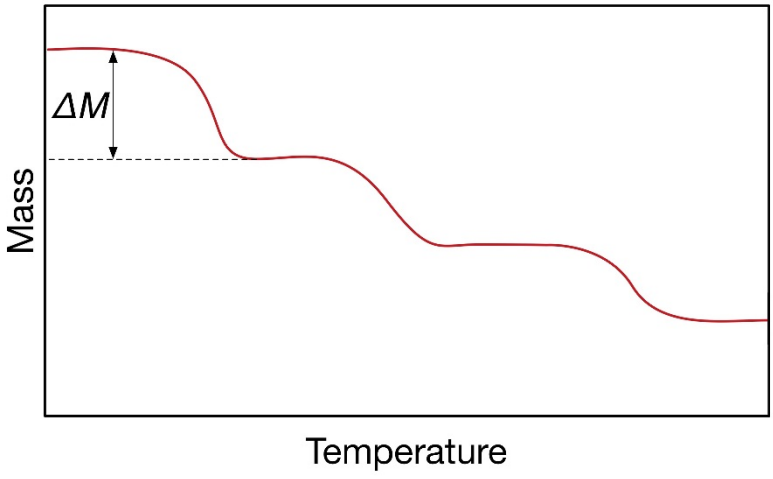

Figure 2.12: Schematic TGA plot for a multistep decomposition

2.9.2 Differential Scanning Calorimetry (DSC)

Differential Scanning Calorimetry is another form of thermal analysis which probes thermal events in the structure. The technique is perhaps more versatile than TGA which is restricted to changes in mass, and can be used to detect phase transitions and determine the purity of compounds. A sample and a reference are heated to the same temperature and with the difference in power required by the sample, and the reference recorded as a function of temperature.[5,29] A schematic diagram of the experiment set up and a typical DSC curve are shown in Figure 2.13 and Figure 2.14.[29] Exothermic processes such as crystallisation result in positive peak in the DSC curve whereas endothermic events are seen as negative peaks. The technique is closely related to Differential Thermal Analysis (DTA) where the power applied to both the reference and the sample are the same and differences in temperature are monitored.[4]

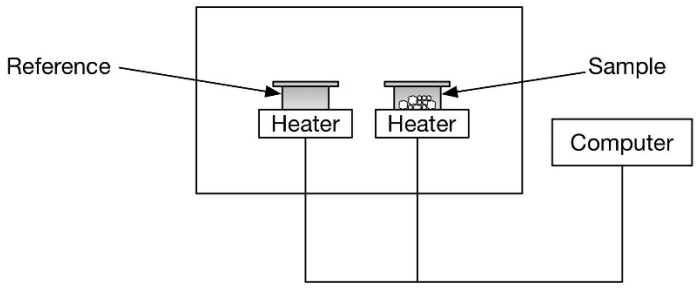

Figure 2.13: Simplified schematic diagram of DSC instrument

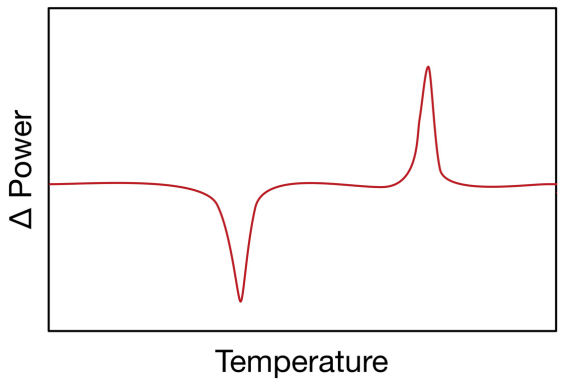

Figure 2.14: Schematic DSC curve

2.10 Scanning Electron Microscopy (SEM)

The morphology and topography of samples can be studied using scanning electron microscopy (SEM). Topological details with the 10^{-2} and 10^{2} μm can be visualised. The Jeol JSM instrument at the University of St Andrews uses a tungsten filament to emit electrons which are then accelerated through a high voltage of 5 – 50 keV and focused upon the sample. After interacting with the materials, the electrons are reflected onto a detector to produce an image of the sample. X-ray radiation is also emitted from the sample during the process which can be used for elemental analysis.[4,5]

Since the emitted X-rays of any element will have characteristic values according to Moseley's law (Equation 2.4), elemental analysis can be carried out using Energy Dispersive X-ray Spectroscopy (EDX). Whilst the technique is able to identify most elements present it is relatively insensitive to very light atoms, and quantitative analysis is slightly more problematic.[4]

2.11 Superconducting Quantum Interference Device (SQUID)

The superconducting quantum interference device (SQUID) is a very sensitive magnetometer able to detect very weak magnetic fields.[4,30] The device utilises the Josephson effect[31] and has surpassed the more conventional magnetometers VSM (Vibrating sample magnetometer) and the Gouy balance in terms of sensitivity.[5,32] The sample is placed within a set of superconducting coils as shown schematically in Figure 2.15. A magnetic field is applied parallel to the sample which is then moved in small increments through this magnetic field. This induces a change in current within the coils of wire and a potential difference across the SQUID, which can be used to calculate the magnetic susceptibility χ of the sample.[33] Data were collected with the assistance of Prof. Stephen Lee from the school of physics at the university of St Andrews.

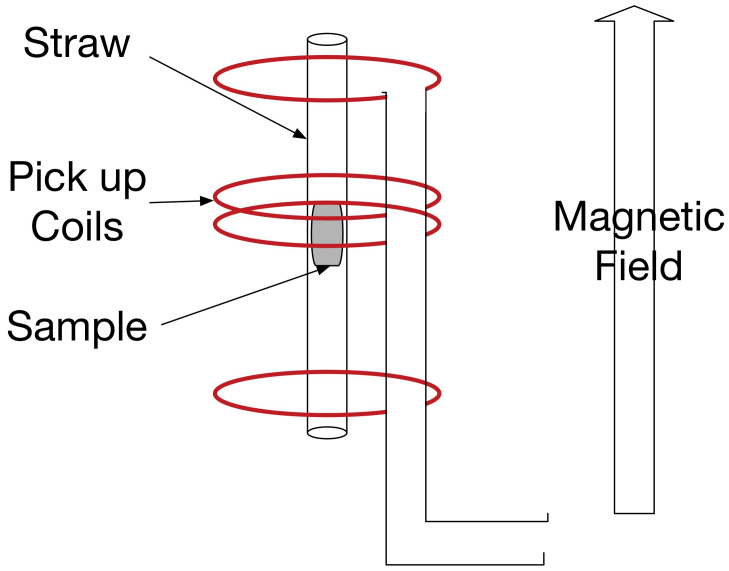

Figure 2.15: Schematic diagram of a superconducting quantum interference device (SQUID) magnetometer

2.12 References

1 D. Yufit, in *The 16th BCA/CCG Intensive Teaching School in X-ray Structure Analysis*, 2017.

2 G. Coquerel, *Chem. Soc. Rev.*, 2014, **43**, 2286–2300.

3 K. Byrappa and M. Yoshimura, *Handbook of Hydrothermal Technology*, Noyes Publications, Norwich, 2001, vol. 4.

4 A. R. West, *Solid State Chemistry and its Applications*, John Wiley & Sons Ltd., Chichester, 2nd edn., 2014.

5 P. Atkins, T. Overton, J. Rourke, M. Weller and F. Armstrong, *Inorganic Chemistry*, Oxford University Press, Oxford, 5th edn., 2010.

6 M. M. Woolfson, *An Introduction to X-ray Crystalography*, Cambridge University Press, Cambridge, second., 1997.

7 P. S. Halasyamani and K. R. Poeppelmeier, *Chem. Mater.*, 1998, **10**, 2753–2769.

8 H. Arnold, E. F. Bertaut, Y. Billiet, M. J. Buerger, H. Burzlaff, J. D. H. Donnay, W. Fischer, D. S. Fokkema, T. Hahn, H. Klapper, E. Koch, G. A. Langlet, A. Vos, P. M. de Wolff, H. Wondratschek and H. Zimmermann, *International Tables for Crystallography Volume A*, Kluwer Academic Publishers, Dordrecht, Fourth., 1995.

9 E. N. Maslen, A. G. Fox and M. A. O'Keefe, in *International Tables for Crystallography Volume C*, ed. A. J. C. Wilson, Kluwer Academic Publishers, Dordrecht, 1995, pp. 476–511.

10 W. Clegg, *X-ray Crystallography*, Oxford University Press, Oxford, 2nd edn., 2014.

11 R. Copley and H. J. Shepherd, in *The 16th BCA/CCG Intensive Teaching School in X-ray Structure Analysis*, 2017.

12 C. Giacovazzo, *Fundamentals of Crystallography*, Oxford University Press, Oxford, 2nd edn., 2002.

13 M. R. Probert, C. M. Robertson, J. A. Coome, A. K. Judith, B. C. Michell and A. E. Goeta, *J. Appl. Crystallogr.*, 2010, **43**, 1415–1418.

14 W. Clegg, in *The 16th BCA/CCG Intensive Teaching School in X-ray Structure Analysis*, 2017.

15 U. Shmueli, *Theories and Techniques of Crystal Structure Determination*, Oxford University Press, Oxford, 1st edn., 2007.

16 L. Palatinus, in *The 16th BCA/CCG Intensive Teaching School in X-ray Structure Analysis*, 2017.

17 W. Clegg, *Crystal Structure Determination*, Oxford University Press, Oxford, 1st Editio., 1998.

18 H. M. Rietveld, *J. Appl. Crystallogr.*, 1969, **2**, 65–71.

19 A. C. Larson and R. B. Von Dreele, *General Structure Analysis System (GSAS)*, 2004.

20 V. F. Sears, *Neutron News*, 2017, **3**, 26–37.

21 Https://www.isis.stfc.ac.uk/Pages/Characteristics-of-a-pulsed-source.aspx, *Accessed 28/01/2019*.

22 Https://www.isis.stfc.ac.uk/Pages/How-ISIS-works.aspx, *Accessed 28/01/2019*.

23 Https://www.isis.stfc.ac.uk/Pages/How-ISIS-works--in-depth.aspx, *Accessed 28/01/2019*.

24 Https://www.isis.stfc.ac.uk/Pages/SXD.aspx, *Accessed 29/01/2019*.

25 Https://www.isis.stfc.ac.uk/Pages/Instruments.aspx, *Accessed 28/01/2019*.

26 N. E. Brese and M. O'Keeffe, *Acta Crystallogr. Sect. B*, 1991, **47**, 192–197.

27 I. D. Brown and D.Altermatt, *Acta Crystallogr. Sect. B*, 1985, **244**, 244–247.

28 P. Atkins, T. Overton, J. Rourke, M. Weller and F. Armstrong, in *Inorganic Chemistry*, Oxford Universty Press, 5th Editio., 2010, pp. 223–254.

29 D. Kealey and P. J. Haines, *Analytical Chemistry*, BIOS Scientific Publishers Limited, Oxford, 2nd edn., 2002.

30 Http://hyperphysics.phy-astr.gsu.edu/hbase/Solids/Squid.html, *Accessed 06/02/2019*.

31 B. D. Josephson, *Rev. Mod. Phys.*, 1974, **46**, 251–255.

32 C. E. Housecroft and A. G. Sharpe, *Inorganic Chemistry*, Pearson Education Limited, Harlow, 5th edn., 2018.

33 P. Atkins and J. De Paula, *Physical Chemistry*, Oxford University Press, Oxford, 9th edn., 2010.

Chapter 3 Tris Sarcosine Calcium Chloride (TSCC)

3.1 Introduction

One example of a metal-organic ferroelectric is tris sarcosine calcium chloride (TSCC), which was first reported by Makita *et al.* in 1965 and was found to have ferroelectric properties below 127 K.[1] Its organic component is the amino acid sarcosine (N-methyl glycine) as shown in Figure 3.1 which links its Ca^{2+} ions in infinite chains. The chains are interconnected by hydrogen bonding with the chloride ion occupying the channels. The compound crystallises in the centrosymmetric *Pnma* space group with unit cell parameters a = 9.156(10) Å, b = 17.460(5) Å and c = 10.265(5) Å at room temperature. The crystal structure is shown in Figure 3.2.[2] The compound exhibits pseudohexagonal symmetry since the ratio of its b/c axes is approximately $\sqrt{3}$. As a result of the metric symmetry, the compound is prone to twinning.[3,4] On cooling below T_C, the symmetry is lowered to the polar $Pn2_1a$ space group and ferroelectric properties are induced.[5]

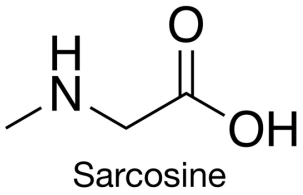

Figure 3.1: structure of sarcosine (N-methyl glycine)

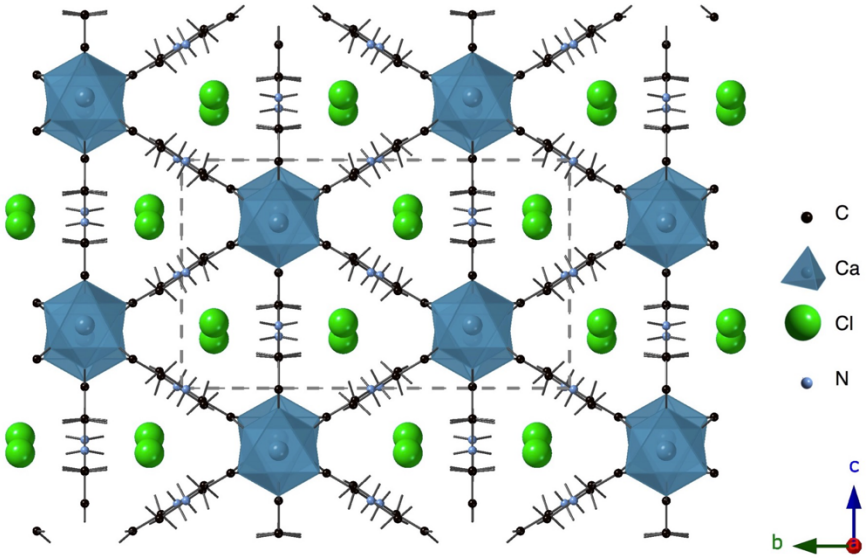

Figure 3.2: Crystal structure of $(C_3NO_2H_7)_3CaCl_2$ TSCC in the paraelectric phase, as reported by Ashida *et al.*[2]

The mechanism for the ferroelectric phase transition has been discussed extensively in the literature[6,7] However, the various findings have been contradictory. Initial research indicated that the transition was likely to occur *via* an order-disorder mechanism since the compound possesses hydrogen bonding and T_C displays a positive pressure dependence.[8] Subsequent soft mode studies revealed an underdamped mode in the ferroelectric phase, suggesting a displacive mechanism.[9] Despite the discovery of the soft phonon, the system still displays some order-disorder character as seen from critical anomalies in the line width and shape of Mn^{2+} EPR spectra surrounding T_C.[6] The mechanism is now believed to be a second order displacive mechanism.[7]

Another major area of interest in TSCC is in its quantum critical point. Substitution of chloride with either bromide or iodide supresses T_C to 0 K at ~72 % and 25 % respectively.[10,11] Subsequently, this effect has been studied in detail by the synthesis of solid solutions.[12] The detrimental effect of halogen substitution on the ferroelectric properties of TSCC could provide an insight into the mechanism of the ferroelectric phase transition.

To study the role of hydrogen bonding, several groups investigated the effect of substituting hydrogen with deuterium. However, there have been contradictory reports regarding its effect. In some cases there was no discernible effect, whilst Blinc *et al.* reported a change in T_C from 127 K in pure TSCC to 149 K in the deuterated sample, which would suggest an order-disorder mechanism.[13,14,15] The effect of hydrogen bonding is also important in understanding the mechanism since an order-disorder mechanism would be affected by deuteration.

In addition to the known ferroelectric phase transition at ~130 K, there have also been reports of several other transitions occurring at 185 K, 64 K and 42 K observed using a variety of techniques.[16] The first example at 185 K was observed by Lee *et al*. and concerned the temperature dependence of the spin lattice relaxation time T_1 in NMR

experiments which exhibits a minimum at this point; their data are shown in Figure 3.3.[17] The transition was thought to be the result of rotational disorder of the sarcosine methyl group and could perhaps explain the contradictory evidence regarding the mechanism of the ferroelectric phase transition.[17] In addition to the anomaly at 185 K, Lee *et al*. also provide evidence of a phase transition at 64 K. Further evidence of this transition was reported by Haga *et al.* in specific heat data as shown in Figure 3.3 and in resonant ultrasound spectroscopy data.[18,7] Earlier work had reported the phase transitions at 42 K and 64 K using different techniques and it was suggested that they were the same transition exhibiting thermal hysteresis. However, more recent work by Lashley *et al.* has been able to observe both transitions during the same experiment.[16] In-fact, the specific heat data reported by Haga *et al*., the irregularity of the peak shape approaching 64 K could suggest the presence of another smaller structural change. The presence of an additional phase transition at 42 K is also supported by resonant ultrasound spectroscopy.[19] The structural changes associated with each of these transitions are yet to be fully investigated. The additional phase is also thought to exist in the brominated forms of TSCC though the ferroelectric transition temperature is supressed. The precise relationship between bromine concentration and phases adopted is reported in full by Jones *et al.*[7]

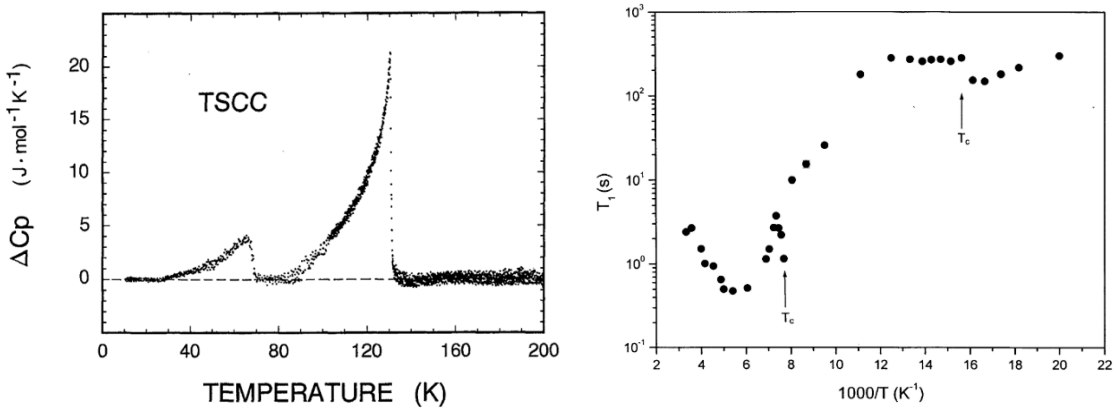

Figure 3.3: Evidence of new phase transitions in TSCC (left) specific heat data collected by Haga *et al.*[18] reproduced with permission from reference 18 ©(1993) J. Phys. Soc. Jpn. and (right) temperature dependence of T_1 relaxation time[17] reproduced with permission from reference 17 (2005) J. Phys. Chem. Solids

An additional phase has also been reported at elevated pressures (above 2.6 kbar). Though its structure is still unknown, it has been hypothesized that the high pressure phase could have antiferroelectric properties.[20] There have also been reports of a hypothetical hexagonal phase at elevated temperatures which should have the space group $P6_3cm$ but this has never been observed since TSCC decomposes at around 503 K before this phase is reached.[7,4]

In light of the various contradictory studies previously undertaken, in this chapter, the mechanism of the known ferroelectric phase transition is investigated by neutron and X-ray diffraction. The role of hydrogen bonding and possible methyl group disorder is examined in detail using neutron diffraction data. Single crystal X-ray diffraction data is also collected in small intervals in the vicinity of T_C to closely examine the non-hydrogen atoms and their role in the transition. Both techniques were used complimentarily to identify any structural changes associated with the four additional phase transitions which have been reported in the literature from physical measurements.

3.2 Experimental Techniques

3.2.1 Synthesis

Stoichiometric quantities of calcium chloride dihydrate and sarcosine were dissolved in deionised water and crystals were produced after approximately six days by a slow evaporation process. The resulting crystals were analysed by powder/single crystal X-ray diffraction and thermal analysis.

3.2.2 Powder X-ray Diffraction

Crystalline samples were ground into a fine powder and loaded into steel discs. Diffraction data were measured between 5-70˚ for one hour at room temperature on PANalytical Empyrean diffractometer using Cu Kα_1 radiation.

3.2.3 Single Crystal X-ray Diffraction

High quality crystals were selected using an optical microscope and mounted in the X-ray beam. All diffraction data were collected using Mo Kα radiation and solved using the SHELX program and the WINGX interface.[21,22]. The initial data sets at 173 K and room temperature were collected using a Rigaku SCXmini desktop instrument and data processed using Rigaku software.[23] A single crystal provided by V. H. Schmidt (*via* Prof Jim Scott) was used for lower temperature analysis. Data sets in the 100 – 150 K temperature range were collected by Prof. Alexandra Slawin at the University of St Andrews on a Rigaku FRX diffractometer and the data were processed using Rigaku software.[23] Further analysis was undertaken by Dr Mike Probert at Newcastle University in the temperature range 20 – 100 K using the XIPHOS 4 circle diffractometer with 3 stage closed-cycle He cryo-refrigerator and processed with APEX2 software.[24,25]

3.2.4 Neutron Diffraction

High quality large single crystals of pure TSCC and TSCC 30 % Br were provided by V. H. Schmidt. Neutron diffraction data were collected at six different temperatures for each of the samples using the SXD instrument at the ISIS Neutron and Muon source with the assistance of Dr Silvia Capelli.[26] The data were processed using SXD 2001 software before the existing structural model from X-ray diffraction was refined using the SHELX program and WINGX.[21,22,27]

3.2.5 Differential Scanning Calorimetry (DSC)

Data were collected on powdered samples of TSCC using a NETZCH DSC 204 instrument between 25 and −170 °C using liquid nitrogen. Several cooling rates, temperature programs and quantities of sample were used.

3.3 Results and Discussion

A single crystal of TSCC was synthesised by a slow evaporation method over the course of six days, the resulting products were analysed by both powder and single crystal X-ray diffraction. Single crystal diffraction data were collected at three temperatures 293, 173 and 93 K and their crystallographic and refinement details are shown in Table 3.1. The crystal structures are consistent with those reported by Ashida *et al.* and Mishima *et al.;* the crystal structure of the paraelectric phase is shown in Figure 3.4.[2,5] The Ca-O and N-H…Cl bond lengths have also been determined for each data set and are shown in Table 3.2.

Table 3.1: Crystallographic and refinement details of TSCC collected at 293 and 173 K

	173 K	**293 K**
Formula	$(C_3NO_2H_7)_3CaCl_2$	$(C_3NO_2H_7)_3CaCl_2$
Formula Weight	378.27	378.27
Density (g cm^{-3})	1.543	1.532
Crystal System	Orthorhombic	Orthorhombic
Space Group	*Pnma*	*Pnma*
a/Å	9.1289(6)	9.1463(6)
b/Å	17.4251(12)	17.4652(12)
c/Å	10.2397(7)	10.2662(7)
α (˚)	90	90
β (˚)	90	90
γ (˚)	90	90
V/$Å^3$	1628.85(19)	1639.94(19)
Z	4	4
Measured Ref	15894	15975
Independent Ref	1926 [R(int) = 0.0971]	1938 [R(int) = 0.0917]
Refined Parameter	149	150
GOOF	0.839	0.959
Final R Indices (I > 2σ(I))	R1 = 0.0412, wR2 = 0.1057	R1 = 0.0442, wR2 = 0.1184

Table 3.2: Selected bond lengths (Å) and bond valence sum (valence units) for TSCC determined from single crystal X-ray diffraction data collected at 173 and 293 K

Bond	173 K	293 K
M-O	2.293(2)	2.294(2)
	2.293(2)	2.294(2)
	2.303(3)	2.303(3)
	2.358(3)	2.357(3)
	2.3695(19)	2.371(2)
	2.3695(19)	2.371(2)
N-H-X	3.1779(15)	3.1861(17)
	3.220(3)	3.220(3)
	3.211(3)	3.231(3)
BVS (Ca)	2.25	2.25

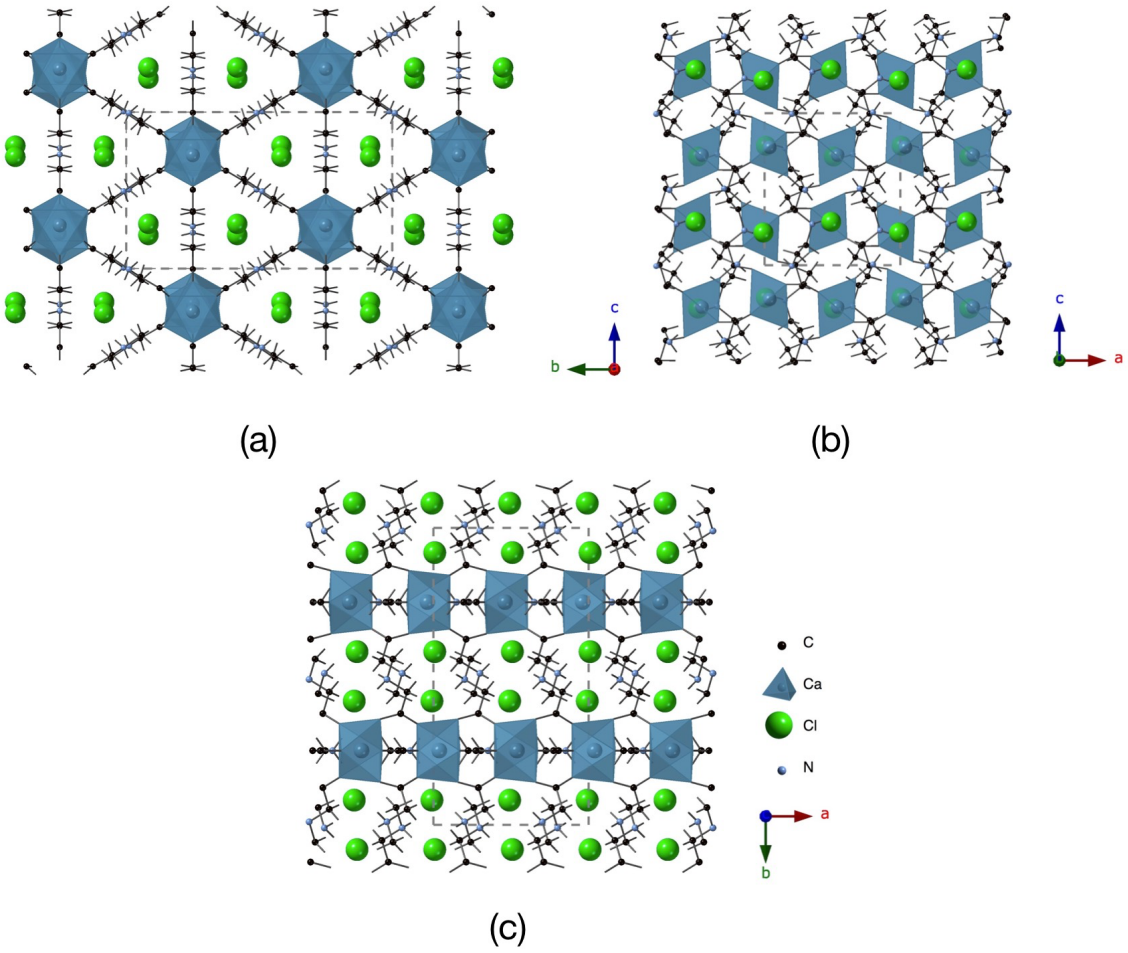

Figure 3.4: Crystal structure of TSCC in the paraelectric phase derived from X-ray diffraction data collected at 173 K

A powder X-ray diffraction pattern was also collected and the results were compared to the simulated diffraction pattern derived from the solved single crystal structure as shown in Figure 3.5. The similarities between both diffraction patterns indicate a high level of purity in the sample.

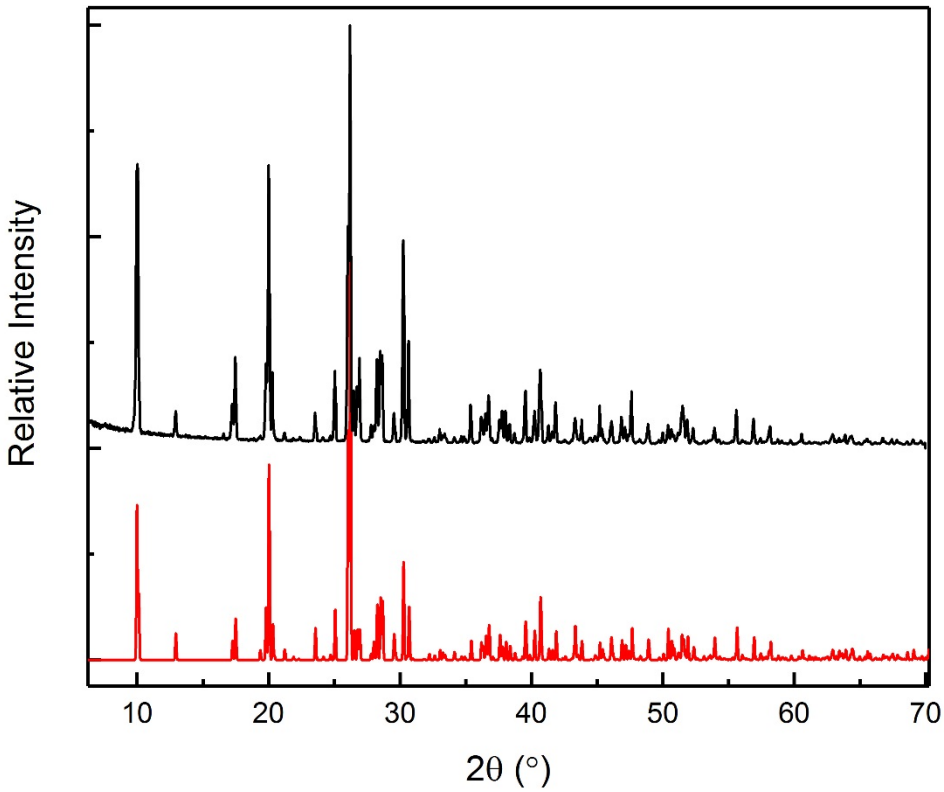

Figure 3.5: Comparison of powder X-ray diffraction data of TSCC collected at ambient temperature and the simulated pattern from single crystal X-ray diffraction data. (red) simulated diffraction pattern and (black) experimental diffraction pattern

The two data sets were entirely consistent with the previous work and did not provide any evidence of an additional phase at 185 K as reported in the literature. Since only two data sets were measured, potential phase transitions were investigated using Differential Scanning Calorimetry (DSC) to investigate the full temperature range. Several methods and temperature programs were used during DSC analysis and the data are shown in Figure 3.6. The optimal method for visualising the known ferroelectric phase transition was by employing initial cooling rate of 10 °C/min between 25 and −170 °C followed by a heating/cooling cycle at 5 °C/min between −170 and −80 °C. The

samples were then heated back to room temperature at 10 °C/min. Despite the numerous strategies attempted, there was no evidence of any other phase transitions within the temperature range of −170 to 25 °C. In this regard, it should be noted that the known ferroelectric phase transition produced a relatively small peak in the DSC data at ~−145 °C.

Due to the relative insensitivity of DSC to potential phase transitions, the structure was analysed in greater detail using both neutron and X-ray diffraction. The detailed analysis of bond lengths, angles, coordinates and atomic displacement parameters (ADPs) was undertaken using the numbering scheme shown in Figure 3.7. At temperatures above 130 K, the compound crystallises in the centrosymmetric *Pnma* space group. As a result the asymmetric unit at this temperature contains only two inequivalent sarcosine molecules, one of which lies on the mirror plane and the other on a general position. Whereas the low temperature model in the polar $Pn2_1a$ space group contains three inequivalent sarcosine molecules. For consistency, atoms which are equivalent in the paraelectric phase are split into A/B in the low temperature ferroelectric phase.

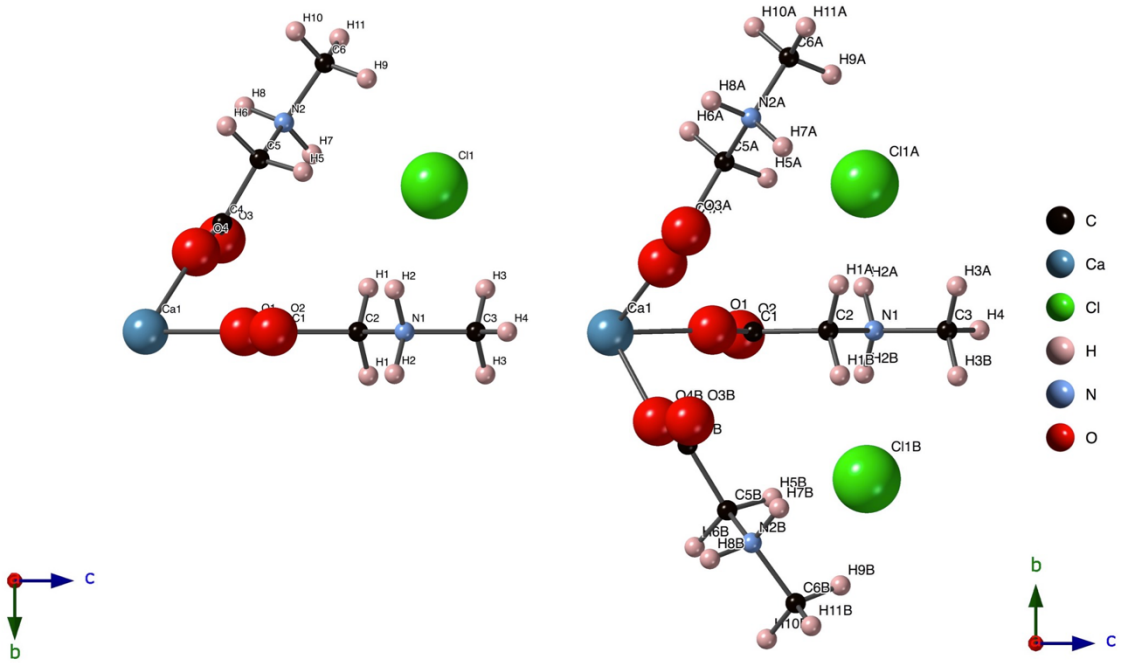

Figure 3.7: Asymmetric units of TSCC in (left) the paraelectric phase and (right) the ferroelectric phase showing their numbering schemes, both derived from single crystal neutron diffraction data at 20 and 300 K

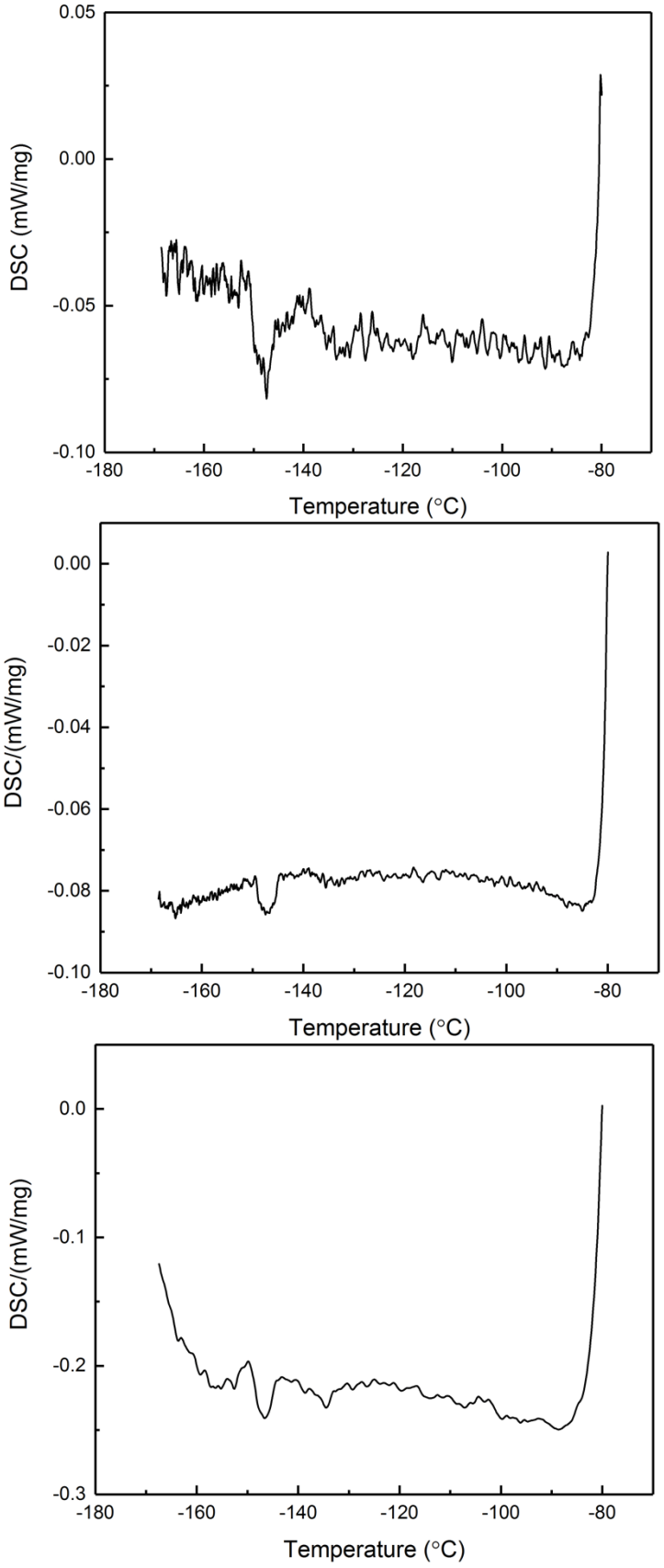

Figure 3.6: Differential Scanning Calorimetry data for TSCC collected at (a) 5 °C/min, 2.5 mg (b) 5 °C/min, 9.1 mg and (c) 10 °C/min, 2.0 mg

3.3.1 TSCC Neutron Diffraction

Neutron diffraction data were collected on the SXD instrument at the ISIS neutron and muon source on a sample synthesised by V. H. Schmidt.[26] The diffraction data were collected at six different temperatures chosen to cover the reported phase transitions of TSCC. The crystallographic and refinement details are shown in Table 3.3. The three data sets collected at 150 K and above were refined in the centrosymmetric *Pnma* model whereas the remaining three were refined to the polar $Pn2_1a$ space group. The unit cell parameters are also shown in Table 3.3 and plotted in Figure 3.8. The data reveal a gradual contraction towards low temperature which is typical of any structure. However, the known ferroelectric phase transition has an almost negligible effect on the unit cell parameters and the structure would benefit from further investigation at finer temperature intervals to observe more subtle structural changes.

Table 3.3: Crystallographic and refinement details of TSCC from single crystal neutron diffraction data collected at 20, 50, 100, 150, 210 and 300 K

Temperature	**20 K**	**50 K**	**100 K**	**150 K**	**210 K**	**300 K**
Formula Weight	378.26	378.26	378.26	378.26	378.26	378.26
Density (g cm^{-3})	1.561	1.560	1.555	1.549	1.544	1.535
Crystal System	Orthorhombic	Orthorhombic	Orthorhombic	Orthorhombic	Orthorhombic	Orthorhombic
Space Group	$Pn2_1a$	$Pn2_1a$	$Pn2_1a$	*Pnma*	*Pnma*	*Pnma*
a/Å	9.094(2)	9.0950(19)	9.106(2)	9.1217(19)	9.130(3)	9.144(2)
b/Å	17.326(4)	17.332(5)	17.357(5)	17.382(4)	17.399(5)	17.436(5)
c/Å	10.215(2)	10.216(2)	10.222(2)	10.230(2)	10.242(3)	10.263(3)
α (˚)	90	90	90	90	90	90
β (˚)	90	90	90	90	90	90
γ (˚)	90	90	90	90	90	90
V/$Å^3$	1609.5(6)	1610.4(6)	1615.5(7)	1622.1(6)	1627.0(8)	1636.3(7)
Z	4	4	4	4	4	4
Measured Ref	17469	15649	12025	9848	8094	5677
Refined Parameter	379	384	384	208	208	208
GOOF	1.227	1.236	1.229	1.251	1.252	1.267
Final R Indices (I > 2σ(I))	R1 = 0.0850, wR2 = 0.2204	R1 = 0.0880, wR2 = 0.2281	R1 = 0.0910, wR2 = 0.2345	R1 = 0.0920, wR2 = 0.2409	R1 = 0.0935, wR2 = 0.2411	R1 = 0.1013, wR2 = 0.2566

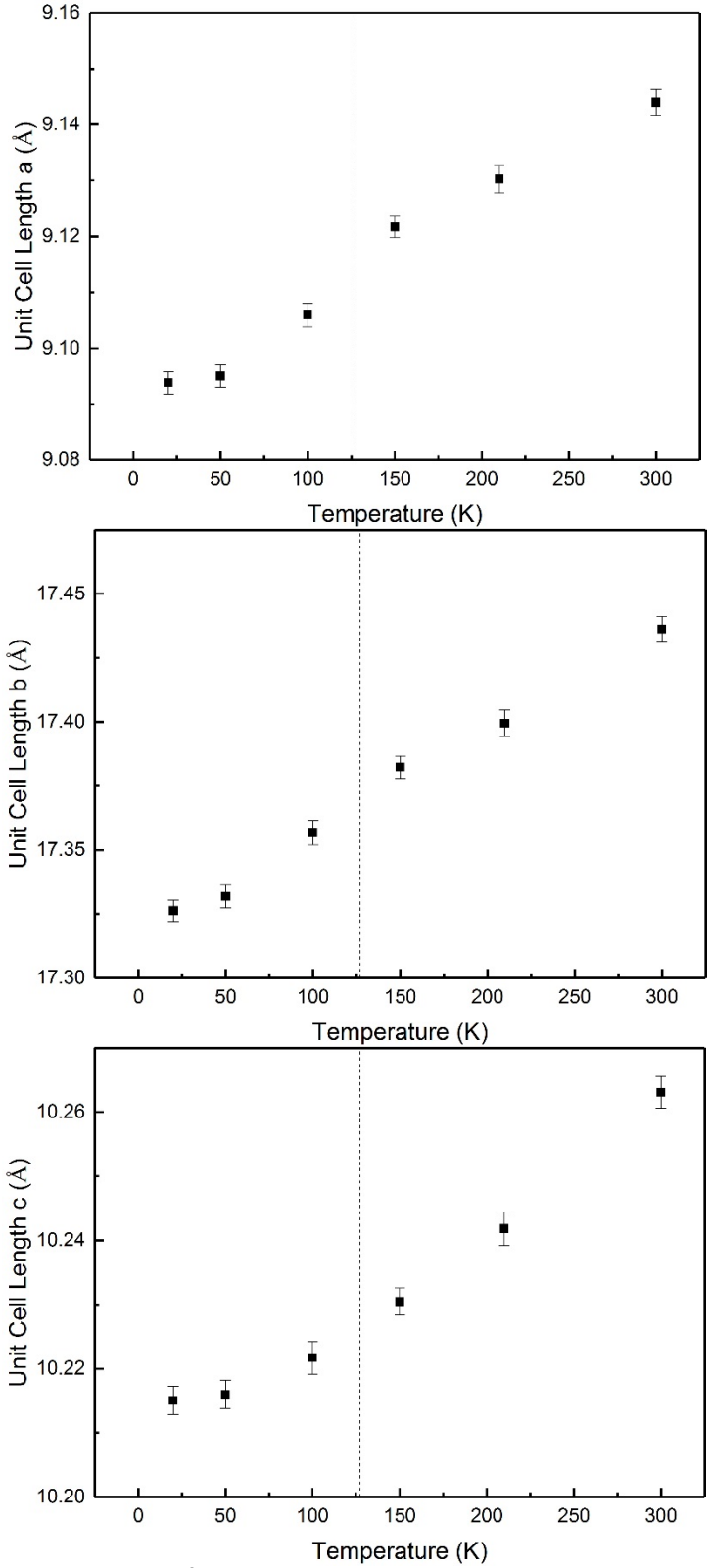

Figure 3.8: Unit cell parameters (Å) of TSCC derived from single crystal neutron diffraction data collected at various temperatures with phase transition shown by the dotted line

3.3.1.1 Hydrogen Bonding

Given the contradictory evidence regarding the role of hydrogen in the ferroelectric properties of TSCC, the hydrogen atomic positions, ADPs, bond lengths and angles were carefully determined at each temperature. The hydrogen bonding scheme and atom numbering is shown more clearly in Figure 3.9. The various hydrogen bond lengths for each data set are shown in Table 3.4 and Table 3.5. On average, the N-H…Cl distances are seen to decrease at low temperatures, whereas the bond angles increase gradually at lower temperatures (Figure 3.10).

The trends in pairs of N-H…Cl bonds are also shown in Figure 3.11. Above T_C both bonds are equivalent due to the presence of a mirror plane and there are gradual trends in the bond lengths. Below T_C there is a change to the polar $Pn2_1a$ space group accompanied by the loss of a mirror plane. At this point the previously equivalent bond lengths begin to diverge slightly. Between the paraelectric 150 K data set and the ferroelectric 20 K data set, the bond lengths change by up to ~1 %. Similar trends are observed in the hydrogen bond angles which are listed in full in Table 3.5 and shown in Figure 3.11. The N1-H2…Cl1 and N2-H8-Cl1 bond angle deviate by ~2˚ but a significantly larger effect of around 8˚ is observed in the N2-H7…Cl1 bond angles.

Table 3.4: Hydrogen bond lengths (Å) of TSCC derived from neutron diffraction data

Bond	20 K	50 K	100 K	150 K	210 K	300 K
N1-H2A…Cl1A	3.182(3)	3.180(4)	3.184(6)	3.173(2)	3.176(2)	3.184(4)
N1-H2B…Cl1B	3.151(3)	3.158(4)	3.158(6)			
N2A-H7A…CL1A	3.229(2)	3.228(3)	3.224(4)	3.213(2)	3.218(3)	3.220(4)
N2B-H7B…Cl1B	3.193(2)	3.193(3)	3.197(4)			
N2A-H8A…Cl1B	3.215(2)	3.211(3)	3.213(4)	3.204(2)	3.211(3)	3.217(4)
N2B-H8B…Cl1A	3.184(2)	3.186(3)	3.188(4)			

Table 3.5: Hydrogen bond angles (°) of TSCC derived from single crystal neutron diffraction data

Bond	20 K	50 K	100 K	150 K	210 K	300 K
N1-H2A…Cl1A	161.7(6)	161.9(7)	160.6(9)	160.5(5)	159.9(5)	160.0(8)
N1-H2B…Cl1B	158.5(6)	158.6(7)	160.0(9)			
N2A-H7A…CL1A	165.2(6)	165.4(7)	163.7(10)	157.2(5)	157.3(6)	156.7(9)
N2B-H7B…Cl1B	152.6(6)	152.0(7)	152.7(10)			
N2A-H8A…Cl1B	164.1(7)	163.9(8)	163.5(11)	162.1(5)	161.4(6)	161.1(8)
N2B-H8B…Cl1A	160.1(7)	160.1(8)	160.3(11)			

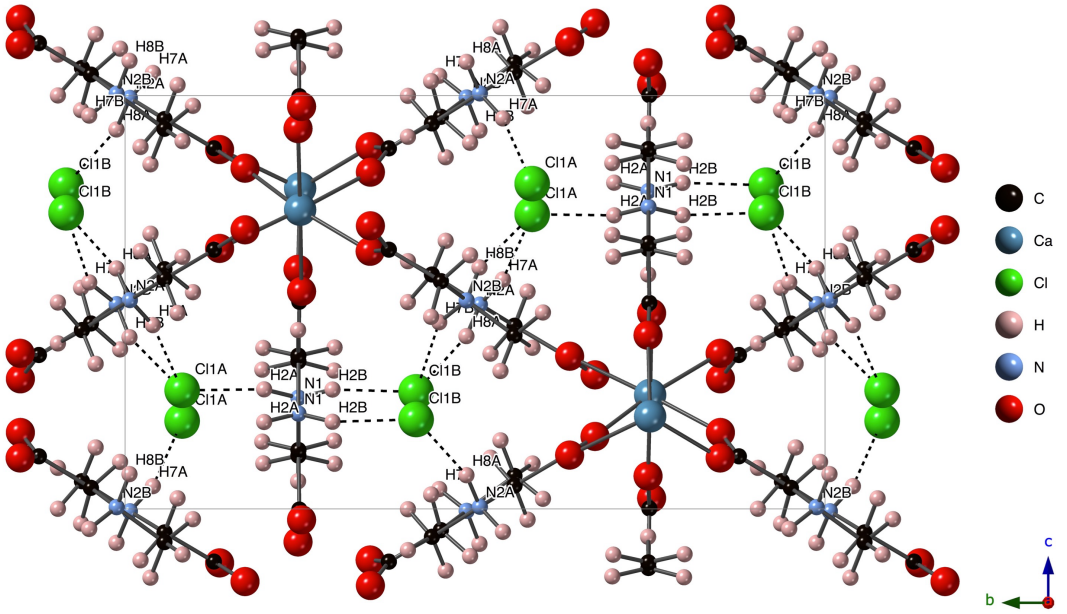

Figure 3.9: Crystal structure of TSCC with hydrogen bonding scheme derived from single crystal neutron diffraction data collected at 20 K

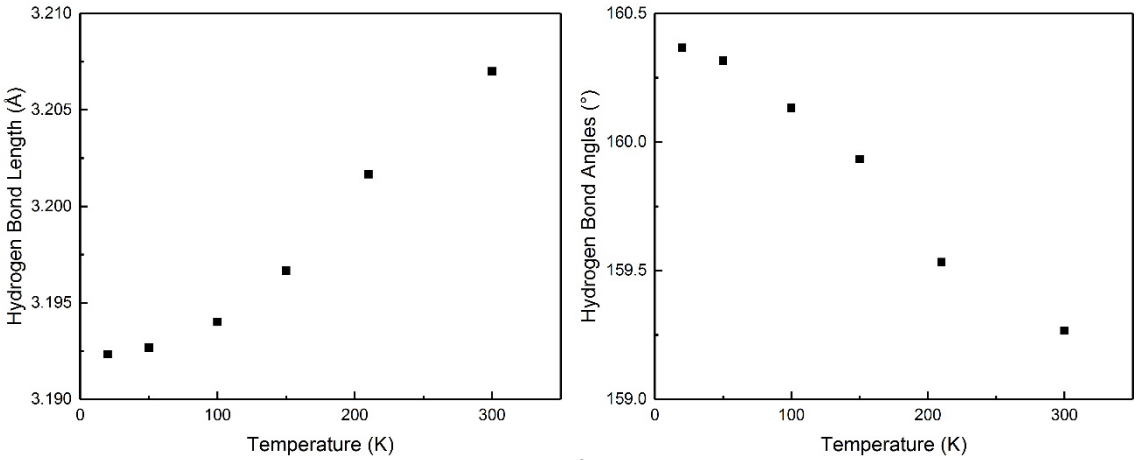

Figure 3.10: Average hydrogen bond lengths (Å) and angles (°) of TSCC derived from single crystal neutron diffraction data collected at 20, 50, 100, 150, 210 and 300 K

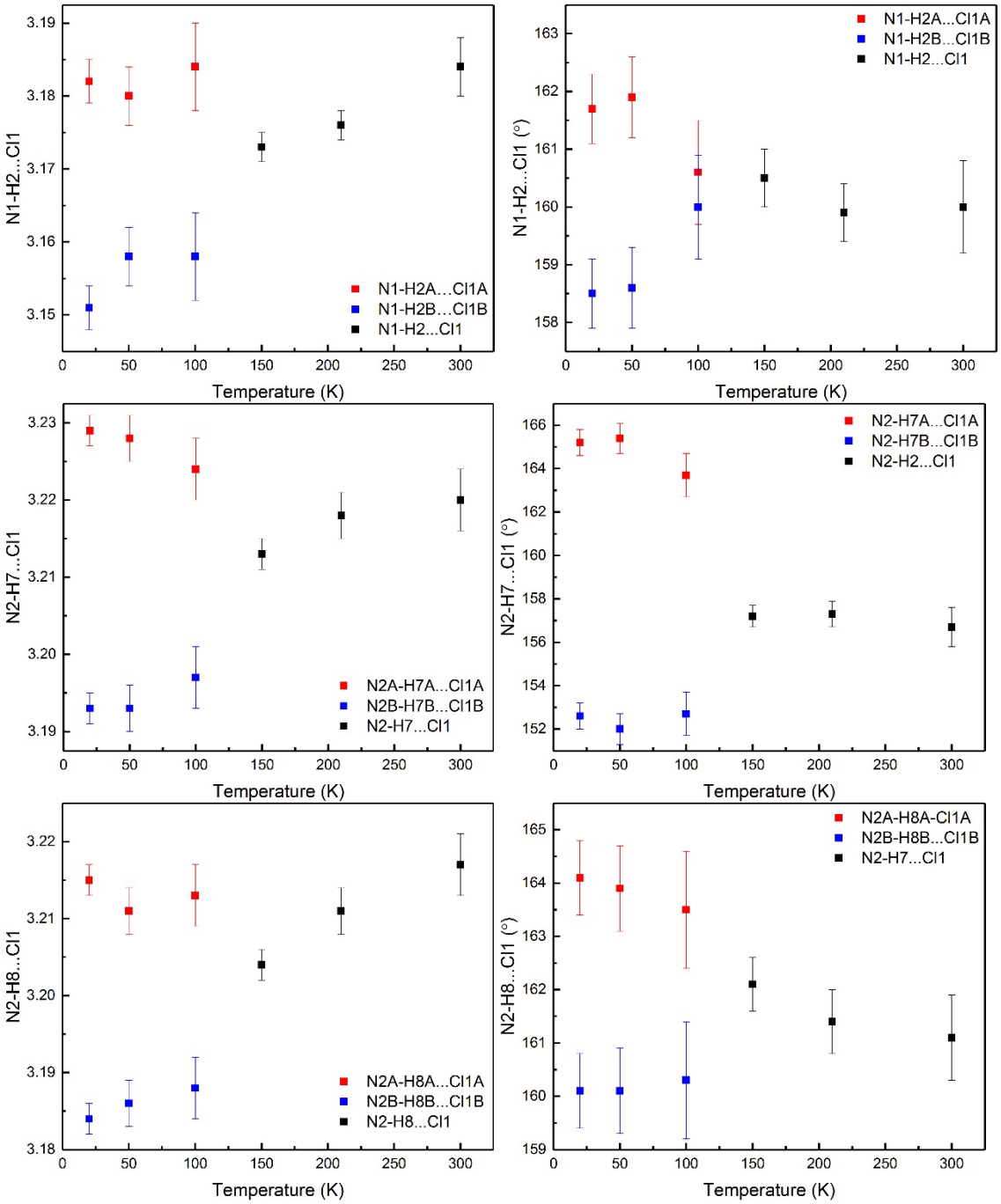

Figure 3.11: Individual hydrogen bond lengths (Å) and angles (°) of TSCC derived from single crystal neutron diffraction data collected at 20, 50, 100, 150, 210 and 300 K

3.3.1.2 Methyl Group Disorder

A second area of interest was in the ADPs of the methyl group hydrogen atoms since they could reveal evidence of disorder. Previous work by Mishima *et al.* had found that

the ADPs of the terminal methyl carbon had been relatively high when compared to the rest of the sarcosine molecule.[5] This could indicate the presence of rotational disorder of the methyl group, the ordering of which could perhaps account for some of the additional phase transitions observed at low temperatures.

The atomic positions and anisotropic (ADPs) of the methyl hydrogen atoms were determined from the neutron diffraction data, the isotropic equivalent values are shown in Table 3.6. Whilst there is a decrease at the lower temperatures, this is largely due to the reduction of thermal motion and not attributable to methyl group disorder. There was no evidence of elongation or unusual behaviour of the hydrogen ADPs for any of the six data sets collected. The ADPs of TSCC determined at 300 K are shown in Figure 3.12 but do not provide evidence of disorder, even in the highest temperature data set.

Table 3.6: Equivalent isotropic ADPs ($Å^2 \times 10^3$) of the terminal methyl group hydrogens of TSCC at 20, 50, 100, 150, 210 and 300 K derived from single crystal neutron diffraction data

Atom	20 K	50 K	100 K	150 K	210 K	300 K
H3A	26(2)	31(3)	37(4)	48(2)	60(3)	78(4)
H3B	26(2)	26(2)	36(4)			
H4	25(2)	28(2)	34(2)	43(2)	55(3)	72(6)
H9A	24(2)	26(2)	38(3)	56(2)	64(3)	85(5)
H9B	26(2)	28(2)	41(4)			
H10A	25(2)	28(2)	35(3)	52(2)	66(3)	84(5)
H10B	26(2)	28(2)	44(4)			
H11A	23(2)	28(2)	35(3)	54(2)	64(3)	80(5)
H11B	26(2)	28(2)	40(3)			

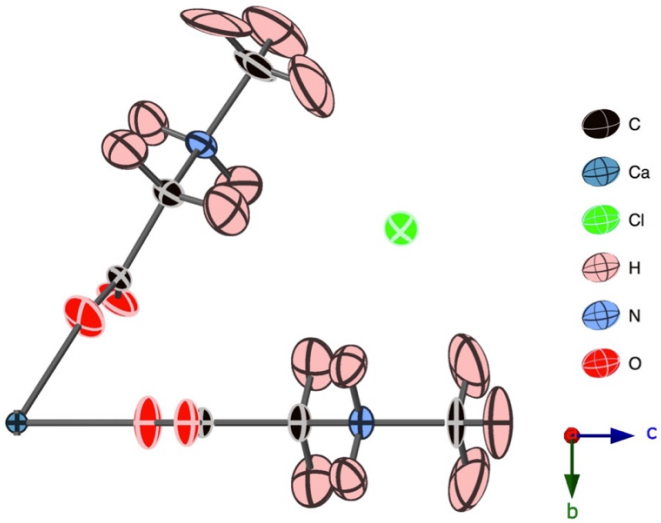

Figure 3.12: Anisotropic ADPs of TSCC at 300 K as derived from single crystal neutron diffraction data

3.3.1.3 Calcium Coordination Environment

The coordination environment of the Ca^{2+} was also studied in detail to investigate any subtle change in structure which could account for the proposed additional phase transitions. Initially, each of the Ca-O bond lengths were determined for the six different temperatures and are shown in Table 3.7 together with their bond valence sums. On average, the Ca-O bond lengths are slightly shorter than expected[28] but do not have a strong dependence on temperature and the bond valence sums remain almost constant for each of the data sets. Both the Ca-O1 and Ca-O2 bond lengths are not significantly affected by temperature or by the known phase transition. Both the Ca-O3 and Ca-O4 bonds split into two inequivalent bonds, A and B, below the known transition temperature as a result of the reduction in symmetry. The effect of temperature on each of the Ca-O bond lengths is shown more clearly in Figure 3.13. Whilst the known ferroelectric phase transition is evident from the variation in Ca-O bond lengths, there was no indication of an additional phase transition at low temperature which had been suggested in earlier work.

Table 3.7: Ca-O bond lengths (Å) of TSCC at 20, 50, 100, 150, 210 and 300 K derived from single crystal neutron diffraction

Bond	20 K	50 K	100 K	150 K	210 K	300 K
Ca-O1	2.308(3)	2.308(4)	2.305(4)	2.303(4)	2.302(5)	2.304(8)
Ca-O2	2.363(3)	2.362(4)	2.361(4)	2.360(4)	2.359(5)	2.360(8)
Ca-O3A	2.391(5)	2.387(6)	2.378(9)	2.368(3)	2.365(4)	2.368(6)
Ca-O3B	2.354(5)	2.352(6)	2.357(8)			
Ca-O4A	2.296(4)	2.299(5)	2.297(8)	2.287(4)	2.292(4)	2.293(6)
Ca-O4B	2.293(5)	2.296(6)	2.294(8)			
BVS	2.24	2.24	2.25	2.27	2.26	2.25

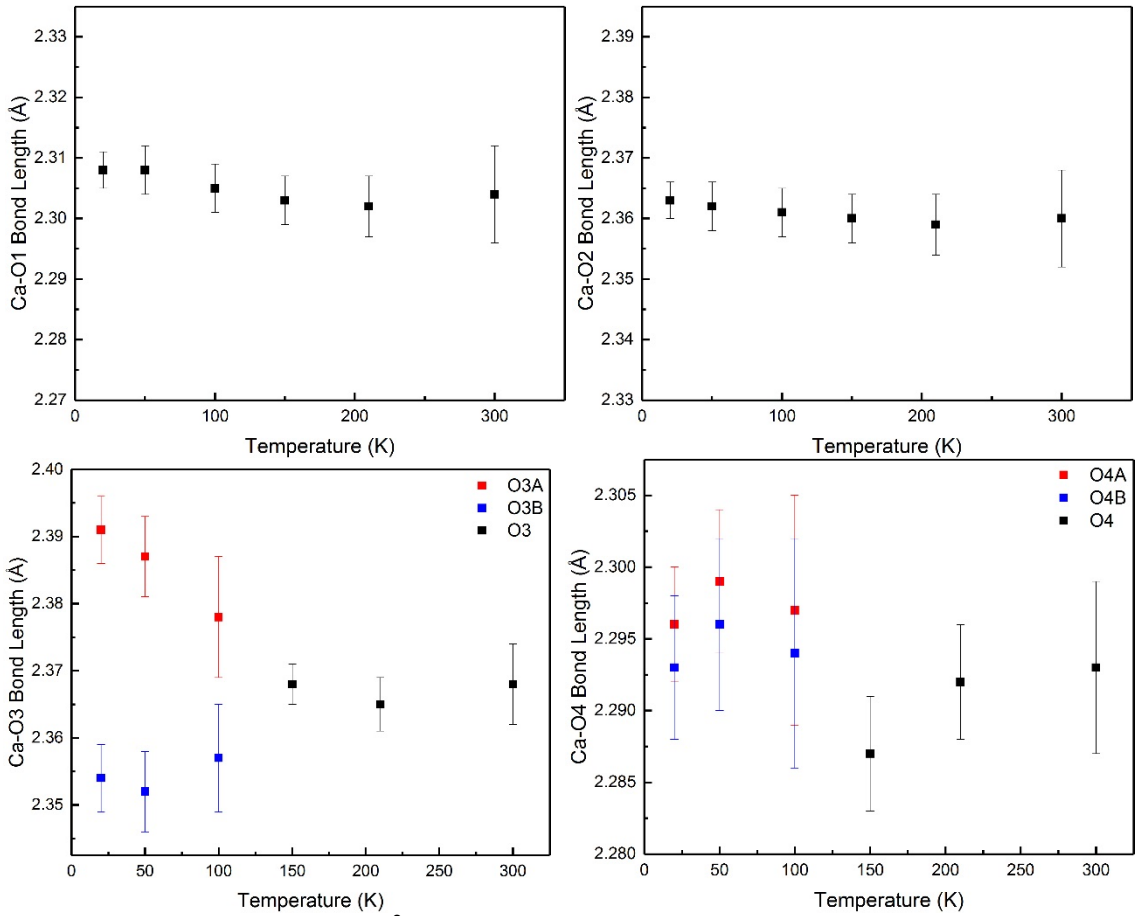

Figure 3.13: Ca-O bond lengths (Å) in TSCC derived from single crystal neutron diffraction data collected at 20, 50, 100, 150, 210 and 300 K

In addition, the bond angles surrounding the Ca^{2+} centre were also probed in detail using the neutron diffraction data, with the results shown in Table 3.8 and Figure 3.14/3.15.

All six bond angles change gradually in the region of 300 K to 150 K before an abrupt change surrounding the known ferroelectric phase transition ~130 K. The Ca-O1-C1 and Ca-O2-C1 bond angles are not affected by a change in symmetry but do deviate significantly around T_C by around 3.5˚ and 2.5° respectively between 300 K and 20 K. The O3 and O4 bond angles exhibit much larger deviation upon cooling through T_C with their bond angles altering by around 10˚ and 15° respectively in the temperature region investigated. As seen in the evolution of Ca-O bond lengths with temperature, the only significant change in bond angle is associated with the ferroelectric phase transition at 127 K and there are no anomalies in these parameters which would suggest the presence of an additional low temperature phase.

Table 3.8: Ca-O-C bond angles (°) in TSCC derived from single crystal neutron diffraction data collected at 20, 50, 100, 150, 210 and 300 K

Bond Angle	20 K	50 K	100 K	150 K	210 K	300 K
Ca-O1-C1	159.4(2)	159.8(2)	161.3(3)	162.6(3)	162.9(4)	163.0(6)
Ca-O2-C1	132.82(17)	132.65(19)	131.9(2)	131.1(2)	131.1(3)	131.3(4)
Ca-O3A-C4A	118.9(2)	119.4(3)	122.0(4)	130.4(2)	130.9(3)	131.6(4)
Ca-O3B-C4B	137.7(2)	137.6(3)	136.5(4)			
Ca-O4A-C4A	176.7(3)	176.9(3)	174.3(5)	164.0(3)	163.1(4)	162.7(6)
Ca-O4B-C4B	151.5(3)	152.2(3)	155.0(5)			

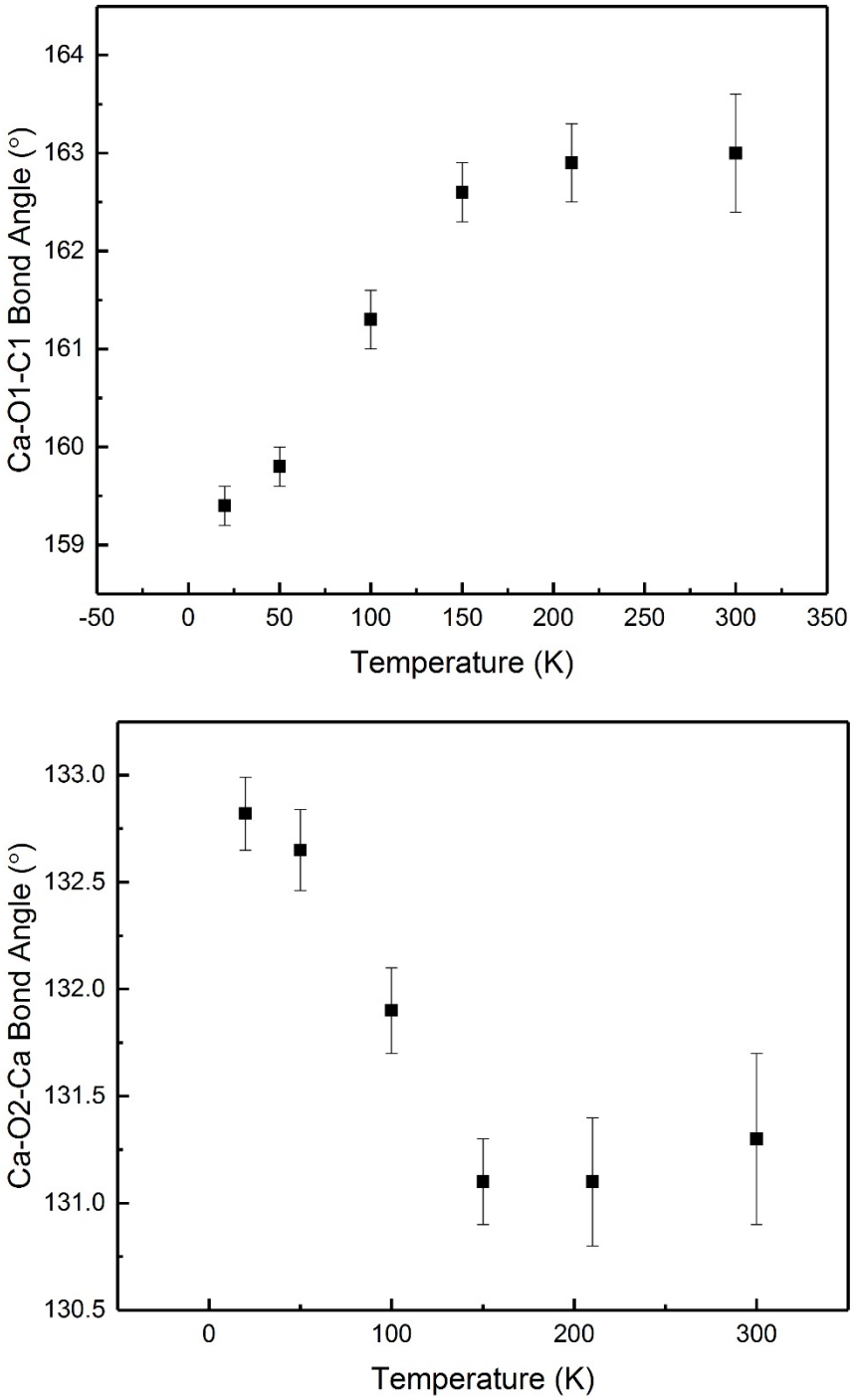

Figure 3.14: (top) Ca-O1-C1 bond angles (°) (bottom) Ca-O2-C1 bond angles (°) of TSCC derived from single crystal neutron diffraction data collected at 20, 50, 100, 150, 210 and 300 K

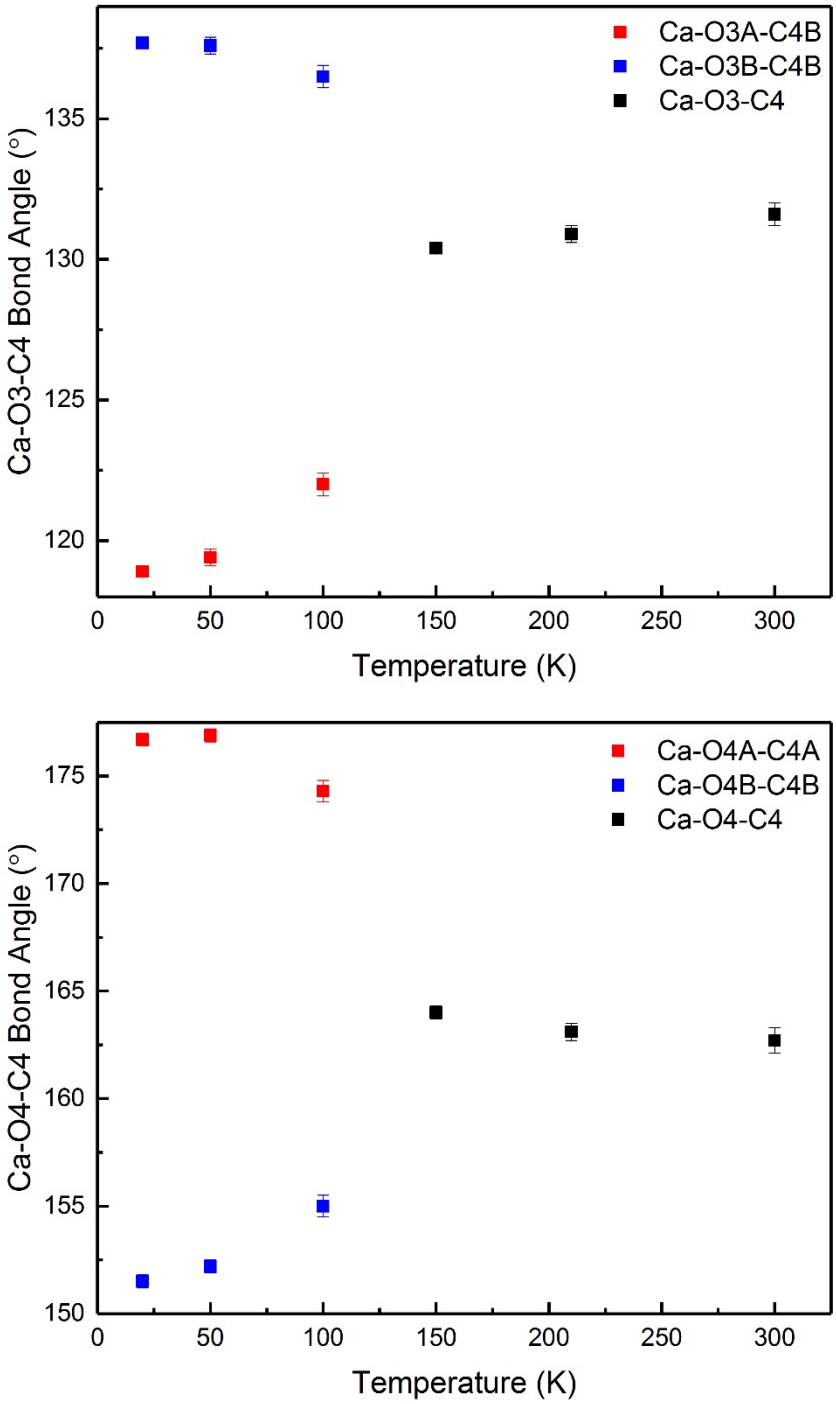

Figure 3.15: (top) Ca-O3-C4 bond angles (˚) and (bottom) Ca-O4-C4 bond angles (˚) of TSCC derived from single crystal neutron diffraction data collected at 20, 50, 100, 150, 210 and 300 K

3.3.2 TSCC 30% Bromine Neutron Diffraction

Since the hydrogen bonding was believed to play an important role in the ferroelectric properties of TSCC, a second sample, TSCC 30 % Br, was also analysed by neutron diffraction. The incorporation of bromine would have significant implications on the hydrogen bonding network of TSCC. The high-quality single crystal of TSCC 30 % Br was again provided by V. H. Schmidt and analysed using the SXD diffractometer and the ISIS neutron and muon source.[26] Several earlier studies have shown the effect of bromine substitution on the transition temperature of TSCC. Consequently, neutron diffraction data were collected at slightly different temperatures from the original pure TSCC sample. At 30% Br the T_C of TSCC is estimated to be ~115 K and the six data sets were collected at 20, 50, 80, 160, 210 and 300 K.[7] The data were analysed in the same manner as the pure TSCC diffraction data, the *Pnma* model was applied to the three highest temperature data sets whereas the $Pn2_1a$ model was utilised for the lower temperatures. For simplicity, the shared chlorine/bromine atomic site were considered to be fully occupied by chlorine atoms. The crystallographic and refinement details for each data set are shown in full in Table 3.9 and the trend in unit cell parameters is shown in Figure 3.16. As seen previously in the pure TSCC sample, each of the unit cell parameters gradually decreases towards lower temperature with no anomalies in their values that would suggest a change in unit cell, symmetry or space group. Interestingly, the known ferroelectric phase transition is not accompanied by a significant change in any of the unit cell parameters, within the limitations of this experiment.

Table 3.9: Crystallographic and refinement details of $(C_3NO_2H_7)_3CaCl_{1.4}Br_{0.6}$TSCC 30% Br derived from single crystal neutron diffraction data collected at 20, 50, 80, 160, 210 and 300 K

Temperature	**20 K**	**50 K**	**80 K**	**160 K**	**210 K**	**300 K**
Formula Weight	404.93	404.93	404.93	404.93	404.93	404.93
Density (g cm^{-3})	1.665	1.664	1.661	1.653	1.648	1.639
Crystal System	Orthorhombic	Orthorhombic	Orthorhombic	Orthorhombic	Orthorhombic	Orthorhombic
Space Group	*Pn*2$_1$*a*	*Pn*2$_1$*a*	*Pn*2$_1$*a*	*Pnma*	*Pnma*	*Pnma*
a/Å	9.087(3)	9.092(3)	9.098(3)	9.110(3)	9.124(3)	9.138(4)
b/Å	17.376(5)	17.381(5)	17.394(6)	17.435(6)	17.450(6)	17.482(6)
c/Å	10.228(3)	10.228(3)	10.231(4)	10.245(3)	10.253(3)	10.275(4)
α (˚)	90	90	90	90	90	90
β (˚)	90	90	90	90	90	90
γ (˚)	90	90	90	90	90	90
V/Å^3	1615.0(9)	1616.4(8)	1619.0(10)	1627.3(9)	1632.4(10)	1641.5(11)
Z	4	4	4	4	4	4
Measured Ref	13755	10391	10916	8385	7236	5443
Refined Parameter	384	384	384	208	208	208
GOOF	1.368	1.362	1.394	1.422	1.410	1.464
Final R Indices (I > 2σ(I))	R1 = 0.0877, wR2 = 0.2221	R1 = 0.0861, wR2 = 0.2199	R1 = 0.0892, wR2 = 0.2244	R1 = 0.0874, wR2 = 0.2250	R1 = 0.0876, wR2 = 0.2217	R1 = 0.0920, wR2 = 0.2307

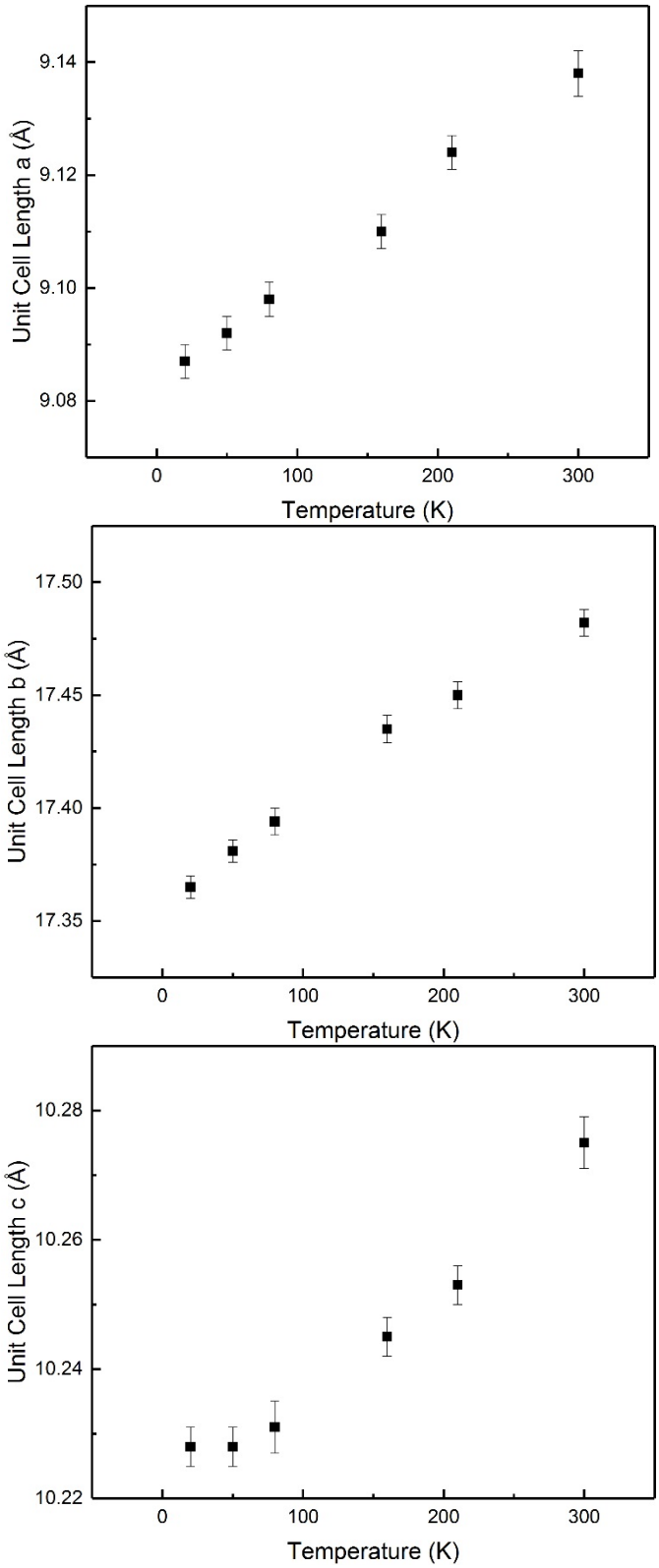

Figure 3.16: Unit cell lengths of TSCC 30 % Br derived from single crystal neutron diffraction data collected at 20, 50, 80, 160, 210 and 300 K

3.3.2.1 Hydrogen Bonding

The hydrogen bonding network was also investigated in detail and compared with the earlier analysis of the pure TSCC structure. The determined hydrogen bond lengths and angles are shown in Table 3.10 and Table 3.11. The general trend remains the same as in the pure TSCC with bond lengths decreasing at low temperatures and bond angles increasing on the whole as shown by their average values in Figure 3.17. When examined in further detail, the hydrogen bond lengths and angles all display gradual trends between 300 and 160 K before the values of the symmetry equivalent bonds begin to diverge as shown in Figure 3.18. As seen previously in the pure TSCC sample, the hydrogen bond lengths do deviate as a result of the known ferroelectric phase transition but only by ~0.03 Å between 300 and 20 K. Perhaps more significant alterations are observed in the hydrogen bond angles, as seen in the pure TSCC sample, the largest deviations are again observed in the N2-H7…Cl1 hydrogen bond angles which change by up to 8° between the ambient and lowest temperature data sets. The deviation in the other hydrogen bond angles is lower at around 2 to 3°. Whilst, the hydrogen bonding is noticeably affected by the phase transition at 127 K, the evolution of both bond angles and lengths do not suggest the presence of any other significant structural changes or phase transition within the 300 – 20 K region.

Table 3.10: Hydrogen bond lengths of TSCC 30 % Br derived from single crystal neutron diffraction collected at 20, 50, 80, 160, 210 and 300 K

Bond	20 K	50 K	80 K	160 K	210 K	300 K
N1-H2A…Cl1A	3.193(3)	3.191(4)	3.194(5)	3.187(2)	3.189(2)	3.193(3)
N1-H2B…Cl1B	3.166(3)	3.169(4)	3.170(5)			
N2A-H7A…CL1A	3.236(3)	3.238(4)	3.234(5)	3.220(2)	3.225(3)	3.231(4)
N2B-H7B…Cl1B	3.201(3)	3.200(4)	3.205(5)			
N2A-H8A…Cl1B	3.222(3)	3.227(4)	3.220(5)	3.212(2)	3.218(3)	3.221(4)
N2B-H8B…Cl1A	3.195(3)	3.190(4)	3.197(5)			

Table 3.11: Hydrogen bond angles of TSCC 30 % Br derived from single crystal neutron diffraction data collected at 20, 50, 80, 160, 210 and 300 K

Bond	20 K	50 K	80 K	160 K	210 K	300 K
N1-H2A…Cl1A	161.9(8)	162.3(9)	161.7(10)	160.1(6)	159.7(6)	159.5(8)
N1-H2B…Cl1B	157.3(8)	158.6(9)	157.9(10)			
N2A-H7A…CL1A	165.3(6)	163.8(7)	163.5(8)	158.1(4)	158.0(5)	157.3(7)
N2B-H7B…Cl1B	152.3(6)	153.4(8)	153.7(8)			
N2A-H8A…Cl1B	163.2(6)	163.5(7)	162.3(8)	160.8(4)	160.6(4)	159.5(6)
N2B-H8B…Cl1A	159.4(6)	159.4(7)	159.5(8)			

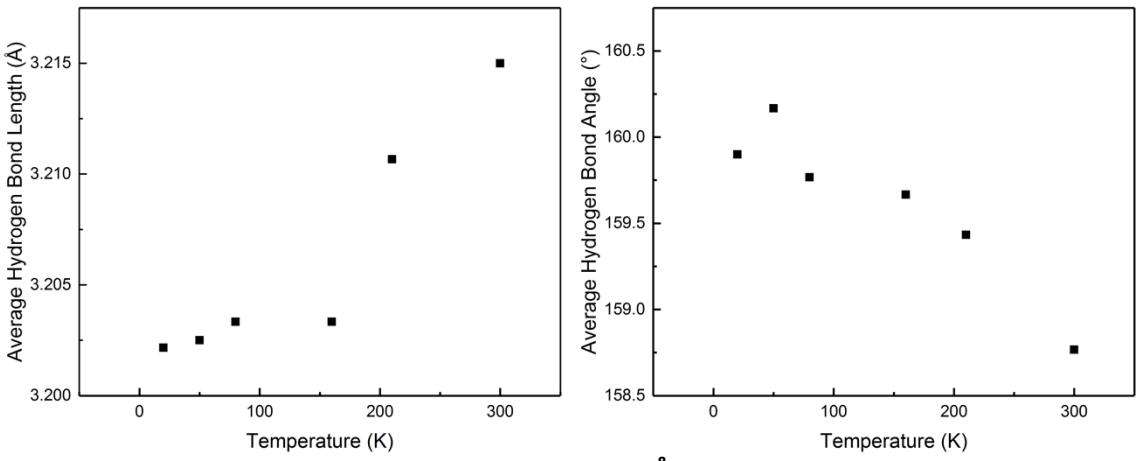

Figure 3.17: (left) average hydrogen bond lengths (Å) and (right) average hydrogen bond angles (°) of TSCC 30 % Br derived from single crystal neutron diffraction data collected at 20, 50, 80, 160, 210 and 300 K

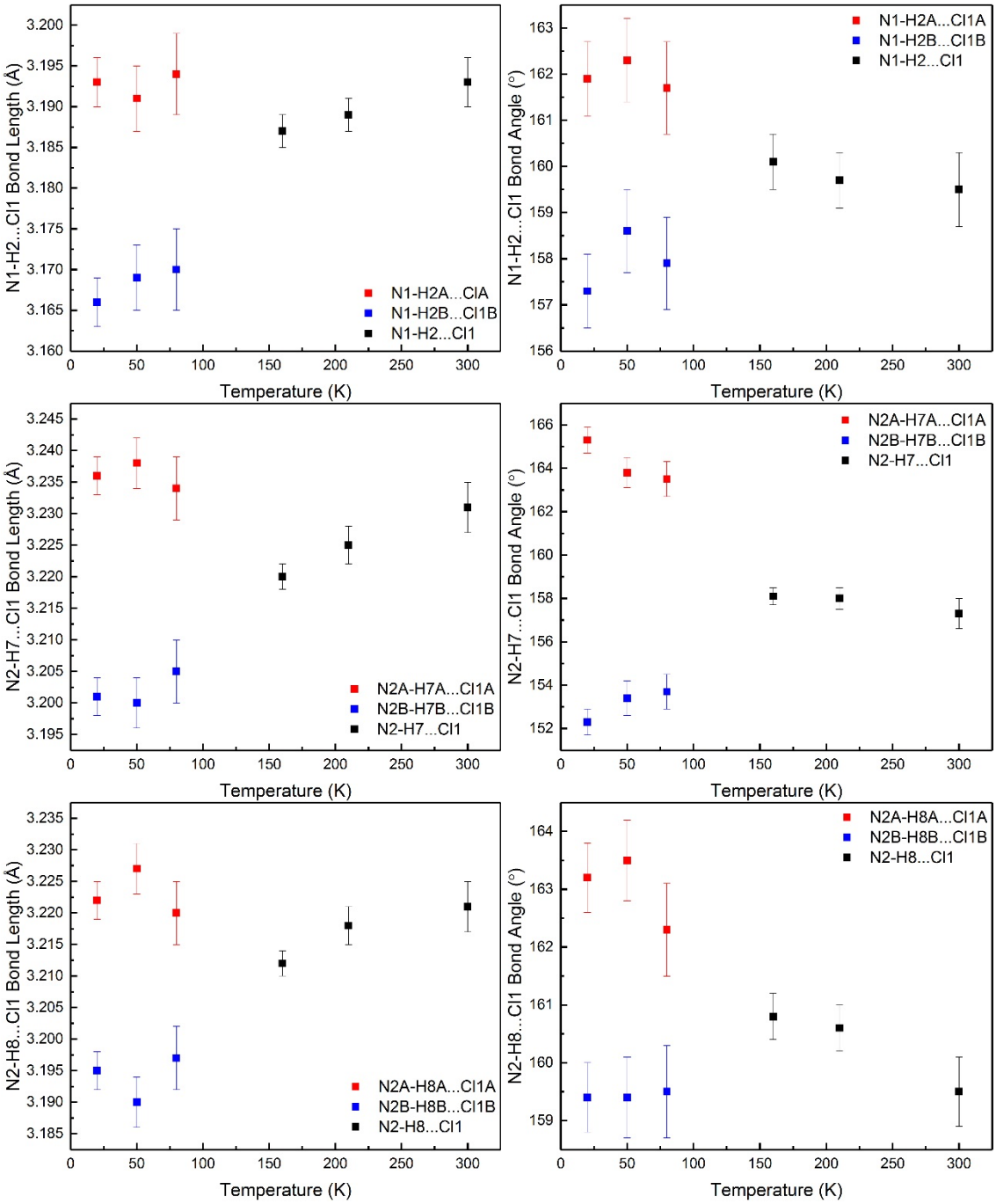

Figure 3.18: Hydrogen bond lengths (Å) and angles (°) of TSCC 30 % Br derived from single crystal X-ray diffraction data collected at 20, 50, 80, 160, 210 and 300 K

3.3.2.2. Methyl Group Disorder

In keeping with the analysis of pure TSCC, the ADPs of the methyl group hydrogens were investigated across the full temperature range to examine potential disorder. The ADPs of the methyl group hydrogen atoms were refined anisotropically, however, only their

equivalent isotropic values are given in Table 3.12. Even in the highest temperature data set at 300 K, there was no unusual behaviour or elongation of the ellipsoids which would suggest rotational disorder. There is a gradual decrease in the ADPs towards lower temperatures as expected given the reduction of thermal motion.

Table 3.12: Equivalent isotropic ADPs ($Å^2 \times 10^3$) of the terminal methyl group hydrogens of TSCC 30 % Br at 20, 50, 100, 150, 210 and 300 K derived from single crystal neutron diffraction data

Atom	20 K	50 K	80 K	160 K	210 K	300 K
H3A	26(2)	27(2)	33(3)	50(2)	59(3)	77(4)
H3B	28(2)	30(3)	37(4)			
H4	27(2)	30(2)	34(2)	49(3)	61(4)	76(6)
H9A	27(2)	32(3)	36(4)	56(3)	67(3)	90(5)
H9B	28(2)	33(3)	42(4)			
H10A	28(2)	32(3)	39(4)	56(3)	66(3)	91(5)
H10B	29(2)	33(3)	38(4)			
H11A	24(2)	27(3)	33(3)	55(2)	66(3)	80(4)
H11B	26(2)	29(3)	34(3)			

3.3.2.3 Calcium Coordination Environment

In addition, the bond lengths and angles surrounding the Ca^{2+} atom were studied in detail. Initially, the six Ca-O bond lengths were determined at each of the six temperatures both to study the mechanism of the known phase transitions and to investigate any potential low temperature phases**.** Their determined values are given in Table 3.13 and plotted in Figure 3.19. Both Ca-O1/O2 bonds do not appear to be significantly affected by temperature or by the ferroelectric phase transition. However, due to the change in symmetry below this point, the Ca-O3 and Ca-O4 bonds split into pairs, Ca-O3A/O3B and Ca-O4A and Ca-O4B. The bond lengths of each are noticeably affected below $T_{C,}$ although, the bond lengths at 20 K are altered by less than 0.2 Å. Again, as seen previously in pure TSCC, there was no evidence of any other significant changes in structure or a phase transition.

Table 3.13: Ca-O bond lengths (Å) of TSCC 30 % Br derived from single crystal neutron diffraction data collected at 20, 50, 80, 160, 210 and 300 K

Bond	20 K	50 K	80 K	160 K	210 K	300 K
Ca-O1	2.309(4)	2.305(4)	2.306(5)	2.302(5)	2.298(6)	2.309(8)
Ca-O2	2.362(4)	2.366(5)	2.365(5)	2.361(5)	2.365(6)	2.364(8)
Ca-O3A	2.392(5)	2.397(6)	2.383(7)	2.371(4)	2.372(4)	2.375(6)
Ca-O3B	2.356(5)	2.352(6)	2.363(7)			
Ca-O4A	2.298(5)	2.296(6)	2.292(7)	2.285(4)	2.286(5)	2.285(6)
Ca-O4B	2.298(5)	2.293(6)	2.296(7)			
BVS	2.22	2.23	2.24	2.27	2.26	2.25

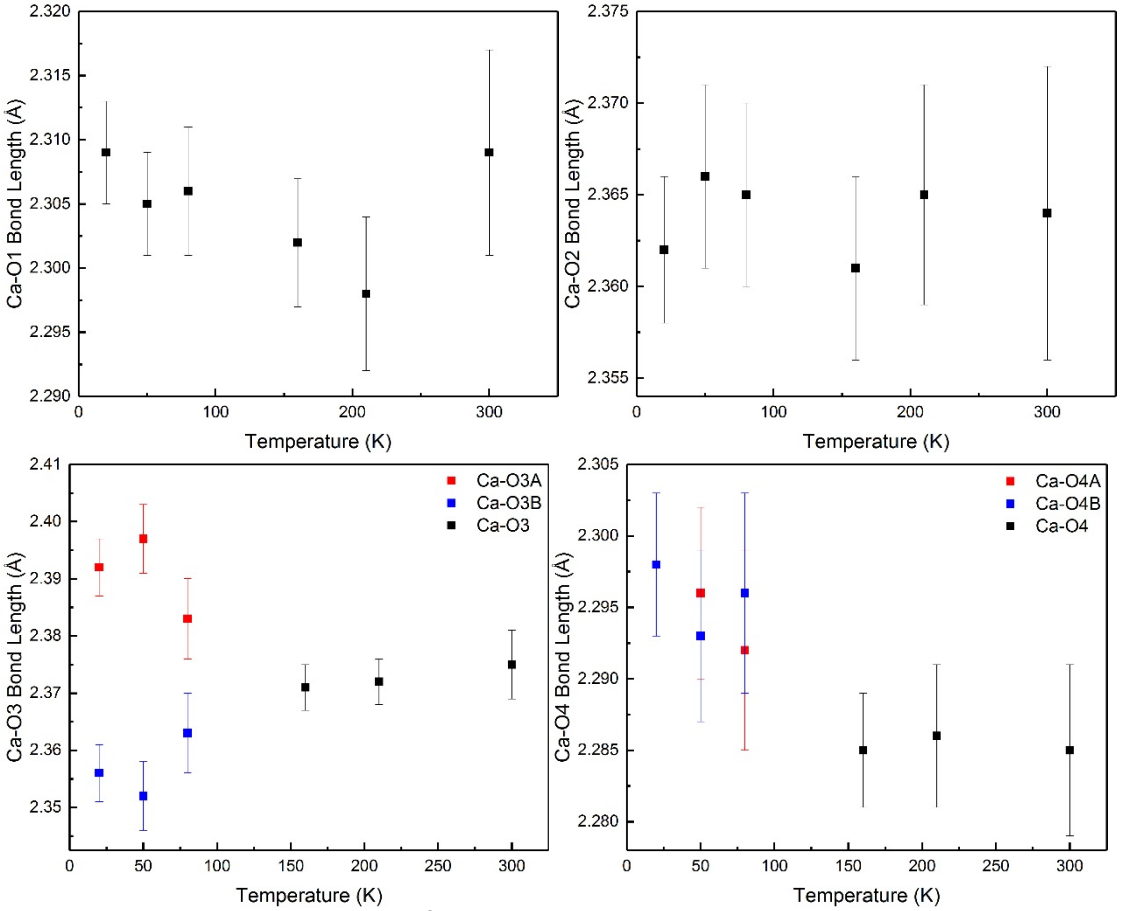

Figure 3.19: Ca-O bond lengths (Å) in TSCC 30 % Br derived from single crystal neutron diffraction data collected at 20, 50, 80, 160, 210 and 300 K

Further analysis of the Ca^{2+} coordination environment was undertaken by determining the surrounding bond angles. As the largest structural changes in pure TSCC were

observed in the Ca-O-C bond angles these were reinvestigated for the bromine doped sample and their values are reported in Table 3.14 and plotted in Figures 3.20 and 3.21. Whilst the Ca-O1-C1 and Ca-O2-C1 are not affected by the change in asymmetric unit, there are distinct changes in bond angle between 80 and 160 K which can be attributed to the known ferroelectric phase transition. Significantly larger deviations are observed in both the Ca-O3-C4 and Ca-O4-C4 bond angles and in both cases, above T_C there are gradual trends in bond angle between 300 and 160 K before symmetry breaking results in a loss of a mirror plane. The previously equivalent angles split into Ca-O3A-C4A and Ca-O3B-C4B with their angles deviating by up to 11 and 13°.

As seen in pure TSCC, the change in Ca-O-C bond angle is the largest structural change occurring at T_C with deviations by as much as 12°. The analysis of the Ca^{2+} coordination environment of the brominated form of TSCC was entirely consistent with earlier analysis of pure TSCC.

Table 3.14: Ca-O-C bond angles (°) in TSCC 30 % Br derived from single crystal neutron diffraction data collected at 20, 50, 80, 160, 210 and 300 K

Bond Angle	20 K	50 K	80 K	160 K	210 K	300 K
Ca-O1-C1	159.8(3)	160.6(3)	161.5(4)	163.3(4)	163.3(5)	163.4(7)
Ca-O2-C1	132.5(2)	132.3(2)	131.8(3)	130.7(3)	130.9(3)	131.4(5)
Ca-O3A-C4A	119.5(2)	119.9(3)	121.7(4)	130.5(2)	130.7(3)	131.2(4)
Ca-O3B-C4B	137.1(3)	136.8(3)	135.8(4)			
Ca-O4A-C4A	176.7(3)	176.5(4)	175.0(5)	163.4(3)	163.3(3)	163.2(5)
Ca-O4B-C4B	152.0(3)	153.2(4)	154.0(4)			

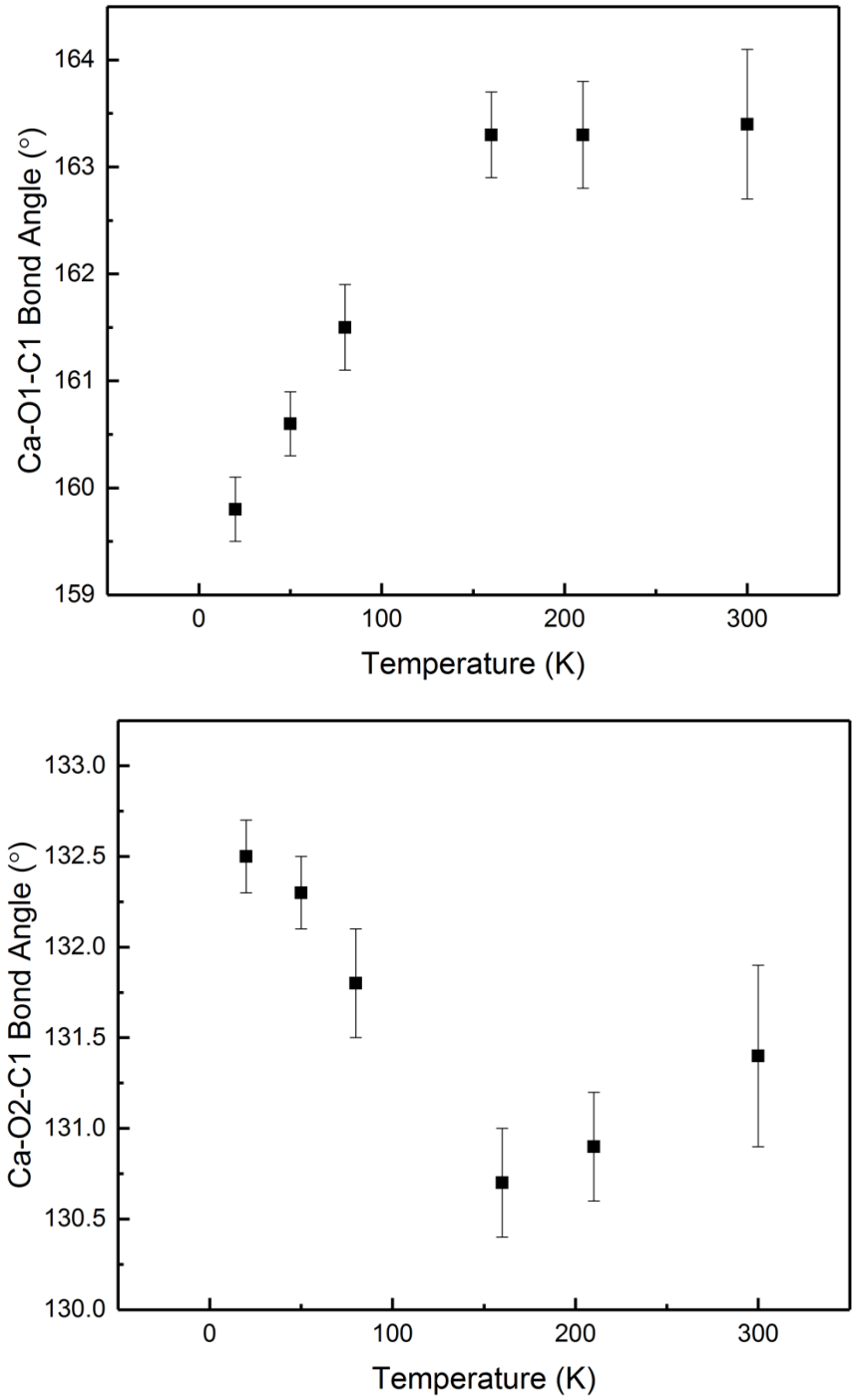

Figure 3.20: (top) Ca-O1-C1 bond angle (°) and (bottom) Ca-O2-C1 bond angle (°) of TSCC 30 % Br derived from single crystal neutron diffraction data collected at 20, 50, 80, 160, 210 and 300 K

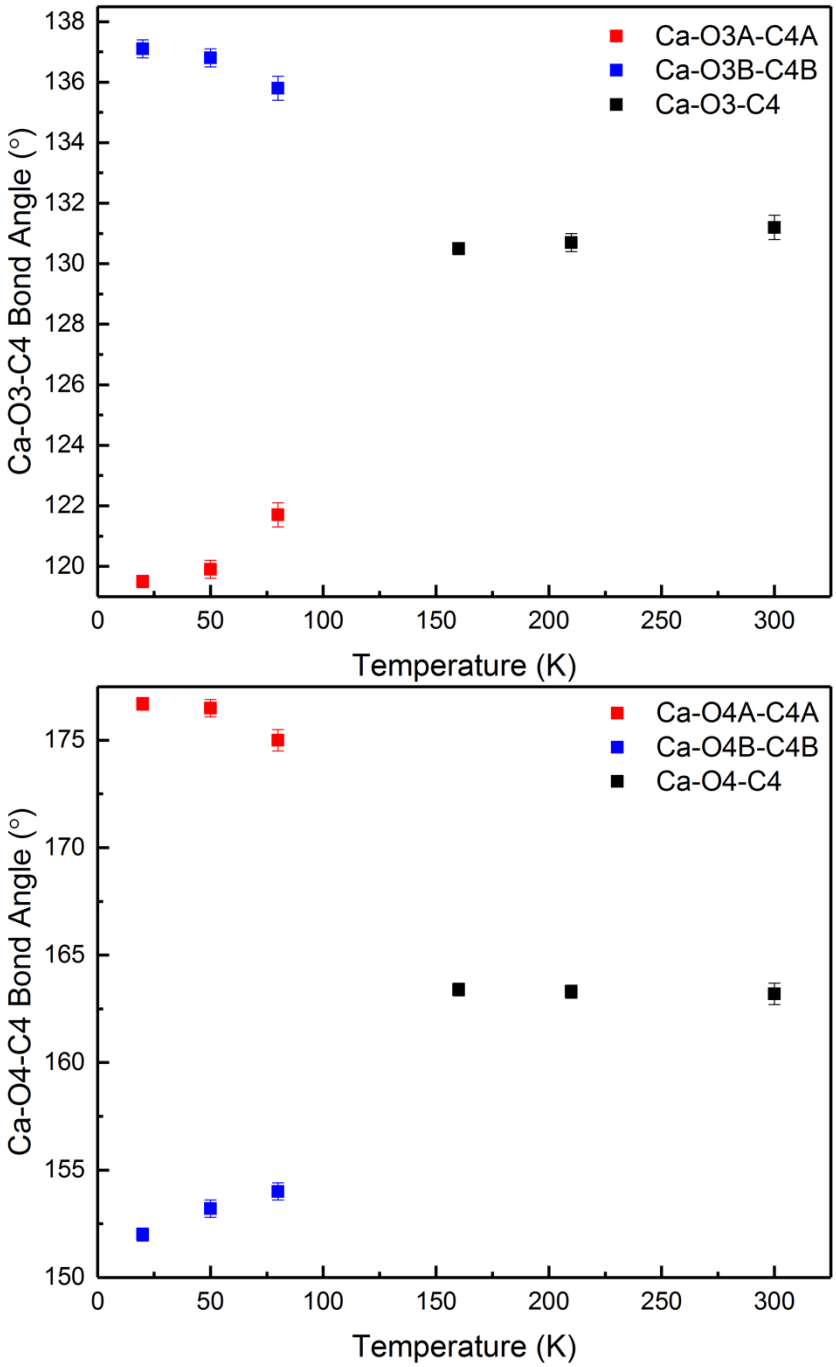

Figure 3.21: (top) Ca-O3-C4 bond angle (°) and (bottom) Ca-O4-C4 bond angle (°) of TSCC 30 % Br derived from single crystal neutron diffraction data collected at 20, 50, 80, 160, 210 and 300 K

3.3.4 TSCC X-ray Diffraction

Since the largest deviations in structure did not concern the very light hydrogen atoms, the structure was reinvestigated using low temperature single crystal X-ray diffraction. Single crystal diffraction data were collected at temperatures of 20, 35, 55, 75 and 100 K by Dr Mike Probert at Newcastle University on a XIPHOS four circle diffractometer using liquid helium to investigate the potential low temperature phase transition. The structure was also studied in detail in the temperature region surrounding the known ferroelectric phase transition with data sets collected at 100, 110, 120, 130 and 150 K by Prof Alex Slawin at the University of St Andrews on a Rigaku FRX instrument. The crystallographic and refinement details of all the single crystal X-ray diffraction data are given in full in Table 3.15 and Table 3.16. The unit cell parameters *a*, *b* and *c* are plotted as a function of temperature as shown in Figure 3.22. Data were collected on two different crystals both provided by V.H. Schmidt using two different instruments, which accounts for the observed discrepancy in the unit cell parameters of the two data sets. As a whole the unit cell parameters contract at low temperature as expected. There are anomalies in all unit cell parameters around 130 K which are attributable to the known ferroelectric phase transition. In keeping with the earlier neutron diffraction studies, there was no evidence of an additional low temperature phase transition in the unit cell parameters or symmetry. Further analysis was required to investigate the structure fully.

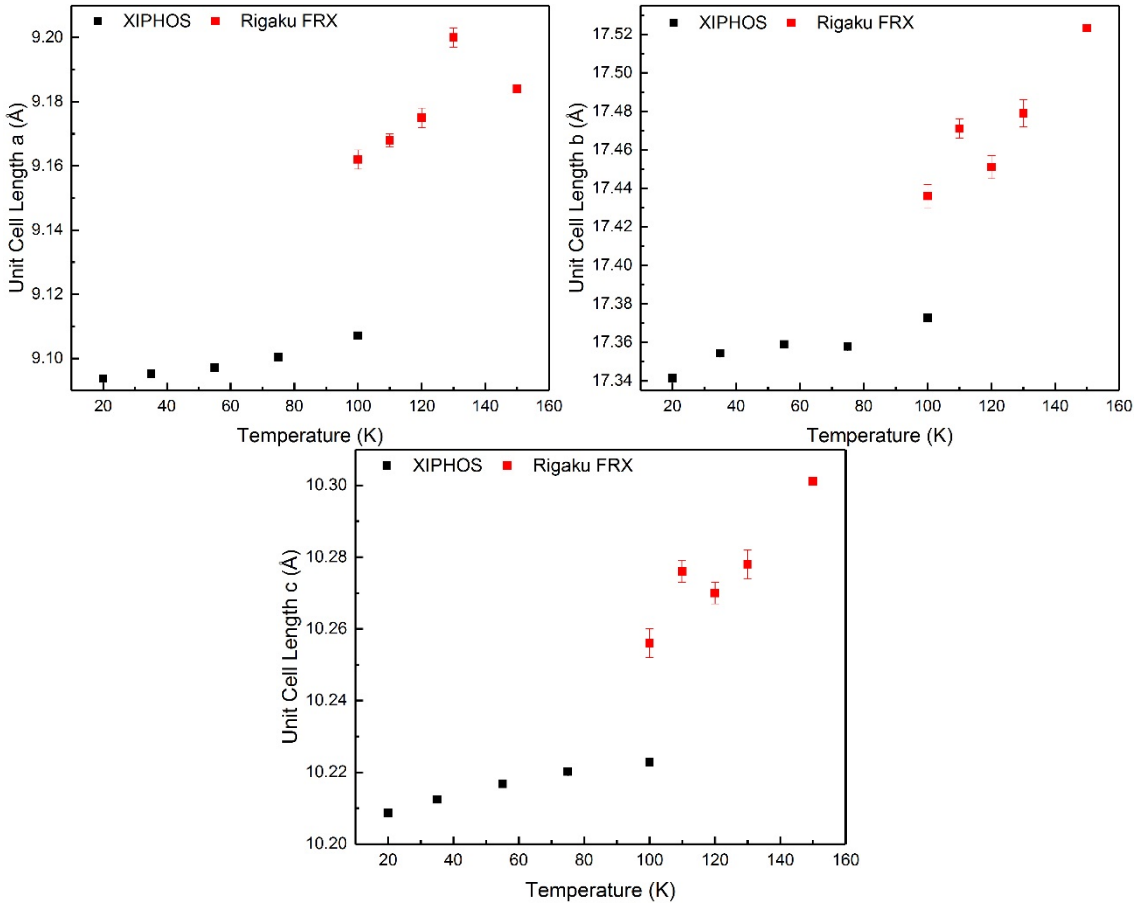

Figure 3.22: Unit cell lengths of TSCC derived from single crystal X-ray diffraction data collected at various temperatures using the XIPHOS four circle diffractometer at Newcastle University and the Rigaku FRX diffractometer at the University of St Andrews

Table 3.15: Crystallographic and refinement details of TSCC derived from single crystal X-ray diffraction data collected by Dr Mike Probert at Newcastle University on a XIPHOS four circle diffractometer collected at 20, 35, 55, 75 and 100 K

Temperature	**25 K**	**35 K**	**55 K**	**75 K**	**100 K**
Formula Weight	378.27	378.27	378.27	378.27	378.27
Density (g cm^{-3})	1.561	1.559	1.557	1.556	1.553
Crystal System	Orthorhombic	Orthorhombic	Orthorhombic	Orthorhombic	Orthorhombic
Space Group	$Pn2_1a$	$Pn2_1a$	$Pn2_1a$	$Pn2_1a$	$Pn2_1a$
a/Å	9.0937(5)	9.0952(5)	9.0971(4)	9.1004(3)	9.1071(3)
b/Å	17.3414(8)	17.3543(9)	17.3590(8)	17.3578(5)	17.3727(5)
c/Å	10.2087(5)	10.2124(5)	10.2168(5)	10.2202(3)	10.2228(3)
α (˚)	90	90	90	90	90
β (˚)	90	90	90	90	90
γ (˚)	90	90	90	90	90
V/$Å^3$	1609.89(14)	1611.93(15)	1613.40(13)	1614.41(9)	1617.40(9)
Z	4	4	4	4	4
Measured Ref	18814	18739	18808	18857	18935
Independent Ref	3347 [R(int) = 0.0350]	3336 [R(int) = 0.0310]	3344 [R(int) = 0.0295]	3349 [R(int) = 0.0285]	3354 {R(int) = 0.0280]
Refined Parameter	193	193	193	193	193
GOOF	1.008	1.050	1.027	1.024	1.060
Final R Indices (I > 2σ(I))	R1 = 0.0282, wR2 = 0.0656	R1 = 0.0270, wR2 = 0.0625	R1 = 0.0270, wR2 = 0.0623	R1 = 0.0277, wR2 = 0.0644	R1 = 0.0277, wR2 = 0.0647

Table 3.16: Crystallographic and refinement details of TSCC derived from single crystal X-ray diffraction data by Prof Alex Slawin on a Rigaku FRX diffractometer at the University of St Andrews collected at 100, 110, 120, 130 and 150

Temperature	**100 K**	**110 K**	**120 K**	**130 K**	**150 K**
Formula Weight	378.27	378.27	378.27	378.27	378.27
Density (g cm^{-3})	1.534	1.526	1.528	1.520	1.516
Crystal System	Orthorhombic	Orthorhombic	Orthorhombic	Orthorhombic	Orthorhombic
Space Group	*Pn*2_1*a*	*Pn*2_1*a*	*Pn*2_1*a*	*Pnma*	*Pnma*
a/Å	9.162(3)	9.168(2)	9.175(3)	9.200(3)	9.1840(5)
b/Å	17.436(6)	17.471(5)	17.451(6)	17.479(7)	17.5233(11)
c/Å	10.256(4)	10.276(3)	10.270(3)	10.278(4)	10.3012(7)
α (˚)	90	90	90	90	90
β (˚)	90	90	90	90	90
γ (˚)	90	90	90	90	90
V/$Å^3$	1638.4(10)	1645.9(8)	1644.4(9)	1652.8(11)	1657.81(18)
Z	4	4	4	4	4
Measured Ref	9010	8566	9902	8281	11143
Independent Ref	2611 [R(int) = 0.0638]	2261 [R(int) = 0.0788]	2965 [R(int) = 0.0499]	1586 [R(int) = 0.1069]	1575 [R(int) = 0.0673]
Refined Parameter	193	193	193	149	149
GOOF	1.035	0.912	0.940	0.907	1.025
Final R Indices (I > 2σ(I))	R1 = 0.0510, wR2 = 0.1328	R1 = 0.0508, wR2 = 0.1182	R1 = 0.0452, wR2 = 0.1223	R1 = 0.0669, wR2 = 0.1567	R1 = 0.0474, wR2 = 0.1188

3.3.4.1 Calcium Coordination Environment

The Ca-O bond lengths were determined across the full temperature range and are shown in Table 3.17 alongside the calculated bond valence sum values. The bond lengths do not have a strong correlation with temperature, although there are distinct changes in their trends at T_C as shown in Figure 3.23. The analysis of Ca-O bond angles is consistent with the earlier neutron diffraction data of both TSCC and TSCC 30 % Br.

Larger deviations are observed in the bond angle surrounding the Ca^{2+} as shown by their values as given in Table 3.18 and combined with neutron diffraction data in Figure 3.24/3.25. The Ca-O1-C1 and Ca-O2-C1 angles are unaffected by the loss of the mirror plane and are still equivalent below the ferroelectric phase transition. There is however a clear change between 120 and 130 K which can be attributed to the known ferroelectric phase transition. In keeping with the neutron diffraction studies, a much larger effect is observed in the Ca-O3-C4 and Ca-O4-C4 bond angles. Changes of up to 11 and 13 % respectively are observed which is consistent with the earlier analysis in this chapter. This change in bond angle and its impact upon the structure of TSCC is shown more clearly in Figure 3.26. The structure has been drawn in the paraelectric *Pnma* phase at 150 K and in the ferroelectric $Pn2_1a$ phase at 20 K. The chloride anions have been omitted for clarity, but the loss of the mirror plane is evident between the two temperatures and the changes in both bond angle and orientation of the sarcosine groups are clearly indicated.

Table 3.17: Ca-O bond lengths (Å) and bond valence sums (valence units) of TSCC derived from single crystal X-ray diffraction data collected at various temperatures using the XIPHOS four circle diffractometer at Newcastle University and the Rigaku FRX diffractometer at the University of St Andrews

Bond	20 K	35 K	55 K	75 K	100 K	100 K	110 K	120 K	130 K	150 K
Ca-O1	2.3050(17)	2.3058(16)	2.3046(16)	2.3037(17)	2.3008(17)	2.311(4)	2.310(4)	2.312(3)	2.314(4)	2.318(3)
Ca-O2	2.3594(18)	2.3606(17)	2.3599(17)	2.3601(18)	2.3607(17)	2.374(4)	2.371(4)	2.373(3)	2.384(4)	2.378(3)
Ca-O3A	2.386(2)	2.387(2)	2.386(2)	2.381(3)	2.375(3)	2.385(7)	2.385(7)	2.386(7)	2.380(3)	2.3870(19)
Ca-O3B	2.355(2)	2.355(2)	2.353(2)	2.356(3)	2.356(3)	2.368(6)	2.364(6)	2.368(7)		
Ca-O4A	2.297(2)	2.297(2)	2.297(2)	2.292(3)	2.289(3)	2.302(6)	2.301(6)	2.302(6)	2.295(3)	2.307(2)
Ca-O4B	2.296(2)	2.296(2)	2.294(2)	2.293(3)	2.293(3)	2.304(7)	2.311(6)	2.303(6)		
BVS	2.25	2.24	2.25	2.25	2.27	2.20	2.20	2.20	2.19	2.16

Table 3.18: Ca-O-C bond angles (˚) of TSCC derived from single crystal X-ray diffraction data collected at various temperatures using the XIPHOS four circle diffractometer at Newcastle University and the Rigaku FRX diffractometer at the University of St Andrews

Bond	20 K	35 K	55 K	75 K	100 K	100 K	110 K	120 K	130 K	150 K
Ca-O1-C1	159.35(17)	159.46(17)	160.08(17)	160.55(17)	161.34(17)	161.4(4)	161.8(3)	162.1(3)	163.1(3)	162.9(3)
Ca-O2-C1	132.55(15)	132.43(14)	132.26(14)	131.96(15)	131.44(14)	132.0(3)	131.4(3)	131.4(3)	130.9(3)	131.0(2)
Ca-O3A-C4A	118.90(19)	119.09(19)	120.1(2)	121.1(2)	123.7(3)	123.7(6)	125.2(5)	126.4(6)	129.8(2)	130.21(18)
Ca-O3B-C4B	137.5(2)	137.3(2)	136.9(2)	136.7(2)	135.4(3)	134.4(6)	134.1(5)	133.7(6)		
Ca-O4A-C4A	176.6(2)	176.4(2)	176.0(2)	175.3(3)	172.4(3)	172.8(7)	173.2(7)	170.1(7)	163.9(3)	163.6(2)
Ca-O4B-C4B	151.3(2)	151.6(2)	152.1(2)	153.3(2)	155.7(3)	154.4(6)	155.6(6)	158.2(6)		

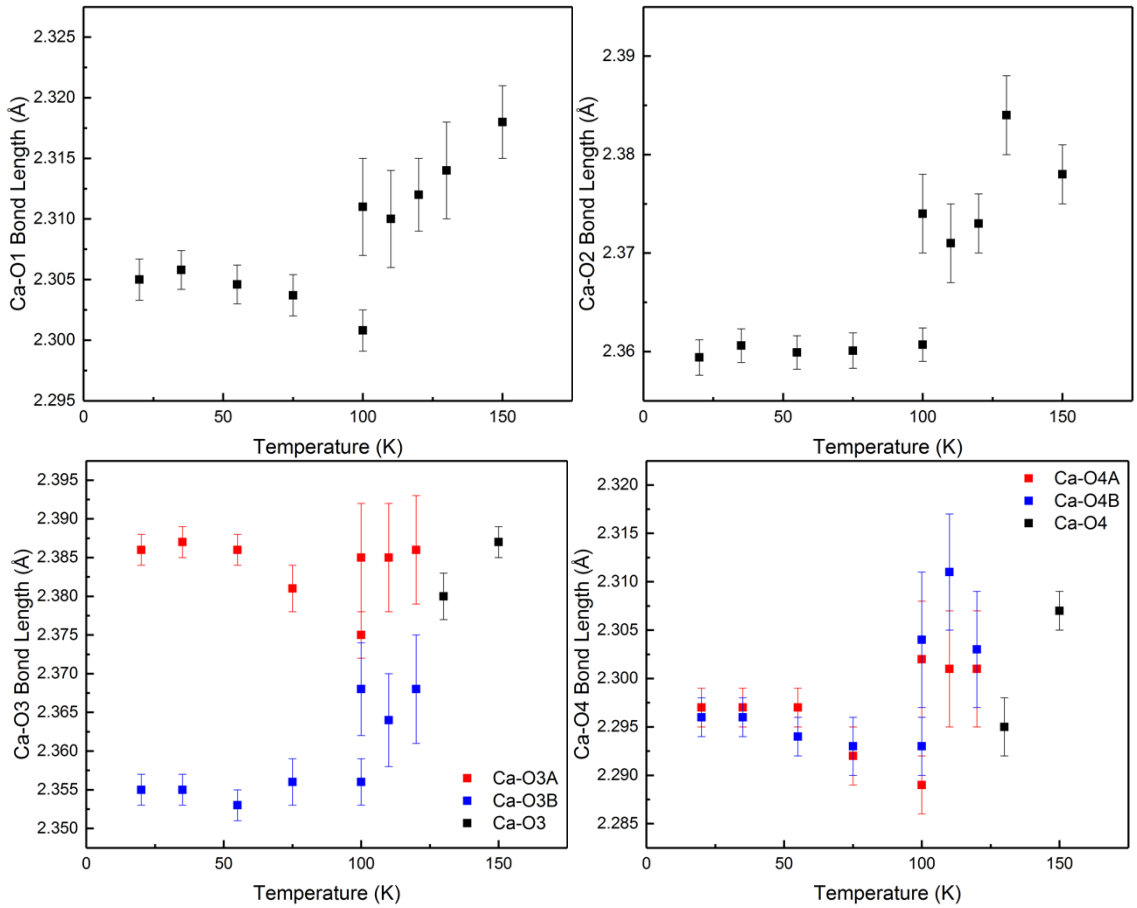

Figure 3.23: Ca-O bond lengths (Å) in TSCC derived from single crystal X-ray diffraction data collected at various temperatures

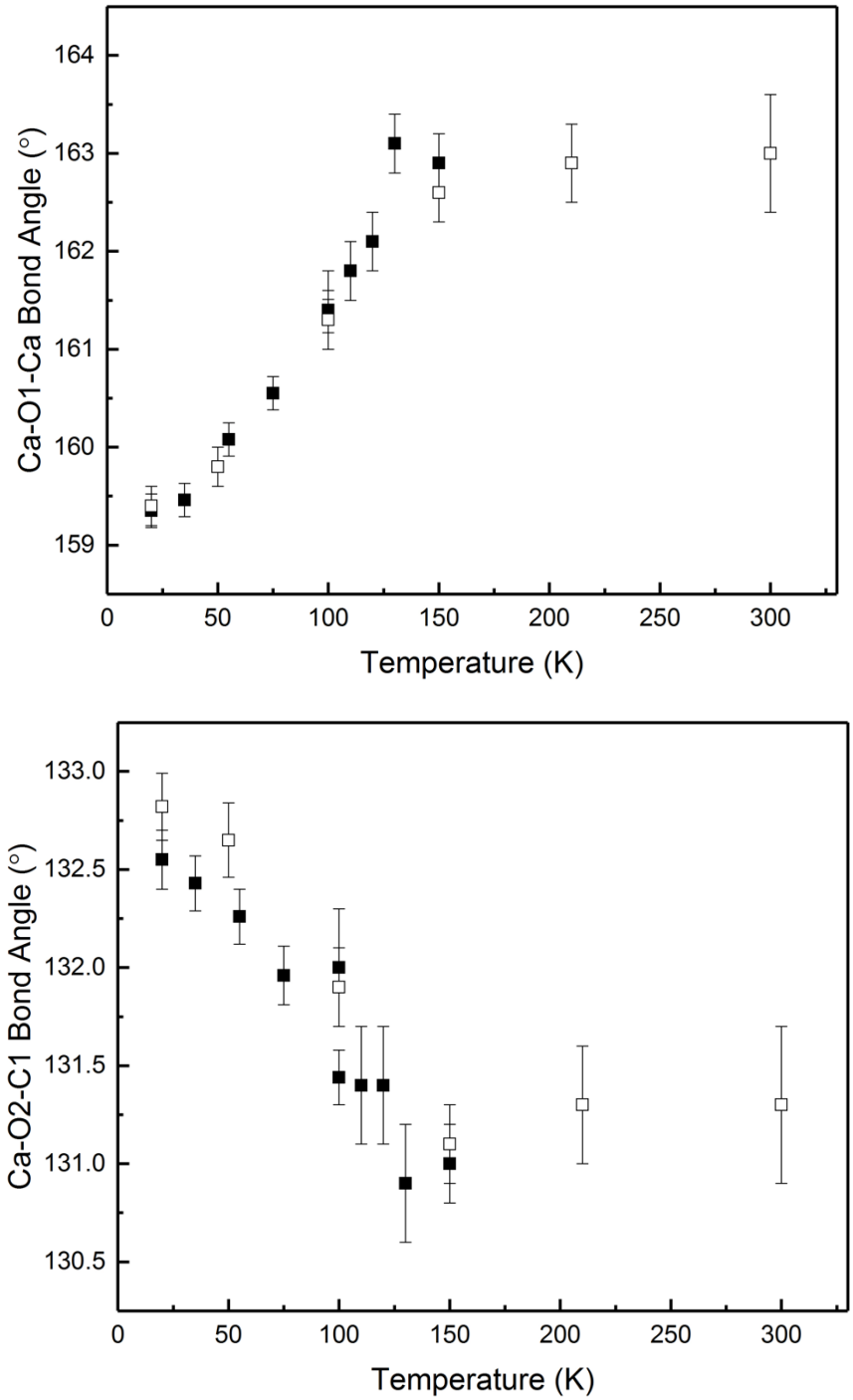

Figure 3.24: (top) Ca-O1-C1 bond angles (°) and (bottom) Ca-O2-C1 bond angles (°) of TSCC derived from single crystal X-ray (solid symbols) and neutron (open symbols) diffraction data collected at various temperatures

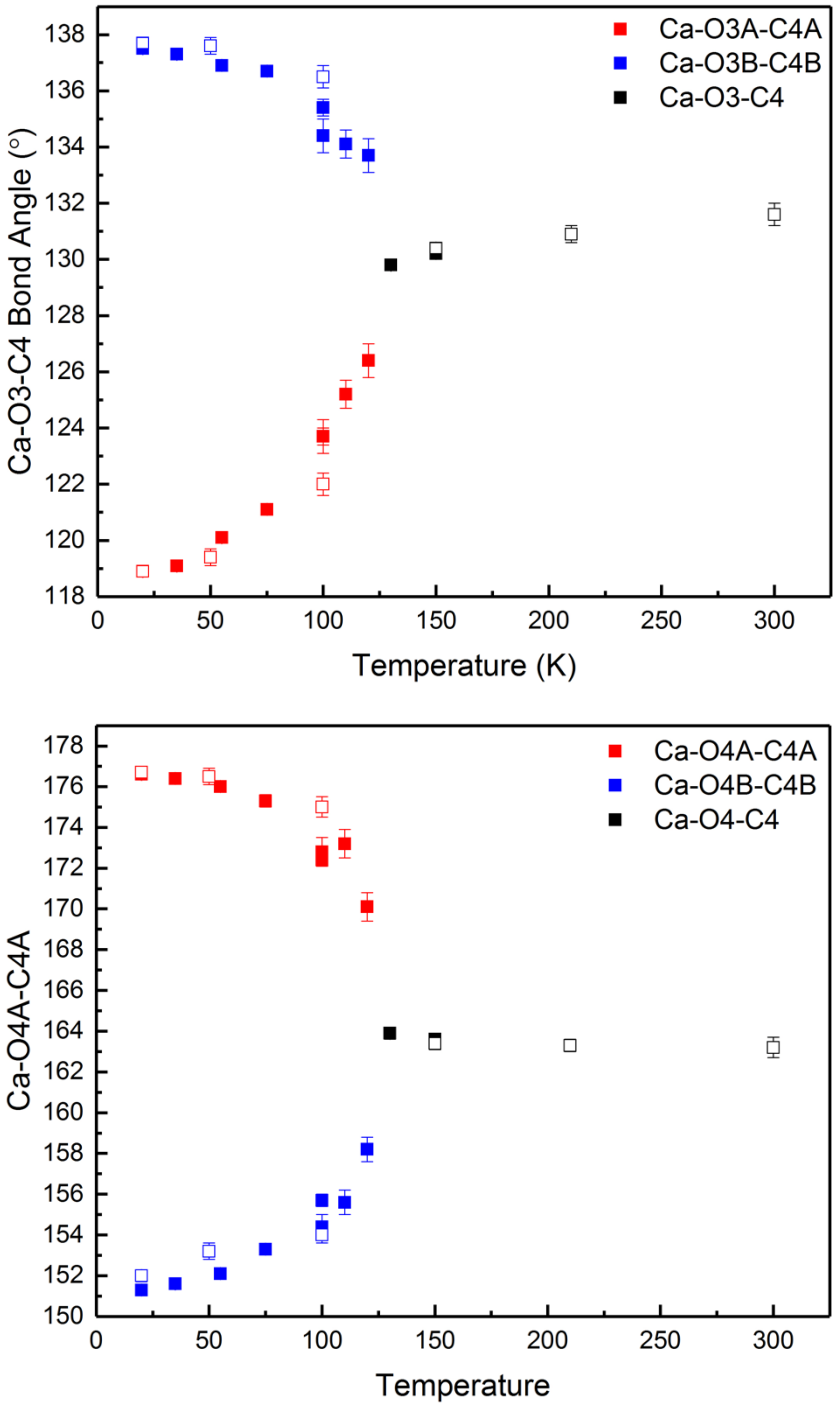

Figure 3.25: (top) Ca-O3-C4 bond angles (°) and (bottom) Ca-O4-C4 bond angles (°) of TSCC derived from single crystal X-ray (solid symbols) and neutron (open symbols) diffraction data collected at various temperatures

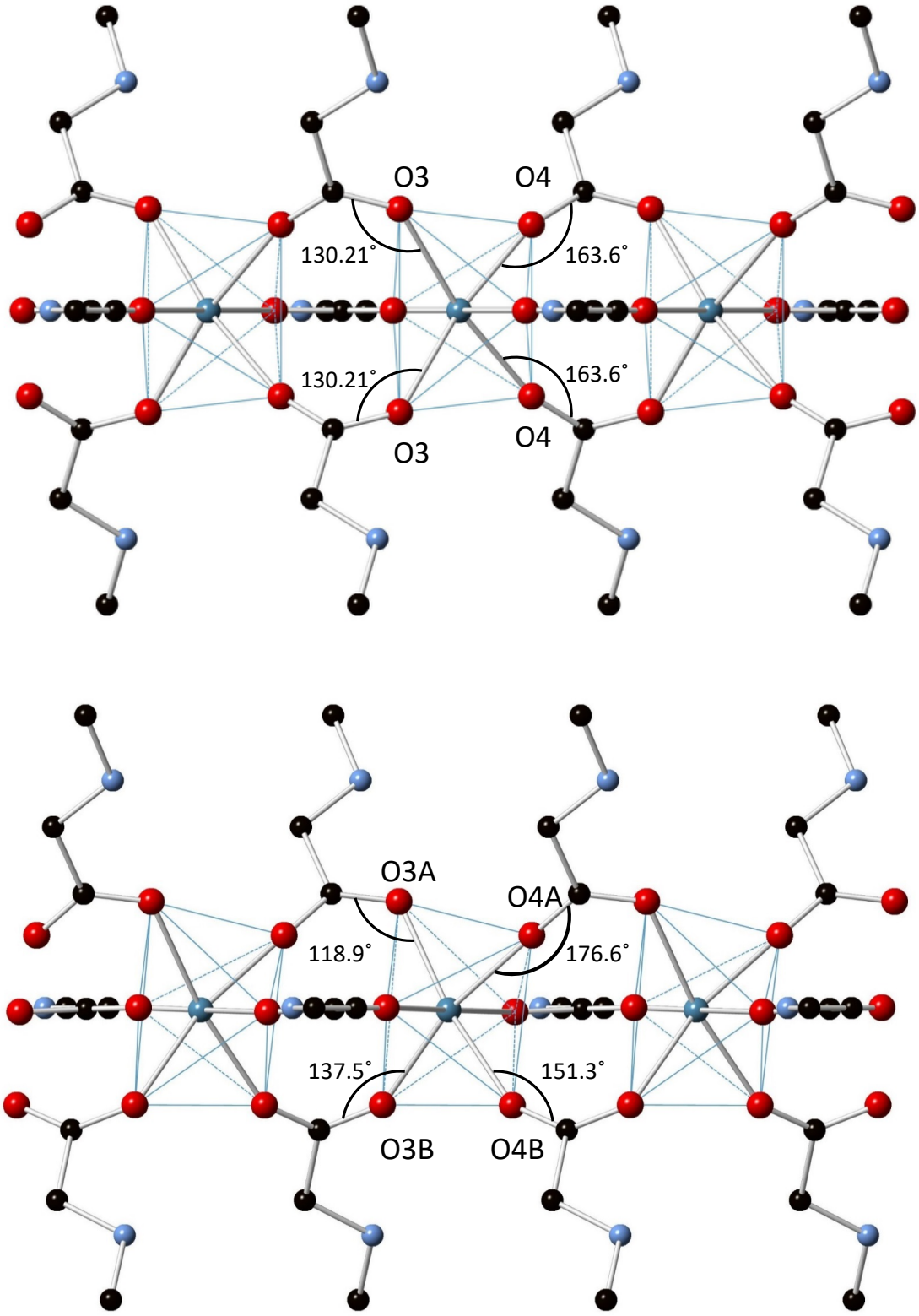

Figure 3.26: (top) structure of TSCC at 150 K in the paraelectric phase and (bottom) at 20 K in the ferroelectric phase derived from single crystal X-ray diffraction data

3.3.4.2 Methyl Group Disorder

The ADPs of the sarcosine molecules were monitored across a range of temperatures to investigate potential ordering, and their values are shown in Table 3.19. The data are consistent with the earlier work by Mishima *et al.* who found that the ADP of the terminal methyl group was unusually high in comparison with the remaining sarcosine atoms.[5] The unusually high ADP could be indicative of disorder in the structure of TSCC which could be resolved at lower temperatures. The determined ADPs of the methyl carbon (C6 in Figure 3.7) remain relatively large, even at extremely low temperatures of 20 K indicative of dynamic disorder rather than static disorder.

Table 3.19: Equivalent isotropic ADPs ($Å^2 \times 10^3$) of the sarcosine molecules of TSCC derived from single crystal X-ray diffraction data collected at various temperatures

Atom	20 K	35 K	55 K	75 K	100 K	100 K	110 K	120 K	130 K	150 K
O1	11(1)	12(1)	15(1)	18(1)	21(1)	25(1)	28(1)	26(1)	33(1)	31(1)
O2	10(1)	11(1)	13(1)	14(1)	16(1)	22(1)	24(1)	21(1)	31(1)	27(1)
C1	8(1)	9(1)	11(1)	12(1)	13(1)	16(1)	20(1)	16(1)	25(1)	20(1)
C2	8(1)	9(1)	10(1)	12(1)	13(1)	19(1)	19(1)	19(1)	26(1)	22(1)
N1	8(1)	9(1)	10(1)	11(1)	13(1)	19(1)	21(1)	17(1)	26(1)	20(1)
C3	12(1)	13(1)	15(1)	17(1)	21(1)	27(2)	26(1)	27(1)	37(2)	31(1)
O3A	11(1)	12(1)	15(1)	17(1)	22(1)	28(2)	30(2)	26(2)	34(1)	29(1)
O4A	11(1)	13(1)	16(1)	20(1)	26(1)	30(2)	33(2)	32(2)	42(1)	37(1)
C4A	9(1)	10(1)	12(1)	13(1)	15(1)	19(2)	20(2)	20(2)	28(1)	21(1)
C5A	9(1)	10(1)	11(1)	13(1)	15(1)	18(2)	22(2)	19(2)	26(1)	20(1)
N2A	8(1)	9(1)	11(1)	12(1)	16(1)	18(2)	20(2)	16(2)	27(1)	21(1)
C6A	11(1)	13(1)	15(1)	18(1)	23(1)	28(2)	33(2)	32(2)	41(1)	35(1)
O3B	10(1)	10(1)	12(1)	14(1)	18(1)	22(1)	24(1)	24(2)		
O4B	11(1)	12(1)	14(1)	17(1)	23(1)	28(2)	29(2)	28(2)		
C4B	10(1)	10(1)	11(1)	12(1)	14(1)	19(2)	20(2)	16(2)		
C5B	7(1)	8(1)	9(1)	10(1)	11(1)	18(2)	19(2)	16(2)		
N2B	8(1)	9(1)	10(1)	11(1)	12(1)	18(2)	22(2)	18(2)		
C6B	11(1)	13(1)	15(1)	18(1)	23(1)	30(2)	31(2)	29(2)		

3.3.4.3 Polar Axis Displacement

Since ferroelectric properties must arise from displacements along the polar *b* axis, the net displacement of the non-hydrogen atoms relative to the room temperature paraelectric phase was calculated with a fixed origin at the Ca^{2+} centre using ISODISTORT.[29] The net displacement of the Cl^- are shown in Table 3.20 but are limited to displacements of less than 0.02 Å and were therefore discounted from the ferroelectric properties.

Table 3.20: Net displacement (i.e. changes in y-coordinate, Δy) of the Cl^- ions in TSCC relative to the room temperature paraelectric phase derived from single crystal X-ray diffraction data at various temperatures

Atom	20 K	35 K	55 K	75 K	100 K	100 K	110 K	120 K
Cl1A	−0.00161	−0.00155	−0.00142	−0.0013	−0.00098	−0.00096	−0.00116	−0.00086
Cl1B	−0.00089	−0.00087	−0.00082	−0.00078	−0.00058	−0.00064	−0.00084	−0.00044

More significant displacements are observed in the net displacements of the sarcosine molecules, the displacements of each atom within each sarcosine were summed for each of the three inequivalent sarcosine molecules. The net displacements were calculated for each temperature below the known ferroelectric phase transition and are shown in Table 3.21. The effect of temperature on these y axis displacements is shown in Figure 3.27. The displacements of each individual atom are shown in Appendix A.

Table 3.21: Net displacements (Δy) of the three inequivalent sarcosine molecules of TSCC and the calculated resultant displacement derived from X-ray diffraction data collected at various temperatures

Molecule	20 K	35 K	55 K	75 K	100 K	100 K	110 K	120 K
Sarcosine 1	0.0083	0.00843	0.00808	0.00721	0.0055	0.003	0.0054	0.004
Sarcosine 2A	0.00062	0.00051	0.00082	0.00064	0.00061	0.00048	0.00158	0.00286
Sarcosine 2B	−0.00847	−0.00784	−0.00732	−0.00737	−0.00669	−0.00808	−0.00448	−0.00558
Resultant	0.0083	0.00843	0.00808	0.00721	0.0055	0.003	0.0054	0.004

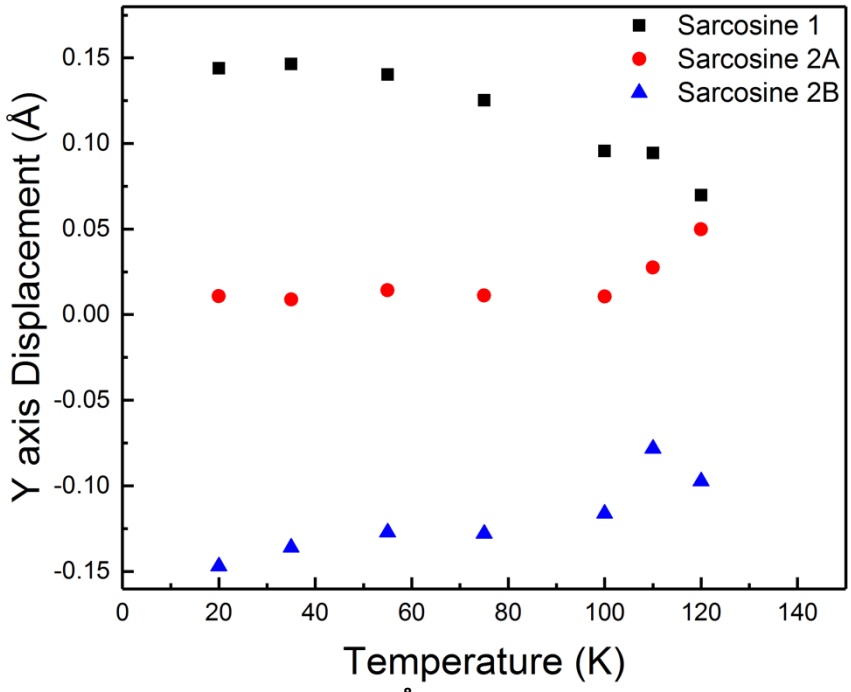

Figure 3.27: Calculated y axis displacement (Å) of the three inequivalent sarcosine molecules of TSCC as a function of temperature

The results reveal an asymmetric displacement of the sarcosine molecules along the polar *b* axis. The sarcosine molecules are displaced in a "two up one down" arrangement which results in a small net displacement. Interestingly, sarcosine 1 and 2B are displaced in opposite directions but with almost equal magnitude. Conversely, sarcosine 2A exhibits a significantly smaller displacement but contributes to the net displacement of the sarcosine molecules. This is perhaps unexpected given the underlying symmetry of the compound. The displacement of each of the sarcosine molecules relative to the asymmetric unit of TSCC is shown in Figure 3.28, and relative to the crystal structure of TSCC in Figure 3.29.

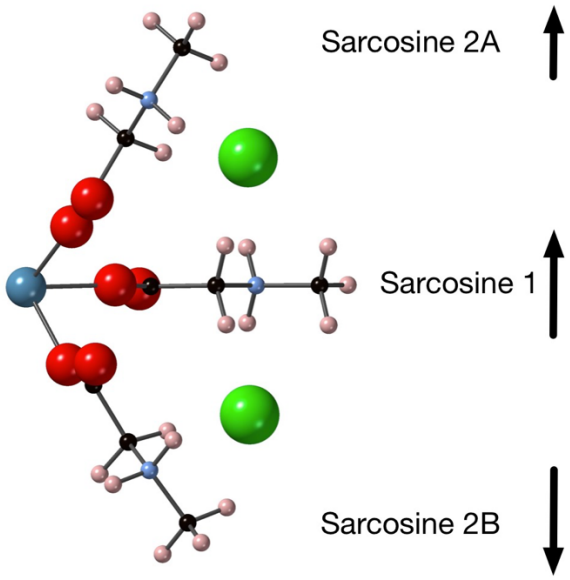

Figure 3.28: Asymmetric unit of TSCC derived from single crystal X-ray diffraction data collected at 293 K with direction of sarcosine displacements shown by arrows

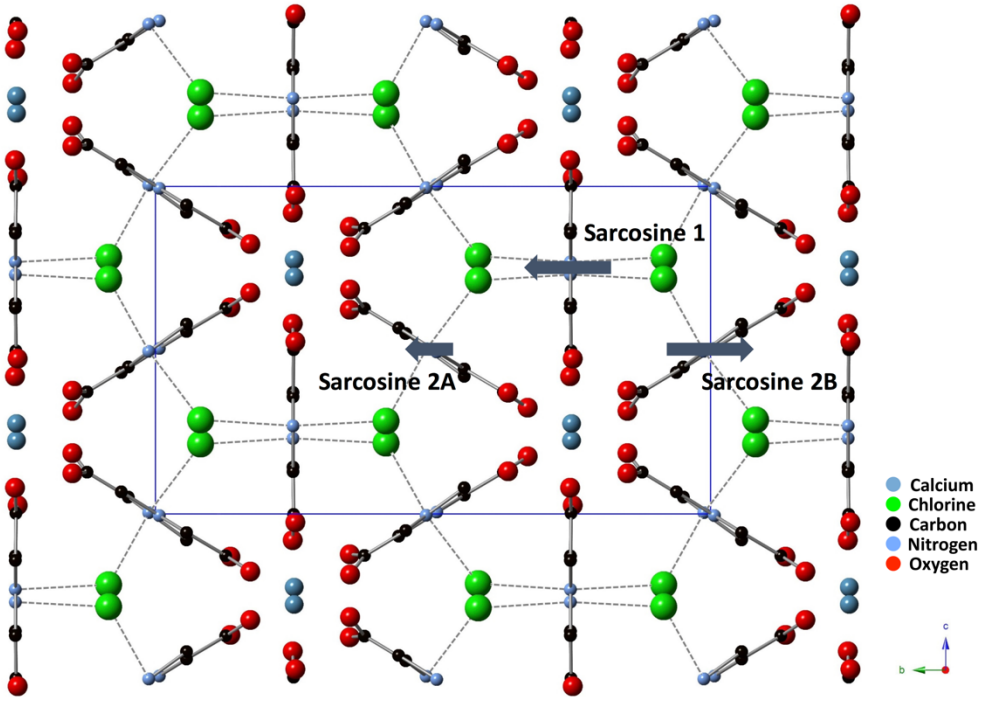

Figure 3.29: Crystal structure of TSCC derived from single crystal X-ray diffraction data collected at 293 K with displacements of sarcosine molecules shown by arrows

The evolution of the displacements with temperature similarly provide no evidence of a further change in either crystal structure or symmetry. It should be noted that the calculated values represent displacements only and not polarisations since charge distribution of the sarcosine molecules was not considered. Nevertheless, the

antiparallel arrangements of these displacements is consistent with ferrielectricity. In addition to the calculated displacements, further evidence of ferrielectricity was found in the Raman and hysteresis data collected by Prof. J. F. Scott and Dr F. D. Morrison.[30] The polarisation versus field data collected for both TSCC and a brominated sample of TSCC are shown in Figure 3.30. Both data sets display a large bias in the hysteresis loop which is indicative of ferrielectricity.

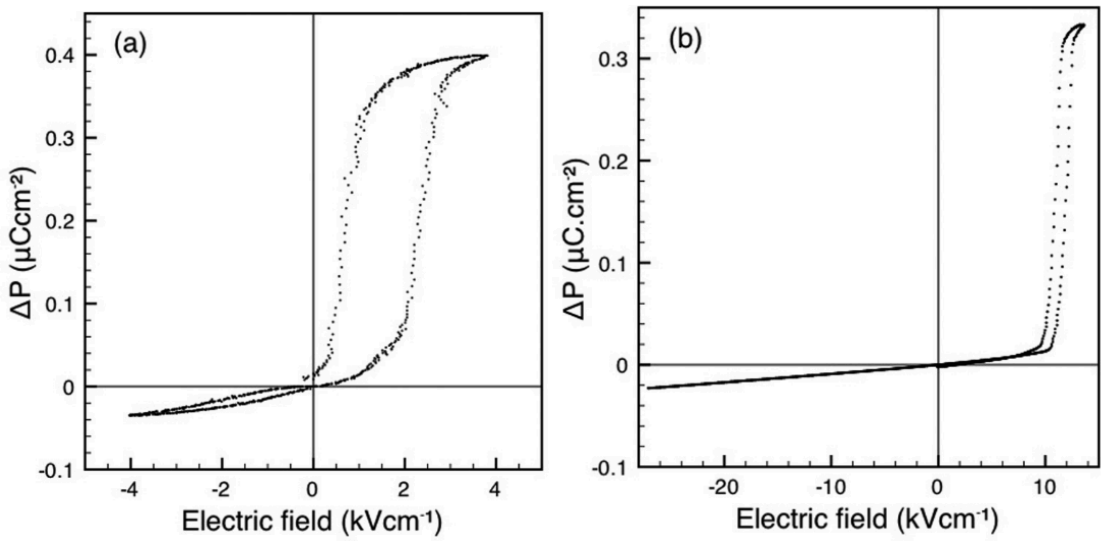

Figure 3.30: Hysteresis data collected at 50 K and 100 Hz (left) pure TSCC (right) TSCC 30 % Br collected by F.D. Morrison [30]

3.4 Conclusions

The structure of TSCC has been studied in detail using both single crystal X-ray and neutron diffraction techniques. The previously reported low temperature phase transitions were investigated by determining the structure at temperatures between 20 and 300 K. The nature of the ferroelectric transition itself was probed by several data sets in the vicinity of T_C.

Both the X-ray and neutron diffraction data were refined to the two known structural models, the paraelectric *Pnma* model and the ferroelectric $Pn2_1a$ model. In both cases, the evolution of the unit cell parameters with temperature do not suggest the presence of any additional phase transitions although there are slight anomalies surrounding the known phase transition. The data also do not provide evidence of a change in unit cell or symmetry and the existing structural models remained valid across all temperatures. Each of the bond lengths and angles were also investigated in detail to analyse more subtle changes in the structure. Aside from the known phase transition which occurs around 130 K there were no anomalies in the bond lengths and angles which would suggest the presence of additional phase transition. Earlier work by Mishima *et al.* had suggested possible rotational disorder of the terminal methyl groups.[5] This was investigated by determining ADPs of both the hydrogen from neutron diffraction and the carbon atoms from X-ray diffraction data. However, the ADPs of the hydrogen atoms do not display any unusual behaviour even at room temperature and the ADPs of the terminal carbon atoms remain relatively large throughout, which is likely due to dynamic rather than static, disorder.

Neutron diffraction data were used to investigate the hydrogen bonding and its role in the ferroelectric phase transition of TSCC and TSCC 30 % Br. In both cases, the average hydrogen bond lengths decrease gradually towards low temperature whereas the hydrogen bond angle increases gradually as temperature is decreased. The individual bond lengths of each symmetry equivalent hydrogen bond diverge slightly below the ferroelectric phase transition, although the change in bond length is relatively small at

around 1 %. A larger effect is seen in the hydrogen bond angles, in particular the N2-H7…Cl1 bond angle which deviates by ~8°. The same result is observed in the brominated sample.

The calcium coordination environment of TSCC was also investigated in detail using the X-ray diffraction data. The Ca-O bond lengths do not reveal a strong correlation with temperature whilst the Ca-O3A/O3B are noticeably affected by the ferroelectric phase transition. At this point the bond lengths begin to diverge. A far larger effect is observed in the bond angles surrounding the Ca^{2+} the Ca-O3A/O3B-C4A/C4B and Ca-O4A/B-C4A/B which are altered by up to 12° which represents the largest change observed in the structure during the ferroelectric phase transition.

Perhaps more excitingly, the y axis displacement of the sarcosine molecules has provided new evidence of potential ferrielectricity. Whilst, the displacements do not necessarily correspond directly to the change in polarisation of the compound, since charge distribution was not considered, the structure is consistent with that associated with ferrielectricity. This new evidence is also supported by hysteresis measurements collected by J. F. Scott and F. D. Morrison which contained a significant bias in the hysteresis loop, indicative of ferrielectric properties. An interesting feature of the displacements is that it is sarcosine 1 and 2B which are displaced by almost equal but opposite amounts not sarcosine 2A and 2B which are equivalent in the high symmetry phase. Instead, sarcosine 2A is displaced in the same direction as sarcosine 1 and contributes to a net displacement.

The combined X-ray and neutron structural studies revealed no evidence of the additional phase transitions at 42, 64 and 185 K despite the strong existing evidence in earlier physical measurements. The $Pn2_1a$ structural model remained valid down to temperatures as low as 20 K with no evidence for a change in structure other than those associated with the known ferroelectric phase transition. If due to long range order, the previously reported phase transitions would be the result of very small displacements,

however, local structural or dynamic effects not observable by diffraction could be playing a significant role.

However, the most significant structural changes associated with the ferroelectric phase transition have been elucidated and were found to occur in the Ca-O-C bond angles, which alter by up to 18° between ambient and 20 K. In depth analysis of sarcosine displacement along the polar *b* axis has uncovered new evidence of ferrielectric properties in TSCC. This work has been published as reference 30.

3.5 References

1 Y. Makita, *J. Phys. Soc. Japan*, 1965, **20**, 2074–2080.

2 T. Ashida, S. Bando and M. Kakudo, *Acta Crystallogr. Sect. B Struct. Crystallogr. Cryst. Chem.*, 1972, **28**, 1560–1565.

3 R. Kripal, M. P. Yadav and H. Govind, *Mol. Phys.*, 2009, **107**, 1555–1562.

4 A. Sawada, Y. Makita and Y. Takagi, *J. Phys. Soc. Japan*, 1977, **42**, 1918–1923.

5 N. Mishima, K. Itoh and E. Nakamura, *Acta Crystallogr. Sect. B Struct. Crystallogr. Cryst. Chem.*, 1984, **C40**, 1824–1827.

6 M. Fujimoto, S. Jerzak and W. Windsch, *Phys. Rev. B*, 1986, **34**, 1668–1676.

7 S. P. P. Jones, D. M. Evans, M. A. Carpenter, S. A. T. Redfern, J. F. Scott, U. Straube and V. H. Schmidt, *Phys. Rev. B*, 2011, **83**, 094102.

8 S. Fujimoto, N. Yasuda, K. Takagi, P. S. Narayanan and H. L. Bhat, *J. Phys. D Appl. Phys*, 1980, **13**, L217-219.

9 G. V Kozlov, A. A. Volkov, J. F. Scott, G. E. Feldkamp and J. Petzelt, *Phys. Rev. B*, 1983, **28**, 255–261.

10 W. Windsch, H. Braeter, U. Gutteck, B. Malige and B. Milsch, *Solid State Commun.*, 1982, **42**, 839–842.

11 S. Fujimoto, N. Yasuda and H. Kashiki, *J. Phys. D. Appl. Phys.*, 1984, **17**, 1019–1028.

12 S. Fujimoto, N. Yasuda and H. Kashiki, *J. Phys. D. Appl. Phys.*, 1982, **15**, 487–495.

13 M. Gergs and D. Michel, *J. Phys. D. Appl. Phys.*, 1986, **19**, 2431–2442.

14 S. Fujimoto, N. Yasuda and S. Funado, *J. Phys. D. Appl. Phys.*, 1982, **15**, 1469–1475.

15 R. Blinc, M. Jamesk-Vilfan, G. Lahajnar and G. Hajdukovic, *J. Chem. Phys.*, 1970, **52**, 6407–6411.

16 J. C. Lashley, J. H. D. Munns, M. Echizen, M. N. Ali, S. E. Rowley and J. F. Scott, *Adv.*

Mater., 2014, **26**, 3860–3866.

17 K. Lee, M. Lee, K. S. Lee and A. R. Lim, *J. Phys. Chem. Solids*, 2005, **66**, 1739–1743.

18 H. Haga, A. Onodera, H. Yamashita and Y. Shiozaki, *J. Phys. Soc. Japan*, 1993, **62**, 1857–1859.

19 R. Mackeviciute, M. Ivanov, J. Banys, N. Novak, Z. Kutnjak, M. Wencka and J. F. Scott, *J. Phys. Condens. Matter*, 2013, **25**, 212201.

20 A. V. H. Schmidt and V. H. Schmidt, *Solid State Commun.*, 1980, **35**, 649–652.

21 G. M. Sheldrick, *Acta Crystallogr. Sect. C Struct. Chem.*, 2015, **71**, 3–8.

22 L. J. Farrugia, *J. Appl. Crystallogr.*, 2012, **45**, 849–854.

23 Rigaku, CrystalClear. Rigaku Corporation, Tokyo, Japan, 2014.

24 APEX2, Ver. 2014. 11-0., Bruker-AXS, 2014.

25 M. R. Probert, C. M. Robertson, J. A. Coome, A. K. Judith, B. C. Michell and A. E. Goeta, *J. Appl. Crystallogr.*, 2010, **43**, 1415–1418.

26 D. A. Keen, J. Gutmann and C. C. Wilson, *J. Appliied Crystallogr.*, 2006, **39**, 714–722.

27 M. J. Gutmann, ISIS Facility, Rutherford Appleton Laboratory, Oxfordshire, UK, 2005.

28 G. Bergerhoff and K. Brandenburg, in *International Tables for Crystallography Volume C*, ed. E. Prince, Wiley, 3rd edn., 2006, pp. 778–789.

29 B. J. Campbell, H. T. Stokes, D. E. Tanner and D. M. Hatch, *J. Appl. Crystallogr.*, 2006, **39**, 607–614.

30 J. F. Scott, F. D. Morrison, A. M. Z. Slawin, P. Lightfoot, R. Clulow, A. S. A. Gherson, A. M. Bumstead, J. Gardner, S. C. Capelli, M. R. Probert, S. Sahoo, J. S. Young, R. S. Katiyar and E. K. H. Salje, *Phys. Rev. B*, 2017, **95**, 094119.

Chapter 4 Derivatives of Tris Sarcosine Calcium Chloride

4.1 Introduction

The metal-organic ferroelectric TSCC has already been extensively studied in the earlier literature and its structure studied in detail in chapter 3. However, very little of the research has concerned the role of its components in regard to its ferroelectric properties. Amongst the preceding work there are examples of both bromine and iodine substitution but very few examples which investigate the impact of the amino acid and alkali earth metal.

Whilst there have been numerous sarcosine halide complexes reported in the literature as summarised in Table 4.1, very few of them have structures related to that of TSCC and aside from TSCC, none have displayed ferroelectric properties. Of the reported compounds, only two crystallise in polar space groups, $SarHZnCl_3$ ($P2_1$)[1] and $Sar_3Eu(ClO_4)_3$. $2H_2O$ ($P1$),[2] however, in both cases, ferroelectric properties have never been reported.

Table 4.1: Summary of the known sarcosine halide complexes[3,4]

Compound	Space Group	a (Å)	b (Å)	c (Å)	α (˚)	β (˚)	γ (˚)
Sar_3CaCl_2[5]	*Pnma*	9.156(10)	17.460(5)	10.265(5)	90	90	90
$SarMnCl_2.2H_2O$[6]	$P2_1/c$	8.314(8)	5.777(10)	18.680(6)	90	95.83(5)	90
$Sar_2MnCl_2.2H_2O$[7,8]	$P\bar{1}$	4.822(4)	5.379(6)	13.873(1)	83.76(5)	80.55(7)	87.58 (6)
Sar_2ZnCl_2[9]	*Pbca*	14.191(2)	10.655(10)	15.917(2)	90	90	90
$SarZnCl_3$[1]	$P2_1$	6.618(12)	7.499(11)	9.900(4)	90	92.62(2)	90
$SarBaCl_2.4H_2O$[10]	$P2_12_12_1$	7.235(1)	10.668(4)	15.686(3)	90	90	90
$SarCdCl_2$[11]	$P2_1/n$	7.960(2)	13.844(1)	6.917(1)	90	92.42(2)	90
Sar_2PtBr_2[12]	$P2_1/a$	10.921(8)	9.562(3)	6.890(5)	90	125.46(5)	90
Sar_3BaBr_2[13]	$P2_1/c$	18.345(4)	10.668(2)	8.921(18)	90	91.86(3)	90
$Sar_4KI.2H_2O$[3]	$C2/c$	13.714(10)	22.799(2)	8.079(5)	90	111.94(4)	90
Sar_2TeI_6[14]	$P4_2/m$	25.00(3)	25.00(3)	8.26(1)	90	90	90
$Sar_3Eu(ClO_4)_3.2H_2O$[2]	$P1$	9.146(2)	11.042(2)	14.696(3)	100.4(3)	104.56(3)	109.2(3)

The only example of a TSCC related compound is Sar_3BaBr_2 reported by Trzebiatowska-Gusowska *et al.*,[13] its crystal structure is shown in Figure 4.1. The structure has clear similarities to TSCC with its pseudohexagonal structure, stoichiometry and connectivity. However, a key difference is observed in the coordination of the alkali metal centre which is seen to increase from six to nine to accommodate the much larger Ba^{2+} cation. Despite these similarities, $(Sar)_3BaBr_2$ has not been found to exhibit ferroelectric properties.

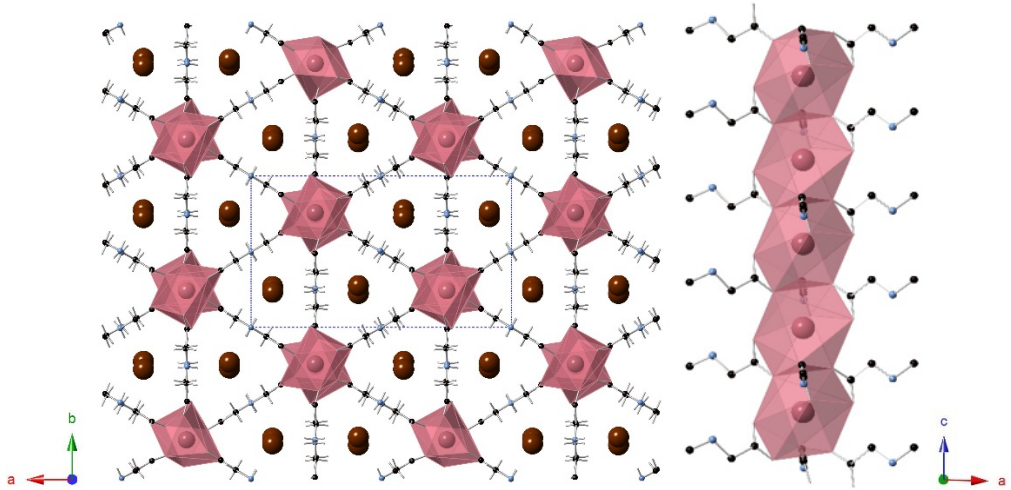

Figure 4.1: Crystal structure of $(CH_3NH_2CH_2COO)_3BaBr_2$ recreated from single crystal data from reference [13]

The brominated derivative, $(CH_3NH_2CH_2COO)_3CaBr_2$ (TSCB) has already been shown to be isostructural to TSCC at room temperature. Though its crystal structure has never been reported, the unit cell parameters have been previously derived from neutron diffraction data (a = 9.01 Å, b = 17.35 Å, c = 10.15 Å).[15] However, unlike TSCC, there is no evidence of a phase transition from the centrosymmetric *Pnma* to the polar $Pn2_1a$ space group in the temperature range 300 – 100 K.[15] Additionally, further electrical analysis by Hikita *et al*. did not reveal any evidence of ferroelectricity at temperatures as low as 4.2 K.[16] However, a ferroelectric transition has been observed at elevated pressures, specifically at 7 kbar and 108 K.[17]

The impact of the halide ion on the ferroelectric phase transition was more closely investigated through the synthesis of solid solutions of the composition

$(CH_3NH_2CH_2COO)_3CaCl_{1-X}Br_x$. The substitution of chloride with bromide causes the transition temperature (T_C) and spontaneous polarisation to decrease rapidly.[17] A quantum critical point, the point where a phase transition occurs at absolute zero, is reached at ~72 % bromine.[18] A similar study was undertaken for iodination, however in this case it is at only ~25 % iodine that the ferroelectric properties have been entirely lost.[19] Whilst the structure of the brominated derivative has been previously reported, an equivalent iodide compound has yet to be synthesised and hence its properties have not yet been thoroughly investigated.

The synthesis and characterisation of TSCC related compounds could provide an insight into the origins of the ferroelectric properties observed in pure TSCC and each of the compounds are potential candidates for ferroelectricity in their own right. In this research several novel derivatives of TSCC have been synthesised and the structures of the extant compounds $(C_3NO_2H_7)_2MnCl_2.2H_2O$ and $(C_3NO_2H_7)_3CaCl_2$ have been reinvestigated. Each of the compounds were characterised *via* X-ray diffraction and thermal gravimetric analysis and are summarised in Table 4.2.

Table 4.2: Summary of the synthesised TSCC related compounds discussed in this chapter

Halide	Divalent Metal			
	Mn	**Mg**	**Ca**	**Sr**
Cl	$(C_3NO_2H_7)_2MnCl_2.2H_2O$	$(C_3NO_2H_7)_2MgCl_2.2H_2O$	$(C_3NO_2H_7)_3CaCl_2$	$(C_3NO_2H_7)_3SrCl_2$
Br		$(C_3NO_2H_7)_3MgBr_2.2H_2O$	$(C_3NO_2H_7)_3CaBr_2$	$(C_3NO_2H_7)_3SrBr_2$
I	$(C_3NO_2H_7)_3MnI_2.2H_2O$		$(C_3NO_2H_7)_3CaI_2.2H_2O$, $(C_3NO_2H_7)_4CaI_2.2H_2O$,	

4.2 Experimental

4.2.1 Synthesis

All the compounds were synthesised from aqueous solutions by slow evaporation at room temperature utilising commercially available reagents in stoichiometric quantities. The products were obtained as high-quality single crystals after approximately 6 days of the evaporation process and the resulting crystals were then filtered and dried overnight at ~50 ˚C prior to analysis by X-ray diffraction and thermal analysis.

4.2.2 Powder X-ray Diffraction

Powder X-ray diffraction data were collected on a PANalytical Empyrean diffractometer using Cu $K_{\alpha 1}$ (λ = 1.5406 Å) radiation. Analysis was carried out by Rietveld refinement using GSAS[20] and the EXPGUI interface.[21]

4.2.3 Single Crystal X-ray Diffraction

High quality single crystals were selected using an optical microscope and subsequently X-ray diffraction data were collected at 173 K and 293 K on a Rigaku SCX mini diffractometer using Mo K_{α} (λ = 0.7107 Å) radiation. The data were processed using crystal clear (Rigaku)[22] and solved using direct methods. The data were modelled using the Shelx package[23] incorporated in the WINGX software.[24] In the case of shared atom sites, the atomic positions of both atoms were constrained to be equal but their occupancies were refined.

4.2.4 Differential Scanning Calorimetry (DSC)

Differential scanning calorimetry data were collected on powdered samples of each of the derivatives using a NETZCH DSC 204 instrument. Samples were initially cooled from 25 ˚C to −170 ˚C at a rate of 10 ˚C/min before a heating/cooling cycle at 5 ˚C/min between −170 and −80 ˚C. Subsequently the samples were heated back to 25 ˚C at a rate of 10 ˚C/min.

4.2.5 Thermal Gravimetric Analysis (TGA)

Thermal gravimetric analysis (TGA) was undertaken using a Stanton Redcroft STA-780 instrument in air with a flow rate of 21 ml/min and data were collected between room temperature and 700 ˚C at a heating rate of 5 ˚C/min throughout. Rheometric Scientific software was used to analyse the data.

4.2.6 Scanning Electron Microscopy (SEM)

Scanning electron microscopy (SEM) data were collected on a Jeol JSM 5600 instrument on both powdered and crystalline samples. The emitted X-rays were used for elemental analysis using an attached Energy Dispersive X-ray (EDX) system.

4.3 Results and Discussion

4.3.1 Bromination

Solid solutions of TSCC and TSCB have been thoroughly investigated in previous work, however, the crystal structure of the pure brominated derivative had never been reported. The introduction of bromine to the structure of TSCC supresses the ferroelectric transition temperature to 0 K at around 72 % bromine.[18] In the pure brominated structure, there was no evidence of ferroelectric properties or a phase transition to a polar phase, even at liquid helium temperatures.

A pure sample of TSCB was synthesised by slow evaporation at room temperature over six days. The structure was initially analysed using single crystal and powder X-ray diffraction. The crystal structure of TSCB was found to be isostructural to TSCC with only subtle differences in their unit cell parameters (Table 4.3).

Table 4.3: Comparison of unit cell parameters of TSCC at 295 K taken from literature[5] and TSCB derived from single crystal diffraction collected at 293 K

Composition	*a* (Å)	*b* (Å)	*c* (Å)
TSCC	9.156(10)	17.460(5)	10.265(5)
TSCB	9.2414(6)	17.6966(13)	10.3565(7)

The structure consists of distorted CaO_6 octahedra which are linked by three sarcosine molecules acting as bridging ligands to the next metal centre, forming infinite chains along the *a* axis (Figure 4.2). The hydrogen bonding network is shown in more detail in Figure 4.3 with the bond distances shown in Table 4.4, and remains unaffected by the change in halide ion. The bromide anions occupy the trigonal channels of the structure with each of the bromide anions accepting 3 Br…N-H hydrogen bonds from three different sarcosine molecules to interconnect the infinite chain structure forming the pseudohexagonal framework.

Table 4.4: Comparison of hydrogen bond lengths (Å) of TSCC at 295 K taken from literature[5] and of TSCB derived from single crystal X-ray diffraction data collected at 293 K in Å

Bond	TSCC	TSCB
N-H-X	3.1829(6)	3.287(3)
	3.221(1)	3.321(6)
	3.222(1)	3.336(7)

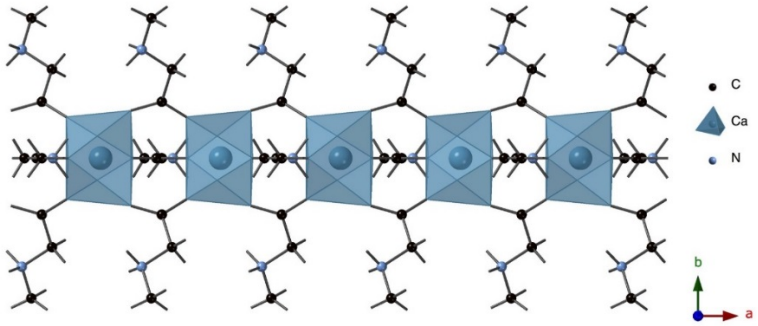

Figure 4.2: TSCB chains derived from single crystal X-ray diffraction data collected at 193 K, viewed along the *c* axis

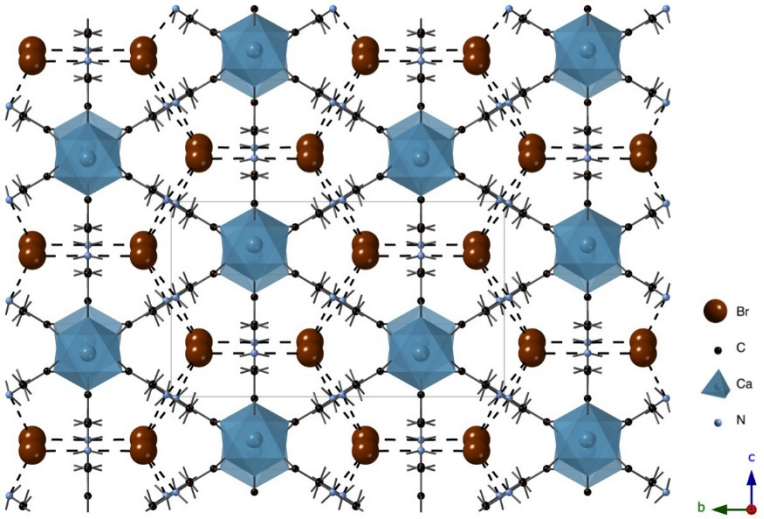

Figure 4.3: The crystal structure of TSCB with hydrogen bonds represented by dashed lines. Derived from single crystal X-ray diffraction data collected at 293 K viewed along the *a* axis

The purity and structure of TSCB were further confirmed by powder X-ray diffraction data as shown in Figure 4.4. The structural model derived from single crystal X-ray was compared to the powder X-ray diffraction data, indicating only trace amounts of impurities in the sample.

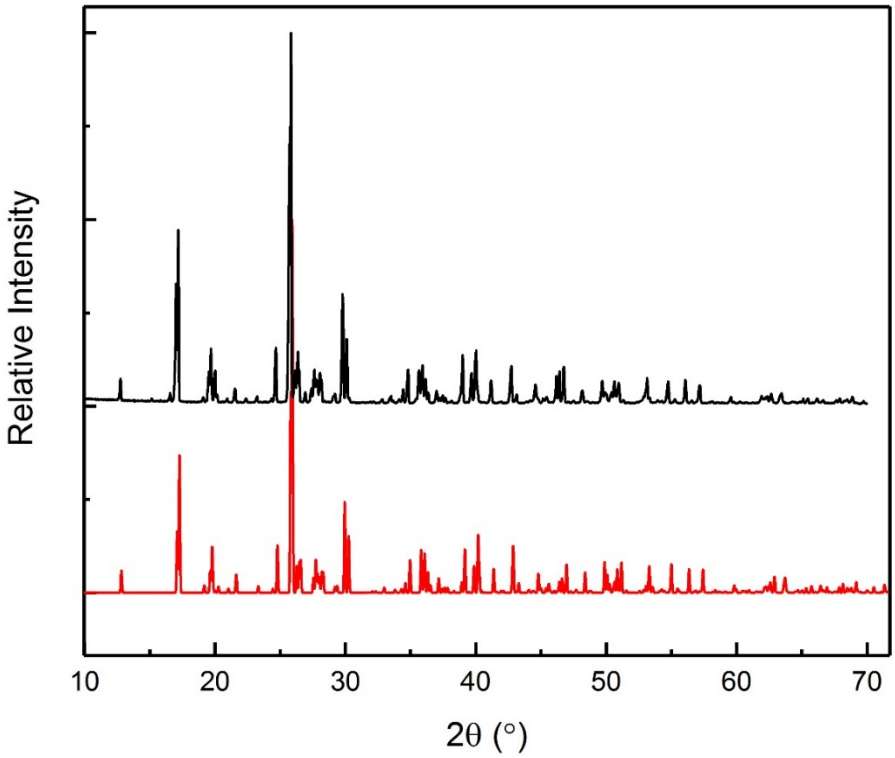

Figure 4.4: Comparison of experimental powder X-ray diffraction data (black) of TSCB and simulated data (red) from powder X-ray diffraction data collected at ambient temperature

Despite the numerous similarities with the parent structure (TSCC at room temperature,) there was no evidence of an additional change in structure or symmetry which would be analogous to TSCC. This supports the research of several previous groups who reported that the *Pnma* structure remained valid between 300 K and 100 K and that the compound did not exhibit ferroelectric properties, even at 4.2 K.[15,16] The unit cell parameters determined from the single crystal X-ray diffraction data at both 293 K and 173 K are reported in Table 4.5. Aside from the expected slight contraction towards lower temperatures, there are no significant changes to these unit cell parameters which would indicate a phase transition. A comparison of selected bond lengths at the two temperatures is also given in Table 4.6 and, as with the unit cell parameters, there are no significant changes that would suggest the presence of a phase transition.

Table 4.5: Crystallographic and refinement details of TSCB derived from single crystal X-ray diffraction data collected at 173 K and 293 K

	173 K	293 K
Formula	$(C_3NO_2H_7)_3CaBr_2$	$(C_3NO_2H_7)_3CaBr_2$
Formula Weight	467.19	467.19
Density (g cm^{-3})	1.832	1.816
Crystal System	Orthorhombic	Orthorhombic
Space Group	*Pnma*	*Pnma*
a/Å	9.2414(6)	9.2403(7)
b/Å	17.6966(13)	17.7845(13)
c/Å	10.3565(7)	10.3994(7)
α (˚)	90	90
β (˚)	90	90
γ (˚)	90	90
V/$Å^3$	1693.7(2)	1709.0(2)
Z	4	4
Measured Ref	15967	16686
Independent Ref	1969 [R(int) = 0.0500]	2017 [R(int) = 0.1593]
Refined Parameter	149	149
GOOF	0.800	0.945
Final R Indices (I > 2σ(I))	R1 = 0.0274, wR2 = 0.0274	R1 = 0.0499, wR2 = 0.1264

Table 4.6: Comparison of selected bond lengths (Å) and bond valence sums (valence units) of TSCB derived from single crystal X-ray diffraction data collected at 173 K and 293 K

Bond	173 K	293 K
M-O	2.2935(15)	2.288(5)
	2.2936(15)	2.288(5)
	2.305(2)	2.296(7)
	2.3671(19)	2.361(7)
	2.3816(14)	2.379(5)
	2.3816(14)	2.379(5)
BVS (Ca)	2.22	2.25

Whilst the single crystal X-ray diffraction data obtained in this research did not reveal any evidence of a phase transition to a polar space group, it should be noted that these X-ray diffraction experiments were limited to a lowest temperature of 173 K. Using differential scanning calorimetry, it was possible to probe the structure at temperatures down to 90 K. The DSC data are shown in Figure 4.5 but unfortunately don't provide evidence of any additional phase transitions. Whilst the compound had numerous similarities to the known ferroelectric TSCC, the substitution of bromide/chloride ions will have a subtle effect upon structure and hydrogen bonding of the compound which could be contributing to the change in properties.

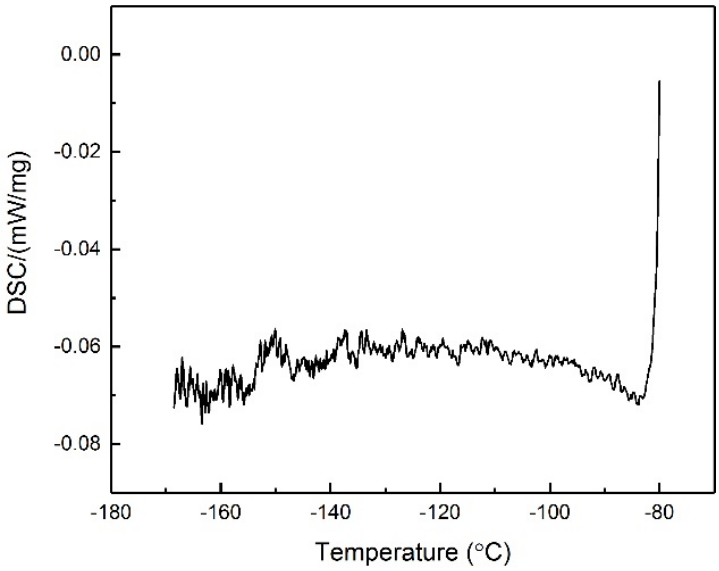

Figure 4.5: Differential Scanning Calorimetry data for TSCB between −170 and −80 °C at a cooling rate of 5 ˚C/min

4.3.2 Iodination

Since iodination was known to have a significant effect on the ferroelectric properties of TSCC, it was also desirable to synthesise a pure iodinated derivative *viz.* $(C_3NO_2H_7)_3CaI_2$. Several reactions using different evaporation rates and ratios of reagent were attempted as summarised in Table 4.7. However, it has not proved possible to synthesise a compound with the same stoichiometry as the parent compound TSCC. Instead both a 2:1 and a 4:1 sarcosine-to-metal salt are formed from reactions containing a 1:2 ratio of CaI_2 and sarcosine.

Table 4.7: Reaction conditions and ratios of CaI_2 and sarcosine for the syntheses of iodide-containing derivatives

Ratio of Reagents CaI_2:Sar	Volume of solvent (ml)	Products
1:1	1	Polycrystalline powder
1:2	1	Colourless crystals
1:3	1	Polycrystalline powder
1:4	1	White powder
1:5	1	Colourless sticky substance
1:1	0.5	Colourless needles
1:2	0.5	Polycrystalline
1:3	0.5	Polycrystalline
1:4	0.5	White Solid
1:5	0.5	White Solid

4.3.2.1 Bis Sarcosine Calcium Iodide Dihydrate

The structure of the 2:1 salt BSCI $(CH_3NO_2H_7)_2CaI_2.2H_2O$ is shown in Figure 4.6. Whilst its constituents are the same as TSCC, there are substantial changes to the stoichiometry, connectivity and structure.

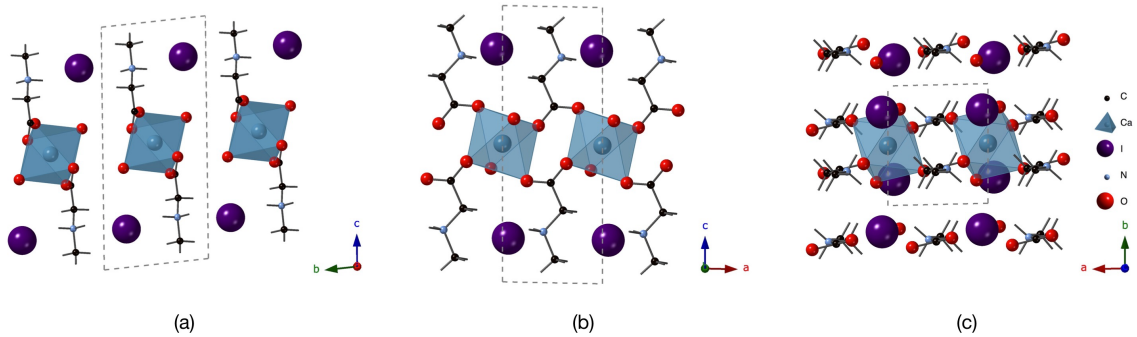

(a) (b) (c)

Figure 4.6: The crystal structure of BSCI viewed along the *a*, *b* and *c* axes derived from single crystal diffraction data collected at 293 K

The sarcosine molecules are still incorporated in their zwitterionic form and act as bridging ligands between the calcium metal centres. Each of the metal cations is linked to the next *via* 2 sarcosine molecules forming infinite chains along the *a* axis. However, two water molecules now occupy the coordination sphere in the calcium cation which remains as a 6 coordinate distorted octahedron. The symmetry and space group of the material have been lowered from orthorhombic *Pnma* to triclinic $P\bar{1}$, but the unit cell parameters are not related to each other. The unit cell parameters and refinement details of the new derivative are shown in Table 4.8.

Table 4.8 Crystallographic and refinement details of BSCI derived from single crystal X-ray diffraction data collected at 173 K and 293 K

	173 K	**293 K**
Formula	$(C_3NO_2H_7)_2CaI_2.2H_2O$	$(C_3NO_2H_7)_2CaI_2.2H_2O$
Formula Weight	508.10	508.10
Density (g cm^{-3})	2.066	2.044
Crystal System	Triclinic	Triclinic
Space Group	$P\bar{1}$	$P\bar{1}$
a/Å	4.9952(4)	5.0003(5)
b/Å	5.9493(5)	5.9936(6)
c/Å	13.8126(12)	13.8450(15)
α (˚)	95.593(13)	95.502(19)
β (˚)	90.980(12)	91.031(19)
γ (˚)	90.965(11)	91.228(17)
V/Å^3	408.40(6)	412.84(7)
Z	1	1
Measured Ref	4214	4252
Independent Ref	1859 [R(int) = 0.0589]	1884 [R(int) = 0.0864]
Refined Parameter	96	96
GOOF	1.107	0.640
Final R Indices (I > 2σ(I))	R1 = 0.0659, wR2 = 0.1615	R1 = 0.0422, wR2 = 0.1041

Since the compound BSCI crystallises in the centrosymmetric triclinic space group $P\bar{1}$, the compound cannot have any ferroelectric properties at ambient temperature. Single crystal X-ray diffraction and DSC experiments were undertaken at low temperatures to investigate any possible phase transitions to a polar phase.

The crystal structures derived from single crystal diffraction data at both 173 K and 293 K did not contain any significant changes to structure, symmetry or bonding. The unit cell parameters reported in Table 4.8 show only a slight contraction at low temperature as expected for any system. The bond lengths determined at both temperatures are also shown in Table 4.9 but also do not suggest the presence of a phase transition.

Table 4.9: Selected bond lengths (Å) and bond valence sums (valence units) for BSCI derived from single crystal X-ray diffraction data collected at 173 K and 293 K

	173 K	**293 K**
M-O	2.335(6)	2.333(5)
	2.335(6)	2.333(5)
	2.338(7)	2.338(5)
	2.338(7)	2.338(5)
	2.394(10)	2.380(8)
	2.394(10)	2.380(8)
	3.483(8)	3.499(6)
N-H-X	3.462(9)	3.481(6)
BVS (Ca)	2.10	2.13

DSC data collected between −170 and 25 ˚C are plotted in Figure 4.7. Whilst there are some fluctuations in the data around −140 ˚C in the initial cooling data, a second data set at a slower ramp rate showed a smooth evolution suggesting that no phase transition has occurred in this temperature range. The decomposition of the compound was investigated through thermal gravimetric analysis as shown in Figure 4.7 revealing a multi-step decomposition where the initial step corresponded to water loss; further confirming the structural model. The purity of the samples was investigated by powder

X-ray diffraction, whilst the data do fit with the crystal structure, several other peaks are also present in the data, suggesting poor purity of the sample (Figure 4.8).

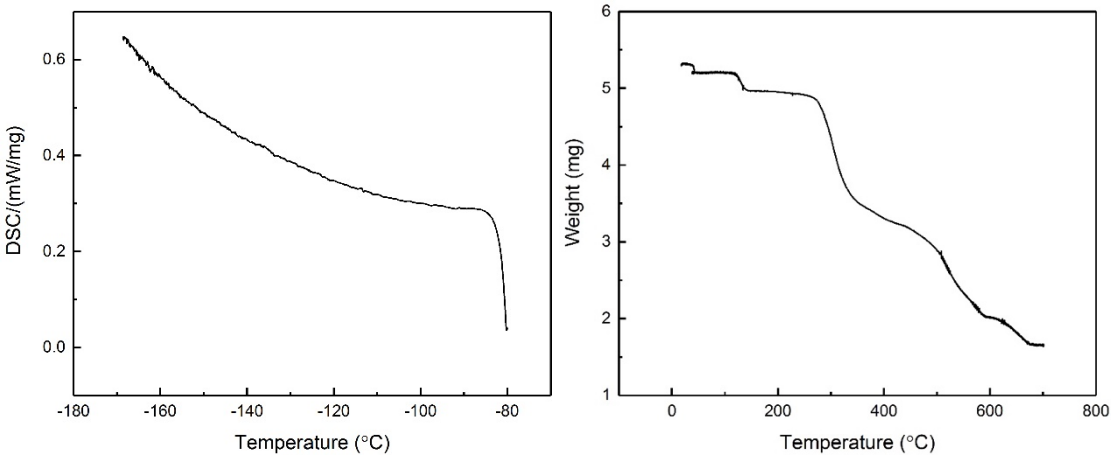

Figure 4.7: (left) Differential Scanning Calorimetry data for BSCI between −170 and −80 °C at a cooling rate of 5 ˚C/min. (right) Thermal Gravimetric Analysis data for BSCI measured between room temperature and 700 °C at 5 °C/min

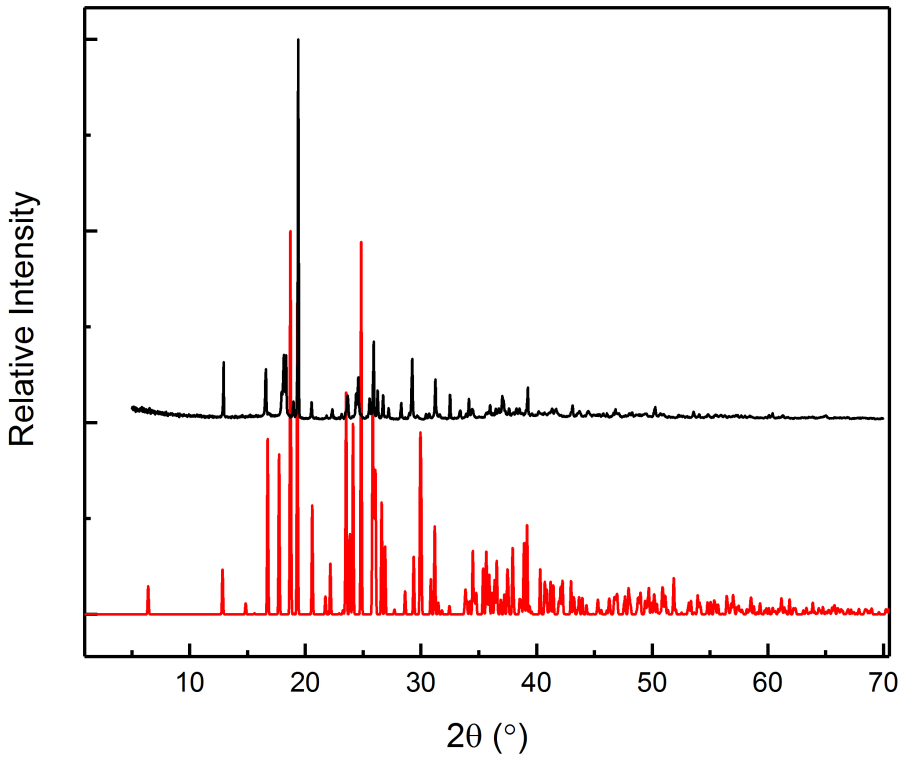

Figure 4.8: Comparison of experimental powder X-ray diffraction data (black) of BSCI and simulated data (red) from powder X-ray diffraction data collected at ambient temperature

4.3.2.2 Tetra Sarcosine Calcium Iodide Dihydrate

In addition to the new compound BSCI $(C_3NO_2H_7)_2CaI_2.2H_2O$, a second iodine containing derivative was synthesised from the same reaction. The structural formula is $(C_3NO_2H_7)_4CaI_2.2H_2O$ (TSCI) and its crystallographic data and refinement details are shown in Table 4.10. This new compound has different stoichiometry and structure to the parent compound TSCC and is one of only two reported 4:1 sarcosine salt complexes the other being diaquaiodidotetrasarcosinepotassium reported by Fleck *et al*.[3] Aside from the ratio of constituents, its structure differs significantly from that of the new compound TSCI which is shown in Figure 4.9. The pseudohexagonal symmetry and stoichiometry of the parent compound has now been completely lost, however the coordination of the calcium centre remains as six. Two sarcosine molecules act as bridging ligands through the oxygen atoms of the carboxylate groups, another two sarcosine molecules are non-bridging and two water molecules are coordinated to the calcium cation. The structure crystallised in the monoclinic $P2_1/n$ space group and its unit cell parameters are given in Table 4.10. Whilst there are numerous similarities, in terms of Ca^{2+} coordination environment, the newly synthesised compound appears to be unrelated to the parent compound TSCC.

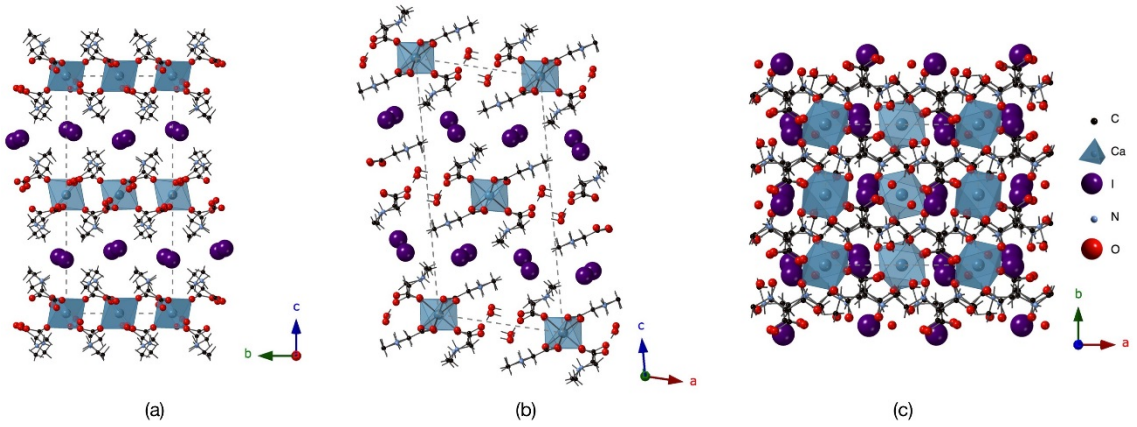

Figure 4.9: Crystal structure of TSCI derived from single crystal data collected at 293 K viewed along the *a*, *b* and *c* axes

Table 4.10: Crystallographic data and refinement details of TSCI derived from single crystal X-ray diffraction data collected at 173 K and 293 K

	173 K	293 K
Formula	$(C_3NO_2H_7)_4CaI_2.2H_2O$	$(C_3NO_2H_7)_4CaI_2.2H_2O$
Formula Weight	686.29	686.29
Density (g cm^{-3})	1.792	1.774
Crystal System	Monoclinic	Monoclinic
Space Group	$P2_1/n$	$P2_1/n$
a/Å	11.2880(8)	11.3056(7)
b/Å	10.0620(7)	10.0982(7)
c/Å	23.0573(16)	23.1494(16)
α (˚)	90	90
β (˚)	103.722(4)	103.484(8)
γ (˚)	90	90
V/Å^3	2544.1(3)	2570.0(3)
Z	4	4
Measured Ref	25445	25644
Independent Ref	5835 [R(int) = 0.0639]	5878 [R(int) = 0.1416]
Refined Parameter	393	393
GOOF	0.878	0.826
Final R Indices (I > 2σ(I))	R1 = 0.0392, wR2 = 0.1050	R1 = 0.0545, wR2 = 0.1360

Table 4.11: Comparison of selected bond lengths (Å) and bond valence sums (valence units) of TSCI derived from single crystal X-ray diffraction data collected at 173 and 293 K

Bond	173 K		293 K	
M-O	2.292(3)	2.304(3)	2.292(5)	2.306(5)
	2.292(3)	2.304(3)	2.292(5)	2.306(5)
	2.323(3)	2.328(4)	2.323(5)	2.333(5)
	2.323(3)	2.328(4)	2.323(5)	2.333(5)
	2.392(3)	2.399(3)	2.394(5)	2.393(5)
	2.392(3)	2.399(3)	2.394(5)	2.393(5)
BVS (Ca)	2.23	2.18	2.23	2.18
N-H-X	3.561(4)		3.558(7)	
	3.612(4)		3.621(7)	
	3.577(5)		3.604(8)	
	3.487(5)		3.514(8)	

In keeping with BSCI, single crystal X-ray diffraction data were also measured at 173 K to identify any changes in structure or the existence of any potential phase transitions. For data collected at 173 K, unit cell parameters are shown in Table 4.10 and the bond lengths shown in Table 4.11. There was no indication of a change in structure, symmetry or crystal system that would indicate a phase transition. Differential scanning calorimetry data were also collected to investigate the structure at even lower temperatures but did not reveal any evidence of a phase transition (Figure 4.10). The purity of the sample was probed by powder X-ray diffraction as shown in Figure 4.11 but comparison of the experimental and simulated data suggests poor purity. The simulated diffraction of BSCI is also shown for comparison, but does not appear to match the impurities seen in the powder diffraction pattern.

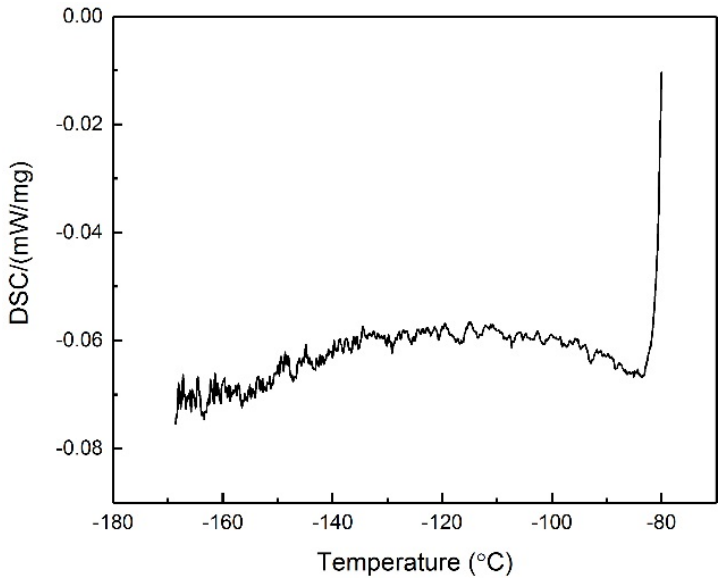

Figure 4.10: Differential Scanning Calorimetry data for TSCI between −170 and −80 °C at a cooling rate of 5 ˚C/min

Whilst we have been able to synthesise two different iodine containing sarcosine complexes, with 2:1 and 4:1 ratios, so far it has not proved possible to synthesise a 3:1 complex with the same stoichiometry as the parent compound TSCC.

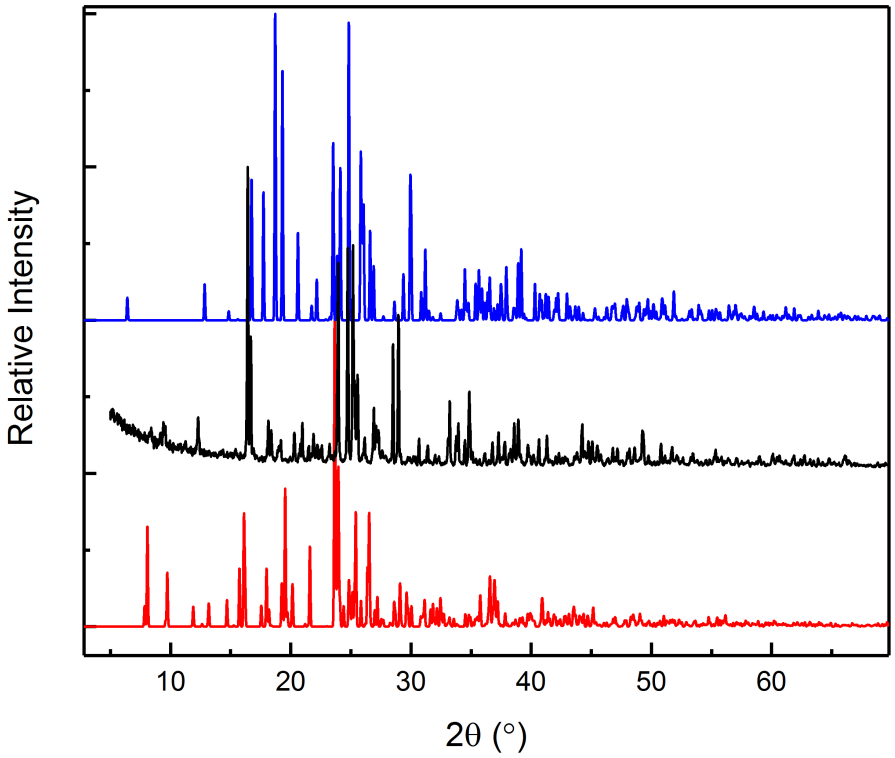

Figure 4.11: Comparison of experimental powder X-ray diffraction data (black) of TSCI, simulated data TSCI (red) and simulated data BSCI (blue) from powder X-ray diffraction data collected at ambient temperature

4.3.3 Strontium Derivatives

Much of the earlier work related to TSCC has concerned the effect of the halogen on the structure and ferroelectric properties. Two strontium containing derivatives, $(C_3NO_2H_7)_3SrCl_2$ (TSSC) and $(C_3NO_2H_7)_3SrBr_2$ (TSSB) where synthesised to investigate this. In both cases, high quality single crystals were synthesised by slow evaporation of aqueous solutions at room temperature and initially analysed by X-ray diffraction.

Single crystal X-ray diffraction data were measured at 293 K for both samples. In both cases, the pseudohexagonal symmetry and stoichiometry of the parent compound TSCC has been retained but with significant changes in their unit cells and their symmetry, as summarised in Table 4.12. One key difference arises in the coordination number of the metal centre, which is seen to increase from six in the parent compound TSCC to seven in both of the new strontium derivatives (Figure 4.12). As a result, the polyhedral chains

now exhibit corner sharing (Figure 4.13) which contributes to the significant changes in symmetry/structure when compared to TSCC. The hydrogen bonding network remains largely unaffected by the incorporation of strontium, and each halide ion accepts three hydrogen bonds. Due to the decrease in unit cell symmetry, the asymmetric unit now contains 2 halide ions giving rise to six hydrogen bond distances as shown in Table 4.14.

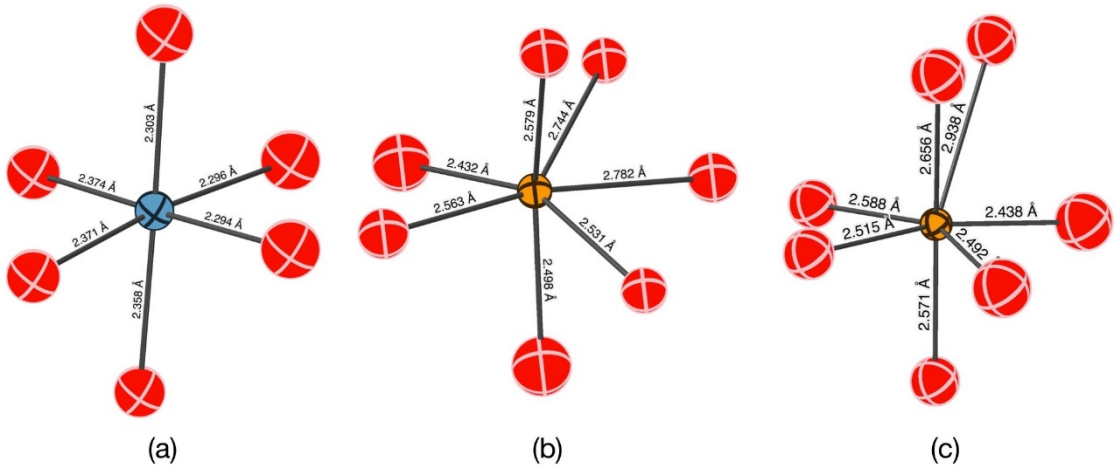

Figure 4.12: Comparison of coordination environments and bond lengths of calcium in TSCC and strontium cation in TSSC and TSSB derived from single crystal X-ray diffraction data collected at 293 K. (blue) calcium, (orange) strontium and (red) oxygen

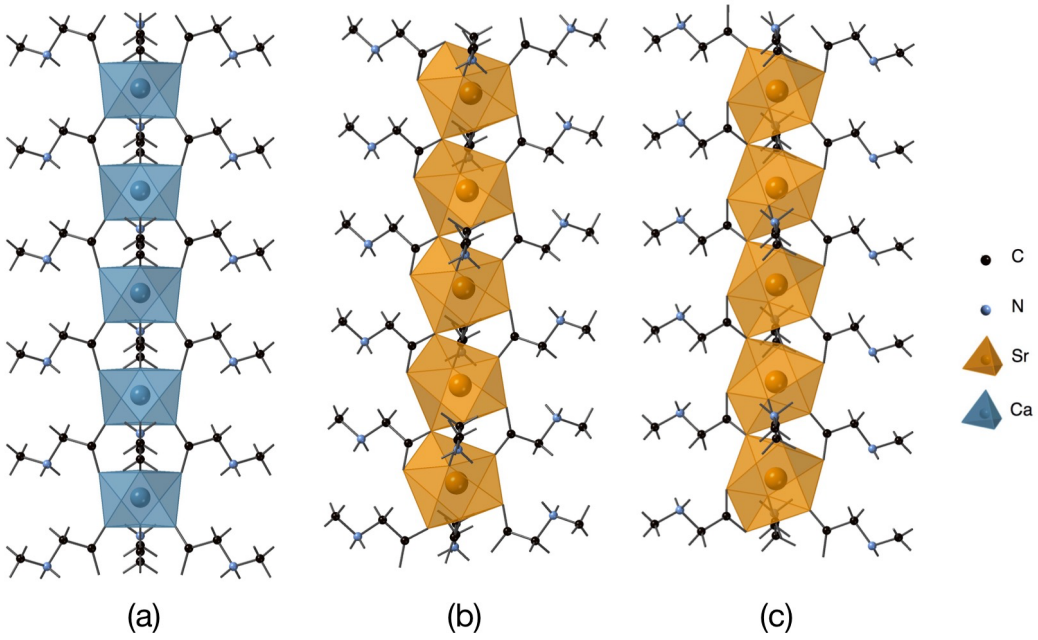

Figure 4.13: Comparison of polyhedra connectivity in (a) TSCC, (b) TSSC and (c) TSSB derived from single crystal X-ray diffraction data collected at 293

Table 4.12: Crystallographic and refinement details of TSSC and TSSB at 173 K and 293 K

	173 K	**293 K**	**173 K**	**293 K**
Formula	$(C_3NO_2H_7)_3SrCl_2$	$(C_3NO_2H_7)_3SrCl_2$	$(C_3NO_2H_7)_3SrBr_2$	$(C_3NO_2H_7)_3SrBr_2$
Formula Weight	425.81	425.81	514.73	514.73
Density (g cm^{-3})	1.747	1.730	2.022	2.000
Crystal System	Monoclinic	Monoclinic	Orthorhombic	Orthorhombic
Space Group	$P2_1/a$	$P2_1/a$	*Pcab*	*Pcab*
a/Å	8.7535(6)	8.7930(6)	8.7723(6)	8.8611(6)
b/Å	10.3752(7)	10.3957(7)	10.5359(7)	10.5404(7)
c/Å	17.8337(13)	17.9000(13)	36.5820(3)	36.6110(3)
α (˚)	90	90	90	90
β (˚)	91.867(6)	91.982(6)	90	90
γ (˚)	90	90	90	90
V/$Å^3$	1618.8(2)	1635.2(2)	3381.1(3)	3419.5(3)
Z	4	4	8	8
Measured Ref	16382	16549	21461	31978
Independent Ref	3726 [R(int) = 0.0856]	3758 [R(int) = 0.1041]	3873 [R(int) = 0.0518]	3923 [R(int) = 0.0815]
Refined Parameter	274	274	274	274
GOOF	0.823	0.857	1.015	1.165
Final R Indices (I > 2σ(I))	R1 = 0.0390, wR2 = 0.1001	R1 = 0.0451, wR2 = 0.1118	R1 = 0.0307, wR2 = 0.1102	R1 = 0.0501, wR2 = 0.1551

Table 4.13: Sr-O bond lengths (Å) and bond valence sum (valence units) calculation for TSSC and TSSB derived from single crystal X-ray diffraction data collected at 293 K and 173 K

Bond	TSSC		TSSB	
Temperature (K)	**173 K**	**293 K**	**173 K**	**293 K**
O1	2.431(3)	2.433(4)	2.438(3)	2.438(5)
O2	2.500(3)	2.498(4)	2.518(3)	2.492(6)
O3	2.537(3)	2.531(4)	2.521(3)	2.515(5)
O4	2.568(3)	2.564(4)	2.572(2)	2.570(5)
O5	2.583(3)	2.579(4)	2.595(3)	2.587(5)
O6	2.721(3)	2.745(4)	2.660(3)	2.656(5)
O1_1	2.796(3)	2.782(4)	2.888(3)	2.937(6)
BVS (Sr)	2.04	2.05	2.01	2.05

Table 4.14: Hydrogen bond lengths (N-H…X) (Å) of TSSC and TSSB derived from single crystal X-ray diffraction data collected at 293 K and 173 K

TSSC		TSSB	
173 K	**293 K**	**173 K**	**293 K**
3.163(4)	3.174(5)	3.288(3)	3.296(5)
3.210(4)	3.229(5)	3.355(3)	3.357(6)
3.173(4)	3.189(5)	3.293(3)	3.305(6)
3.234(4)	3.245(5)	3.374(3)	3.386(6)
3.226(4)	3.232(5)	3.320(3)	3.327(6)
3.251(4)	3.259(5)	3.311(3)	3.329(6)

4.3.3.1 Tris Sarcosine Strontium Chloride (TSSC)

One example of a strontium derivative is TSSC $(C_3NO_2H_7)_3SrCl_2$. The crystal structure is shown in Figure 4.14, the compound maintains the same stoichiometry and pseudohexagonal symmetry as the original compound TSCC. The sarcosine molecules again act as bridging ligands connecting the infinite strontium-centred chains. However, the increase in coordination number of the metal cation causes one of the oxygen atoms to be shared between two of these metal centres (O1_1), resulting in the observed corner sharing of polyhedra. An additional outcome of this subtle change in connectivity

is a lowering in symmetry from the orthorhombic *Pnma* space group to the monoclinic $P2_1/a$ space group. This is reminiscent of a previously reported TSCC derivative, TSBaBr,[13] although in that case the coordination is seen to increase to nine, perhaps due to the even larger relative size of the barium cation relative to the strontium and calcium cations. Aside from the difference in coordination surrounding the metal centre, the structure and connectivity of TSSC remain largely the same as the parent compound TSCC.

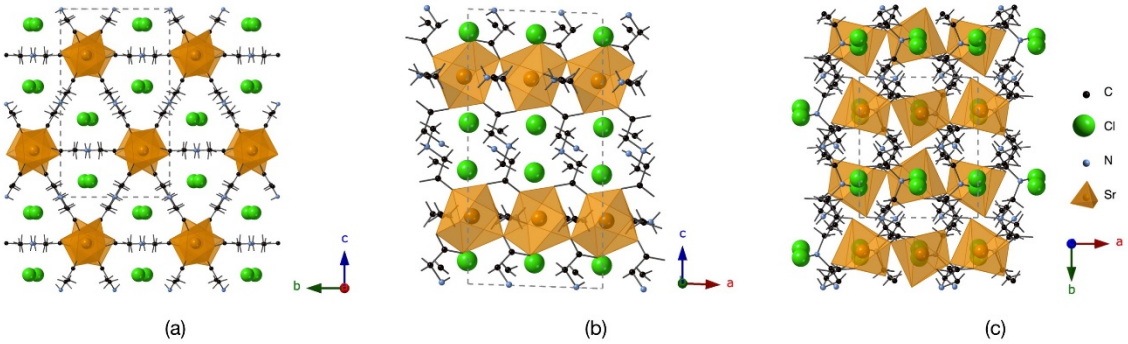

Figure 4.14: The crystal structure of TSSC derived from single crystal X-ray diffraction data collected at 173 K viewed along the *a*, *b* and *c* axes

Since TSSC crystallises in a centrosymmetric space group, it cannot have any ferroelectric properties at 293 K. However, single crystal X-ray diffraction data was also collected at 173 K to observe any potential phase transitions to a polar space group. Unfortunately, there is no evidence for a phase transition in the unit cell parameters (Table 4.12), bond lengths (Table 4.13) and no change in crystal system or space group was observed.

Whilst the X-ray diffraction data was limited to a low temperature of 173 K, differential scanning calorimetry data allowed analysis down to ~90 K as shown in Figure 4.15. The DSC data revealed no phase transitions in the temperature range −80 to −140 °C, but the presence of a small peak in the data at ~−150 °C which could correspond to a change in structure. Subsequently the crystal structure was re-determined at a lower temperature of −180 °C to investigate this potential phase transition. The crystallographic data and refinement details are shown in Table 4.15. Despite the

supporting evidence from the DSC data, the single crystal X-ray diffraction data did not reveal any changes to the structure, symmetry or bonding which would indicate a phase transition. The structure and purity are confirmed by the powder X-ray diffraction data which is shown in Figure 4.16.

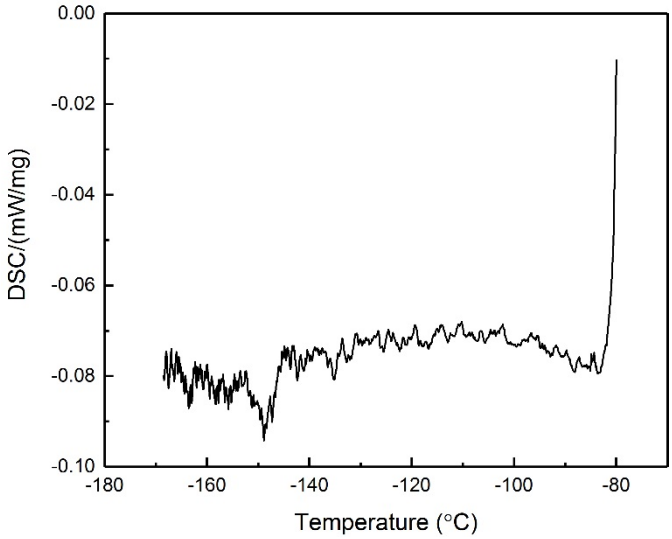

Figure 4.15: Differential Scanning Calorimetry data for TSSC between −170 and −80 °C at a cooling rate of 5 ˚C/min

Table 4.15: Crystallographic and refinement details of TSSC derived from single crystal X-ray diffraction data collected at 93 K

Parameter	TSSC
Formula	$(C_3NO_2H_7)_3Sr_0Cl_2$
Formula Weight	425.81
Density (g cm^{-3})	1.760
Crystal System	Monoclinic
Space Group	$P2_1/a$
a/Å	8.7250(3)
b/Å	10.3574(3)
c/Å	17.7949(6)
α (˚)	90
β (˚)	91.909(3)
γ (˚)	90
V/$Å^3$	1607.20(9)
Z	4
Measured Ref	24757
Independent Ref	4193 [R(int) = 0.0491]
Refined Parameter	217
GOOF	0.797
Final R Indices (I > 2σ(I))	R1 = 0.0297, wR2 = 0.0958

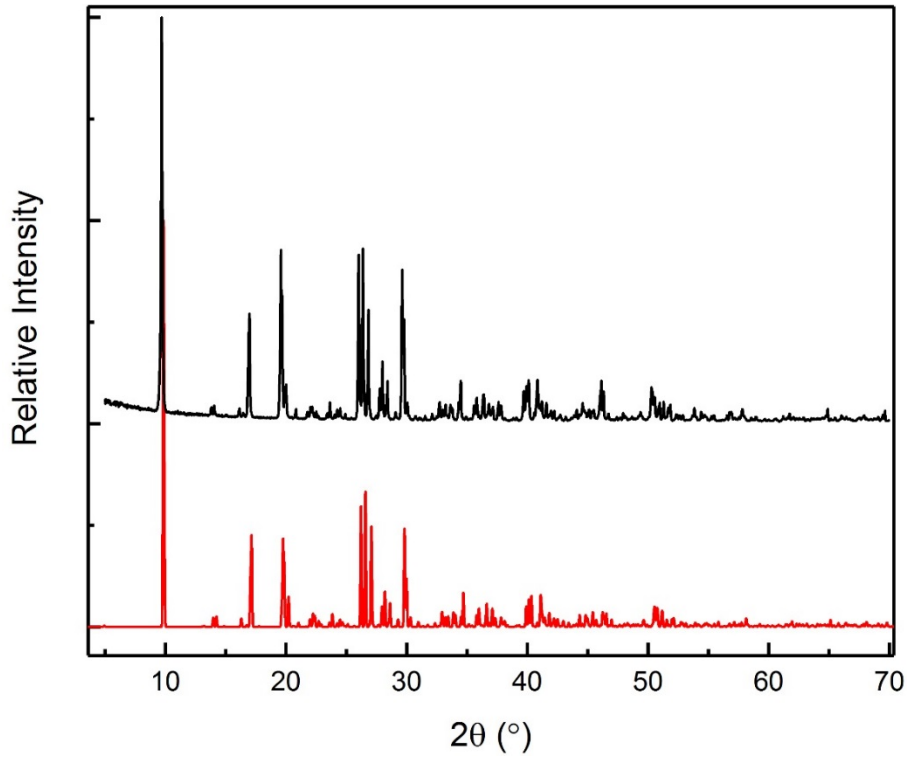

Figure 4.16: Comparison of experimental powder X-ray diffraction data (black) of TSSC and simulated data (red) from powder X-ray diffraction data collected at ambient temperature

4.3.3.2 Tris Sarcosine Strontium Bromide

An analogous derivative was synthesised for strontium bromide with the formula $(C_3NO_2H_7)_3SrBr_2$. The compound has many similarities to the parent compound TSCC and the initial strontium derivative TSSC as shown in Figure 4.17. The pseudohexagonal symmetry is maintained and the coordination of the strontium cation is unaffected by the substitution of the chloride ion with a bromide ion. However, there is a significant difference in the unit cell, space group and symmetry. The cell parameters and refinement details are shown in Table 4.12.

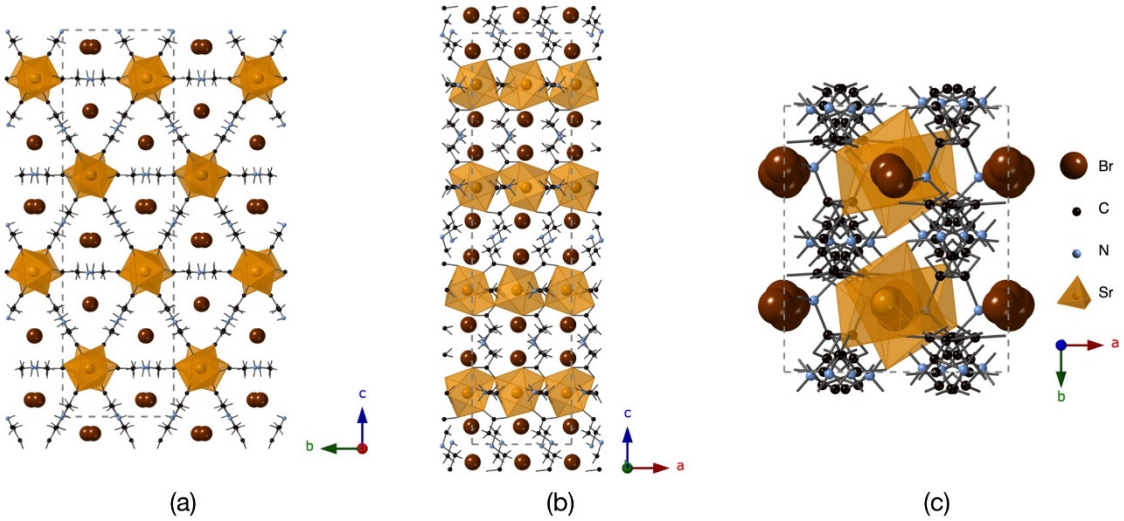

Figure 4.17: Crystal structure of TSSB derived from single crystal X-ray diffraction data collected at 293 K viewed along the *a*, *b* and *c* axes

Unlike all the previously reported TSCC derivatives, TSSB does not crystallise in a lower symmetry crystal system, but in fact the structure remains orthorhombic. Although there is a significant difference seen in the unit cell parameters, there is a relationship to the values observed in TSCC. The most apparent difference is in the unit cell length *c* axis which approximately doubles. This is a result of differences in Sr-O bonding which can be observed more clearly in Figure 4.18.

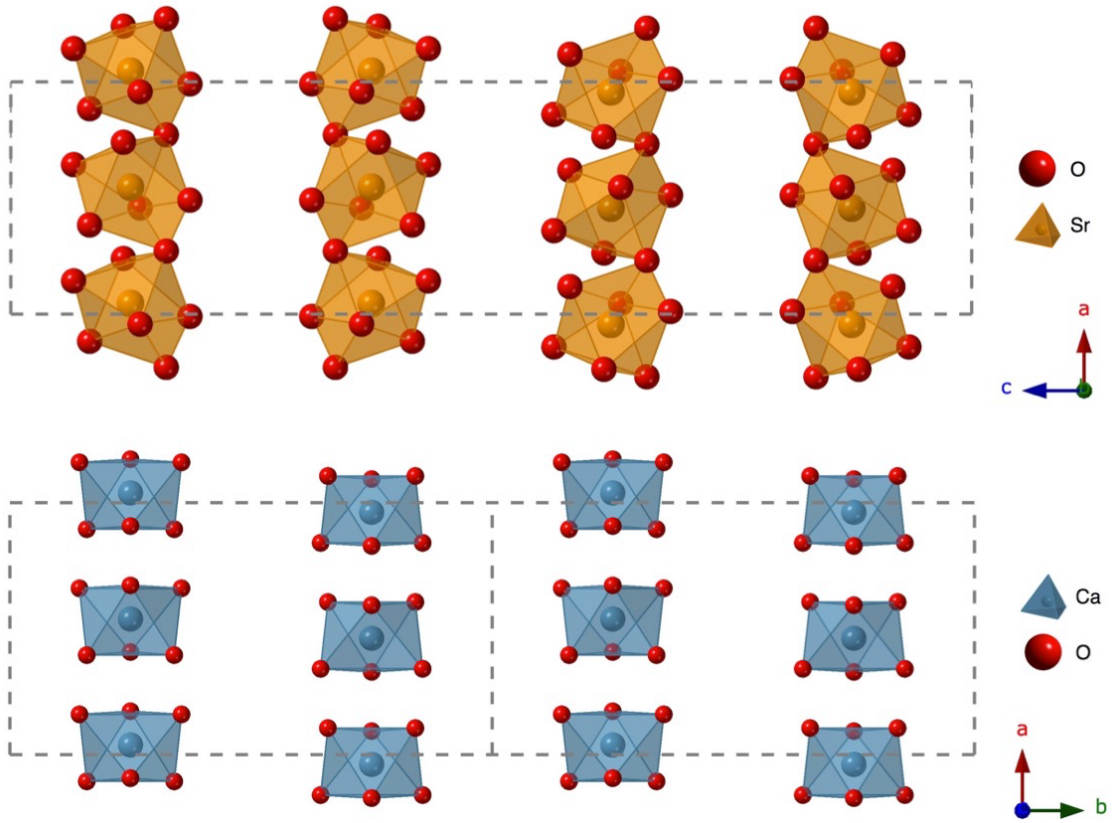

Figure 4.18: (top) Corner linked SrO_7 polyhedra in TSSB, (bottom) CaO_6 Octahedra in TSCC, derived from single crystal X-ray diffraction data collected at 293 K.

In this case, strontium forms seven bonds to the oxygen atoms of the sarcosine molecules, their bond lengths and the bond valence sum calculation for strontium are shown in Table 4.13. Six of the strontium oxygens bonds are similar in length whilst the seventh is noticeably elongated. The orientation of the seventh longer bond gives rise to the unit cell doubling which is observed along the *c* axis.

As in the previous derivatives, the crystal structure was determined at low temperature to investigate any changes in structure. However, from the crystallographic details and bond lengths shown in both Table 4.12 and Table 4.13, there are no significant structural changes occurring within this temperature region. The unit cell parameters are seen to contract slightly at lower temperature as expected and there is very little deviation in Sr-O bond lengths (Table 4.13).

Differential scanning calorimetry data covering this temperature range and down to 90 K also supports this data as no significant peaks are observed in the data as shown in Figure 4.19.

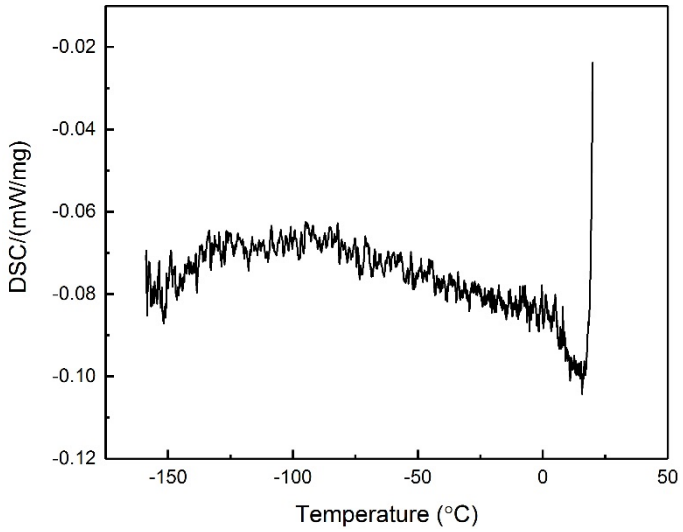

Figure 4.19: Differential scanning calorimetry data of TSSB between −170 ˚C and −80 ˚C collected at a cooling rate of 5˚C/min

The structure and purity of the sample was confirmed by powder X-ray diffraction. A comparison of the measured diffraction data and simulated diffraction pattern are shown in Figure 4.20.

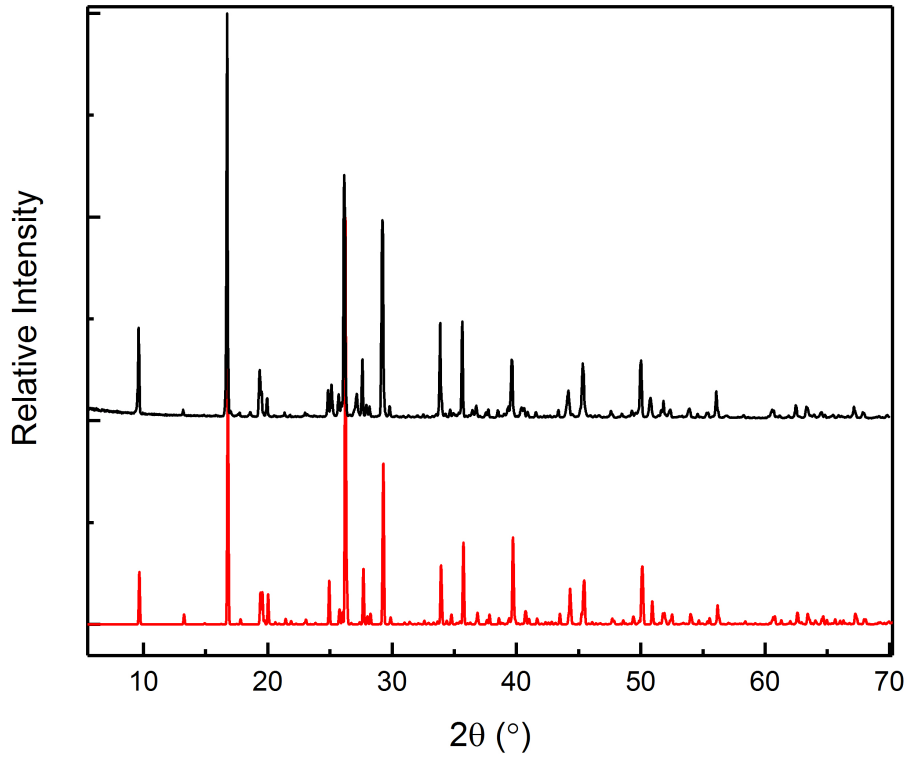

Figure 4.20: Comparison of experimental powder X-ray diffraction data (black) of TSSB and simulated data (red) from powder X-ray diffraction data collected at ambient temperature

4.3.4 Strontium Doping of TSCC

As bromination is known to have a negative effect on the ferroelectric properties of TSCC, and induce a quantum critical point, strontium doping was also investigated in detail to observe its effect on the system. Samples of compositions $(Sar)_3Ca_{0.9}Sr_{0.1}Cl_2$ to $(Sar)_3Ca_{0.1}Sr_{0.9}Cl_2$ were synthesised in ten percent intervals from their stoichiometric components. The products of each reaction were often polycrystalline; however, single crystal X-ray diffraction was carried out on a sample of TSCC containing ~50 % Sr, the crystallographic and refinement details are shown in Table 4.16.

Table 4.16: Crystallographic and refinement data for $(C_3NO_2H_7)_3Ca_{0.5}Sr_{0.5}Cl_2$ (TSCC 50 % Sr) derived from single crystal X-ray diffraction data collected at 173 K

Parameter	TSCC 50 % Sr
Formula	$(C_3NO_2H_7)_3Ca_{0.5}Sr_{0.5}Cl_2$
Formula Weight	398.71
Density (g cm^{-3})	1.620
Crystal System	Orthorhombic
Space Group	*Pnma*
a/Å	8.9965(7)
b/Å	17.6045(3)
c/Å	10.3191(15)
α (˚)	90
β (˚)	90
γ (˚)	90
V/$Å^3$	1634.3(3)
Z	4
Measured Ref	15958
Independent Ref	1926 [R(int) = 0.0732]
Refined Parameter	150
GOOF	1.079
Final R Indices (I > 2σ(I))	R1 = 0.0522, wR2 = 0.1460

At 50 % Sr, the structure remains almost identical to the pure TSCC structure but there is clear evidence for the incorporation of strontium onto the metal sites. The symmetry and space group remain as *Pnma* orthorhombic with evident pseudohexagonal structure. However, there are subtle changes in the unit cell parameters. The unit cell parameter *a* exhibits a slight contraction but there is elongation along both the *b* and *c* axes. There are also changes in the metal to oxygen bond length, which increase notably from an average of 2.303 Å to 2.392 Å (Table 4.17). The atomic displacement parameter of the metal centre also increases substantially to accommodate the extra electron density of the strontium over the calcium. Once the shared metal site had been included in the model, its occupancy was refined to 56.6(6) % Ca.

Table 4.17: Comparison of metal oxygen bond lengths (Å) in TSCC 50 % Sr and TSCC as derived from single crystal X-ray diffraction data collected at 173 K

Bond	TSCC	TSCC 50 % Sr
M-O	2.292(2)	2.341(3)
	2.292(2)	2.341(3)
	2.302(3)	2.346(4)
	2.358(3)	2.430(4)
	2.369(2)	2.448(3)
	2.369(2)	2.448(3)

Whilst it has not been possible to synthesise single crystal samples of the remaining compositions of sufficient quality, the samples were analysed by powder X-ray diffraction. Their unit cell parameters were determined for each composition using powder diffraction and Rietveld refinement. The diffraction patterns were each refined to two different models *viz. Pnma* (TSCC) and $P2_1/a$ (TSSC), with the best results shown in Table 4.18. A typical Rietveld refinement profile for the series is shown in Figure 4.21. For strontium concentrations exceeding 50 %, the TSCC structural model was no longer valid and the powder X-ray diffraction data displayed a better fit to the monoclinic TSSC model.

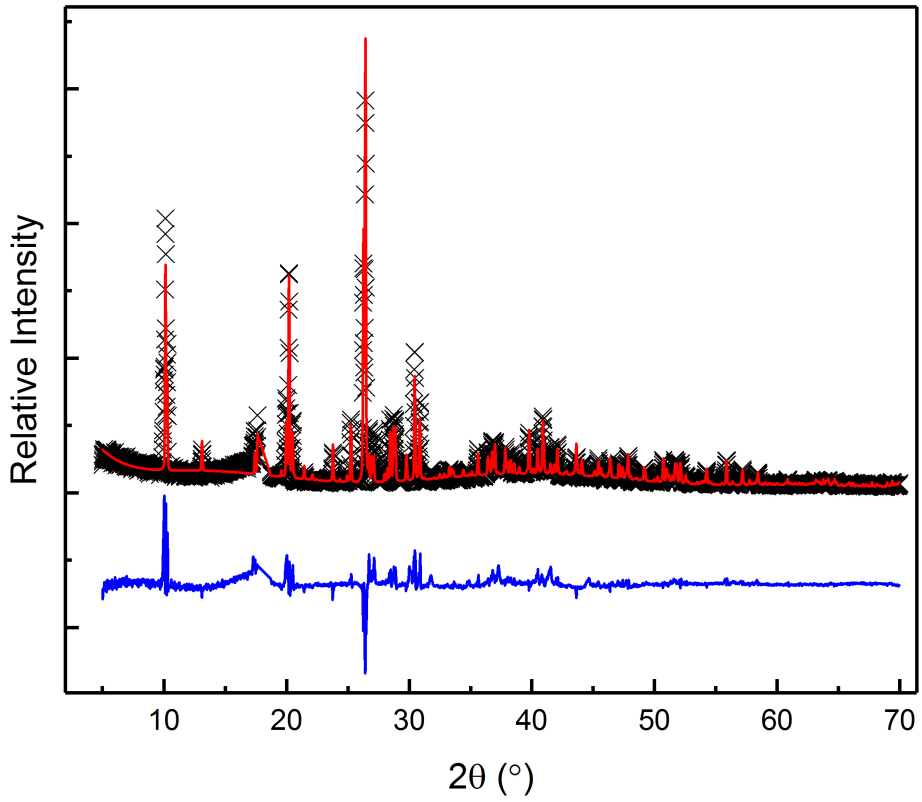

Figure 4.21: Rietveld refinement profile of $(C_3NO_2H_7)_3Ca_{0.9}Sr_{0.1}Cl_2$ (TSCC 10 % Sr). (black) observed diffraction patter, (red) simulated pattern and (blue) calculated difference. χ^2 = 11.14, wRp = 19.04 % and Rp = 14.44 %

Table 4.18: Lattice parameters of TSCC-TSSC solid solutions from Rietveld refinement of powder X-ray diffraction data

Composition	Space group	*a* (Å)	*b* (Å)	*c* (Å)	β (°)	χ^2	Rp (%)	wRp (%)
TSCC	*Pnma*	9.1589(8)	17.481(1)	10.2746(8)	90.00	37.51	17.21	23.34
TSCC 10 % Sr	*Pnma*	9.1198(5)	17.4424(9)	10.2504(6)	90.00	11.14	14.44	19.04
TSCC 20 % Sr	*Pnma*	9.1278(8)	17.471(1)	10.2682(8)	90.00	13.38	08.34	25.06
TSCC 30 % Sr	*Pnma*	9.1379(8)	17.491(1)	10.2770(9)	90.00	110.3	24.66	34.08
TSCC 40 % Sr	*Pnma*	9.1191(1)	17.495(2)	10.279(1)	90.00	126.4	27.52	37.58
TSCC 50 % Sr	*Pnma*	9.1038(1)	17.517(3)	10.291(1)	90.00	114.6	27.62	37.18
TSCC 60 % Sr	$P2_1/a$	8.8124(8)	17.906(1)	10.392(1)	92.026(5)	128.9	27.46	36.02
TSCC 70 % Sr	$P2_1/a$	8.8104(6)	17.907(1)	10.3892(8)	92.024(4)	81.92	20.91	28.82
TSCC 80 % Sr	$P2_1/a$	8.8077(5)	17.9046(7)	10.387(1)	92.033(4)	88.65	22.59	30.22
TSCC 90 % Sr	$P2_1/a$	8.7987(3)	17.9106(7)	10.3993(4)	92.002(2)	63.69	18.04	24.20
TSSC	$P2_1/a$	8.8027(3)	17.9131(4)	10.4025(7)	92.001(2)	22.84	12.65	17.19

The evolution of each of the unit cell parameters with apparent strontium content is depicted in Figure 4.22. The unit cell parameter *a* decreases gradually as additional strontium is incorporated into the structure. However, there is a distinct jump in the lattice parameter at around 60 % strontium where the orthorhombic *Pnma* model is surpassed by the monoclinic $P2_1/a$ model. This suggests that a complete solid solution is not formed between the two end members of the series, strontium can be substituted into the structure to a certain extent forming partial solid solutions. Similar trends are observed in the *b* and *c* unit cell parameters, however, the β angle remains almost constant within each structural model.

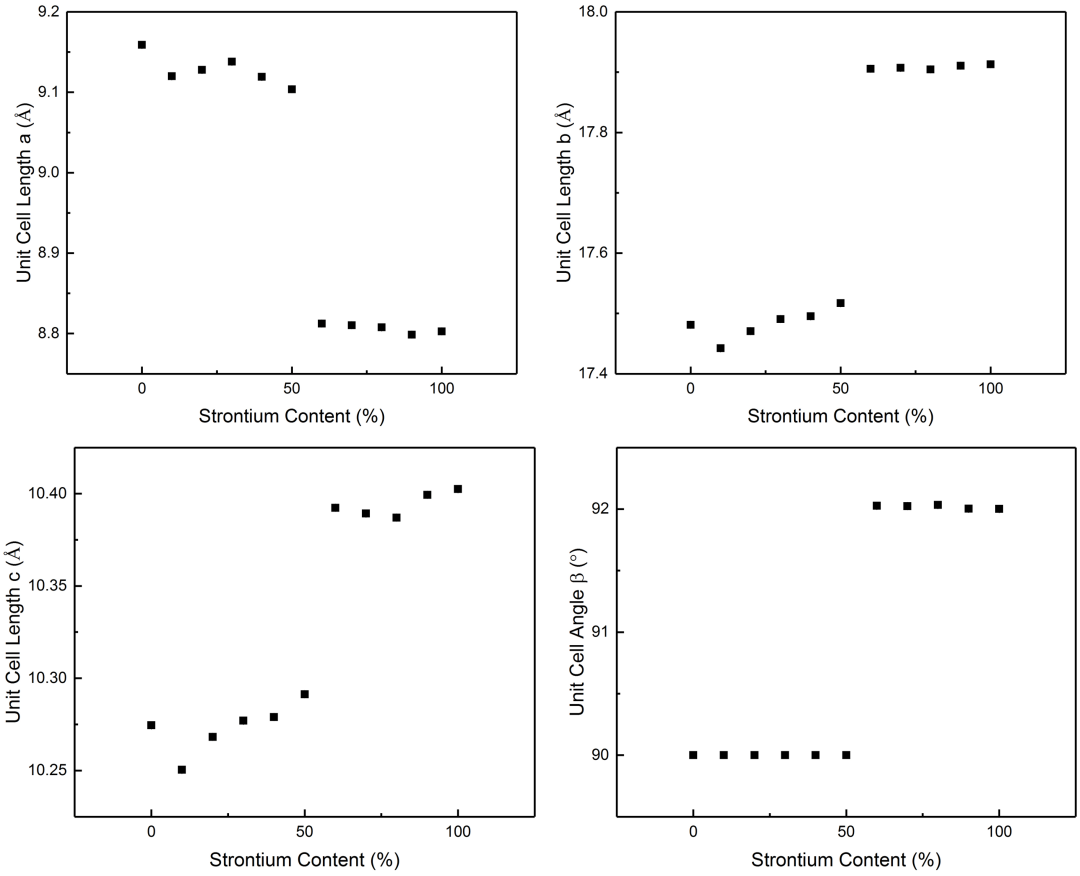

Figure 4.22: Evolution of lattice parameters *a*, *b*, *c* and β with strontium content of TSCC as determined from powder X-ray diffraction data collected at ambient temperature using the Rietveld method

Since bromination of the parent structure TSCC was known to supress the transition temperature towards zero, it was decided to investigate the effect of strontium doping.

Differential scanning calorimetry was employed as a means of tracking the Curie temperature, T_C. Initially, the non-doped TSCC compound was measured, and did exhibit a small peak around −150 ˚C corresponding roughly to the known ferroelectric phase transition. Similar analysis was undertaken for the lower concentrations of strontium doping as shown in Figures 4.23 and 4.24. Despite the large amount of background noise in the acquired data, the presence of a phase transition can be observed at low amounts of strontium substitution. Unlike bromination, which altered the transition temperature, strontium doping does not appear to have a significant effect on the temperature at which this occurs. The region surrounding the known transition temperature was investigated in more detail as shown in Figure 4.24. Above 20 % strontium substitution, there is no evidence of a phase transition.

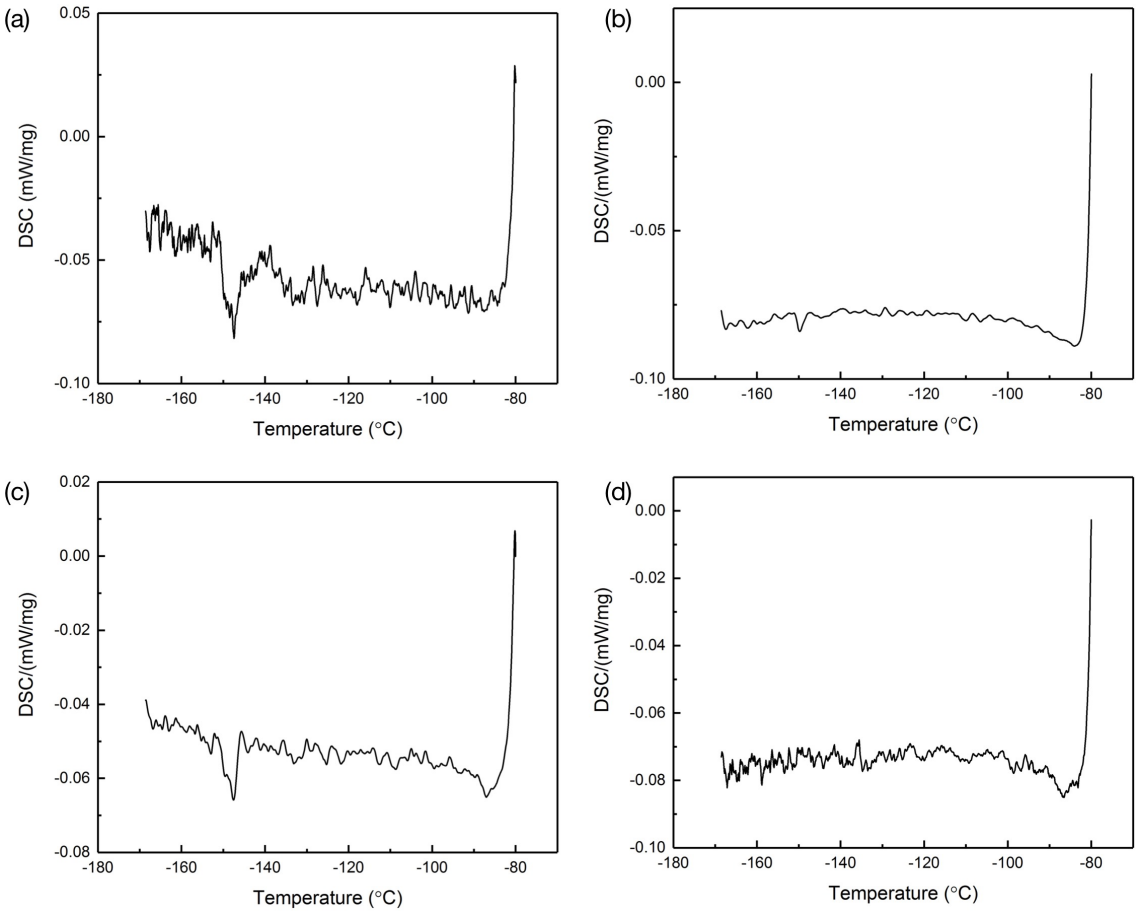

Figure 4.23: Differential scanning calorimetry data collected between −170 and −80 °C at a cooling rate of 5 °C/min. (a) TSCC, (b) TSCC 10 % Sr, (c) TSCC 20 % Sr and (d) TSCC 30 % Sr

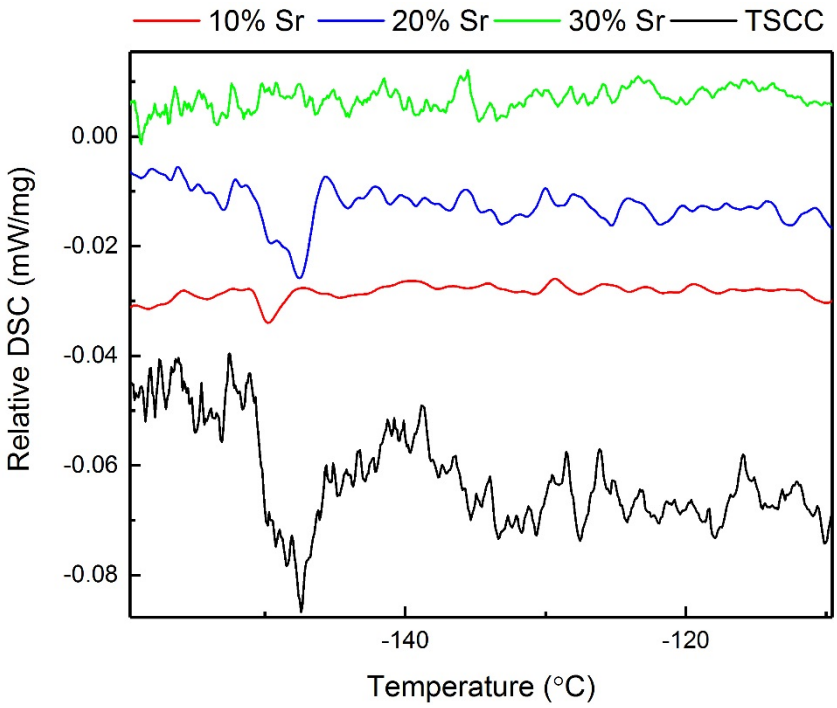

Figure 4.24: Differential scanning calorimetry data from left to right of TSCC, TSCC 10 % Sr, TSCC 20 % Sr and TSCC 30 % Sr between −160 and −110 ˚C

4.3.5 Strontium Doping of TSCB

A similar series of compounds were synthesised with the compositions $(Sar)_3Ca_{0.9}Sr_{0.1}Br_2$ to $(Sar)_3Ca_{0.1}Sr_{0.9}Br_2$ using the same methods. As previously seen in the chloride series, single crystals of each composition proved to be difficult to synthesise in high quality and therefore the majority of the analysis was undertaken using powder X-ray diffraction.

A single crystal sample containing ~50 % strontium was also analysed using X-ray diffraction and again the structure was more consistent with the parent compound TSCB than with the strontium bromide analogue. The crystallographic and refinement details are shown in Table 4.19. The structure remains in the orthorhombic *Pnma* space group with no indication of the unit cell doubling which is observed in TSSB. However, the incorporation of strontium is suggested by changes in the unit cell parameters and in the elongation of the Ca/Sr-O bond (Table 4.20). The atomic displacement parameters

also suggest the incorporation of an atom with a higher electron density than calcium. The occupancy of the metal site was refined to 60. 5(6) % calcium.

Table 4.19: Crystallographic and refinement details of $(C_3NO_2H_7)_3Ca_{0.5}Sr_{0.5}Br_2$ (TSCB 50 % Sr) derived from single crystal X-ray diffraction data collected at 173 K

Parameter	TSCB 50 % Sr
Formula	$(C_3NO_2H_7)_3Ca_{0.5}Sr_{0.5}Br_2$
Formula Weight	486.60
Density (g cm^{-3})	1.895
Crystal System	Orthorhombic
Space Group	*Pnma*
a/Å	9.1728(7)
b/Å	17.8422(14)
c/Å	10.4200(8)
α (˚)	90
β (˚)	90
γ (˚)	90
V/$Å^3$	1705.4(2)
Z	4
Measured Ref	16650
Independent Ref	2020 [R(int) = 0.0841]
Refined Parameter	150
GOOF	0.895
Final R Indices (I > 2σ(I))	R1 = 0.0384, wR2 = 0.1120

Table 4.20: Comparison of metal oxygen bond lengths (Å) in TSCB 50 % and pure TSCB derived from single crystal X-ray diffraction data collected at 173 K

Bond	TSCB	TSCB 50 % Sr
M-O	2.2935(15)	2.324(4)
	2.2936(15)	2.324(4)
	2.305(2)	2.344(5)
	2.3671(19)	2.428(5)
	2.3816(14)	2.444(4)
	2.3816(14)	2.444(4)

Since the single crystal data indicated that strontium could be introduced into the structure, an entire series of compositions were synthesised between TSCB and TSSB in 10 % increments. Their lattice parameters and strontium content were determined using powder X-ray diffraction and the Rietveld method. The lattice parameters and refinement details are shown in Table 4.21.

Table 4.21: Lattice parameters of TSCB-TSSB solid solutions from Rietveld refinement of powder X-ray diffraction data collected at ambient temperature

Composition	Space group	a (Å)	b (Å)	c (Å)	χ^2	Rp (%)	wRp (%)
TSCB	*Pnma*	9.2670(4)	17.7680(6)	10.4004(4)	43.08	16.74	21.39
TSCB 10 % Sr	*Pnma*	9.2350(5)	17.7742(9)	10.4017(6)	138.1	26.89	35.45
TSCB 20 % Sr	*Pnma*	9.260(1)	17.786(1)	10.4047(7)	118.4	26.87	34.77
TSCB 30 % Sr	*Pnma*	9.2490(5)	17.808(1)	10.4118(6)	89.15	20.13	26.54
TSCB 40 % Sr	*Pnma*	9.2432(7)	17.814(1)	10.4162(7)	75.6	19.08	26.46
TSCB 50 % Sr	*Pnma*	9.1846(6)	17.936(1)	10.4480(7)	63.63	18.01	23.88
TSCB 60 % Sr	*Pnma*	9.1796(7)	17.971(1)	10.4609(7)	92.36	20.71	28.02
TSCB 70 % Sr	*Pnma*	9.1354(5)	17.971(1)	10.4809(6)	38.3	14.95	20.09
TSCB 80 % Sr	*Pnma*	9.1245(6)	18.038(1)	10.4844(7)	75.57	20.11	25.98
TSCB 90 % Sr	*Pnma*	9.058(1)	18.055(2)	10.496(1)	63.26	29.78	38.07
TSSB	*Pcab*	8.8802(5)	36.633(2)	10.5521(7)	68.12	19.44	25.78

Unlike the chloride analogues, the smooth evolution of the lattice parameters indicate that a solid solution is formed between the two parent compounds as shown in Figure 4.25. Even at high concentrations of strontium the TSCB *Pnma* model remains valid until almost 100 % strontium content. Since neither of the end members of the solid solution showed any evidence of a low temperature phase transition, DSC analysis was not undertaken for the intervening compositions.

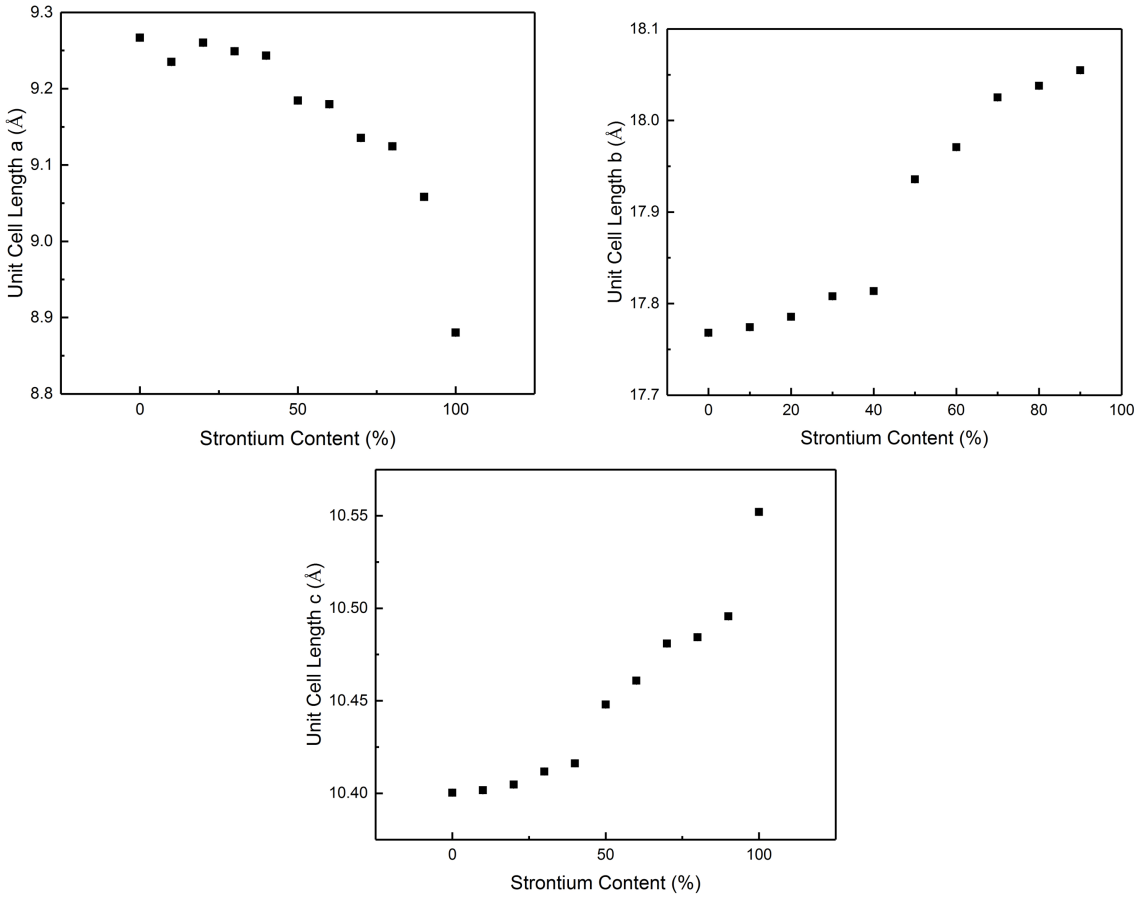

Figure 4.25: Evolution of lattice parameters *a*, *b* and *c* of TSCB with increasing strontium content as determined from powder X-ray diffraction data collected at ambient temperature using the Rietveld method

4.3.6 Hydrated 3:1 Compositions

4.3.6.1 Tris Sarcosine Manganese Iodide Dihydrate

A TSCC derivative containing manganese iodide was also synthesised by the same slow evaporation method and its crystal structure was determined from X-ray diffraction. The compound's structure has many similarities to TSCC and its crystal structure is shown in Figure 4.26. The overall ratio of metal to halide remains as 3:1 and the pseudohexagonal symmetry is maintained. A key difference is observed in the coordination environment of the manganese centre which now contains two additional water molecules. The complete refinement and crystallographic details are shown in Table 4.22. The space group remains as orthorhombic *Pnma* and the unit cell parameters *a* and *c* remain virtually unchanged, but the unit cell parameter *b* increases by ~2 Å to accommodate the extra water molecules.

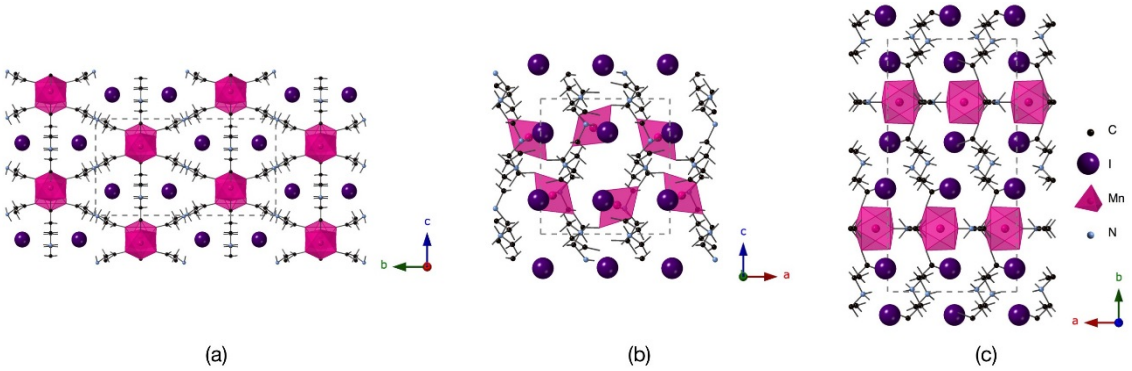

Figure 4.26: Crystal structure of $(C_3NO_2H_7)_3MnI_2.2H_2O$ (TSMnI) derived from single crystal X-ray diffraction data collected at 293 K viewed along the *a*, *b* and *c* axes

Table 4.22: Crystallographic data and refinement details of TSMnI collected at 173 and 293 K

	93 K	**173 K**	**293 K**
Formula	$(C_3NO_2H_7)_3MnI_2$	$(C_3NO_2H_7)_3MnI_2$	$(C_3NO_2H_7)_3MnI_2$
Formula Weight	612.06	612.06	612.06
Density (g cm^{-3})	2.110	2.093	2.073
Crystal System	Orthorhombic	Orthorhombic	Orthorhombic
Space Group	*Pnma*	*Pnma*	*Pnma*
a/Å	9.8036(15)	9.8288(7)	9.8652(7)
b/Å	19.1420(3)	19.2160(15)	19.2670(15)
c/Å	10.2673(17)	10.2845(8)	10.3186(8)
α (˚)	90	90	90
β (˚)	90	90	90
γ (˚)	90	90	90
V/$Å^3$	1926.8(4)	1942.4(3)	1961.3(3)
Z	4	4	4
Measured Ref	11309	18998	19214
Independent Ref	1797 [R(int) = 0.0393]	2301 [R(int) = 0.0992]	2323 [R(int) = 0.0978]
Refined Parameter	158	147	147
GOOF	1.178	0.978	0.977
Final R Indices (I > 2σ(I))	R1 = 0.0349, wR2 = 0.1189	R1 = 0.0406, wR2 = 0.0947	R1 = 0.0421, wR2 = 0.0964

Table 4.23: Selected bond lengths (Å) and bond valence sums (valence units) of TSMnI derived from single crystal X-ray diffraction data collected at 173 and 293 K

Bond	93 K	173 K	293 K
M-O	2.151(4)	2.155(6)	2.151(6)
	2.198(4)	2.192(6)	2.199(6)
	2.200(2)	2.200(4)	2.203(4)
	2.200(2)	2.200(4)	2.203(4)
	2.207(2)	2.208(4)	2.209(5)
	2.207(2)	2.208(4)	2.209(5)
N-H-X	3.495(3)	3.503(4)	3.515(4)
	3.539(3)	3.549(5)	3.565(6)
	3.692(3)	3.692(5)	3.709(5)
BVS (Mn)	2.02	2.02	2.04

The coordination of the manganese centre remains as six as seen in the previous calcium containing derivatives, but the incorporation of water molecules results in a significant change in the connectivity of the octahedra within the structure. Each of the manganese cations is coordinated to four different sarcosine molecules, two of which act as bidentate bridging ligands and two as monodentate ligands. The water molecules occupy the remainder of the coordination environment, as shown more clearly in Figure 4.27. As a result, each octahedron is connected to the next by only one sarcosine molecule as opposed to the three in the original compounds. The alteration of the octahedra chains is shown in Figure 4.28 and compared to TSCC.

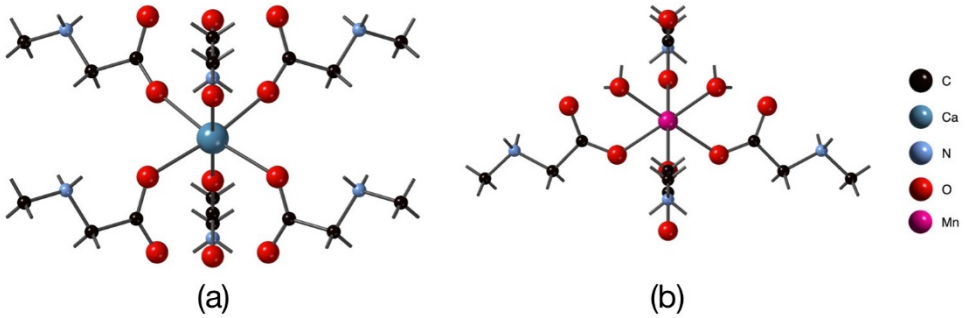

Figure 4.27: Coordination sphere and connectivity of the manganese octahedra in TSMnI derived from single crystal X-ray diffraction data collected at 293 K

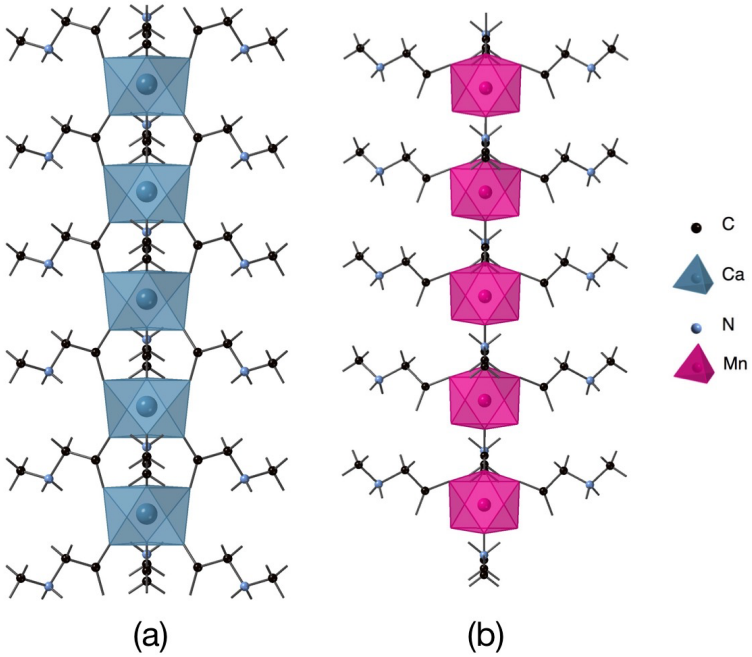

Figure 4.28: Comparison of polyhedra connectivity in (a) TSCC and (b) TSMnI derived from single crystal X-ray diffraction data collected at 293 K

Due to the similarities with the TSCC structure, the compound did not possess any ferroelectric properties at 293 K, but further investigation was undertaken to probe both its structure and properties at low temperatures. Initially the structure was analysed by X-ray diffraction at 173 K to analyse any differences in structure from the room temperature model. The crystallographic and refinement details are shown in Table 4.22 and the bond lengths in Table 4.23. However, upon inspection of the diffraction data, there were no indications of a significant change in the compound's structure which could produce ferroelectric properties and the orthorhombic *Pnma* model remains valid down to this temperature.

Even lower temperatures could be reached using differential scanning calorimetry analysis and the results for TSMnI are show in Figure 4.29. However, the data do not provide any evidence of a phase transition within the temperature range of −170 °C to −80 °C. The thermal gravimetric analysis showed that the compound was stable to ~100 °C, the initial loss of mass corresponds to the loss of the hydrates.

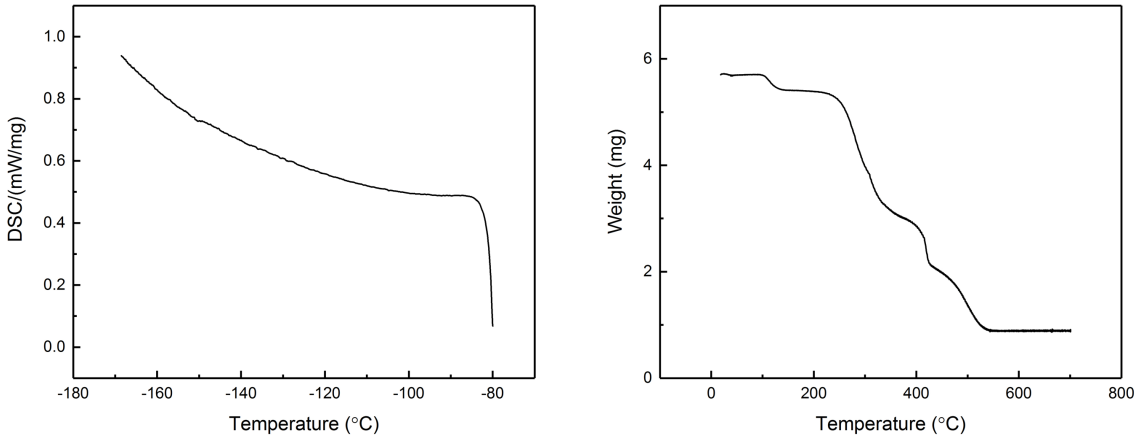

Figure 4.29: (left) Differential Scanning Calorimetry data of TSMnI measured between −170 ˚C and −80 ˚C at a cooling rate of 5 °C/min. (right) Thermal Gravimetric Analysis data of TSMnI between room temperature and 700 °C collected at 5 °C/min

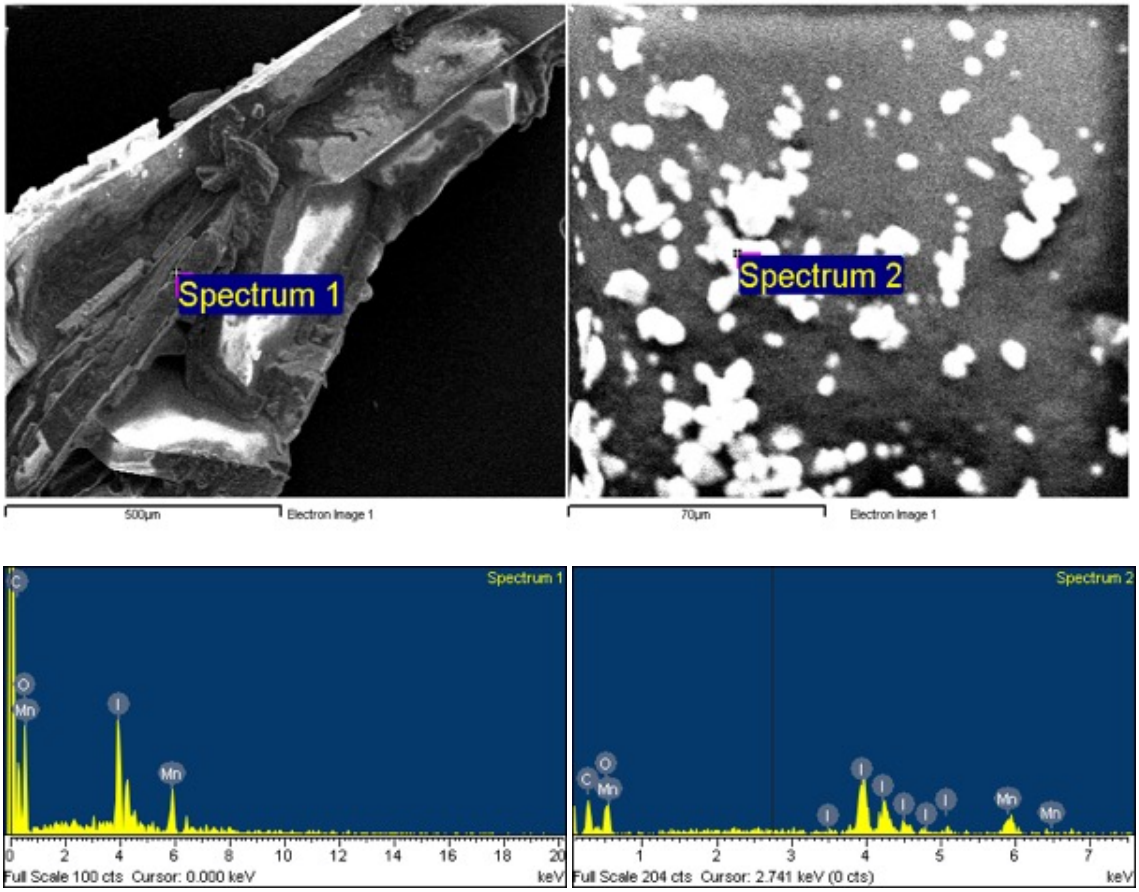

Figure 4.30: Scanning Electron Microscopy images and Energy Dispersive X-ray data of TSMnI. (left) crystalline samples and (right) powdered sample

The structure and purity of the compound were probed using Energy Dispersive X-ray analysis and powder X-ray diffraction. Both the crystalline and powdered products were

analysed and their data shown in Figure 4.30. The data confirm the composition of the compound as a manganese iodide. The purity of the compound was further confirmed with the powder X-ray diffraction data refined to the structural model derived from X-ray diffraction data. This revealed a reasonably good fit to the proposed model with only trace amounts of impurity as shown in Figure 4.31.

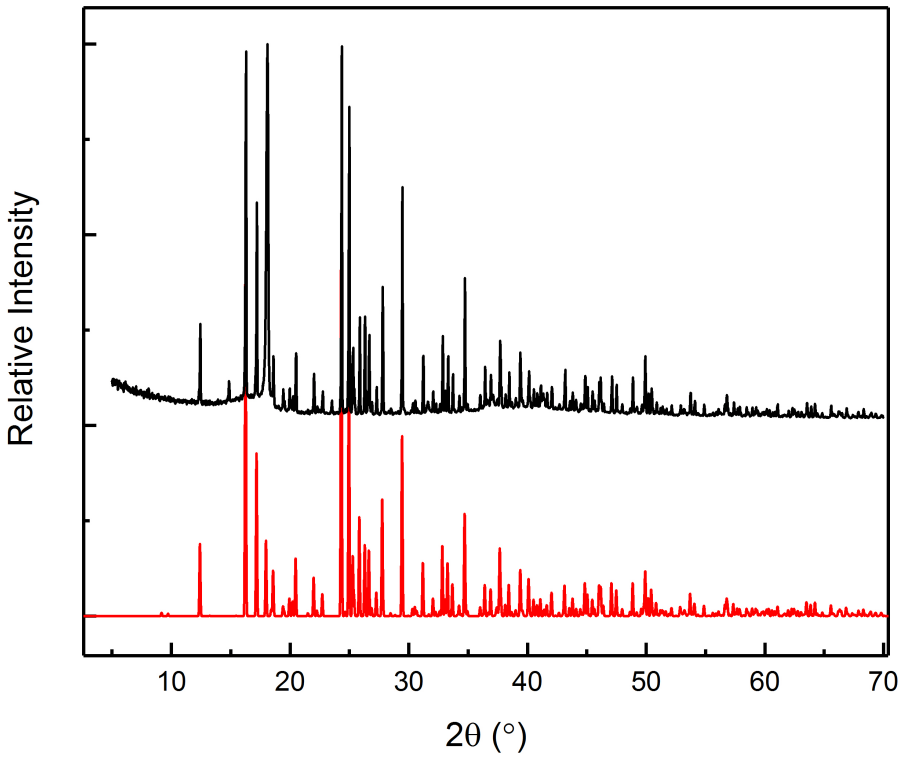

Figure 4.31: Comparison of experimental powder X-ray diffraction data (black) of TSMnI and simulated data (red) from powder X-ray diffraction data collected at ambient temperature

4.3.6.2 Tris Sarcosine Magnesium Bromide Dihydrate

A second compound, isostructural to the manganese iodide derivative (TSMnI) was synthesised in the form of $(C_3NO_2H_7)_3MgBr_2.2H_2O$ (TSMgB) starting from stoichiometric quantities of the reagents. The structure was determined using single crystal X-ray diffraction at room temperature and at 173 K. The crystal structure is shown in Figure 4.32 and the crystallographic data and refinement details are shown in Table 4.24. The compound has the same structure, bonding and connectivity previously seen in the manganese iodide derivative. Since the compound crystallises in the orthorhombic

Pnma space group at room temperature, it does not have any ferroelectric properties at room temperature.

A second data set was measured at 173 K to investigate any structural changes which could produce a phase transition. The crystallographic details and selected bond lengths are shown in Tables 4.24 and 4.25. The bond lengths remain almost unaffected by temperature, but the unit cell parameters decrease slightly at lower temperatures as expected. However, there was no evidence for a change in unit cell or symmetry which would indicate a phase transition.

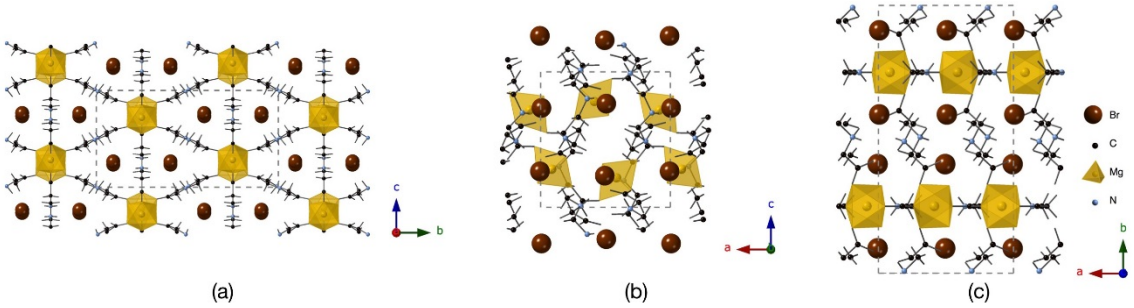

Figure 4.32: The crystal structure of TSMgB derived from single crystal X-ray diffraction data collected at 293 K viewed along the *a*, *b* and *c* axes

Table 4.24: Crystallographic and refinement details of TSMgB from single crystal X-ray diffraction data collected at 173 K and 293 K

	173 K	**293 K**
Formula	$(C_3NO_2H_7)_3MgBr_2.2H_2O$	$(C_3NO_2H_7)_3MgBr_2.2H_2O$
Formula Weight	487.45	487.45
Density (g cm^{-3})	1.793	1.779
Crystal System	Orthorhombic	Orthorhombic
Space Group	*Pnma*	*Pnma*
a/Å	9.5844(6)	9.6161(8)
b/Å	18.9445(13)	18.9415(18)
c/Å	9.9448(6)	9.9930(9)
α (˚)	90	90
β (˚)	90	90
γ (˚)	90	90
V/$Å^3$	1805.7(2)	1820.2(3)
Z	4	4
Measured Ref	17644	5918
Independent Ref	2139 [R(int) = 0.0624]	1952 [R(int) = 0.0977]
Refined Parameter	166	166
GOOF	0.794	0.892
Final R Indices (I > 2σ(I))	R1 = 0.0288, wR2 = 0.0868	R1 = 0.0506, wR2 = 0.1188

Table 4.25: Selected bond lengths (Å) and bond valence sums (valence units) of TSMgB determined at 173 K and 293 K

Bond	173 K	293 K
M-O	2.019(3)	2.018(7)
	2.082(2)	2.083(5)
	2.082(2)	2.083(5)
	2.096(2)	2.094(5)
	2.096(2)	2.094(5)
	2.102(3)	2.110(7)
N-H-X	3.3203(17)	3.318(5)
	3.422(3)	3.437(7)
	3.483(3)	3.487(7)
BVS (Mg)	2.12	2.11

A second technique, differential scanning calorimetry, was used to investigate low temperature structural changes in TSMgB. The cooling data between −170 and −80 °C is shown in Figure 4.33. Despite a slight peak in the data around 150 °C there is no strong evidence for a significant structural change or phase transition in the data obtained. The powder X-ray diffraction data were measured and compared to the simulated data to examine the purity of the sample as shown in Figure 4.34 indicating a high level of purity.

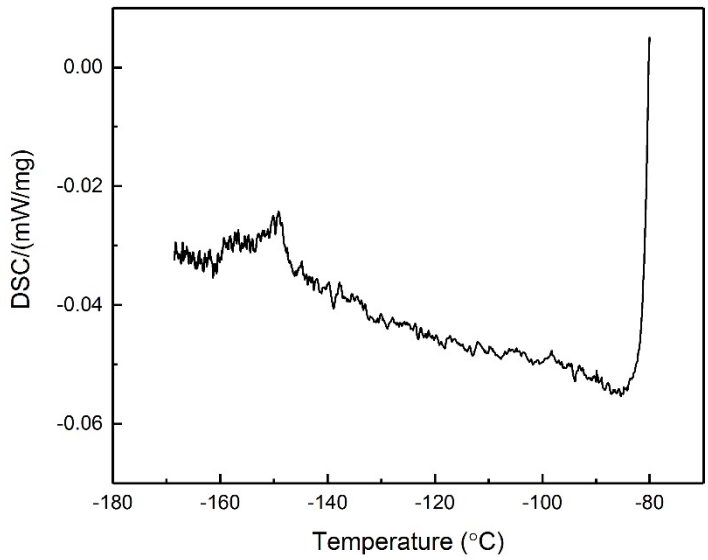

Figure 4.33: Differential scanning calorimetry data of TSMgB collected between −170 °C and −80 °C at a cooling rate of 5 ˚C/min

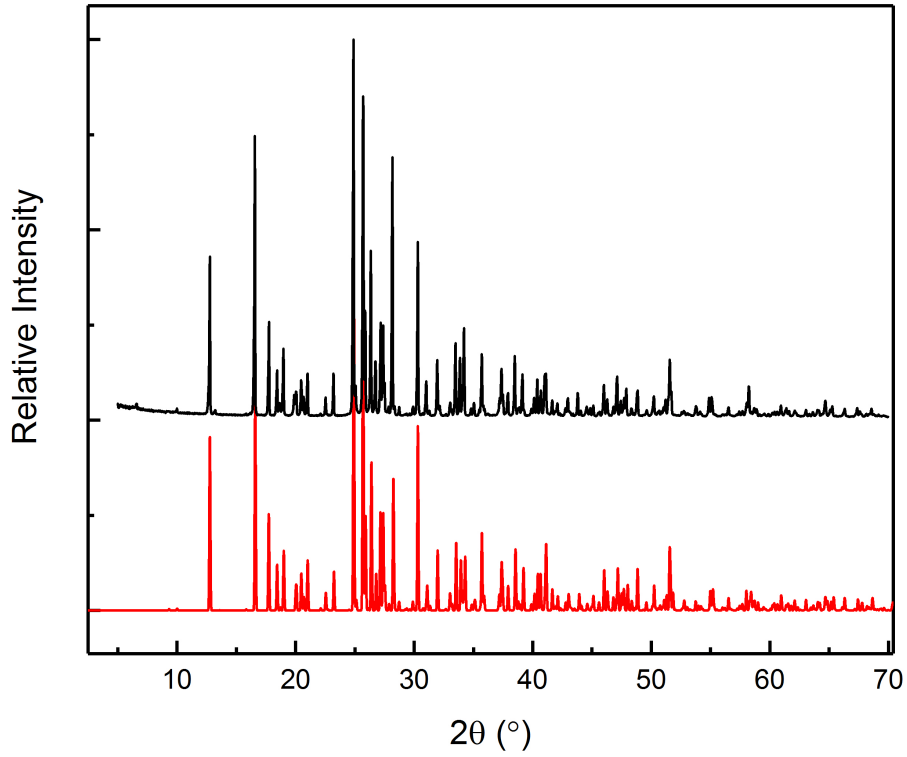

Figure 4.34: Comparison of experimental powder X-ray diffraction data (black) of TSMgB and simulated data (red) from powder X-ray diffraction data collected at ambient temperature

4.3.7 Hydrated 2:1 Compositions

Two further compounds with a 2:1 sarcosine to metal ratio were synthesised by the same methods. The two compounds, bis sarcosine magnesium chloride dihydrate and bis sarcosine manganese chloride dihydrate, are isostructural although the manganese chloride compound has been previously synthesised.[7,8] The compounds are also isostructural to the 2:1 calcium iodide derivative reported earlier in this chapter and their crystallographic data are shown in Table 4.26.

Table 4.26: Crystallographic data and refinement details of $(C_3NO_2H_7)_2MgCl_2.2H_2O$ (BSMgC) and $(C_3NO_2H_7)_2MnCl_2.2H_2O$ (BSMnC) collected at 173 K and 293 K

Parameter	BSMgC	BSMgC	BSMnC
Formula	$(C_3NO_2H_7)_2MgCl_2.2H_2O$	$(C_3NO_2H_7)_2MgCl_2.2H_2O$	$(C_3NO_2H_7)_2MnCl_2.2H_2O$
Temperature (K)	173	293	173
Formula Weight	309.43	309.43	340.06
Density (g cm^{-3})	1.520	1.499	1.630
Crystal System	Triclinic	Triclinic	Triclinic
Space Group	$P\bar{1}$	$P\bar{1}$	$P\bar{1}$
a/Å	4.7711(4)	4.7825(5)	4.8078(4)
b/Å	5.3186(4)	5.3422(5)	5.3548(4)
c/Å	13.5193(12)	13.6722(14)	13.6620(12)
α (˚)	84.365(12)	84.343(17)	83.825(12)
β (˚)	82.080(12)	80.426(17)	82.288(12)
γ (˚)	87.969(12)	88.026(17)	87.503(12)
V/Å^3	338.06(5)	342.71(6)	346.37(5)
Z	1	1	1
Measured Ref	3423	3529	3548
Independent Ref	1536 [R(int) = 0.0467]	1560 [R(int) = 0.0600]	1574 [R(int) = 0.0497]
Refined Parameter	96	96	115
GOOF	1.639	1.335	0.815
Final R Indices (I > 2σ(I))	R1 = 0.0625, wR2 = 0.2379	R1 = 0.0648, wR2 = 0.2188	R1 = 0.0429, wR2 = 0.1082

4.3.7.1 Bis Sarcosine Magnesium Chloride Dihydrate

The crystal structure of the newly synthesised BSMgC is shown in Figure 4.35. The structure consists of MgO_6 octahedra which are connected by sarcosine ligands and weak hydrogen bonding. Selected bond lengths and bond valence sum values are shown in Table 4.27. The second data set collected at 173 K did not provide any evidence of a phase transition, the unit cell lengths do not alter significantly with temperature and the unit cell parameters merely contract slightly at lower temperatures. This is supported

by DSC data measured between −80 °C and −170 °C (Figure 4.36) which showed no significant changes in structure in this temperature range. The structure and purity are further confirmed by the powder X-ray diffraction data as shown in Figure 4.37.

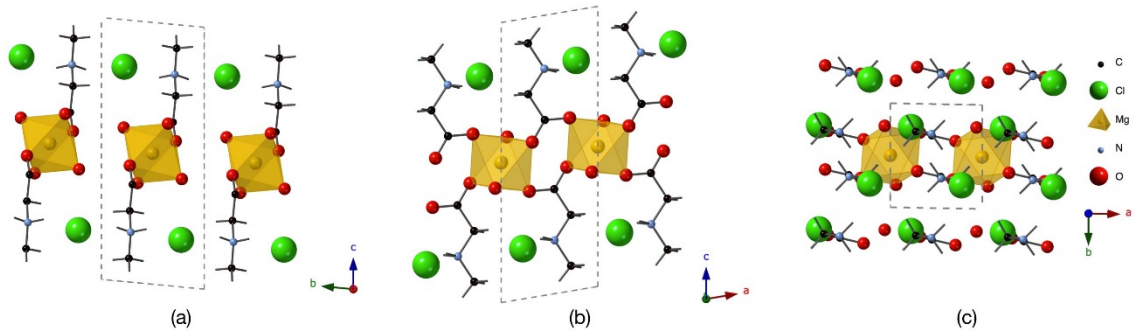

Figure 4.35 The crystal structure of BSMgC derived from single crystal X-ray diffraction data collected at 293 K viewed along the *a*, *b* and *c* axes

Table 4.27: Selected bond lengths (Å) and bond valence sums (valence units) of BSMgC determined at 173 K and 293 K

Bond	173 K	293 K
M-O	2.066(4)	2.069(3)
	2.066(4)	2.069(3)
	2.073(4)	2.075(3)
	2.073(4)	2.075(3)
	2.102(4)	2.105(4)
	2.102(4)	2.105(4)
N-H-X	3.124(4)	3.130(4)
	3.079(5)	3.098(5)
BVS (Mg)	2.11	2.09

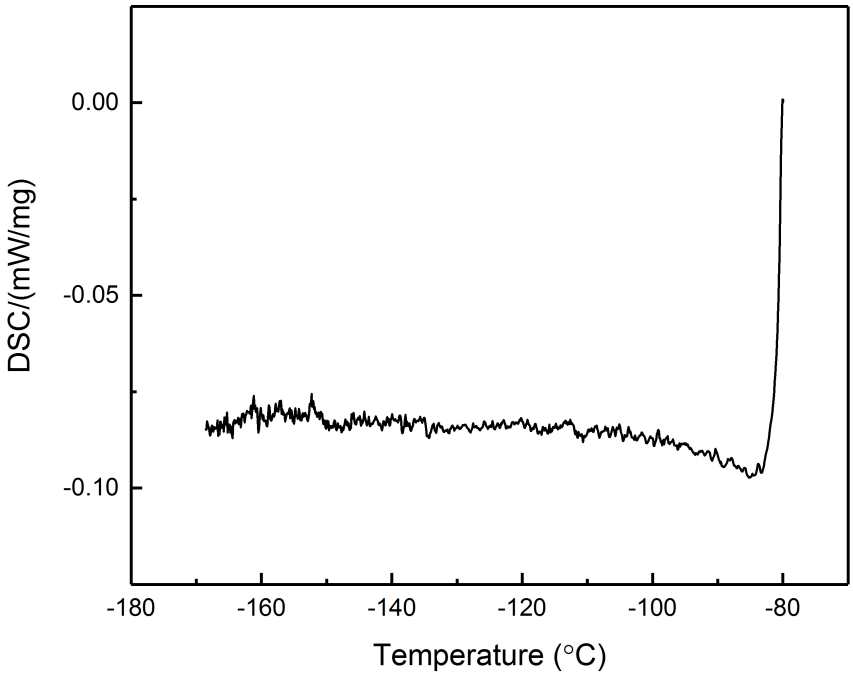

Figure 4.36: Differential Scanning Calorimetry data of BSMgC collected between −170 and −80 °C at a cooling rate of 5 °C/min

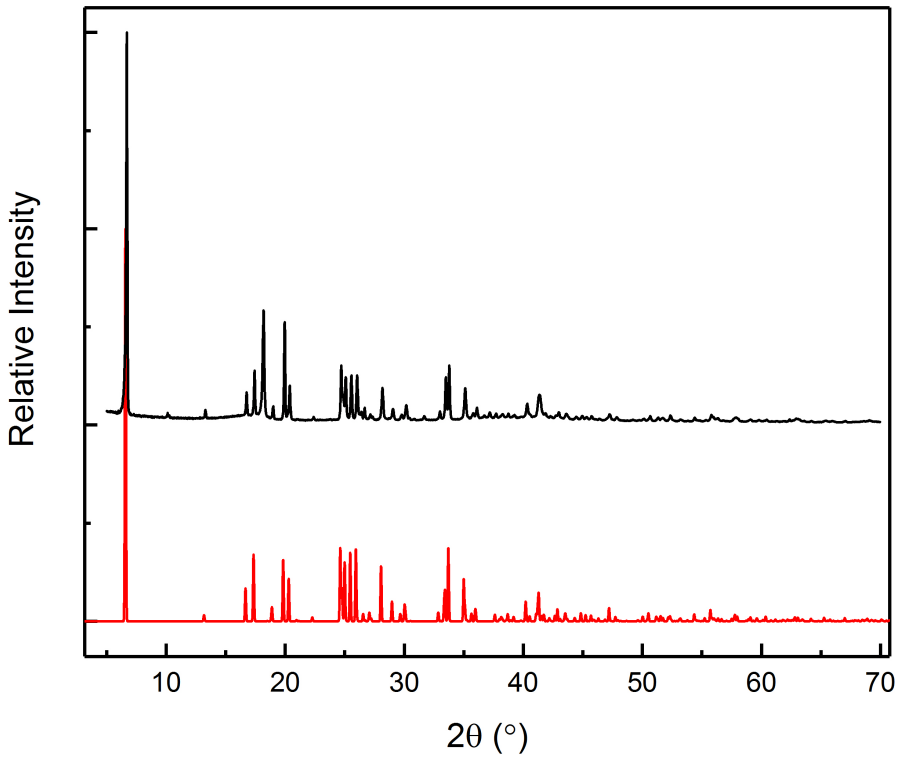

Figure 4.37: Comparison of experimental powder X-ray diffraction data (black) of BSMgC and simulated data (red) from powder X-ray diffraction data collected at ambient temperature

4.3.7.2 Bis Sarcosine Manganese Chloride Dihydrate

Single crystals of $(C_3NO_2H_7)_2MnCl_2.2H_2O$ were synthesised in the same way as the earlier derivatives and analysed by X-ray diffraction. The structure of $(C_3NO_2H_7)_2MnCl_2.2H_2O$ (BSMnC) has been previously reported by both Rzaczynska *et al*. and Pedras *et al*. but was only determined at room temperature.[7,8] The data were recollected at 173 K to investigate any changes to the structure at low temperature. The crystallographic data are shown in Table 4.26 and its crystal structure is shown in Figure 4.38. The low temperature data set is consistent with the room temperature data from the literature, indicating that there was no phase transition between room temperature and 173 K. This conclusion is supported by the differential scanning calorimetry data, Figure 4.39, which showed no substantial changes in structures.

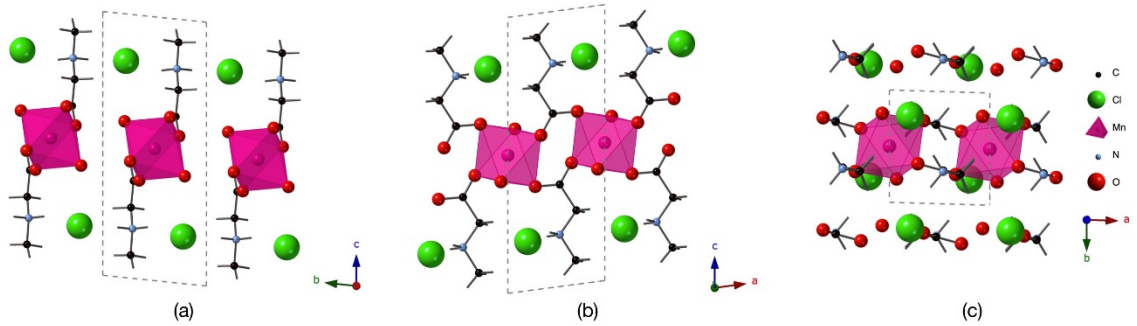

Figure 4.38: The crystal structure of BSMnC derived from single crystal X-ray diffraction data collected at 293 K viewed along the *a*, *b* and *c* axes

Thermal gravimetric analysis revealed that the compound was stable to ~100 °C and that the initial decomposition step corresponds to the loss of both water molecules from the structure, further confirming the proposed structural model. The purity of the compound is also confirmed by the powder X-ray diffraction data which is shown in Figure 4.40.

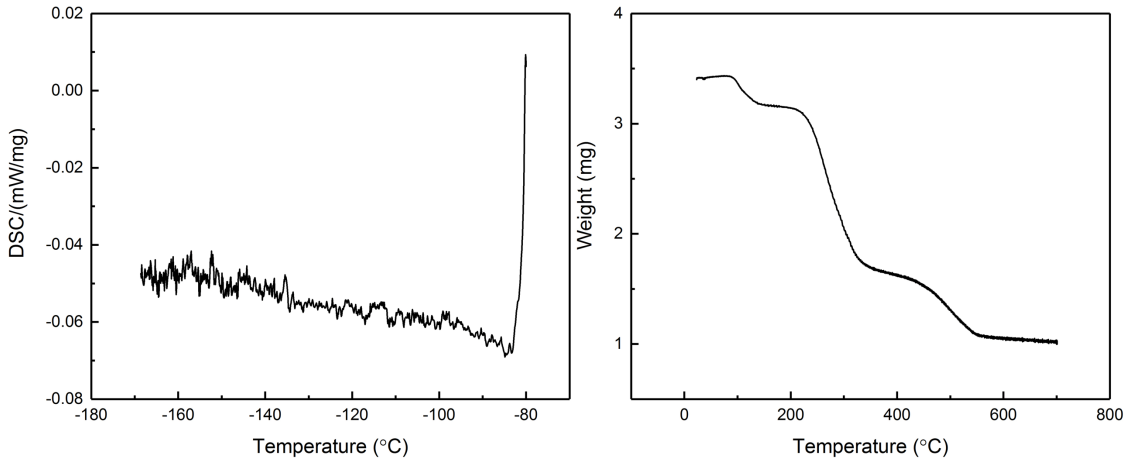

Figure 4.39: (left) Differential scanning calorimetry data of BSMnC measured between −170 and −80 °C at a cooling rate of 5 °C/min. (right) Thermal Gravimetric Analysis Data of BSMnC between room temperature and 700 °C

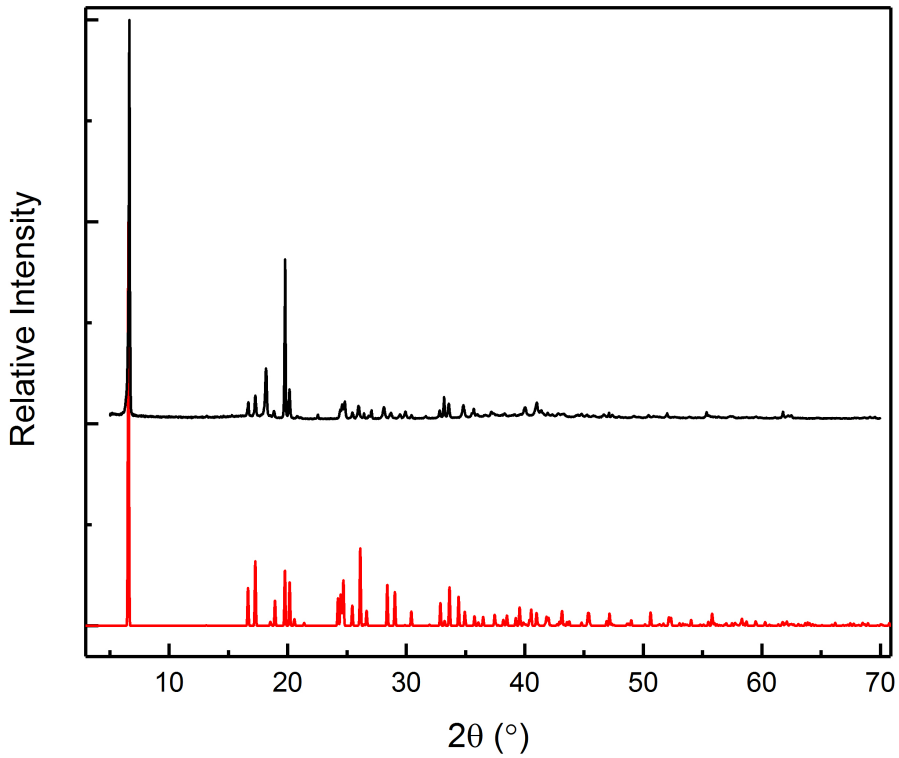

Figure 4.40: Comparison of experimental powder X-ray diffraction data (black) of BSMnC and simulated data (red) from powder X-ray diffraction data collected at ambient temperature

4.4 Conclusions

Several new sarcosine complexes related to TSCC have been synthesised using a simple slow evaporation method from stoichiometric quantities of reagents and generally in the form of single crystals. Several different structure types were formed but all containing the same building blocks of bidentate sarcosine ligands which form linkages between metal centres to create infinite polyhedron chains. In each case, the halide ions interconnect the structures by weak hydrogen bonding. The structures can be classified into four distinct types, anhydrous 3:1, hydrated 3:1, hydrated 2:1 and hydrated 4:1 compositions. Each of the structure types displays slightly different connectivity of its metal two plus cations as shown in Figure 4.41.

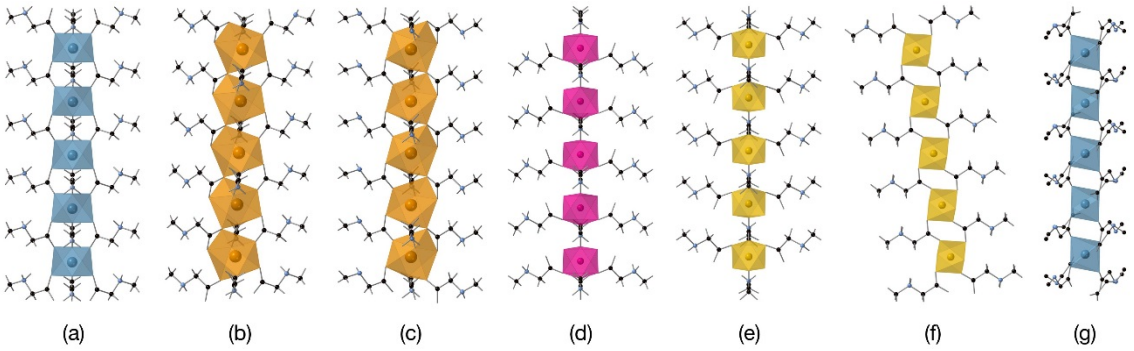

Figure 4.41: Connectivity of the metal cation polyhedra in various TSCC derivatives all derived from single crystal X-ray diffraction data collected at 293 K. (a) TSCB, (b) TSSC, (c) TSSB, (d) TSMnI, (e) TSMgB, (f) BSMgC and (g) TSCl

The previously unreported crystal structure of TSCB was determined using X-ray diffraction data and was consistent with the work of several previous groups who did not observe any ferroelectric properties in the material, even at temperatures approaching absolute zero. This can be rationalised by the non-polar nature of the determined single crystal structure. Similar analysis was undertaken for iodinated derivatives, although in this case the loss of ferroelectric properties can now be attributed to the deviation of the crystal structure from the structure of TSCC to form 2:1 and 4:1 sarcosine metal halide complexes.

The incorporation of the larger metal cation, strontium, led to an increase in coordination around the metal centre and consequently corner sharing of polyhedra for both the chloride and bromide derivatives. The change in coordination number is consistent with the work of Trzebiatowska-Gusowska *et al.*[13] which showed an increase in the coordination number to nine upon the inclusion of the substantially larger barium cation. An interesting result of the change in strontium-oxygen bonding arises in the strontium bromide derivative which exhibits unit cell doubling along the *c* axis.

The third structure type, hydrated 3:1 compositions were formed by the manganese iodide and magnesium bromide derivatives and are the first examples of this structure type in the literature. Both structures were very much reminiscent of the parent compound TSCC but unfortunately were not seen to possess any ferroelectric properties or low temperature phase transitions. However, the manganese containing derivative could potentially have some interesting magnetic properties which should be investigated for completeness.

Three examples of the third structure type, hydrated 2:1 compositions were synthesised in BSCl, BSMnC and BSMgC although the manganese chloride has been previously reported. The newly collected data for BSMnC was consistent with the earlier work of Rzaczynska *et al*.[7] The structures of all three compounds were non-polar and there was no evidence of any structural changes to the compounds within the temperature range of −170 and 25 °C.

The types of structure formed appears to be closely linked to the relative sizes of both the halogen and the metal cation. Incorporation of larger cations resulted in increases in the coordination number of the metal centres and resultant corner sharing of polyhedra, whilst the hydrated 2:1 structures were favoured by the inclusion of smaller metal cations. The substitution of either the halogen or the metal cation appears to be detrimental to the ferroelectric properties of TSCC. The change in properties could potentially be due to changes in composition and the relative sizes of the ions involved,

which affect the structure types formed, however, further work will be needed to investigate this in detail. Both the X-ray diffraction data and the thermal analysis are limited to a low temperature of −180 °C and −170 °C respectively, so there could be additional phase transitions or ferroelectric properties below this point.

4.5 References

1 R. V Krishnakumar and M. Subha, *Acta Crystallogr. Sect. E Struct. Reports Online*, 2001, **3**, m192–m194.

2 P. P. Gawryszewska, L. Jerzykiewicz, P. Sobota and J. Legendziewicz, *J. Alloys Compd.*, 2000, **300**–**301**, 275–282.

3 M. Fleck, V. V. Ghazaryan and A. M. Petrosyan, *Acta Crystallogr. Sect. C Cryst. Struct. Commun.*, 2013, **69**, 11–16.

4 M. Fleck and A. M. Petrosyan, in *Salts of Amino Acids: Crystallization, Structure and Properties*, Springer, 2014, pp. 139–206.

5 T. Ashida, S. Bando and M. Kakudo, *Acta Crystallogr. Sect. B Struct. Crystallogr. Cryst. Chem.*, 1972, **28**, 1560–1565.

6 M. R. Silva, A. M. Beja, J. A. Paixäo, L. A. Veiga, O. H. Ä and O. Mŋ, *Zeitschrift für Krist. NCS*, 2001, **216**, 419–420.

7 Z. Rzaczynska, R. Mrozek and M. Sikorska-Iwan, *Pol. J. Chem.*, 2002, **76**, 29–35.

8 M. Pedras, B. Hachula, M. Nowak and J. Kusz, *CCDC Commun.*, 2014.

9 M. Subha Nandhini, R. V. Krishnakumar and S. Natarajan, *Acta Crystallogr. Sect. E Struct. Reports Online*, 2001, **57**, m435–m437.

10 R. V. Krishnakumar and S. Natarajan, *Cryst. Res. Technol.*, 1995, **30**, 825–830.

11 J. Yamada, H. Hashimoto, Y. Inomata and T. Takeuchi, *Bull. Chem. Soc. Jpn*, 1994, **67**, 3224–3230.

12 T. J. Sabo, V. M. Dinovic, G. N. Kaluderovic, T. P. Stanojkovic, G. A. Bogdanovic and Z. D. Juranic, *Inorganica Chim. Acta*, 2005, **358**, 2239–2245.

13 M. Trzebiatowska-Gusowska, A. Gągor, J. Baran and M. Drozd, *J. Raman Spectrosc.*, 2009, **40**, 315–322.

14 Z. Dauter, A. Hempel and H. Jedrzejczak, *Zeitschrift für Krist.*, 1977, **146**, 320–321.

15 R. Navalgund and L. Gupta, *J. Phys. Soc. Japan*, 1975, **39**, 880–883.

16 T. Hikita and T. Maruyama, *J. Phys. Soc. Japan*, 1992, **61**, 2840–2847.

17 S. Fujimoto, N. Yasuda and H. Kashiki, *J. Phys. D. Appl. Phys.*, 1982, **15**, 487–495.

18 W. Windsch, H. Braeter, U. Gutteck, B. Malige and B. Milsch, *Solid State Commun.*, 1982, **42**, 839–842.

19 S. Fujimoto, N. Yasuda and H. Kashiki, *J. Phys. D. Appl. Phys.*, 1984, **17**, 1019–1028.

20 A. C. Larson and R. B. Von Dreele, *General Structure Analysis System (GSAS)*, 2004.

21 B. H. Toby, *J. Appl. Crystallogr.*, 2001, **34**, 210–213.

22 Rigaku, CrystalClear. Rigaku Corporation, Tokyo, Japan, 2014.

23 G. M. Sheldrick, *Acta Crystallogr. Sect. C Struct. Chem.*, 2015, **71**, 3–8.

24 L. J. Farrugia, *J. Appl. Crystallogr.*, 2012, **45**, 849–854.

Chapter 5 A New Family of Hybrid Perovskites

5.1 Introduction

Perovskites have dominated the field of functional materials and exhibit a wide range of properties including superconductivity, ferroelectricity and magnetism.[1] The introduction of organic components into the traditional perovskite structure could improve both the toxicity and sustainability of the compounds and introduce greater structural diversity. Hybrid perovskites are already a prevalent group of materials and can combine the properties of organic and inorganic components.[2] There are many examples of such compounds with interesting properties.[3,4] Examples incorporating cyanide, formate, azide and tetrahydroborate anions as bridging ligands are numerous.[5,6,7] Whilst the oxalate ligand is already extensively used in coordination polymers, it is still rare in perovskite-related materials.

The oxalate ligand is of particular interest since it can act as a mono, bi, tri or tetradentate ligand and also as a chelating or bridging ligand.[8,9] Consequently, oxalate coordination compounds have vast structural diversity and are known to form chains, layers and 3D structures.[10] In addition, the oxalate ligand is known to provide both ferromagnetic and antiferromagnetic exchange pathways,[11,12] making these materials significant in the field of magnetic materials.[13,14] Metal carboxylates in general are already known to have applications for catalysis, optics and batteries[15,16] but additionally, the low melting point of oxalic acid (103.5 °C) allows for relatively mild synthesis conditions.[10]

Two recent examples of oxalate-containing perovskites are the compounds, $KLi_3Fe(C_2O_4)_3$ and $NH_4Li_3Fe(C_2O_4)_3$ as reported by Yao *et al.* and Li *et al*.[16,17] The compounds adopt the trigonal $R\bar{3}c$ space group and are isostructural with unit cell parameters a ~11.5 Å and c ~15 Å. The crystal structure of $KLi_3Fe(C_2O_4)_3$ is shown in Figure 5.1. The compounds have a perovskite-like structure; the A site has conventional 12-fold coordination but is only one quarter occupied by the potassium/ammonium

cation in an ordered manner. The B site of the perovskite exhibits 1:3 cation ordering of the lithium and iron atoms. The oxalate ligand acts as the X anion and forms single atom oxygen bridges. As a result, the structure contains Li-O-Li and Li-O-Fe but no Fe-O-Fe linkages. The relationship to a conventional perovskite can be more clearly seen in Figure 5.2, which shows a single octahedral layer, together with the cation ordering scheme.

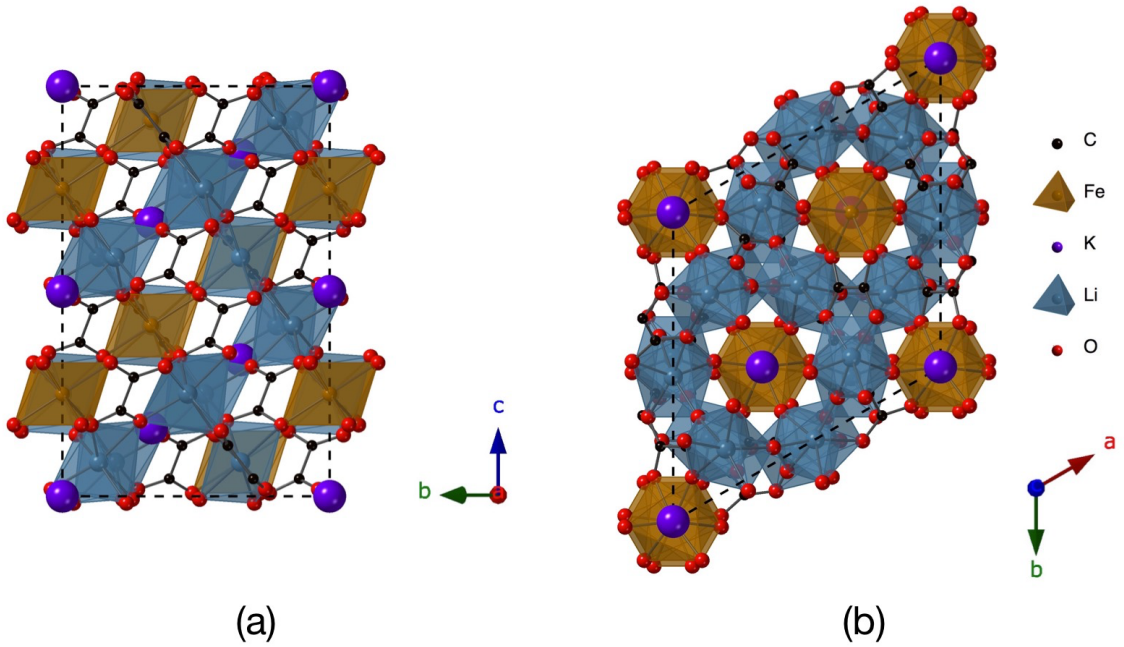

Figure 5.1: Crystal structure of $KLi_3Fe(C_2O_4)_3$ viewed along the *a*, and *c* axes as reported by Yao *et al.*[17]

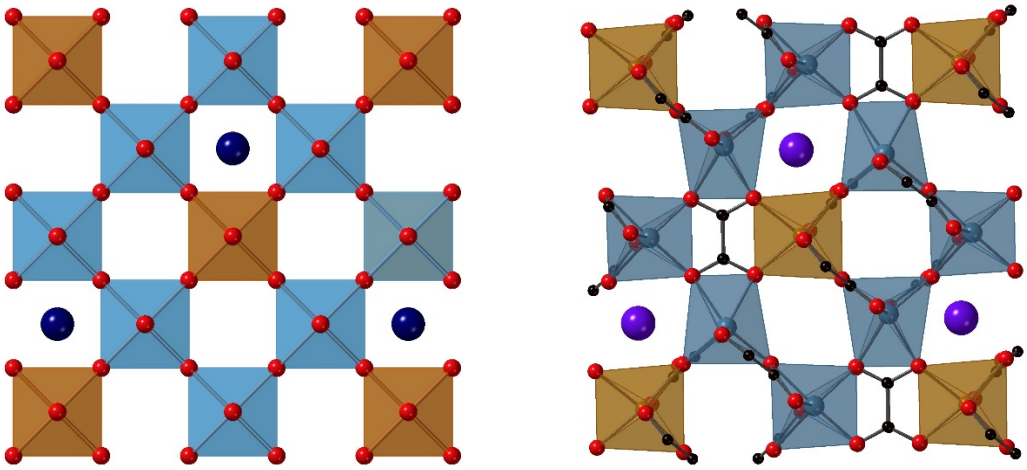

Figure 5.2: (left) ideal perovskite with 1:3 ordering (right) single octahedral layer of $KLi_3Fe(C_2O_4)_3$ as reported by Yao *et al.*[17]

Due to 1:3 ordering of the A site cation, the compound contains two different types of A sites, K sites and empty sites, both are shown in Figure 5.3. For comparison, the A site of an ideal perovskite $SrTiO_3$ is also depicted. A key difference between the potassium and vacant sites is the presence of two oxalate molecules on opposing faces of the cube. As a result, the oxalate oxygen atoms sit approximately on the edge centre of each cube as they do in conventional perovskites.

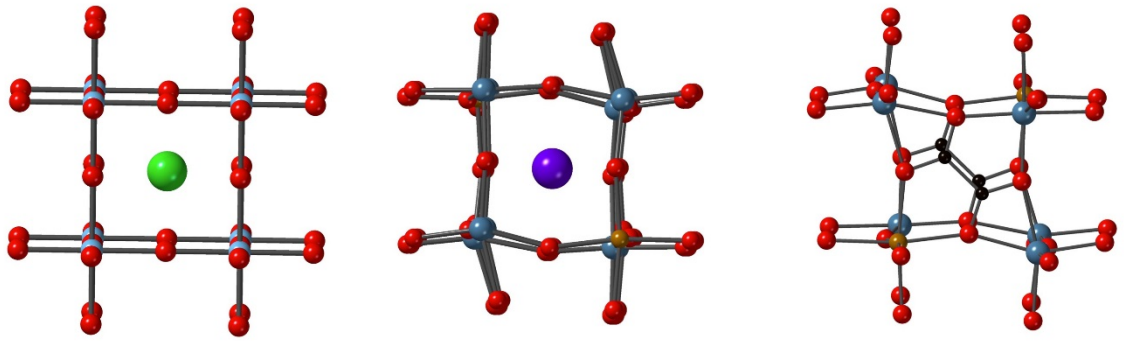

(a) (b) (c)

Figure 5.3: Comparison of perovskite A sites; (a) $SrTiO_3$,[18] (b) K site of $KLi_3Fe(C_2O_4)_3$ and (c) vacant site of $KLi_3Fe(C_2O_4)_3$

The magnetic properties of $NH_4Li_3Fe(C_2O_4)_3$ have previously been investigated by Li *et al.* revealing evidence of weak magnetic exchange interactions, whilst the magnetic properties of $KLi_3Fe(C_2O_4)_3$ have yet to be investigated.

In this chapter, a family of hybrid perovskite-like compounds based on the oxalate ligand are reported. Their structures are analysed by single crystal X-ray diffraction and their magnetic properties are probed. The effect of cation A site substitution upon the structure and subsequent distortions of the polyhedra are studied in detail. In addition, the synthesis and structures of several related oxalate polymers are also reported.

5.2 Experimental Techniques

5.2.1 Synthesis

Crystalline samples were synthesised *via* a hydrothermal method from commercially available reagents. The reactions mixtures were heated between 160 and 220 ˚C in a Teflon lined autoclave for 3 to 6 days. The resultant products were subsequently filtered and dried overnight at 50 ˚C prior to analysis by X-ray diffraction.

5.2.2 Single Crystal X-ray Diffraction

Single crystals were selected using an optical microscope and X-ray diffraction data were collected on a Rigaku SCXmini desktop instrument using Mo Kα_1 radiation (λ = 0.7107 Å) at 173 K. The data were processed using Rigaku CrystalClear software and were solved and refined using the SHELX package within the WINGX program.[19,20,21]

5.2.3 Powder X-ray Diffraction

Powder X-ray diffraction data were collected on a PANalytical Empyrean diffractometer using Cu Kα_1 radiation (λ = 1.5406 Å) at ambient temperature. The data were collected between 5 - 70˚ 2θ for one hour, and subsequently analysed using the Rietveld method using GSAS and the Expgui interface.[22,23,24]

5.2.4. SQUID Measurements

Magnetic data were collected on a quantum design MPMS SQUID instrument between 300 K and 2 K. Data were collected at zero field and at 100 Oe at 10 K intervals between 300 and 20 K and 2 K increments between 20 K and 2 K. Samples initially underwent a zero field cool (ZFC) followed by a field heating/cooling cycle (FC).

5.3 Results and Discussion

5.3.1 $KLi_3Fe(C_2O_4)_3$

A sample of $KLi_3Fe(C_2O_4)_3$ was synthesised *via* the hydrothermal method using potassium carbonate, lithium carbonate, iron (II) chloride tetrahydrate and oxalic acid dihydrate in a 1:2:1:4 ratio at 190 ˚C over a period of four days. The resulting product contained a mixture of orange crystals and powder. The crystals were manually separated from bulk sample for further analysis.

Several reagent ratios, temperatures and heating times were investigated to improve the purity of the product as summarised in Table 5.1. The best results were achieved using the 1:2:1:4 ratio at 190 °C and a 3 day reaction time.

Table 5.1: Summary of reaction conditions for the synthesis of $KLi_3Fe(C_2O_4)_3$

Ratio of Reagents	Temperature (˚C)	Volume of Solvent (ml)	Heating Time (days)
1:2:1:3	190	1	3
1:2:1:3	160	1	3
1:2:1:4	190	1	3
1:2:1:4	160	1	3
1:2:1.5:4	190	1	3
1:2:1.5:4	190	0.5	3
1:2:1.5:4	190	0.25	3
1:2:1.5:4	220	0.5	3
1:2:2:4	190	1	3
1:3:1:3	190	1	3
1:3:1:3	190	2	3
1:3:1:4	190	1	3

The purity and structure of the compound were confirmed by powder X-ray diffraction data, and the Rietveld refinement profile is shown in Figure 5.4. The data reveal a good

agreement with the crystal structure reported by Yao *et al.* and a high level of purity in the sample.[17]

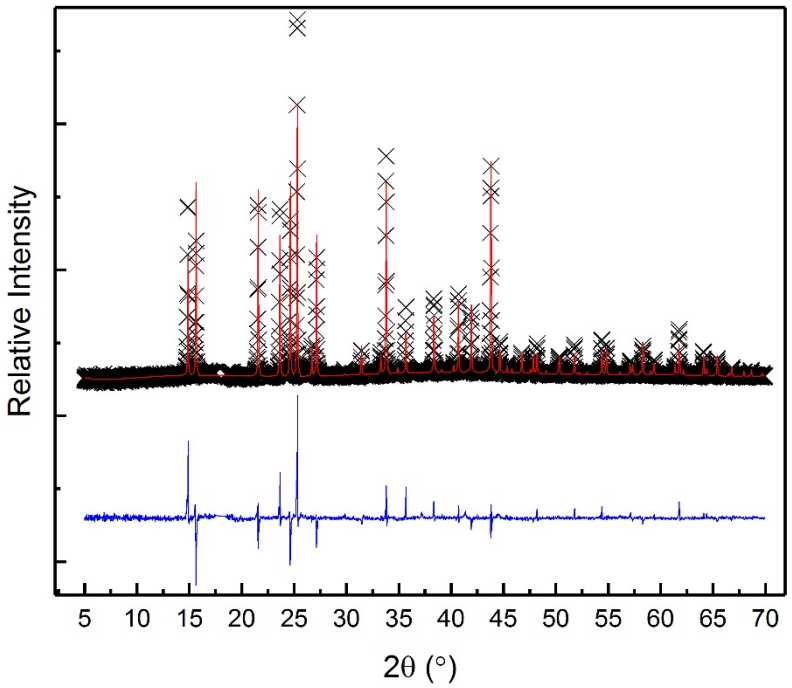

Figure 5.4: Rietveld refinement profile of $KLi_3Fe(C_2O_4)_3$ derived from powder X-ray diffraction data collected at ambient temperature; (black) observed diffraction pattern, (red) predicted diffraction pattern and (blue) calculated difference. wRp = 0.0597, Rp = 0.0353 and χ^2 = 5.497

Subsequently, the magnetic properties of the compound were probed using a powdered sample of high purity utilising a SQUID instrument. The dependence of the magnetic susceptibility on temperature is shown in Figure 5.5, there is a significant anomaly in both the χ vs T and $1/\chi$ ~100 K. As a result, Curie-Weiss fitting was not attempted, and the magnetic properties of the compound will need further investigation.

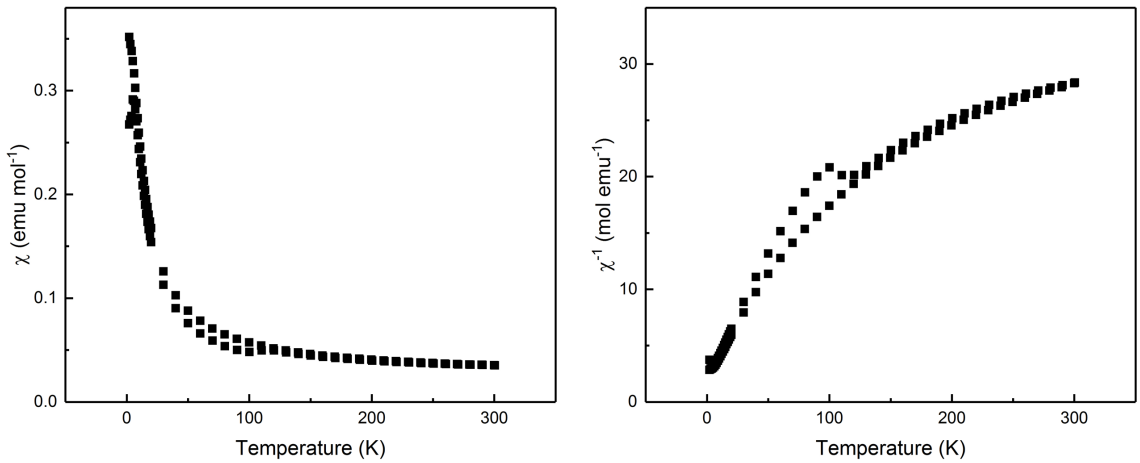

Figure 5.5: Magnetic data for $KLi_3Fe(C_2O_4)_3$; (left) magnetic susceptibility (χ) vs temperature (right) $1/\chi$ vs temperature

5.3.2 $KLi_3Co(C_2O_4)_3$

A cobalt containing analogue of $KLi_3Fe(C_2O_4)_3$ was also synthesised *via* a hydrothermal method from potassium carbonate, lithium carbonate, cobalt chloride hexahydrate and oxalic acid dihydrate. A summary of the reaction conditions employed is given in Table 5.2. The most successful reactions utilised a 1:2:1.5:4 ratio of reagents and were heated at 190 °C for a period of 4 days. Despite the multiple reaction conditions investigated, a pure sample was never synthesised, the products were obtained as a mixture of dark pink hexagonal crystals and a pink powder. The single crystals were manually separated from the bulk sample and analysed by single crystal X-ray diffraction.

Table 5.2: Summary of reaction conditions for the synthesis of $KLi_3Co(C_2O_4)_3$

Ratio of Reagents	Temperature (˚C)	Volume of Solvent (ml)	Heating Time (days)
1:2:1.5:4	190	1	4
1:2:1.5:4	190	0.5	4
1:2:1.5:4	190	0.25	4
1:2:1.5:4	220	0.5	4
1:2:1.5:4	160	0.5	4
1:2:1.5:4	160	1	2
1:2:2:4	190	0.5	4
1:2:2:4	190	1	4
1:3:1:3	190	1	4
1:3:1:3	190	0.5	4
1:3:1:3	190	2	4
1:3:1:4	190	1	4
1:3:1.5:4	190	0.5	4
1:3:1.5:4	190	1	4
1:3:1.5:4	160	1	3
1:3:1.5:4	190	1	3

Table 5.3: Crystallographic and refinement details of $KLi_3Co(C_2O_4)_3$ for single crystal X-ray diffraction data collected at 173 K

Formula	$KLi_3Co(C_2O_4)_3$
Formula Weight	382.91
Density (g cm^{-3})	2.277
Crystal System	Trigonal
Space Group	$R\bar{3}c$
a/Å	11.3215(9)
b/Å	11.3215(9)
c/Å	15.0942(13)
α (˚)	90
β (˚)	90
γ (˚)	120
V/$Å^3$	1675.5(3)
Z	6
Measured Ref	5415
Independent Ref	436 [R(int) = 0.1083]
Refined Parameter	37
GOOF	0.631
Final R Indices (I > 2σ(I))	R1 = 0.0329, wR2 = 0.0808

The crystallographic and refinement details of $KLi_3Co(C_2O_4)_3$ are shown in Table 5.3. The compound is isostructural to the initial iron-containing derivative is shown in Figure 5.1. The unit cell parameters remain virtually unaffected by the variation of the transition metal; however, they do contract very slightly. The bond lengths and bond valence sums are reported in Table 5.4. The determined bond lengths do not differ significantly from the iron-containing compound and the bond valence sums are within the expected range.

Table 5.4: Selected bond lengths (Å) and bond valence sums (valence units) of $KLi_3Co(C_2O_4)_3$ derived from single crystal X-ray diffraction data collected at 173 K

Bond	$KLi_3Co(C_2O_4)_3$
Li-O	2.019(6) × 2
	2.130(3) × 2
	2.165(6) × 2
BVS	1.08
Co-O	2.083(2) × 6
BVS	2.09
K-O	3.007(2) × 6
	3.152(2) × 6
BVS	0.94

As seen with the iron derivative, the hydrothermal synthesis did not yield a pure product, however, the crystalline product can be easily manually separated from the bulk sample. Powder X-ray diffraction of the crystalline product revealed a high level of purity in the sample and good fit to the structural model determined from single crystal X-ray diffraction data. The powder diffraction pattern and Rietveld refinement profile are given in Figure 5.6.

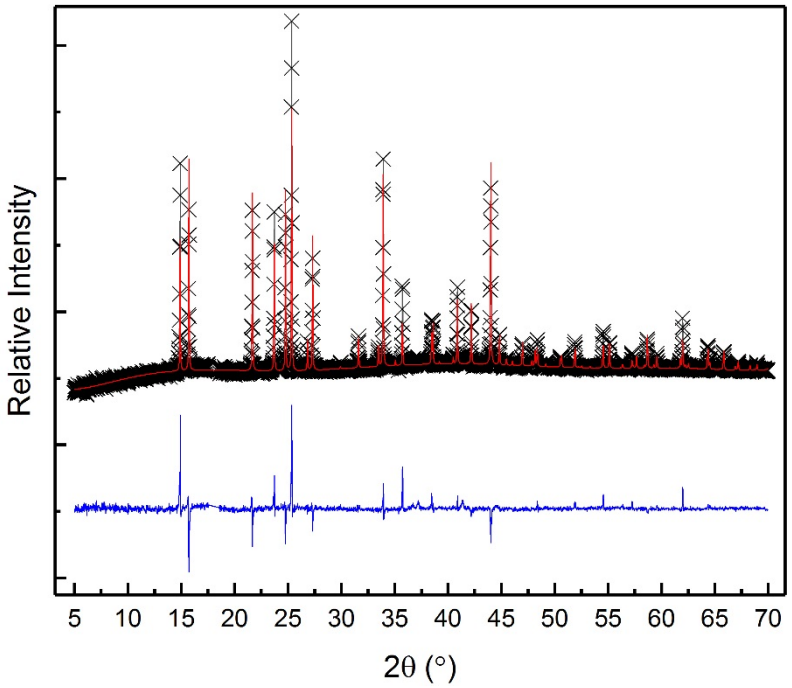

Figure 5.6: Rietveld refinement profile of $KLi_3Co(C_2O_4)_3$ derived from powder X-ray diffraction data collected at ambient temperature; (black) observed diffraction pattern, (red) predicted diffraction pattern and (blue) calculated difference. wRp = 0.0406, Rp = 0.0229 and χ^2 = 4.897

5.3.2.1 Magnetometry

The magnetic properties of $KLi_3Co(C_2O_4)_3$ where probed using a SQUID instrument and the molar magnetic susceptibility of the compound and its relationship to temperature was determined. The magnetometry data are shown in Figure 5.7. The data show no evidence of magnetic ordering in measurements down to 2 K. Linear fitting and extrapolation of the χ^{-1} vs T plot reveals a Weiss constant of −2.00 K which would indicate very weak antiferromagnetic interactions. The Curie constant is 2.899 $cm^3\ mol^{-1}$ K giving a μ_{eff} of 4.815 μ_B. The spin only magnetic moment for Co^{2+} is 3.87 μ_B, however, the calculated value from Curie-Weiss fitting is within the expected range for observed magnetic moments.[25]

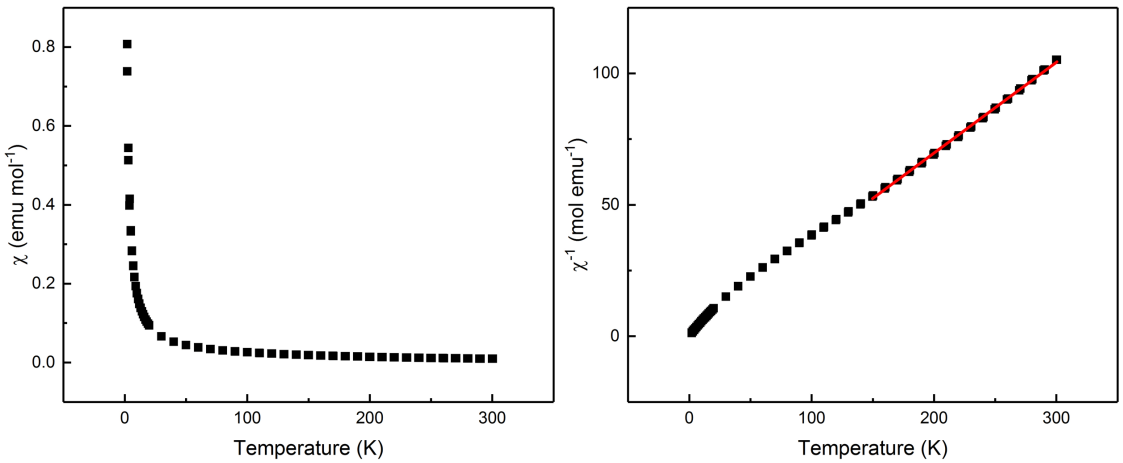

Figure 5.7: Magnetic data for $KLi_3Co(C_2O_4)_3$; (left) magnetic susceptibility (χ) vs temperature (right) $1/\chi$ vs temperature

The synthesis of a sodium containing analogue, namely $NaLi_3Co(C_2O_4)_3$ would be of particular interest due to its possible application as a battery material. In addition, the relative size difference of the sodium cation to both the potassium and lithium cations would provide an insight into the structural and compositional flexibility and versatility of the oxalate perovskite family. Several reaction conditions were utilised to synthesise a sodium-containing derivative, however, a pure sodium analogue ($NaLi_3Co(C_2O_4)_3$) was never produced. Subsequently, substitution (at the 10-40% level) of sodium was attempted at both the A (K) and B (Li) sites of the compound. Stoichiometric quantities of sodium carbonate were added to synthesise the varying sodium doping levels. The products produced were similar in appearance to $KLi_3Co(C_2O_4)_3$ samples and exhibited the same issues surrounding their purity. The crystals of 10/30 % sodium B site doping and 40 % sodium A site doping samples were analysed by single crystal X-ray diffraction; their crystallographic and refinement details are shown in Table 5.5. There are no significant changes in symmetry, space group or unit cell parameters, which would suggest no substantial incorporation of the sodium cation.

Table 5.5: Crystallographic and refinement details of $KLi_3Co(C_2O_4)_3$ with 10, 30 and 40 % sodium doping from single crystal X-ray diffraction data collected at 173 K

	10 % Na	30% Na	40 % Na
Formula Weight	382.91	382.91	382.91
Density (g cm^{-3})	2.272	2.275	2.277
Crystal System	Trigonal	Trigonal	Trigonal
Space Group	$R\bar{3}c$	$R\bar{3}c$	$R\bar{3}c$
a/Å	11.3300(7)	11.3240(7)	11.3231(8)
b/Å	11.3300(7)	11.3240(7)	11.3231(8)
c/Å	15.1070(10)	15.0970(10)	15.0926(10)
α (˚)	90	90	90
β (˚)	90	90	90
γ (˚)	120	120	120
V/$Å^3$	1679.5(2)	1676.6(2)	1675.8(3)
Z	6	6	6
Measured Ref	5410	5319	5394
Independent Ref	438 [R(int) = 0.0493]	434 [R(int) = 0.0457]	438 [R(int) = 0.0551]
Refined Parameter	37	37	37
GOOF	0.785	0.746	0.755
Final R Indices (I > 2σ(I))	R1 = 0.0239, wR2 = 0.0815	R1 = 0.0247, wR2 = 0.0788	R1 = 0.0286, wR2 = 0.0810

The bond lengths were also analysed in detail and compared to $KLi_3Co(C_2O_4)_3$; their values are shown in Table 5.6. The Li-O and K-O bond lengths appear unaltered across the range of sodium-doped samples suggesting that no compositional change had occurred in the structure. Furthermore, the atomic displacement parameters do not suggest the presence of atoms with differing atomic number. Despite the numerous attempts to incorporate sodium into the structure, neither the bond lengths nor the unit cell parameters have significant deviations that would suggest a change in composition.

Table 5.6: Selected bond lengths (Å) and bond valence sums (valence units) of $KLi_3Co(C_2O_4)_3$ sodium doped $KLi_3Co(C_2O_4)_3$

Bond	Pure	10 %	30 %	40 %
Li-O	2.019(6) × 2	2.016(4) × 2	2.019(3) × 2	2.017(4) × 2
	2.130(3) × 2	2.132(2) × 2	2.1241(16) × 2	2.126(2) × 2
	2.165(6) × 2	2.171(4) × 2	2.165(3) × 2	2.167(4) × 2
BVS	1.08	1.08	1.09	1.09
Co-O	2.083(2) × 6	2.0878(15) × 6	2.0902(11) × 6	2.0884(15) × 6
BVS	2.09	2.06	2.04	2.06
K-O	3.007(2) × 6	3.0102(15) × 6	3.0077(10) × 6	3.0065(15) × 6
	3.152(2) × 6	3.1557(16) × 6	3.1513(11) × 6	3.1533(16) × 6
BVS	0.94	0.94	0.94	0.94

5.3.3 $KLi_3Ni(C_2O_4)_3$

A third member of the series was synthesised in the form of $KLi_3Ni(C_2O_4)_3$ utilising the same hydrothermal method. The products were obtained as dark green hexagonal crystals within a light green impurity phase. Several reaction conditions were attempted to improve the purity and yield of the reaction as summarised in Table 5.7. The most efficient reaction conditions proved to be at a ratio of 1:2:1.5:4 of reagents and at temperature of 190 °C. Single crystal X-ray diffraction was used to analyse the crystalline products.

Table 5.7: Summary of reaction conditions for the synthesis of $KLi_3Ni(C_2O_4)_3$

Ratio of Reagents	Temperature (˚C)	Volume of Solvent (ml)	Heating Time (days)
1:2:1.5:4	190	1	4
1:2:1.5:4	190	0.5	4
1:2:1.5:4	190	0.25	4
1:2:1.5:4	220	0.5	4
1:2:1.5:4	160	0.5	4
1:3:1:3	190	1	4
1:3:1:3	190	2	4
1:3:1:4	190	1	4

The crystal structure of $KLi_3Ni(C_2O_4)_3$ is isostructural with the original iron-containing compound with no significant changes in symmetry, space group, or bonding. The binding modes of each of the B site polyhedra is shown in Figure 5.8.

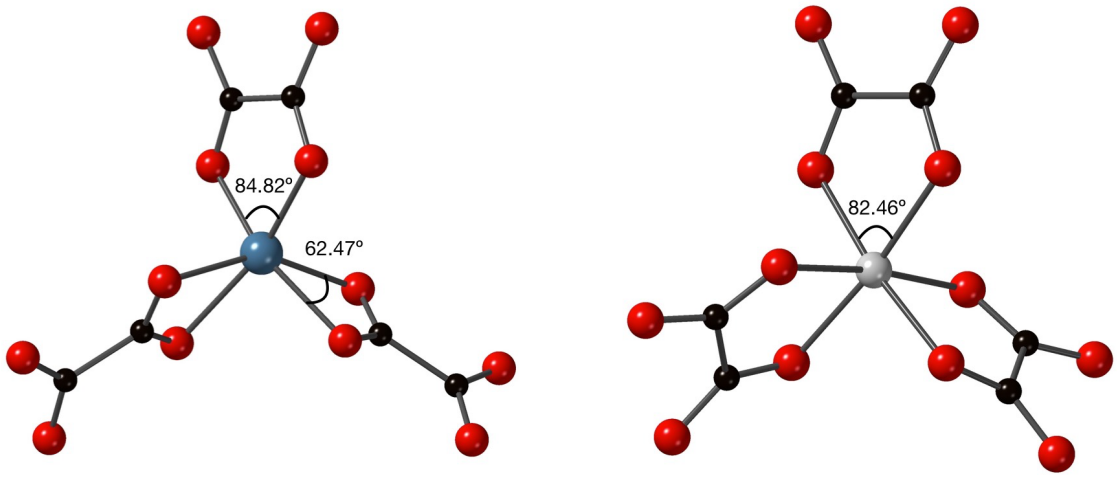

Figure 5.8: $Li(C_2O_4)_3$ and $Ni(C_2O_4)_3$ octahedra with bite angles (°) derived from single crystal X-ray diffraction data collected at 173 K

The compound adopts the trigonal $R\bar{3}c$ space group with unit cell parameters of a = 11.3071 Å and c = 11.9434 Å at 173 K. The crystal structure was also determined at 293 K to examine any potential structural changes or phase transitions. The crystallographic and refinement details are reported in Table 5.8. Aside from a slight expansion of the unit cell, there are no significant change in the crystal structure within the temperature

range. A comparison of the bond lengths at both temperatures is also given in Table 5.9, but only subtle changes are observed in the structure.

Table 5.8: Crystallographic and refinement details of $KLi_3Ni(C_2O_4)_3$ from single crystal X-ray diffraction data collected at 173 K and 293 K

	293 K	**173 K**
Formula	$KLi_3Ni(C_2O_4)_3$	$KLi_3Ni(C_2O_4)_3$
Formula Weight	382.69	382.69
Density (g cm^{-3})	2.291	2.304
Crystal System	Trigonal	Trigonal
Space Group	$R\bar{3}c$	$R\bar{3}c$
a/Å	11.3708(18)	11.3071(8)
b/Å	11.3708(18)	11.3071(8)
c/Å	14.863(3)	14.9434(12)
α (˚)	90	90
β (˚)	90	90
γ (˚)	120	120
V/$Å^3$	1664(3)	1654.6(3)
Z	6	6
Measured Ref	5306	5246
Independent Ref	431 [R(int) = 0.0412]	426 [R(int) = 0.0432]
Refined Parameter	37	37
GOOF	0.772	0.711
Final R Indices (I > 2σ(I))	R1 = 0.0228, wR2 = 0.0787	R1 = 0.0216, wR2 = 0.0748

Table 5.9: Selected bond lengths (Å) and bond valence sums (valence units) of $KLi_3Ni(C_2O_4)_3$ derived from single crystal X-ray diffraction data collected at 173 K and 293 K

Bond	293 K	173 K
Li-O	2.032(4) × 2	2.020(3) × 2
	2.140(3) × 2	2.1344(14) × 2
	2.151(4) × 2	2.152(3) × 2
BVS	1.07	1.09
M-O	2.0534(18) × 6	2.0523(10) × 6
BVS	2.16	2.16
K-O	3.0395(12) × 6	3.0179(9) × 6
	3.115(5) × 6	3.1215(11) × 6
BVS	0.94	0.96

The structural model was further confirmed from powder X-ray diffraction data and the purity of the sample was investigated. The powder X-ray diffraction and Rietveld refinement profile are shown in Figure 5.9 and reveal a high level of purity in the sample and the material was subsequently used for magnetic property measurements.

The magnetic properties of the sample were measured using a SQUID instrument, allowing the magnetic susceptibility and its dependence on temperature to be determined (Figure 5.10). The $1/\chi$ vs T data were used for Curie-Weiss analysis, linear fitting of the data points between 300 K and 150 K revealed a Weiss constant of −25.02 K indicative of a weak antiferromagnetic interaction. The Curie constant of the material was 1.635 $cm^3\ mol^{-1}$ K and the μ_{eff} was 3.62 μ_B. The spin only magnetic moment of Ni^{2+} is 2.83 μ_B, however, the μ_{eff} is in the typical range observed for nickel compounds.[25]

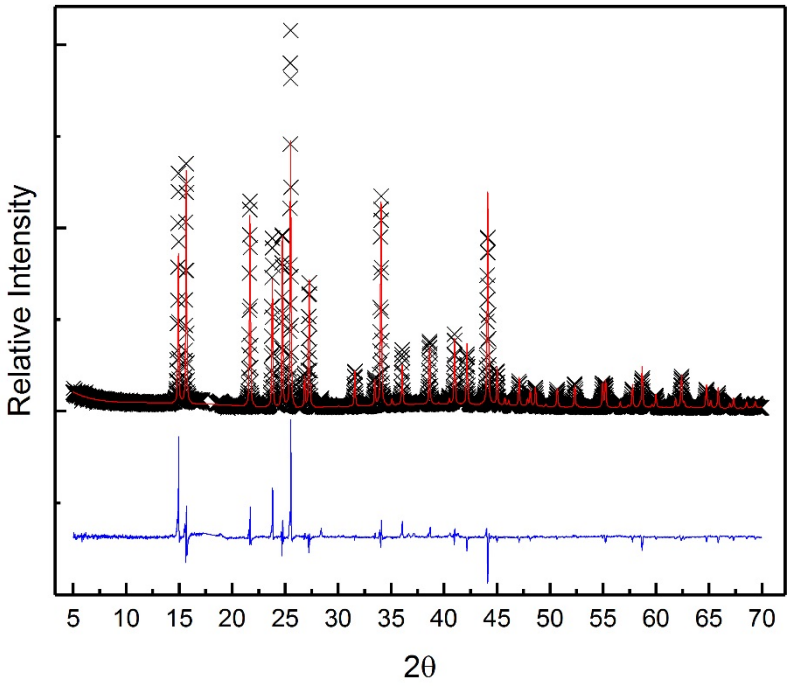

Figure 5.9: Rietveld refinement profile of $KLi_3Ni(C_2O_4)_3$ derived from powder X-ray diffraction data collected at ambient temperature; (black) observed diffraction pattern, (red) predicted diffraction pattern and (blue) calculated difference. wRp = 0.1404, Rp = 0.1093 and χ^2 = 6.444

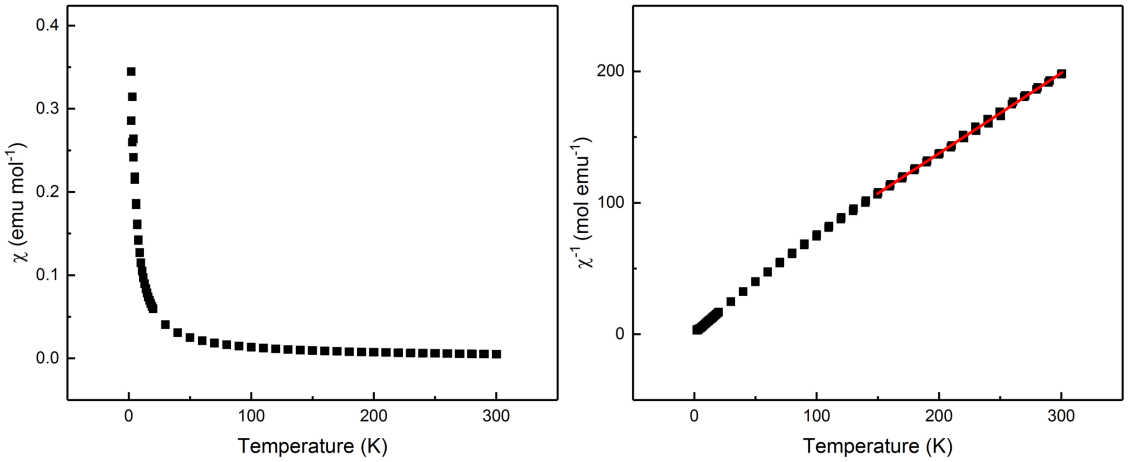

Figure 5.10: Magnetic data for $KLi_3Ni(C_2O_4)_3$; (left) magnetic susceptibility (χ) vs temperature (right) 1/χ vs temperature

5.3.4 Rubidium Substitution

The structural flexibility of the system was probed by the substitution of potassium with rubidium upon the A site of the perovskite. The ionic radius of rubidium when compared to potassium is substantially larger (K^+ 12-coord: 1.64 Å, Rb^+, 12-coord: 1.72 Å) and could produce interesting distortions of the structure of the original potassium-containing

compound. A series of rubidium-based containing derivatives, containing Fe, Co and Ni, were synthesised using conventional hydrothermal methods as summarised in Table 5.10.

Table 5.10: Summary of the most efficient reaction conditions for each of the caesium containing compounds

Composition	Reagent Ratio	Temperature (°C)	Volume (ml)	Time (days)
$RbLi_3Fe(C_2O_4)_3$	1:2:1.5:4	160	1	4
$RbLi_3Co(C_2O_4)_3$	1:2:1.5:4	160	1	4
$RbLi_3Ni(C_2O_4)_3$	1:2:2:4	160	1	4

All three compounds adopted the same perovskite-like structure and are isostructural with the potassium-containing compounds, adopting the trigonal $R\bar{3}c$ space group. Their refinement and crystallographic details are shown in Table 5.11. Each of the unit cell parameters are slightly enlarged, in comparison to the potassium analogues, as might be expected due to the increased relative size of the rubidium cation relative to the potassium cation, but as a whole the parameters are unaffected by rubidium substitution. The bond lengths and bond valence sum values are also shown in Table 5.12.

Table 5.11: Crystallographic and refinement details of $RbLi_3Fe(C_2O_4)_3$, $RbLi_3Co(C_2O_4)_3$ and $RbLi_3Ni(C_2O_4)_3$ from single crystal X-ray diffraction data collected at 173 K

Formula	$RbLi_3Fe(C_2O_4)_3$	$RbLi_3Co(C_2O_4)_3$	$RbLi_3Ni(C_2O_4)_3$
Formula Weight	426.20	429.28	429.06
Density (g cm^{-3})	2.465	2.515	2.542
Crystal System	Trigonal	Trigonal	Trigonal
Space Group	$R\bar{3}c$	$R\bar{3}c$	$R\bar{3}c$
a/Å	11.4780(8)	11.4019(8)	11.3796(7)
b/Å	11.4780(8)	11.4019(8)	11.3796(7)
c/Å	15.1001(12)	15.1029(12)	14.9962(10)
α (˚)	90	90	90
β (˚)	90	90	90
γ (˚)	120	120	120
V/$Å^3$	1722.8(3)	1700.4(3)	1681.8(2)
Z	6	6	6
Measured Ref	5535	5449	5226
Independent Ref	446 [R(int) = 0.0542]	444 [R(int) = 0.0803]	441 [R(int) = 0.0747]
Refined Parameter	37	37	37
GOOF	0.815	0.610	0.876
Final R Indices (I > 2σ(I))	R1 = 0.0251, wR2 = 0.0886	R1 = 0.0274, wR2 = 0.0736	R1 = 0.0328, wR2 = 0.1025

Table 5.12: Bond lengths (Å) and bond valence sums (valence units) of $RbLi_3Fe(C_2O_4)_3$, $RbLi_3Co(C_2O_4)_3$ and $RbLi_3Ni(C_2O_4)_3$ derived from single crystal X-ray diffraction data collected at 173 K where M = Fe, Co and Ni

Bond	$RbLi_3Fe(C_2O_4)_3$	$RbLi_3Co(C_2O_4)_3$	$RbLi_3Ni(C_2O_4)_3$
Li-O	2.024(6) × 2	2.029(7) × 2	2.023(6) × 2
	2.138(3) × 2	2.147(3) × 2	2.161(3) × 2
	2.196(6) × 2	2.178(6) × 2	2.174(5) × 2
BVS	1.05	1.05	1.04
M-O	2.127(2) × 6	2.089(2) × 6	2.053(2) × 6
BVS	2.07	2.05	2.16
Rb-O	3.057(2) × 6	3.048(2) × 6	3.0560(17) × 6
	3.193(2) × 6	3.164(2) × 6	3.139(2) × 6
BVS	1.19	1.24	1.27

The polyhedral bond lengths, Li-O and M-O, remain almost unaffected by the substitution although the Rb-O bond lengths, with an average of 3.1095 Å, are slightly longer than the K-O bond lengths, which had an average of 3.0746 Å. The bond valence sums for the lithium and transition metal centres are within the expected range for our structural model, however, the values for rubidium are significantly higher than expected (>1.19). The incorporation of the rubidium cation leads to significant distortion in the structure relative to the potassium containing compounds which will be discussed in further detail in section 5.3.6.

Table 5.13: Bite angles (°) of $RbLi_3Fe(C_2O_4)_3$, $RbLi_3Co(C_2O_4)_3$ and $RbLi_3Ni(C_2O_4)_3$ derived from single crystal X-ray diffraction data collected at 173 K where M = Fe, Co and Ni

Angle	$RbLi_3Fe(C_2O_4)_3$	$RbLi_3Co(C_2O_4)_3$	$RbLi_3Ni(C_2O_4)_3$
O1-Li1-O1	84.6(3)	84.6(4)	84.7(3)
O1-Li1-O2 × 2	61.72(14)	61.91(17)	61.86(13)
O1-M1-O1 × 3	78.58(11)	80.72(12)	82.31(11)

The coordination environments and binding modes of the $Li(C_2O_4)_3$ and $Fe(C_2O_4)_3$ moieties were analysed in detail as shown in Table 5.13 and Figure 5.11. The binding modes remain unaffected by the incorporation of rubidium. Although there is a clear trend for bite angles to increase as the radii of the transition metal decreases, the substitution of potassium with rubidium does not have a significant effect. The relationship between bite angle and M-O bond lengths are shown in Figure 5.12, longer bond lengths led to a decrease in O-M-O bite angle. The synthesis of each of the compounds consistently resulted in mixtures of compounds and therefore it has not proven possible to analyse the structure by powder X-ray diffraction or magnetometry.

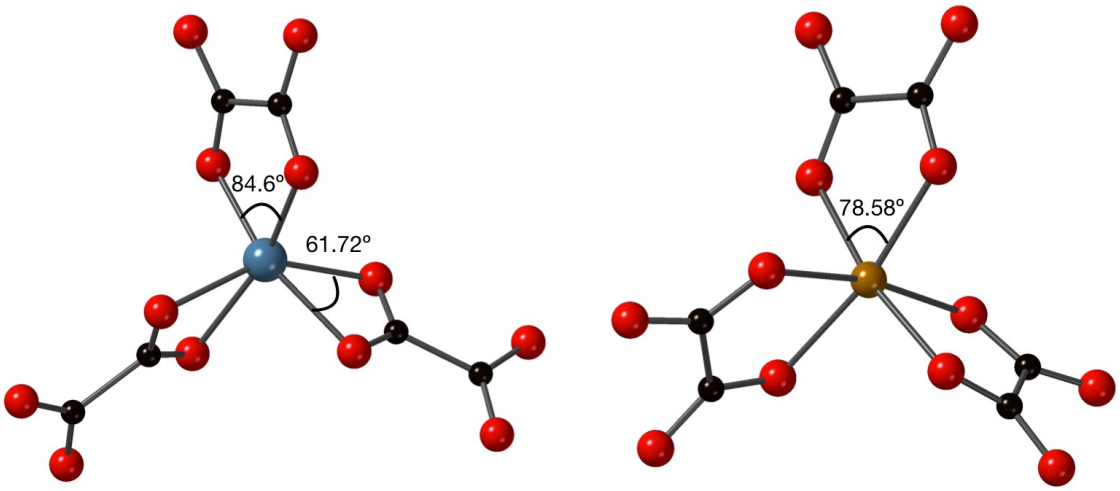

Figure 5.11: The coordination modes and bite angles (°) of the $Li(C_2O_4)_3$ (left) and $Fe(C_2O_4)_3$ (right) octahedra of $RbLi_3Fe(C_2O_4)_3$ derived from single crystal X-ray diffraction data collected at 173 K

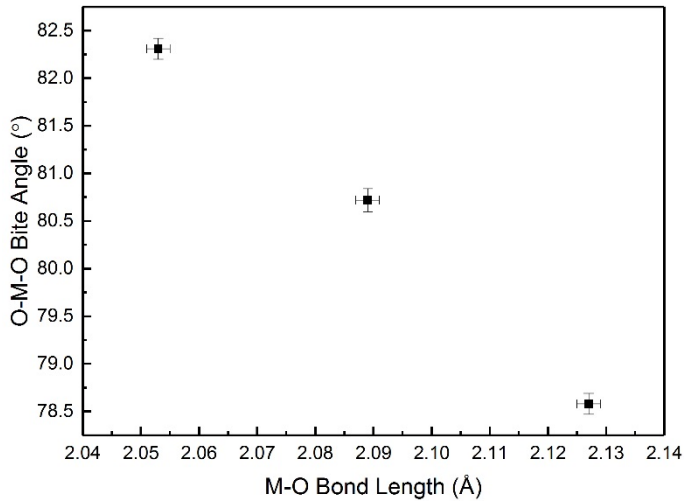

Figure 5.12: Evolution of O-M-O bite angle (˚) and M-O bond lengths (Å) for $RbLi_3M(C_2O_4)_3$ compounds where M = Fe, Co and Ni

5.3.5 Caesium Substitution

The family of oxalate hybrid perovskites can be further expanded by the incorporation of the caesium cation. Three compounds containing iron, cobalt and nickel cations were synthesised by hydrothermal methods. The most efficient reaction conditions for each composition are summarised in Table 5.14, but, the reactions typically yielded a mixture of products.

Table 5.14: Summary of the most efficient reaction conditions for each of the caesium containing compounds

Composition	Reagent Ratio	Temperature (°C)	Volume (ml)	Time (days)
$CsLi_3Fe(C_2O_4)_3$	1:2:1:4	160	1	5
$CsLi_3Co(C_2O_4)_3$	1:2:1.5:4	160	1	4
$CsLi_3Ni(C_2O_4)_3$	1:2:2:4	160	1	4

Single crystal X-ray diffraction data were collected on crystals of each of the three compounds; their crystallographic and refinement details are shown in Table 5.15. The compounds are isostructural with the K and Rb analogues reported earlier in the chapter and adopt the trigonal $R\bar{3}c$ space group. $CsLi_3Ni(C_2O_4)_3$ is isostructural to $KLi_3Fe(C_2O_4)_3$ whose crystal structure is shown in Figure 5.1. The unit cell parameters are again slightly elongated in comparison with both the potassium and rubidium compounds, as expected given the larger radius of the caesium cation.

Table 5.15: Crystallographic and refinement details of $CsLi_3Fe(C_2O_4)_3$, $CsLi_3Co(C_2O_4)_3$ and $CsLi_3Ni(C_2O_4)_3$ from single crystal X-ray diffraction data collected at 173 K

Formula	$CsLi_3Fe(C_2O_4)_3$	$CsLi_3Co(C_2O_4)_3$	$CsLi_3Ni(C_2O_4)_3$
Formula Weight	473.64	476.72	476.50
Density (g cm^{-3})	2.666	2.713	2.740
Crystal System	Trigonal	Trigonal	Trigonal
Space Group	$R\bar{3}c$	$R\bar{3}c$	$R\bar{3}c$
a/Å	11.6046(8)	11.5264(8)	11.4908(8)
b/Å	11.6046(8)	11.5264(8)	11.4908(8)
c/Å	15.1779(12)	15.2164(1)	15.1534(10)
α (˚)	90	90	90
β (˚)	90	90	90
γ (˚)	120	120	120
V/$Å^3$	1770.1(3)	1750.8(3)	1732.8(3)
Z	6	6	6
Measured Ref	5297	5481	5412
Independent Ref	447 [R(int) = 0.0994]	444 [R(int) = 0.0439]	442 [R(int) = 0.0384]
Refined Parameter	37	37	37
GOOF	1.145	0.853	0.935
Final R Indices (I > 2σ(I))	R1 = 0.0346, wR2 = 0.1153	R1 = 0.0202, wR2 = 0.0920	R1 = 0.0229, wR2 = 0.1012

The bond lengths, bond valence sums and the coordination of each of the metal sites were analysed in detail and the values are reported in Table 5.16. The coordination of the Li and transition metal centres is six-fold and 12-fold for the caesium cation. The bite angles at each of the bidentate oxalate ligands are shown in Table 5.17 and Figure 5.13. The bite angles of O-Li-O remain virtually unaffected my transition metal but there is a noticeable trend in the O-M-O angles which increase for the larger transition metals. The effect of M-O bond length on the bite angles is plotted in Figure 5.14 with longer bond lengths leading to smaller bite angles

Table 5.16: Bond lengths (Å) and bond valence sums (valence units) of $CsLi_3Fe(C_2O_4)_3$, $CsLi_3Co(C_2O_4)_3$ and $CsLi_3Ni(C_2O_4)_3$ derived from single crystal X-ray diffraction data collected at 173 K where M = Fe, Co and Ni

Bond	$CsLi_3Fe(C_2O_4)_3$	$CsLi_3Co(C_2O_4)_3$	$CsLi_3Ni(C_2O_4)_3$
Li-O	2.032(7) × 2	2.038(5) × 2	2.042(5) × 2
	2.177(4) × 2	2.185(3) × 2	2.197(3) × 2
	2.230(7) × 2	2.215(5) × 2	2.203(5) × 2
BVS	0.98	0.98	0.97
M-O	2.132(3) × 6	2.095(2) × 6	2.059(2) × 6
BVS	2.05	2.02	2.13
Cs-O	3.1228(19) × 6	3.1199(15) × 6	3.1240(17) × 6
	3.234(4) × 6	3.207(2) × 6	3.186(2) × 6
BVS	1.55	1.61	1.64

Table 5.17: Bite angles (°) of $CsLi_3Fe(C_2O_4)_3$, $CsLi_3Co(C_2O_4)_3$ and $CsLi_3Ni(C_2O_4)_3$ derived from single crystal X-ray diffraction data collected at 173 K where M = Fe, Co and Ni

Angle	$CsLi_3Fe(C_2O_4)_3$	$CsLi_3Co(C_2O_4)_3$	$CsLi_3Ni(C_2O_4)_3$
O1-Li1-O1	84.0(3)	83.61(3)	83.5(3)
O1-Li1-O2 × 2	60.63(17)	60.87(11)	60.86(11)
O1-M1-O1 × 3	78.08(18)	80.51(12)	82.16(12)

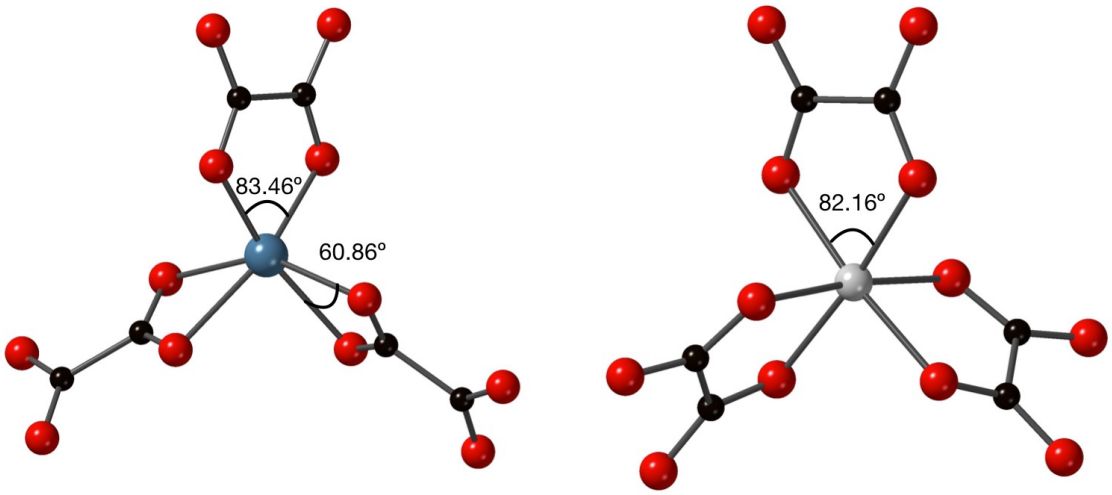

Figure 5.13: The coordination modes and bite angles (°) of the $Li(C_2O_4)_3$ (left) and $Ni(C_2O_4)_3$ (right) octahedra of $CsLi_3Ni(C_2O_4)_3$ derived from single crystal X-ray diffraction data collected at 173 K

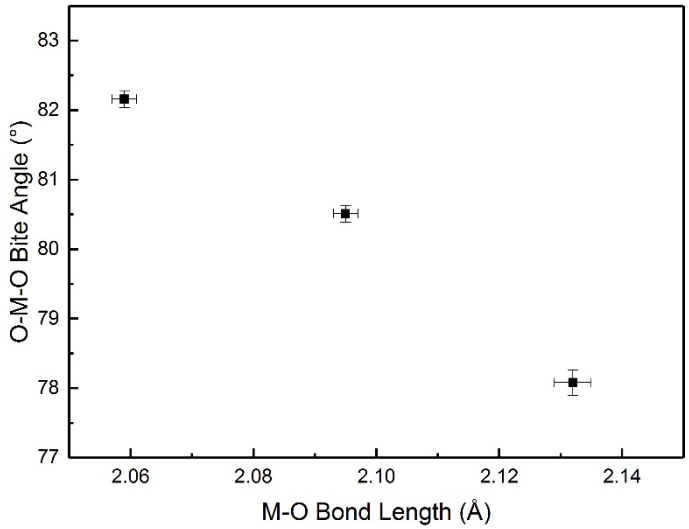

Figure 5.14: Evolution of O-M-O bite angle (˚) and M-O bond Lengths (Å) for $CsLi_3M(C_2O_4)_3$ compounds where M = Fe, Co and Ni

5.3.6 Distortion Parameters

The incorporation of multiple cations in varying size and combinations demonstrates the flexibility of the system but also impacts the distortion of the structure. Perhaps the most interesting variation is the incorporation of the substantially larger caesium cation in place of potassium. The effect of cation substitution upon the distortion of the compound was investigated by considering tolerance factors, bond valence sums, traditional polyhedral distortion parameters, Δ and δ^2, and by using Minimum Bounding Ellipsoid (MBE) and the PIEFACE (Polyhedra Inscribing Ellipsoids For Analysing Crystallographic Environments) program.[26]

5.3.6.1 Tolerance Factors

The tolerance factors of each of the new compounds were calculated using Equation 5.1, where R_A is the radius of A site cation, R_B the radius of the B site cation and R_O the ionic radius of an oxide anion. The radius of the B site cation was estimated using a weighted 3:1 average of Li^{2+} and the divalent transition metal. The oxalate ions were excluded from the calculations and considered as simple oxide anions since the carbon atoms perform a secondary role in the structure's connectivity.

Equation 5.1 $$t = \frac{R_A + R_O}{\sqrt{2}(R_B + R_O)}$$

Table 5.18: Calculated tolerance factors of the eight new hybrid perovskites and the previously reported $KLi_3Fe(C_2O_4)_3$

Metal	Fe	Co	Ni
K	1.000	1.004	1.010
Rb	1.026	1.031	1.037
Cs	1.080	1.084	1.091

B Site radii used; Li_3Fe = 0.765 Å, Li_3Co = 0.756 Å and Li_3Ni = 0.742 Å

The calculated tolerance factors are reported in Table 5.18. As a whole, the values are higher than expected for the perovskite structure and it is perhaps surprising that even the rubidium and caesium containing compounds adopt a perovskite like structure. Whilst there are examples of fluoride perovskite incorporating the rubidium and caesium cations for example $RbPdF_3$, $RbCuF_3$ and $CsPbF_3$, a caesium/rubidium-containing conventional oxide perovskite has never been reported.[27,28,29]

5.3.6.2 Bond Valence Sums

The bond valence sums have also been calculated for each metal cation at each of the compositions, from derived bond lengths. Whilst the values have already been quoted individually earlier in this chapter, they are summarised in Table 5.19 to facilitate comparison between structures. The bond valence sums of Li and transition metals remain within the expected range for each composition. However, the 12 coordinate Rb and Cs cations have values substantially higher than ideal. A survey of existing caesium carboxylate compounds revealed a much larger range of caesium oxygen bond lengths, between ~3 Å and ~3.5 Å, than observed in the newly synthesised oxalate perovskite structures. The observed Cs-O bond lengths in these compounds were in the range of 3.12 – 3.23 Å. Whilst the bond lengths are not unrealistically short, they do lie on the lower extreme of expected values and hence, the bonding environment of the caesium is particularly interesting since it contains multiple shorter bond lengths.

Table 5.19: Bond valence sums (valence units) of the nine oxalate perovskite compounds calculated from bond lengths determined from single crystal X-ray diffraction data collected at 173 K. Where A is an alkali metal (K, Rb, Cs) and M is a transition metal (Fe, Co, Ni). * values taken from lliterature[17]

Alkali Metal		$ALi_3Fe(C_2O_4)_3$	$ALi_3Co(C_2O_4)_3$	$ALi_3Ni(C_2O_4)_3$
	Li	1.08*	1.08	1.09
K	**M**	2.08*	2.09	2.16
	K	1.09*	0.94	0.96
	Li	1.05	1.05	1.04
Rb	**M**	2.07	2.05	2.16
	Rb	1.19	1.24	1.27
	Li	0.98	0.98	0.97
Cs	**M**	2.05	2.02	2.13
	Cs	1.55	1.61	1.64

5.3.6.3 Traditional Distortion Parameters

To accommodate the large variation in cation size the LiO_6 polyhedra become significantly distorted, depending on the relative sizes of the cations. The level of polyhedral distortion can be quantified using the parameters Δ and δ^2 which are defined by Equations 5.2 and 5.3[30,31] where d_n is the bond length, d the average bond length and θ the bond angle. The values of Δ and δ^2 were calculated for each of the eight new perovskite like compounds with the full results reported in Table 5.20 and Table 5.21.

Equation 5.2 $$\Delta = \frac{1}{6}[(d_n - d)d]^2$$

Equation 5.3 $$\delta^2 = \frac{1}{11}\sum(\theta_i - 90)^2$$

Table 5.20: Distortion parameter Δ as defined by Equation 5.2 calculated from bond angles determined from single crystal X-ray diffraction data collected at 173 K. Where A is an alkali metal (K, Rb, Cs) and M is a transition metal (Fe, Co, Ni)

Alkali Metal		$ALi_3Fe(C_2O_4)_3$	$ALi_3Co(C_2O_4)_3$	$ALi_3Ni(C_2O_4)_3$
K	Li	0.000939	0.000874	0.000775
	M	0	0	0
Rb	Li	0.001016	0.000919	0.001039
	M	0	0	0
Cs	Li	0.001520	0.001299	0.001204
	M	0	0	0

The results are in good agreement with the previously reported crystal structure of Yao *et al*., with no distortion observed in the Δ parameter of the transition metal polyhedra but an effect observed in the LiO_6 polyhedra.[17] The distortion of the bond lengths of the LiO_6 polyhedra remain almost unaffected by the choice of transition metal. However, the incorporation of the substantially larger A site cations leads to an increase in the distortion parameter Δ, with the largest values observed in $CsLi_3Fe(C_2O_4)_3$.

Table 5.21: Distortion parameter δ^2 as defined by Equation 5.3 calculated from bond angles determined from single crystal X-ray diffraction data collected at 173 K. Where A is an alkali metal (K, Rb, Cs) and M is a transition metal (Fe, Co, Ni)

Alkali Metal		$ALi_3Fe(C_2O_4)_3$	$ALi_3Co(C_2O_4)_3$	$ALi_3Ni(C_2O_4)_3$
K	Li	196.76	195.05	194.07
	M	47.94	32.63	21.24
Rb	Li	206.11	202.17	202.40
	M	49.44	32.64	22.16
Cs	Li	222.74	218.26	218.04
	M	54.41	33.99	23.83

The variation in bond angles were also determined using Equation 5.3. In general, the values are lower for transition metal polyhedra than LiO_6 octahedra but some clear trends throughout the series can be observed. The values of δ^2 for both polyhedra increase with the incorporation of the larger alkali metals but also decreases with transition metal radius.

5.3.6.4 Polyhedra Inscribing Ellipsoids For Analysing Crystallographic Environments (PIEFACE) Analysis

Another method for analysing the distortion of polyhedra is the recently developed PIEFACE (Polyhedra Inscribing Ellipsoids For Analysing Crystallographic Environments) program. [26] Existing methods measure the deviation from ideal polyhedra, which can be problematic when considering irregular polyhedra. The PIEFACE program uses a Khachiyan algorithm to determine the minimum value ellipsoid which encompasses each polyhedron.[32] The three principal radii of the ellipsoid are determined and then ordered as R1>R2>R3 and these values are used to quantify the distortion of the polyhedra.

The mean radii of the ellipsoids for each of the newly synthesised oxalate perovskite compounds are reported in Table 5.22. The average radius of the LiO_6 polyhedra is not significantly affected by alteration of the transition metal. However, the magnitude of the transition metal ellipsoid decreases across the periodic table in keeping with the relative radii of the three transition metals. The incorporation of the larger alkali metal cations increases the mean radii of each ellipsoid indicative of greater polyhedral distortion.

Table 5.22: Mean ellipsoid radius R (Å) calculated using the Minimum Bounding Ellipsoid (MBE) fitting algorithm within the Polyhedra Inscribing Ellipsoids For Analysis Crystallographic Environments (PIEFACE) software[26]

Alkali Metal		$ALi_3Fe(C_2O_4)_3$	$ALi_3Co(C_2O_4)_3$	$ALi_3Ni(C_2O_4)_3$
K	Li	2.092	2.091	2.089
	M	2.121	2.082	2.051
Rb	Li	2.103	2.103	2.104
	M	2.124	2.088	2.052
Cs	Li	2.127	2.128	2.130
	M	2.128	2.093	2.057

The standard deviation of the ellipsoid radii can also be determined to quantify the distortion of the polyhedra; their values are shown in Table 5.23. Similar trends to the mean radii are observed with transition metals having a negligible effect on the σR of the LiO_6 and a decrease in MO_6 across the periodic table. The standard deviation in the radii is noticeably increased upon the incorporation of both rubidium and caesium cations, indicative of higher polyhedral distortion.

Table 5.23: σ(R) standard deviation of R (the radius of three ellipsoids) calculated using the Minimum Bounding Ellipsoid (MBE) fitting algorithm within the Polyhedra Inscribing Ellipsoids For Analysis Crystallographic Environments (PIEFACE) software

Alkali Metal		$ALi_3Fe(C_2O_4)_3$	$ALi_3Co(C_2O_4)_3$	$ALi_3Ni(C_2O_4)_3$
K	Li	0.180	0.178	0.173
	M	0.096	0.069	0.069
Rb	Li	0.189	0.186	0.184
	M	0.111	0.080	0.076
Cs	Li	0.213	0.215	0.214
	M	0.135	0.099	0.091

The method also defined the parameter *S* which provides information on the shape of the ellipsoids. The value can be determined from the ellipsoid radii using Equation 5.4. The value of *S* can vary between −1 and 1 where $S < 0$ indicates an axially compressed ellipsoid, $S > 0$ an axially elongated ellipsoids and $S = 0$ a perfect sphere. These values were determined for each of the compositions and are reported in Table 5.24.

Equation 5.4

$$S = \frac{R3}{R2} - \frac{R2}{R1}$$

The behaviour of the ellipsoids is consistent for the whole family of hybrid perovskites compounds with all *S* values below zero indicating an axially compressed ellipsoid. The more extreme values are again observed in the caesium containing compounds. Little deviation is observed in the *S* parameters of the Li polyhedron with changing transition metals although there are differences observed for the transition metal polyhedra themselves.

Table 5.24: *S* parameters calculated using the Minimum Bounding Ellipsoid (MBE) fitting algorithm within the Polyhedra Inscribing Ellipsoids For Analysis Crystallographic Environments (PIEFACE) software

Alkali Metal		$ALi_3Fe(C_2O_4)_3$	$ALi_3Co(C_2O_4)_3$	$ALi_3Ni(C_2O_4)_3$
K	Li	−0.10709	−0.10027	−0.10672
	M	−0.09316	−0.06894	−0.07017
Rb	Li	−0.13363	−0.12131	−0.12126
	M	−0.10649	−0.07877	−0.07631
Cs	Li	−0.15986	−0.15163	−0.14713
	M	−0.12854	−0.09715	−0.09074

5.3.7 Oxalate Coordination Compounds

Whilst hydrothermal methods can be used to prepare the oxalate perovskite compounds, the reactions often result in mixtures of products. Several additional

oxalate coordination polymers with interesting structures have been synthesised in this manner and are reported in the following sections.

5.3.7.1 Rubidium Compounds

Table 5.25: Crystallographic and refinement details of $Rb_2Co(C_2O_4)_2.4H_2O$, $Rb_2CoCl_2(C_2O_4)$ and $Rb_2Cu(C_2O_4)_2.2H_2O$ from single crystal X-ray diffraction data collected at 173 K

Formula	$Rb_2Co(C_2O_4)_2.4H_2O$	$Rb_2CoCl_2(C_2O_4)$	$Rb_2Cu(C_2O_4)_2.2H_2O$
Formula Weight	477.97	388.79	444.54
Density (g cm^{-3})	2.687	2.981	2.883
Crystal System	Monoclinic	Orthorhombic	Triclinic
Space Group	$P2_1/n$	*Immm*	$P\bar{1}$
a/Å	7.8434(5)	5.3445(3)	6.9766(4)
b/Å	7.0795(4)	6.4380(4)	8.8546(6)
c/Å	10.9133(7)	12.5866(8)	8.9421(6)
α (˚)	90	90	107.643(8)
β (˚)	102.836(8)	90	98.028(8)
γ (˚)	90	90	97.650(8)
V/$Å^3$	590.84(7)	433.08(5)	512.17(6)
Z	2	2	2
Measured Ref	5799	2218	5301
Independent Ref	1343 [R(int) = 0.0387]	310 [R(int) = 0.0340]	2340 [R(int) = 0.0270]
Refined Parameter	104	22	165
GOOF	0.528	0.543	0.539
Final R Indices (I > 2σ(I))	R1 = 0.0208, wR2 = 0.0580	R1 = 0.0182, wR2 = 0.0561	R1 = 0.0225, wR2 = 0.0629

5.3.7.1.1 $Rb_2Co(C_2O_4)_2.4H_2O$

The rubidium cobalt oxalate compound was synthesised *via* a hydrothermal reaction of rubidium carbonate, sodium carbonate, cobalt chloride hexahydrate and oxalic acid

dihydrate in a 2:2:1:1.5 ratio and heating at 160 °C for a period of four days. The resulting product is a mixture of red/purple crystals and other solids. The crystals were analysed by single crystal X-ray diffraction and their crystallographic and refinement details are shown in Table 5.25. The crystal structure of $Rb_2Co(C_2O_4)_2.4H_2O$ is shown in Figure 5.15.

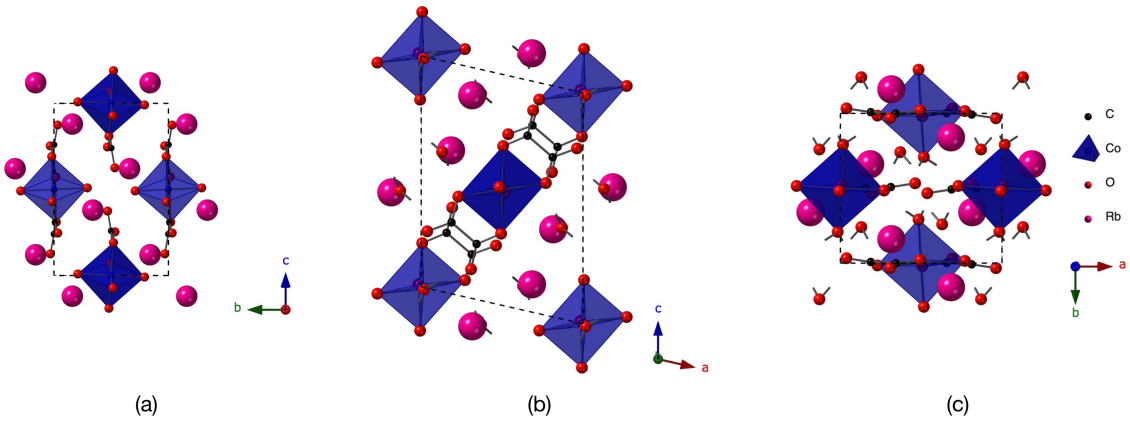

Figure 5.15: Crystal structure of $Rb_2Co(C_2O_4)_2.4H_2O$ viewed along the *a*, *b* and *c* axes derived from single crystal X-ray diffraction data collected at 173 K

The compound adopts the monoclinic $P2_1/n$ space group with unit cell parameters of a = 7.8434(5) Å, *b* = 7.0795(4) Å, *c* = 10.9133(7) Å and β = 102.836(8)°. The structure consists of isolated Co^{2+} octahedra which are coordinated to two oxalate ligands and two water molecules; the Co^{2+} coordination environment is shown in Figure 5.16. The bond lengths at the cobalt centre are reported in Table 5.26 with an average Co-O bond length of 2.080 Å and a bond valence sum of 2.10.

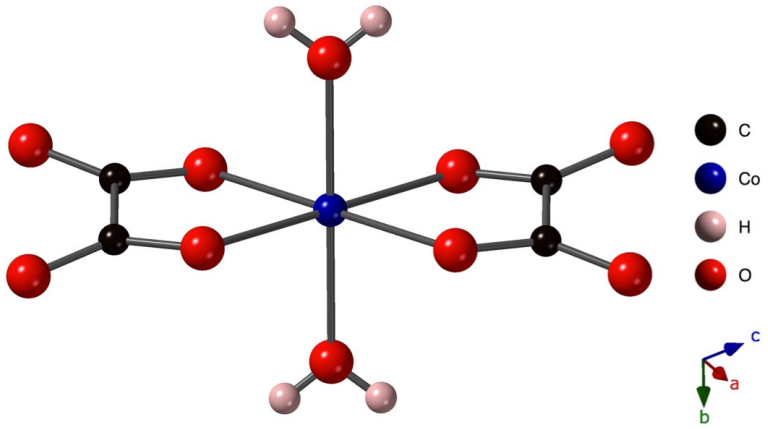

Figure 5.16: Coordination environment of Co^{2+} in $Rb_2Co(C_2O_4)_2.4H_2O$ derived from single crystal X-ray diffraction data collected at 173 K

Table 5.26: Selected bond lengths (Å) and bond valence sums (valence units) of $Rb_2Co(C_2O_4)_2.4H_2O$ derived from single crystal X-ray diffraction data collected at 173 K

Bond	Bond Length (Å)
Co-O	2.0694(16) × 2
	2.0744(14) × 2
	2.0961(15) × 2
BVS	2.10

5.3.7.1.2 $Rb_2CoCl_2(C_2O_4)$

A second rubidium containing oxalate coordination compound was synthesised in the form of $Rb_2CoCl_2(C_2O_4)$. Rubidium carbonate, sodium carbonate, cobalt chloride hexahydrate and oxalic acid dihydrate were used in a 1:1.5:1:1.5 ratio and heated at 190 °C for four days. The products were a mixture of pink powder and purple crystals which were analysed by single crystal X-ray diffraction and their crystallographic and refinement details are given in Table 5.25. The structure crystallises in the orthorhombic *Immm* space group and its unit cell parameters are a = 5.3445(3) Å, b = 6.4380(4) Å and c = 12.5866(8) Å. The crystal structure derived from X-ray diffraction data is shown in Figure 5.17.

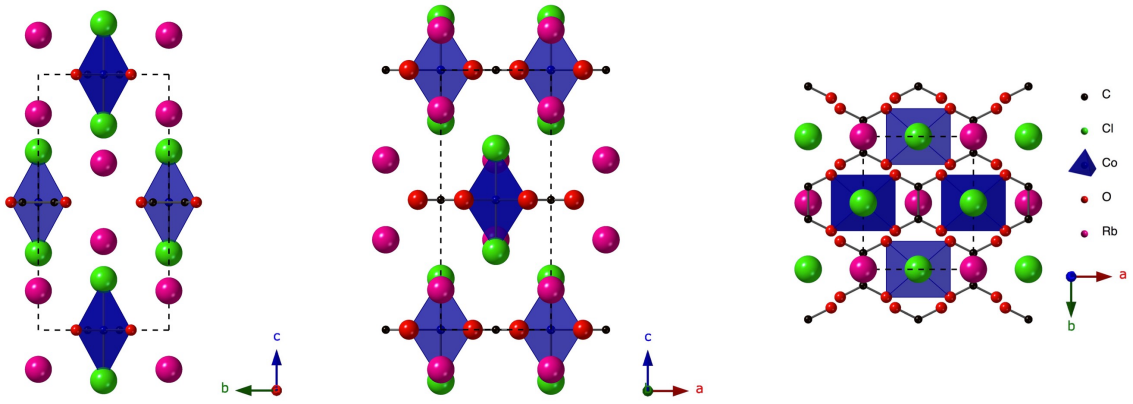

(a) (b) (c)

Figure 5.17: Crystal structure of $Rb_2CoCl_2(C_2O_4)$ viewed along the *a*, *b* and *c* axes derived from single crystal X-ray diffraction data collected at 173 K

The structure consists of infinite $CoCl_2(C_2O_4)$ chains along the *a* axis, with each of the Co^{2+} cations coordinated to two mutually *trans*-oxalate anions which act as tetradentate bridging ligands. Each of the metal centres is linked to the next *via* one oxalate ligand, whilst the remainder of the coordination sphere is occupied by two mutually *trans*-chloride anions as shown in Figure 5.18. The determined cobalt lengths are reported in Table 5.27 with Co-O bond lengths of 2.0596(18) Å, Co-Cl bond lengths of 2.4864 Å and a bond valence sum of 2.01. Whilst the compound adopts a centrosymmetric space group and therefore will not have ferroelectric properties, the presence of cobalt oxalate chains could provide magnetic exchange pathways. The magnetic properties of the compound should be investigated in the future once a pure sample can be synthesised.

Table 5.27: Selected bond lengths (Å) and bond valence sum (valence units) of $Rb_2CoCl_2(C_2O_4)$ derived from single crystal X-ray diffraction data collected at 173 K

Bond	Bond Length (Å)
Co-O	2.0596(18)
Co-O	2.0596(18)
Co-O	2.0596(18)
Co-O	2.0596(18)
Co-Cl	2.4864(9)
Co-Cl	2.4864(9)
BVS	2.03

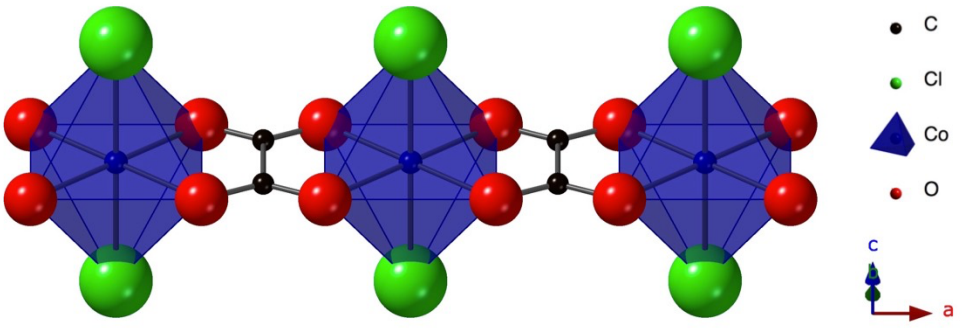

Figure 5.18: Co^{2+} chains in $Rb_2CoCl_2(C_2O_4)$ derived from single crystal X-ray diffraction data collected at 173 K

5.3.7.1.3 $Rb_2Cu(C_2O_4)_2.2H_2O$

A sample of $Rb_2Cu(C_2O_4)_2.2H_2O$ was also synthesised during the course of the project using the starting reagents rubidium carbonate, lithium carbonate, copper chloride dihydrate and oxalic acid dihydrate in a 1:2:1.5:4 ratio. The reactants were heated at 190 °C for a period of four days, resulting in a product consisting of a mixture of different solids. Single crystals were extracted from the mixture and analysed by single crystal X-ray diffraction. The crystallographic and refinement details are shown in Table 5.25 and the structure has been previously reported by Alig *et al.*[33] The crystal structure is shown in Figure 5.19 and selected bond lengths in Table 5.28.

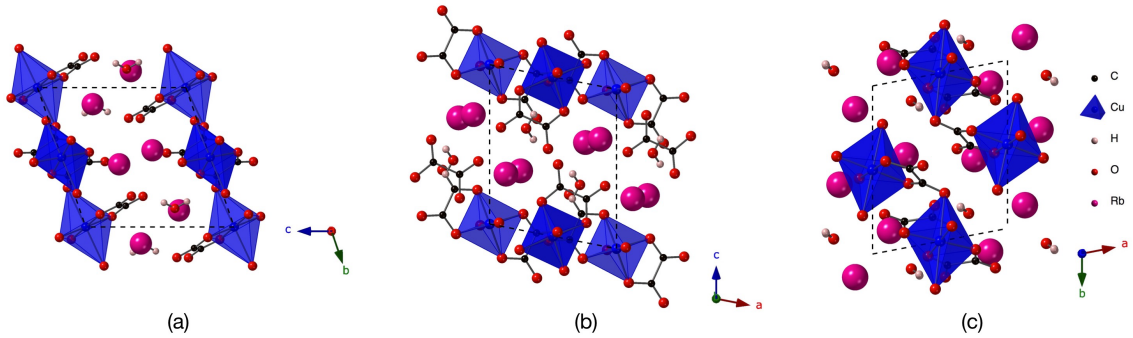

Figure 5.19: Crystal structure of $Rb_2Cu(C_2O_4)_2.2H_2O$ viewed along the *a*, *b* and *c* axes derived from single crystal X-ray diffraction data collected at 173 K

Table 5.28: Selected bond lengths (Å) and bond valence sums (valence units) of $Rb_2Cu(C_2O_4)_2.2H_2O$ derived from single crystal X-ray diffraction data collected at 173 K

Bond	Cu1	Cu2
Cu-O	1.942(2)	1.9399(19)
	1.946(2)	1.9530(19)
	2.620(5)	2.479(5)
BVS	2.11	2.17

5.3.7.2 Lithium and potassium containing compounds

Table 5.29: Crystallographic and refinement details of $Li_4Co(C_2O_4)_3$, $K_2Li_2Cu(C_2O_4)_3.2H_2O$ and $K_2Cu(C_2O_4)_3.2H_2O$ from single crystal X-ray diffraction data collected at 173 K

Formula	$Li_4Co(C_2O_4)_3$	$K_2Li_2Cu(C_2O_4)_3.2H_2O$	$K_2Cu(C_2O_4)_3.2H_2O$
Formula Weight	350.75	455.7	353.81
Density (g cm^{-3})	2.537	2.310	2.376
Crystal System	Monoclinic	Triclinic	Triclinic
Space Group	$P2_1/c$	$P\bar{1}$	$P\bar{1}$
a/Å	9.3597(7)	6.1847(4)	6.9213(4)
b/Å	5.0579(4)	7.2575(5)	8.6768(6)
c/Å	10.0364(8)	8.1795(5)	8.9562(6)
α (˚)	90	101.327(11)	108.028(9)
β (˚)	104.892(9)	91.723(11)	99.720(9)
γ (˚)	90	113.563(11)	97.410(9)
V/$Å^3$	459.17(6)	327.56(5)	494.60(6)
Z	2	1	2
Measured Ref	4455	3403	5135
Independent Ref	1054 [R(int) = 0.0364]	1500 [R(int) = 0.0951]	2259 [R(int) = 0.0285]
Refined Parameter	106	132	173
GOOF	0.836	0.718	0766
Final R Indices (I > 2σ(I))	R1 = 0.0323, wR2 = 0.0913	R1 = 0.0447, wR2 = 0.1206	R1 = 0.0299, wR2 = 0.0860

5.3.7.2.1 $Li_4Co(C_2O_4)_3$

The compound was synthesised *via* the reaction of sodium carbonate, lithium carbonate, cobalt chloride hexahydrate and oxalic acid in a 1:2:1:4 ratio. The reaction utilised a hydrothermal method and the reagents were heated at 160 °C for a period of four days. The products were a mixture of colourless and purple crystals. The colourless single crystals were analysed by single crystal X-ray diffraction with their crystallographic and refinement details shown in Table 5.29. The compound adopts the monoclinic $P2_1/c$ space group with unit cell parameters of a = 9.3597(7) Å, b = 5.0579(4) Å, c = 10.0364(8) Å and β = 104.892(9)°. The crystal structure is shown in Figure 5.20 and the bond lengths are reported in Table 5.30.

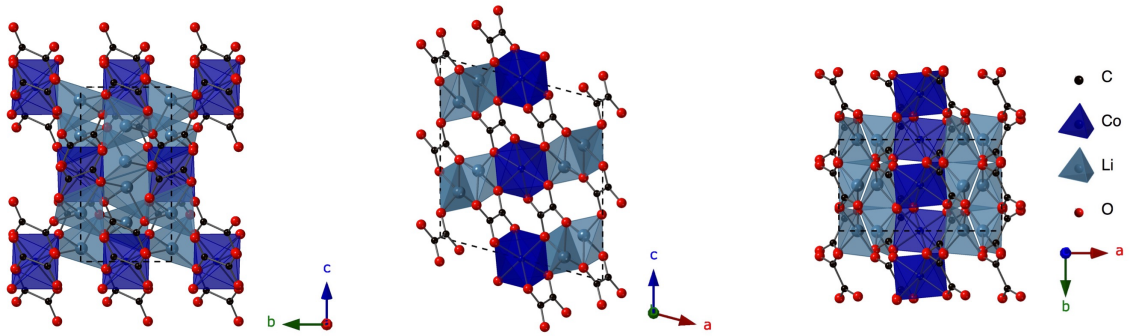

Figure 5.20: Crystal structure of $Li_4Co(C_2O_4)_3$ viewed along the a, *b* and *c* axes derived from single crystal X-ray diffraction data collected at 173 K.

The Co^{2+} atoms are coordinated to six oxalate oxygens which form infinite chains along the *c* direction. Each of the cobalt atoms are linked to the next by two oxalates which act as tridentate bridging ligands. The average Co-O bond length is 2.122 Å and the bond valence sum of the Co^{2+} is 1.91. The presence of the cobalt oxalate chains could provide interesting magnetic properties and the high concentration of Li^+ cations might have interesting electrochemical properties.

Table 5.30: Selected bond lengths (Å) and bond valence sums (valence units) of $Li_4Co(C_2O_4)_3$ derived from single crystal X-ray diffraction data collected at 173 K

Bond	Bond Length (Å)
Co-O	2.20455(18) × 2
	2.1027(19) × 2
	2.2174(18) × 2
BVS	1.91
Li1-O	1.919(5)
	2.003(5)
	2.014(5)
	2.118(5)
BVS	0.93
Li2-O	1.898(5)
	1.981(5)
	2.011(5)
	2.177(6)
	0.94

5.3.7.2.2 $K_2Li_2Cu(C_2O_4)_3.2H_2O$

A new copper oxalate coordination polymer was synthesised in the form of $K_2Li_2Cu(C_2O_4)_3.2H_2O$ using potassium carbonate, lithium carbonate, copper chloride dihydrate and oxalic acid dihydrate in a 1:3:1:3 ratio. The reagents were heated in a teflon lined autoclave at 190 °C for a period of four days. The resulting products were analysed by single crystal X-ray diffraction with the crystallographic and refinement details shown in Table 5.29 and the crystal structure of the compound is shown in Figure 5.21. Despite the numerous reaction conditions and ratios of reagent attempted, a compound with the same stoichiometry as the oxalate perovskites was never synthesised. Instead, the new compound contains a 2:2 ratio of potassium and lithium

cations with a substantially different structure. The compound adopts the triclinic $P\bar{1}$ space group and the unit cell parameters are shown in Table 5.29.

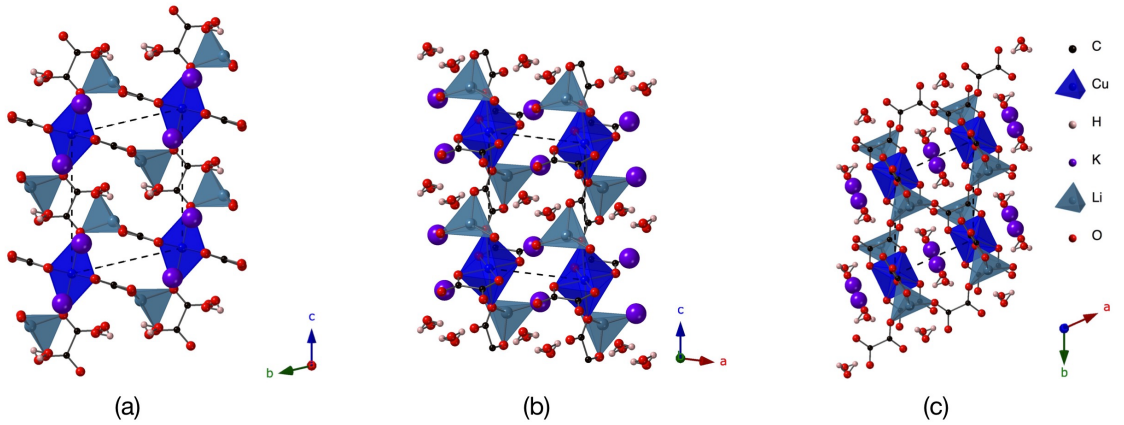

Figure 5.21: Crystal structure of $K_2Li_2Cu(C_2O_4)_3.2H_2O$ viewed along the *a*, *b* and *c* axes derived from single crystal X-ray diffraction data collected at 173 K

Selected bond lengths and bond valence sums are shown in Table 5.31. The Cu^{2+} cations with their d^9 electron configuration display the Jahn-Teller effect with significant elongation of the axial Cu-O bond lengths. The equatorial Cu-O bond lengths are 1.939(3) Å and 1.945(3) Å, whereas the axial Cu-O bond lengths are 2.473(7) Å. The coordination environment consists of four oxalate anions only two of which act as bidentate bridging ligands linking the Cu^{2+} cations along the *c* axis as shown in Figure 5.22.

Table 5.31: Selected bond lengths (Å) and bond valence sums (valence units) of $K_2Li_2Cu(C_2O_4)_3.2H_2O$ derived from single crystal X-ray diffraction data collected at 173 K

Bond	Bond Length (Å)
Cu-O	1.939(3) × 2
	1.945(3) × 2
	2.473(7) × 2
BVS	2.20
Li-O	1.901(7)
	1.908(8)
	1.996(8)
	2.050(9)
BVS	1.06

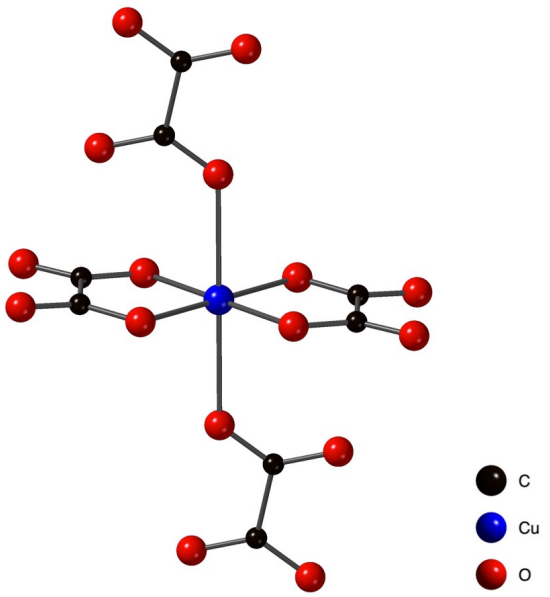

Figure 5.22: Coordination environment of Cu^{2+} in $K_2Li_2Cu(C_2O_4)_3.2H_2O$ derived from single crystal X-ray diffraction data collected at 173 K

5.3.7.2.3 $K_2Cu(C_2O_4)_3.2H_2O$

A further attempt to synthesise a copper analogue of the oxalate hybrid perovskites resulted in the synthesis of $K_2Cu(C_2O_4)_3.2H_2O$. The reaction mixture consisted of a 1:3:1.5:4 ratio of potassium carbonate, lithium carbonate, copper oxalate and oxalic acid dihydrate. The reaction was carried out at 190 °C over the course of four days. The product was a mixture of colourless and blue crystals which were analysed by single crystal X-ray diffraction. The crystallographic and refinement details of the blue crystals are shown in Table 5.29, the crystal structure shown in Figure 5.23 and selected bond lengths in Table 5.32. The crystal structure has been previously reported by Zhang *et al.*[34] The compound can be produced from the dehydration of $K_2Cu(C_2O_4)_2.4H_2O$ and can be further dehydrated to form $K_2Cu(C_2O_4)_2$.[34]

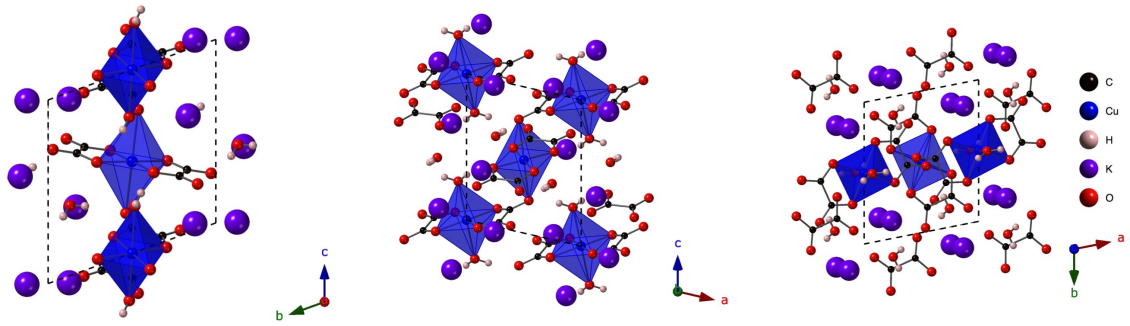

(a) (b) (c)

Figure 5.23: Crystal structure of $K_2Cu(C_2O_4)_3.2H_2O$ viewed along the a, *b* and *c* axes derived from single crystal X-ray diffraction data collected at 173 K

Table 5.32: Selected bond lengths (Å) and bond valence sums (valence units) of $K_2Cu(C_2O_4)_3.2H_2O$ derived from single crystal X-ray diffraction data collected at 173 K

Bond	Bond Length (Å)
Cu1-O	1.939(2) × 2
	1.950(2) × 2
	2.592(5) × 2
BVS	2.13
Cu2-O	1.944(2) × 2
	1.952(2) × 2
	2.435(3) × 2
BVS	2.19

5.4 Conclusions

Eight new hybrid perovskites utilising the oxalate ligand as the X anion have been synthesised using conventional hydrothermal methods. The reaction conditions have been optimised for each of the composition and pure samples of $KLi_3Fe(C_2O_4)_3$, $KLi_3Co(C_2O_4)_3$ and $KLi_3Ni(C_2O_4)_3$ were obtained. Equivalent compounds incorporating the alkali metals rubidium and caesium were also synthesised resulting in six further perovskite-like compounds, although purity of these products was poor. All eight compounds are isostructural and adopt the trigonal $R\bar{3}c$ space group with unit cell parameters of a ~11.5 Å and c ~15 Å. The binding modes of the oxalic acid group remain constant across the series of compounds.

The structural flexibility of the system was tested by the incorporation of both rubidium and caesium into the same structure type. The effect of these substitutions upon the distortions of the B site polyhedra was quantified using bond valence sum calculations, tolerance factors, distortion parameters and the PIEFACE program. Bond valence sums of K, Li, Fe, Co and Ni were all within the expected range, however, the calculated values for Cs and Rb were substantially higher than ideal.

Whilst these compounds can be regarded as perovskite-like, their structures are not conventional. However, tolerance factor calculations can provide an insight into the relative sizes of the A, B and X ions. The calculated tolerance factors suggested that both the rubidium and caesium cations are too large to adopt a 'perovskite-like' structure, however it should be noted that the occupancy of the A site is only ¼. Nevertheless, it is noteworthy that these cations can be accommodated in such a 'cramped' environment; there are no corresponding examples of traditional ABO_3 perovskites, for A = Rb or Cs. Conversely, attempts to substitute K for the smaller Na cation in this family proved unsuccessful, thus defining an unusually 'large' requirement for A-site cations in this structure type. Since the structure could accommodate the caesium cation, the largest monoatomic cation, compositions incorporating methylammonium were also

attempted. However, its effective radius is significantly larger (methylammonium 2.17 Å, Cs 12-coord 1.88 Å) and crystalline samples were never obtained.[35]

The variation of bond lengths and angles was also determined to quantify the polyhedral distortions of each composition. The values of Δ, based upon the bond lengths of each polyhedra, are zero for each of the transition metal octahedra but are more significant for the LiO_6 octahedra. The general trend in Δ values is an increase with the incorporation of rubidium and caesium. δ^2 values calculated from polyhedral bond angles display very similar trends. Whilst the variation at the transition metal is no longer zero, their values are significantly lower than those observed for the lithium octahedron and in general there is an increase in variation which is accompanied by an increase in radii of the alkali metal.

Further analysis of polyhedral distortion was carried out using the PIEFACE program. The results were in agreement with the earlier analysis with greater distortions observed for the LiO_6 polyhedra versus the MO_6 polyhedra and also increases in distortion with increasing alkali metal radii.

The magnetic properties of $KLi_3Fe(C_2O_4)_3$, $KLi_3Co(C_2O_4)_3$ and $KLi_3Ni(C_2O_4)_3$ were studied using a SQUID instrument between 300 K and 2 K. In the case of $KLi_3Co(C_2O_4)_3$ and $KLi_3Ni(C_2O_4)_3$ the data did not reveal any evidence of magnetic ordering. Curie-Weiss fitting of the data points between 300 K and 150 K revealed slightly negative Weiss constants and magnetic moments of 4.82 μ_B and 3.62 μ_B for $KLi_3Co(C_2O_4)_3$ and $KLi_3Ni(C_2O_4)_3$ respectively. More unusual behaviour was observed in the $KLi_3Fe(C_2O_4)_3$ sample with a noticeable anomaly in the magnetic susceptibility around 100 K. Further experiments would be warranted to investigate these properties fully.

The products of hydrothermal syntheses were often a mixture of crystals/solids and several other oxalate coordination compounds were synthesised during the project. Four new oxalate containing compounds were synthesised in this way namely,

$Rb_2Co(C_2O_4)_2.4H_2O$, $Rb_2CoCl_2(C_2O_4)$, $Li_4Co(C_2O_4)_3$ and $K_2Li_2Cu(C_2O_4)_3.2H_2O$. The latter three contain transition metal chains linked by oxalate bridging ligands which could result in interesting magnetic properties. The high lithium content of $Li_4Co(C_2O_4)_3$ would also be of significant interest for battery applications and both warrant investigation in further detail.

5.5 References

1 R. D. J. Tilley, *Perovskites*, John Wiley & Sons Inc., Chichester, 1st edn., 2016.

2 W. Yao, A. R. Armstrong and P. Lightfoot, *Zeitschrift fur Anorg. und Allg. Chemie*, 2016, **642**, 1345–1349.

3 A. Kojim, K. Teshima, Y. Shirai and T. Miyasaka, *J. Am. Chem. Soc.*, 2009, **131**, 6050–6051.

4 D. B. Mitzi, C. A. Feild, W. T. A. Harrison and A. M. Guloy, *Nature*, 1994, **369**, 467–469.

5 P. Jain, V. Ramachandran, R. J. Clark, D. Z. Hai, B. H. Toby, N. S. Dalal, H. W. Kroto and A. K. Cheetham, *J. Am. Chem. Soc.*, 2009, **131**, 13625–13627.

6 X. H. Zhao, X. C. Huang, S. L. Zhang, D. Shao, H. Y. Wei and X. Y. Wang, *J. Am. Chem. Soc.*, 2013, **135**, 16006–16009.

7 Ľ. Smrčok, H. Hagemann, P. Schouwink, R. Černý, A. Tissot, T. R. Jensen and M. B. Ley, *Nat. Commun.*, 2014, **5**, 1–10.

8 S. Yang, G. Li, S. Tian, F. Liao and J. Lin, *Eur. J. Inorg. Chem.*, 2006, 2850–2854.

9 G. M. Miskelly, C. R. Clark, J. I. M. Simpson and D. A. Buckingham, *Inorg. Chem.*, 1983, **22**, 3237–3241.

10 D. Abeysinghe, M. D. Smith, J. Yeon, G. Morrison and H. C. Zur Loye, *Cryst. Growth Des.*, 2014, **14**, 4749–4758.

11 J. S. Miller and M. Drillon, *Magnetism: Molecules to Materials IV*, Wiley-VCH, Weinheim, 2002, vol. 5.

12 E. J. Baran, *J. Coord. Chem.*, 2014, **67**, 3734–3768.

13 J. Fan, W. Sun, T. Okamura, K. Yu and N. Ueyama, *Inorganica Chim. Acta*, 2001, **319**, 240–246.

14 W. Yao, P. Lightfoot, T. Li, S. L. Lee, M. Xia and L. Clark, *Chem. Mater.*, 2017, **29**, 6616–6620.

15 W. Yao, M. Sougrati, K. Hoang, J. Hui, P. Lightfoot and A. R. Armstrong, *Chem. Mater.*, 2017, **29**, 2167–2172.

16 J. H. Li, H. Liu, L. Wei and G. M. Wang, *Solid State Sci.*, 2015, **48**, 225–229.

17 W. Yao, Y. Guo and P. Lightfoot, *Dalt. Trans.*, 2017, **46**, 13349–13351.

18 W. Gong, H. Yun, J. B. Ning, J. E. Greedan, W. R. Datars and C. V Stager, *J. Solid*

State Chem., 1991, **90**, 320–330.

19 Rigaku, CrystalClear. Rigaku Corporation, Tokyo, Japan, 2014.

20 G. M. Sheldrick, *Acta Crystallogr. Sect. C Struct. Chem.*, 2015, **71**, 3–8.

21 L. J. Farrugia, *J. Appl. Crystallogr.*, 2012, **45**, 849–854.

22 H. M. Rietveld, *J. Appl. Crystallogr.*, 1969, **2**, 65–71.

23 A. C. Larson and R. B. Von Dreele, *General Structure Analysis System (GSAS)*, 2004.

24 B. H. Toby, *J. Appl. Crystallogr.*, 2001, **34**, 210–213.

25 F. A. Cotton and G. Wilkinson, *Advanced Inorganic Chemistry: a Comprehensive Text*, John Wiley & Sons Ltd., New York, 2nd edn., 1966.

26 J. Cumby and J. P. Attfield, *Nat. Commun.*, 2017, **8**, 1–8.

27 B. Bachmann and B. G. Muller, *Zeitschrift fur Anorg. und Allg. Chemie*, 1993, **619**, 387–391.

28 V. Kaiser, M. Otto, F. Binder and D. Babel, *Z. anorg. allg. Chem.*, 1990, **585**, 93–104.

29 P. Berastegui, S. Hull and S.-G. Eriksson, *J. Phys.*, 2001, **13**, 5077–5088.

30 M. W. Lufaso and P. M. Woodward, *Acta Crystallogr. Sect. B Struct. Sci.*, 2004, **60**, 10–20.

31 M.E. Fleet, *Mineral. Mag.*, 1976, **40**, 531–3.

32 M. J. Todd and E. A. Yildirim, *Discret. Appl. Math.*, 2007, **155**, 1731–1744.

33 E. Alig, C. Buchsbaum, L. Fink and L. Bolte, *CSD Commun.*, 2003.

34 B. Zhang, Y. Zhang, J. Zhang, X. Yan and D. Zhu, *CrystEngComm*, 2016, **18**, 5062–5065.

35 G. Kieslich, S. Sun and A. K. Cheetham, *Chem. Sci.*, 2014, **5**, 4712–4715.

Chapter 6 Conclusions and Future Work

6.1 Conclusions

The synthesis, structure and properties of several carboxylate coordination polymers have been studied. The compounds were synthesised using both slow evaporation and hydrothermal methods, typically in the form of single crystals, which were analysed using X-ray and neutron diffraction. Further characterisation was carried out using thermal analysis, electron microscopy and magnetometry.

The ferroelectric phase transition of the metal-organic ferroelectric TSCC was described in detail in chapter 3 using a combination of single crystal X-ray and neutron diffraction experiments. The hydrogen bonding network of the systems were studied in detail using neutron diffraction data to elucidate their role in the ferroelectric properties of the compound. However, the data revealed minimal changes to the hydrogen bond lengths and angles as a result of the ferroelectric phase transition suggesting that they did not play a critical role in these properties. The detailed crystallographic study was able to identify the largest structural changes which occur during the phase transition. These are observed in the Ca-O-C bond angles which deviate by up to 12˚. The structure was determined at multiple temperatures between 300 K and 20 K to investigate potential low temperature phase transitions which were suggested in the earlier literature.[1] However the evolution of unit cell parameters, bond lengths and ADPs did not suggest the presence of any alternate phases and the structural $Pn2_1a$ model remained valid even at the lowest temperature of 20 K. This discrepancy could be due to local structure effects or dynamics which are not easily observed by diffraction. The X-ray diffraction data has unearthed new evidence of ferrielectricity in TSCC with the sarcosine molecules displaced in a '2 up 1 down' arrangement, resulting in a net displacement. Whilst our values do not account for the charge distribution within the sarcosine molecules, the data are consistent with ferrielectricity and are supported by the polarisation versus electric field data collected, which contained a large bias in the hysteresis loop.[2]

Chapter 4 reported the syntheses of seven TSCC-related compounds from simple slow evaporation. The new compounds incorporated Mg, Sr, Mn, I and Br to study their effect upon the ferroelectric properties of TSCC. Each of the compounds were analysed by X-ray diffraction and thermal analysis techniques. None of the compounds adopted a polar space group which would allow ferroelectric properties and the DSC data did not suggest the presence of a phase transition to a polar phase at low temperatures. The types of structures formed appears to be closely linked with the relative sizes of the metal cation and halide ions. The incorporation of larger cations led to an increase in the coordination number of the metal and resulted in corner sharing of the polyhedral chains. For relatively small metal cations, the composition was typically altered to a 2:1 ratio of sarcosine to metal cation (as opposed to 3:1 in the original compound) and the remainder of the coordination spheres were occupied by water molecules.

The final results chapter concerned the perovskite-like family of oxalate coordination polymers based on $KLi_3Fe(C_2O_4)_3$ and $NH_4Li_3Fe(C_2O_4)_3$ with the general formula $ALi_3M(C_2O_4)_3$, where A is an alkali metal and M a divalent transition metal.[3,4] Eight new isostructural compounds including K, Rb, Cs, Fe, Co and Ni were synthesised to explore the structural flexibility of the system. Surprisingly, both the rubidium and caesium containing analogues still adopt the perovskite-like structure despite their substantially larger radii (K^+ = 1.64 Å, Rb^+ = 1.72 Å and Cs^+ = 1.88 Å). The inclusion of both rubidium or caesium results in significant distortion of the LiO_6 polyhedra, which was quantified using distortion parameters and the PIEFACE program. The largest distortions are observed with the inclusion of the caesium cation, although no significant effect is observed with transition metal substitution. Four new oxalate-containing compounds $Rb_2Co(C_2O_4)_2.4H_2O$, $Rb_2CoCl_2(C_2O_4)$, $K_2Li_2Cu(C_2O_4)_3$ and $Li_4Co(C_2O_4)_3$ were also synthesised during this work.

6.2 Future work

Whilst the crystallographic data did not suggest any additional phase transitions at low temperature despite the strong supporting evidence in the earlier literature, the data are limited to relatively few different temperatures. It would be desirable to collect powder X-ray diffraction data at much closer intervals between 300 K and 20 K at a high intensity (synchrotron) X-ray source. The unit cell parameters could be determined from the powder diffraction data using the Rietveld method to unambiguously investigate the potential phase transitions.

Several compositions of TSCC-related compounds have been synthesised during the course of the project, however, the syntheses of magnesium iodide, manganese bromide and strontium iodide were never attempted and these compound should be synthesised and analysed for completeness. Whilst the X-ray diffraction data and thermal analysis did not reveal any evidence of a phase transition to a potentially polar space group, the measurements were limited to a lowest temperature of 90 K. The compounds should be analysed below this point to investigate any potential phase transitions. Additionally, one of the new TSCC related compounds TSMnI consists of Mn^{2+} chains which are connected by sarcosine bridging ligands which could provide magnetic exchange pathways, therefore, the magnetic properties of the compound should also be investigated.

Eight new oxalate perovskite compounds were synthesised utilising different A and B site cations. However, ammonium-containing analogues were never synthesised in the form of high-quality crystals or as a pure compound despite $NH_4Li_3Fe(C_2O_4)_3$ being previously reported in the literature. The compounds $NH_4Li_3Co(C_2O_4)_3$ and $NH_4Li_3Ni(C_2O_4)_3$ should be synthesised and their structures analysed for completeness. It is likely that Zn^{2+} could also be incorporated, on size grounds. Additionally, since the relatively large caesium cation can be incorporated in the structure, it would be of interest to synthesise methyl ammonium analogues. The attempted syntheses of the

oxalate perovskites also resulted in three new oxalate bridged transition metal complexes, $Rb_2CoCl_2(C_2O_4)$, $K_2Li_2Cu(C_2O_4)_3$ and $Li_4Co(C_2O_4)_3$. The presence of oxalate bridging ligands and the formation of infinite M^{2+} chains could be interesting in regard to the materials magnetic properties. The compounds were originally synthesised as by-product and the purity of each will need to be improved before analysis of their magnetic properties. Additionally, the $Li_4Co(C_2O_4)_3$ compound could be of interest for battery materials due to its high quantity of lithium and further studies would be worthwhile.

6.3 References

1 S. P. P. Jones, D. M. Evans, M. A. Carpenter, S. A. T. Redfern, J. F. Scott, U. Straube and V. H. Schmidt, *Phys. Rev. B*, 2011, **83**, 094102.

2 J. F. Scott, F. D. Morrison, A. M. Z. Slawin, P. Lightfoot, R. Clulow, A. S. A. Gherson, A. M. Bumstead, J. Gardner, S. C. Capelli, M. R. Probert, S. Sahoo, J. S. Young, R. S. Katiyar and E. K. H. Salje, *Phys. Rev. B*, 2017, **95**, 094119.

3 W. Yao, Y. Guo and P. Lightfoot, *Dalt. Trans.*, 2017, **46**, 13349–13351.

4 J. H. Li, H. Liu, L. Wei and G. M. Wang, *Solid State Sci.*, 2015, **48**, 225–229.

Appendix A

Table A1: Atomic displacements (atomic coordinates) of each of the sarcosine atoms along the polar b axis relative to the paraelectric phase at 295 K

Atomic Labels	Temperature (K)							
	20	**35**	**55**	**75**	**100**	**100**	**110**	**120**
O1	-0.00274	-0.00258	-0.00245	-0.00236	-0.0018	-0.00160	-0.0017	-0.0013
O2	0.00203	0.00198	0.00182	0.00175	0.0014	0.00130	0.0006	0.0008
C1	-0.0012	-0.0013	-0.0012	-0.0011	-0.0011	-0.00010	-0.001	-0.0006
C2	-0.0022	-0.0021	-0.002	-0.0018	-0.001	-0.00060	-0.0006	-0.0003
C3	-0.0021	-0.0023	-0.0022	-0.002	-0.0015	-0.00100	-0.0011	-0.0015
N1	-0.00209	-0.00213	-0.00205	-0.0017	-0.0015	-0.00100	-0.0016	-0.0011
Sarcosine 1	-0.0083	-0.00843	-0.00808	-0.00721	-0.0055	-0.00300	-0.0054	-0.004
O3A	-0.00893	-0.00882	-0.00819	-0.00728	-0.00543	-0.00595	-0.00495	-0.00395
O4A	0.01141	0.0112	0.01042	0.00952	0.00699	0.00714	0.00644	0.00484
C4A	0.00161	0.00154	0.00125	0.00118	0.00098	0.00088	-0.00012	0
C5A	0.00376	0.00371	0.00342	0.00321	0.00262	0.00242	0.00242	0.00162
C6A	-0.00449	-0.0044	-0.0042	-0.0039	-0.0033	-0.00270	-0.0034	-0.0033
N2A	-0.00398	-0.00374	-0.00352	-0.00337	-0.00247	-0.00227	-0.00197	-0.00207
Sarcosine 2A	-0.00062	-0.00051	-0.00082	-0.00064	-0.00061	-0.00048	-0.00158	-0.00286
O3B	-0.00545	-0.00546	-0.00505	-0.00457	-0.00328	-0.00305	-0.00365	-0.00215
O4B	0.00988	0.00957	0.00893	0.00811	0.00618	0.00706	0.00576	0.00436
C4B	0.00217	0.00195	0.00169	0.00172	0.00132	0.00092	0.00012	0.00082
C5B	0.00367	0.00359	0.00335	0.00334	0.00278	0.00308	0.00298	0.00208
C6B	-0.00086	-0.00102	-0.0009	-0.0006	-0.0003	-0.00010	-0.0002	1E-04
N2B	-0.00094	-0.00079	-0.0007	-0.00063	-1E-05	0.00017	-0.00053	0.00037
Sarcosine 2B	0.00847	0.00784	0.00732	0.00737	0.00669	0.00808	0.00448	0.00558